Physics-Based Pressure Field and Fluid Forcing Inference for Cylindrical Bluff Body Experiments

by

Jeffrey E.J. McClure

A thesis
presented to the University of Waterloo
in fulfillment of the
thesis requirement for the degree of
Doctor of Philosophy
in
Mechanical and Mechatronics Engineering

Waterloo, Ontario, Canada, 2024

Examining Committee Membership

The following served on the Examining Committee for this thesis. The decision of the Examining Committee is by majority vote.

External Examiner	Prof. Andrea Sciacchitano Associate Professor Faculty of Aerospace Engineering Delft University of Technology
Supervisor	Prof. Serhiy Yarusevych Professor Dept. of Mechanical and Mechatronics Engineering University of Waterloo
Internal Member	Prof. Sean Peterson Professor Dept. of Mechanical and Mechatronics Engineering University of Waterloo
Internal Member	Prof. Kyle Daun Professor Dept. of Mechanical and Mechatronics Engineering University of Waterloo
Internal Member	Dr. Zhao Pan Assistant Professor Dept. of Mechanical and Mechatronics Engineering University of Waterloo
Internal-external Member	Prof. Marek Stastna Professor Dept. of Applied Mathematics University of Waterloo

Author's Declaration

This thesis consists of material all of which I authored or co-authored: see Statement of Contributions included in the thesis. This is a true copy of the thesis, including any required final revisions, as accepted by my examiners.

I understand that my thesis may be made electronically available to the public.

Statement of Contributions

Jeffrey McClure was the sole author of **Chapters 1, 2, 8, 9**, and **Appendices A, B**. These sections were written under the supervision of Prof. Serhiy Yarusevych, and are not intended for journal publication. Funding for this research was provided by the Natural Sciences and Engineering Research Council (NSERC) and the Ontario Graduate Scholarship Program (OGS).

The results chapters consist of five manuscripts written for journal publication. Details on exceptions to sole authorship are as follows:

Chapter 3:

Performed under the supervision of Prof. Serhiy Yarusevych at the University of Waterloo.

- Citation: McClure, J., and Yarusevych, S. (2017) "Optimization of planar PIV-based pressure estimation in laminar and turbulent wakes," *Experiments in Fluids*, 58(5), 62.

Chapter 4:

Performed under the supervision of Prof. Serhiy Yarusevych at the University of Waterloo.

- Citation: McClure, J., and Yarusevych, S. (2017) "Instantaneous PIV/PTV-based pressure gradient estimation: a framework for error analysis and correction," *Experiments in Fluids*, 58(8), 92.

Chapter 5:

Performed under the supervision of Prof. Serhiy Yarusevych at the University of Waterloo.

- Citation: McClure, J., and Yarusevych, S. (2019) "Generalized PIV-based pressure gradient error correction for Lagrangian pseudo-tracking," *Measurement Science and Technology*, 30(8), 084005.

Chapter 6:

Performed under the supervision of Prof. Serhiy Yarusevych at the University of Waterloo.

- Citation: McClure, J., and Yarusevych, S. (2019) "On the planar momentum balance in three-dimensional flow: applications to load estimation," *Experiments in Fluids*, 60(3), 41.

Chapter 7:

Performed under the supervision of Prof. Serhiy Yarusevych. The experimental apparatus was designed and built by Graham Riches at the University of Calgary under the supervision of Dr. Chris Morton. Experiments were performed at the University of Calgary with data collection performed by Jeffrey McClure and Graham Riches. Data analysis and manuscript preparation were performed at the University of Waterloo with contributions from Jeffrey McClure, Prof. Serhiy Yarusevych, and Dr. Chris Morton.

- Citation: McClure, J., Morton, C., and Yarusevych, S. (2019) “Forcing function and volumetric flow field estimation for a cylinder undergoing VIV,” *13th International Symposium on Particle Image Velocimetry*, 22-24 July, Munich, Germany.

Abstract

The proceeding work details contributions to the state-of-the-art of velocimetry-based experimental fluid mechanics through the application of novel pressure and force estimation methods to studies in bluff-body aerodynamics and the problem of vortex-induced vibrations. Together, these techniques allow the measurement of fluid velocity and pressure, in space and time, for an area of interest surrounding an immersed body, along with the estimation of the total forcing on the immersed body. Conditions for optimal data sampling from the velocimetry data for the estimation of pressure fields are approximated analytically, and a variety of common pressure integration techniques are compared. The assessed integration techniques are characterized as having similar accuracy, with minor differences in error sensitivity observed. The errors in the estimated pressure fields can be expressed by considering the conformity of the obtained velocimetry data with the governing equations of motion. Accordingly, an analytical framework is developed which propagates the errors in the velocity field measurement through the pressure calculation. A subset of the error terms may be resolved in practical experiments, while others must remain neglected, in the absence of an extended model. Once equipped with the time-resolved pressure field, a control-volume-based analysis then allows the estimation of time-resolved forcing data. The dependence of the time-resolved force estimations on an often neglected three-dimensional term in the planar momentum balance is shown analytically. As a result, specific recommendations are provided for experimental best practises and field of view selection for obtaining accurate time-resolved forcing data from planar velocimetry measurements. Finally, following the previous methodological verification studies, the post-processing techniques are applied to an experiment of a stationary cylinder and that undergoing forced oscillations in a steady free-stream. The three-dimensional flow field surrounding the body is statistically reconstructed along with the pressure estimates in order to resolve the velocity/pressure and force distributions in the volume immediately surrounding the cylinder.

Acknowledgments

I would like to thank my supervisor, Prof. Serhiy Yarusevych, for his invaluable mentorship in research and academic life. I also extend my thanks to Prof. Chris Morton, Prof. Sean Peterson, Prof. Zhao Pan, and Prof. Jean-Pierre Hickey, for always lending a hand with a document or entertaining a discussion when called upon. A special thanks to Prof. Chris Morton for his mentorship during the beginning of my graduate studies and for later lending his experimental facilities at the University of Calgary while we performed renovations on the water flume facility in Waterloo.

To all my fellow students whose studies overlapped with mine in the fluid mechanics research laboratory: Holly Neatby, Tom Kirk, Winston Hu, Manpreet Bansal, Andrew Lambert, Sahil Mahey, John Kurelek, Eugene Zivkov, David Sommer, Chekema Prince, Jennifer Book, Brian Kettlewell, Ajith Airody, Theo Michelis, Laura Haya, Mark Istvan, Erik Marble, Burak Ahmet Tuna, Super Pieris, Amitvikram Dutta, Qihang Yuan, Dallyn Wynnychuk, Caddie Zhang, Cedrick Landry, Ben Pocock, Jon Deng, Allie Fawcett, Alireza Pirnia, Julien Joly, Susanne Vanicat, Khaled Younes, Colin Pavan, Elise Belakebi-Joly, Jeremy Dennis Newton, Charlotte Simon, thanks for all the laughs and always lending a hand when needed.

Thank you to the technical support staff and management: Michael Herz, Jason Benninger, Richard Gordon, Robert Wagner, James Merli, Terry Ridgeway, Juan Ulloa, Neil Griffett, Andy Barber, Martha Morales and William Penney, for their support; particularly, during advanced manufacturing tasks such as the large scale renovation of the water flume facility.

Thank you to my examination committee for the time spent towards the evaluation and refinement of my thesis work.

Table of Contents

List of Figures

List of Tables

Nomenclature

Accents and Subscripts

Example	**Description**
$\hat{a}$	normalized quantity
a'	fluctuating quantity
a_{rms}	root-mean-square quantity

Dimensionless Quantities

Symbol	**Description**	**Definition**
AR	aspect ratio	L/D
A_x^*	normalized amplitude of streamwise vibration	A_x/D
A^*, A_y^*	normalized amplitude of transverse vibration	A/D
C_A	added mass coefficient	–
C_D	drag coefficient	–
C_{EA}	effective added mass coefficient	–
C_L	lift coefficient	–
C_p	pressure coefficient	–
C_{pp}	correlation coefficient between two pressure signals	–
C_x	local amplitude of drag coefficient fluctuations of a vibrating circular cylinder	–
C_y	local amplitude of lift coefficient fluctuations of a vibrating circular cylinder	–
f_x^*	normalized streamwise vibration frequency	f_x/f_n
f^*, f_y^*	normalized transverse vibration frequency	f_y/f_n

m^*	mass ratio	m/m_d
$m^*\zeta$	mass-damping parameter	$m\zeta/m_d$
Re	Reynolds number	U_0D/ν
t^*	normalized time in a periodic system	tf
U_c^*	coupling-frequency based reduced velocity	U_0/f_cD
U^*, U_r	reduced velocity	U_0/f_nD
ζ	damping ratio	$c/2\sqrt{k(m+m_A)}$

Roman Symbols

Symbol	**Description**	**Units**
A_x	amplitude of streamwise vibrations	m
A_y	amplitude of transverse vibrations	m
$a_i(t)$	temporal POD coefficients	–
c	damping coefficient	$\mathrm{kg\,s^{-1}}$
CCW	counter-clockwise	–
CW	clockwise	–
D	cylinder diameter	m
f_{acq}	sampling frequency	Hz
f_c	coupling frequency	Hz
f_n	natural frequency	Hz
f_s	vortex shedding frequency	Hz
f_x	frequency of streamwise vibrations	Hz
f_y	frequency of transverse vibrations	Hz
F_x	fluid force per unit length in the streamwise direction	$\mathrm{N\,m^{-1}}$
F_y	fluid force per unit length in the transverse direction	$\mathrm{N\,m^{-1}}$

$\mathbf{g}$	acceleration due to gravity	$\mathrm{m\,s^{-2}}$
H	the Hilbert transform	$-$
$\hat{i}$	x-direction unit vector	$-$
$\hat{j}$	y-direction unit vector	$-$
k	spring stiffness coefficient	$\mathrm{N\,m^{-1}}$
$\hat{k}$	z-direction unit vector	$-$
L	length of the cylinder	m
L_f	formation length	m
L_{CV}	square control volume length	m
m	mass of the cylinder	kg
m_A	added mass	kg
m_d	mass of the displaced fluid	kg
m_{sys}	mass of the system	kg
M_x	fluid moment in the streamwise direction	N m
M_y	fluid moment in the transverse direction	N m
$\mathbf{n}$	normal unit vector	$-$
$p(\mathbf{x})$	probability distribution	$-$
p_0, p_∞	free stream static pressure	Pa
$p_{bernoulli}$	pressure obtained from Bernoulli equation	Pa
p_{ex}	ground-truth pressure	Pa
p_m	PIV-based pressure estimation	Pa
PSD	power spectrum density	dB
t	time	s
U_0, U_∞	free stream velocity	$\mathrm{m\,s^{-1}}$
$\mathbf{u}$	velocity field	$\mathrm{m\,s^{-1}}$
$\overline{\mathbf{u}}$	mean velocity field	$\mathrm{m\,s^{-1}}$

$\mathbf{u}'$	fluctuating component of the velocity field	$\mathrm{m\,s^{-1}}$
$\mathbf{u_{ex}}$	ground-truth velocity field	$\mathrm{m\,s^{-1}}$
$\mathbf{u_m}$	measured PIV velocity field	$\mathrm{m\,s^{-1}}$
x	streamwise direction	–
$\mathbf{x}$	position vector	–
y	transverse direction	–
z	spanwise direction	–

Greek Symbols

Symbol	**Description**	**Units**
Γ	circulation	$\mathrm{m^2\,s^{-1}}$
Δt	PIV frame separation	s
$\Delta\theta$	phase bin size	rad
$\boldsymbol{\epsilon}_u$	velocity field error	$\mathrm{m\,s^{-1}}$
$\boldsymbol{\epsilon}_{\boldsymbol{\nabla} p}$	pressure gradient field error	$\mathrm{Pa\,m^{-1}}$
$\boldsymbol{\epsilon}_p$	pressure field error	Pa
θ, ϕ	phase angle	degrees (°)
λ_i	POD mode energy	–
δ_{ij}	Kronecker delta	–
ν	kinematic viscosity	$\mathrm{m\,s^{-2}}$
ρ	water density	$\mathrm{kg\,m^{-3}}$
$\phi_i(x, y)$	spatial POD modes	$\mathrm{m\,s^{-1}}$
$\boldsymbol{\omega}$	vorticity field	$\mathrm{s^{-1}}$
ω_n	angular natural frequency	$\mathrm{rad\,s^{-1}}$

Chapter 1

Introduction

One of the principal motivations of the study of aerodynamics is the prediction of performance variables which are dependent on the integrated forces acting on an immersed body. In a basic aerodynamic design context, this means the prediction of the time-averaged lift, drag, and aerodynamic moments over a range of operating conditions (Anderson 1999, Anderson 2011). The temporal variations of the loading parameters may also be crucial, such as in the study of most fluid-structure interactions (FSI), where the dynamics is often unsteady (Bearman 1984). Moreover, in the case of flexible structures, the stresses acting on the immersed body are of further interest, as they influence local deformations of the body and consequently may strongly influence the flow development (Dowell and Hall 2001).

For FSI systems, the level of analysis needed to characterize system performance, in principle, expands in complexity from time-averaged measurements (figure 1.1a), time-resolved measurements (figure 1.1b), to full spatio-temporal measurements (figure 1.1c) depending on the characteristics of the structural response of the immersed body. Correspondingly, the respective experimental techniques required to obtain a high fidelity inference of the principal performance parameters must follow a similar trend in complexity.

The phenomena of Vortex-Induced-Vibration (VIV) is a FSI problem with two-way coupling between the structural and fluid dynamics caused by the periodic forces induced on bluff-bodies from von Kármán vortex shedding (Roshko 1955, Feng 1968, Williamson and Govardhan 2004). In the case of a rigid body, with structural damping and stiffness properties of the system determined at the end conditions (e.g., elastically supported cylinder, figure 1.1b), the fluid-induced forces ($\mathbf{F}(t)$) and moments ($\mathbf{M}(t)$) acting on the body cause a structural response characterized by both translational ($\mathbf{x}(t)$) and angular ($\boldsymbol{\theta}(t)$) displacement parameters. These forcing and response functions are the key performance parameters of VIV, and they exhibit a complex dependence on a multitude of fluid flow and structural parameters (Govardhan and Williamson 2000).

In experiment, the forcing and response functions may be measured by an apparatus

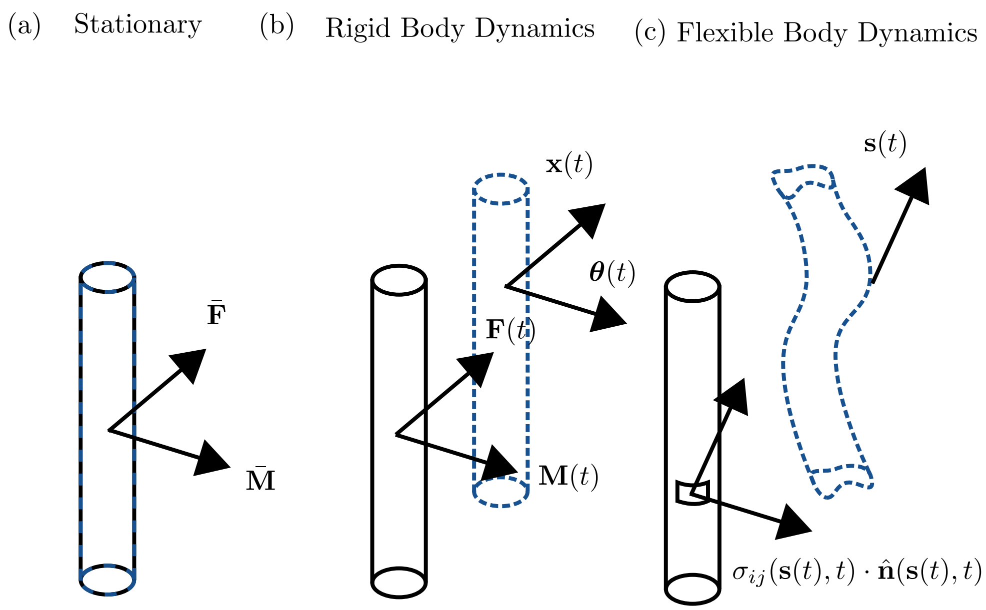

Figure 1.1: Complexity of fluid-inducing forcing diagnostics for (a) stationary body, (b) rigid body dynamics, and (c) flexible body dynamics.

equipped with a load cell and displacement sensors (Khalak and Williamson 1996, Dahl *et al.* 2006); however, such an apparatus is limited to measurement of the integrated loading. The distribution of loads along the span of the bluff-body provides a deeper connection to salient elements of the flow development by permitting the analysis of the effects of variations in vortex shedding phase, variations in the mode of vortex shedding, and end conditions on the integrated loads (Morse *et al.* 2008). In the case of the stationary cylinder, it has been shown (Norberg 2003) that isolating the sectional loading parameters is necessary to compare data from different experimental facilities. An alternative method for the estimation of the structural loads in VIV involves the use of Particle Image Velocimetry (PIV) measurements to infer fluid pressure fields (van Oudheusden 2013) and structural loads (Rival and Oudheusden 2017). However, when applied in practice in previous studies, the results can often be subject to high uncertainty (van Oudheusden 2013) compared to synthetic studies (Liu and Katz 2006, Charonko *et al.* 2010), due to either noisy data sources in experiment or possible methodological errors. The technique is readily applicable to both free and forced vibration experiments, allowing a detailed evaluation of the ability of forced sinusoidal motion vibration experiments to emulate the flow development and forcing present in free vibration (Bearman 2011). Furthermore, besides facilitating structural loading estimates, the development of more accurate pressure inference techniques has ancillary applications. For example, the quantification of aeroacoustic sources in a flow field depends critically on an accurate inference of the spatio-temporal coherence of pressure fluctuations near the surface of bodies of interest (Pröbsting *et al.* 2013) and the spectral distribution of the fluctuations (Curle 1955, Haigermoser 2009).

This thesis advances the state-of-the-art of Particle Image Velocimetry (PIV) measurements to estimate the spatio-temporal evolution of fluid pressure and the temporal evolution of integrated loads. The developments are applied to the flow over stationary and oscillating uniform, circular cylinders in order to validate the accuracy of the methodology and provide enhanced diagnostics for these flows. The time-resolved pressure fields and attendant structural loads facilitate the identification of physical mechanisms in the wake vortex dynamics related to the flow-induced forcing, which can be exploited for simplified modelling of the fluid forcing function to reproduce response parameters in vortex-induced vibrations (VIV). Further, the ability to construct low-order models and estimate the three-dimensional flow state from a combination of PIV measurements is considered.

1.1 Motivation

The developments enclosed in this thesis pertain to problems in bluff body aerodynamics with a specific focus on the flow over circular cylinders and those undergoing VIV. In addition, contributions to the development of data post-processing methodologies for Particle Image Velocimetry (PIV) measurements, including the reduction and estimation of their uncertainty, are made to support the undertaken experimental investigations.

A primary impetus for the study of the flow surrounding cylindrical bluff bodies is to understand the flow-induced forces. For fluid structure interaction problems, the structural dynamics becomes essential in a complete description of the physics, as a response may be excited by the flow-induced fluctuating loads. When dominant vibrational modes are excited by periodic vortex shedding in the wake of the cylinder, the ensuing vibrations are termed Vortex Induced Vibrations (VIV). Broad-band fluctuations caused by incoming free-stream turbulence typically do not cause significant vibration compared to those induced by vortex shedding, which have been shown to reach response amplitudes up to two cylinder diameters in laboratory and field measurements (Bearman 1984). Characterization of the VIV of cylindrical bluff bodies entails the amplitude (A^*) and frequency (f^*) responses, as well as forcing function ($\mathbf{F}(t)$), and is complicated by dependence on a number of structural, fluid, and geometric parameters (Williamson and Govardhan 2004). In general, the parameters which most significantly affect VIV include Reynolds number ($\mathrm{Re_D} = U_0 D/\nu$), mass ratio ($m^* = 4m/\rho_{fluid} D^2 L$), structural damping ratio ($\zeta = c/2\sqrt{k(m+m_A)}$), and reduced velocity ($U^* = U_0/f_n D$). Detrimental VIV occur in a variety of hydrodynamic applications, such as deep water oil and gas risers, submerged floating tunnels, tethered structures, and marine vehicles, as well as in heat exchangers and general civil structures (Roshko 1955, Bearman 1967, Gerrard 1978, Zdravkovich 1981, Roshko 1993, Williamson 1996c). The use of VIV for energy harvesting (Bernitsas *et al.* 2008, Grouthier *et al.* 2014) has also been explored. With cylindrical bluff bodies being ubiquitous in engineering design, and the parameter space pertaining to vortex induced vibration (VIV) quite large, the full characterization of the vibrational response remains an area of active research (Williamson and Govardhan 2008, Bearman 2011, Wu *et al.* 2012, Liu *et al.* 2020).

The forcing mechanism which gives rise to VIV for cylindrical bodies is the periodic loads transferred to the structure by fluctuating surface pressures induced from periodic vortex shedding in the wake (Williamson 1996c, Norberg 2003). Initially, the forcing is independent of the presence of a response; however, it undergoes substantial modulations as a result of the response, and the system exhibits strong two-way fluid-structure coupling. When the vortex shedding frequency (f_s) is in proximity to the structural natural frequency (f_n), a strong structural response occurs. Previous studies have approached the problem of VIV from two different paradigms: (i) the study of free vibrations, in which the response is a natural consequence of the experimental conditions, and (ii) the study of forced vibrations, in which the structure is actuated with ideal sinusoidal vibrations at a prescribed amplitude ratio (A/D) and reduced velocity (U_0/Df_n).

However, not all cases studied in forced vibration may be physically realizable in free-vibration, as VIV will only occur naturally if the integral energy transfer from the fluid to the structure is positive over a period of a shedding cycle. Such energy transfer is highly dependent on the phase difference (ϕ) between the fluctuating side force on the cylinder and the response of the cylinder, and is dependent on both the Reynolds number and the wake vortex topology. It is unclear, and the subject of some discussion in the literature, how well forced vibration cases replicate the forcing functions for the corresponding free vibration case, due to the single harmonic assumption applied and the differing flow histories (Williamson and Govardhan 2008, Bearman 2011). Different modes of vortex shedding can create deviations from the assumed sinusoidal response used in modelling forced vibration studies. Particularly for long slender bodies, the harmonics of the shedding frequency $2f_s, 3f_s$ have been shown to dominate the response trajectory (Wu *et al.* 2012), and at low mass-ratios, the response can be characterized by multiple frequencies (Khalak and Williamson 1999, Williamson and Govardhan 2008).

A variety of analytical and semi-empirical models have been proposed to approximate a multitude of the fluid structure interaction characteristics of VIV. Such models rely on appropriate ansatz of the forcing function induced by the fluid on the vibrating structure (Facchinetti *et al.* 2004, Gabbai and Benaroya 2005) and range from simple harmonic models to more complex decompositions of the fluid induced forcing function. The research proposed herein is motivated by the need to estimate forcing on cylindrical bluff-bodies undergoing free vibration without affecting the structural response, while allowing a more in depth analysis of the fluid forcing by facilitating the estimating of sectional loading parameters. This can be achieved using Particle Image Velocimetry (PIV) measurements and data assimilation, including pressure estimation.

With recent developments in Time-Resolved Particle Image Velocimetry (TR-PIV) measurements, time resolved pressure estimation (van Oudheusden 2013) is possible from the velocity field data, and structural loads can be estimated through an appropriate control volume formulation (Noca *et al.* 1999, van Oudheusden *et al.* 2007). However, instantaneous pressure estimates obtained from PIV measurements are known to suffer from considerable errors in experiment, with correlation coefficients with embedded sur-

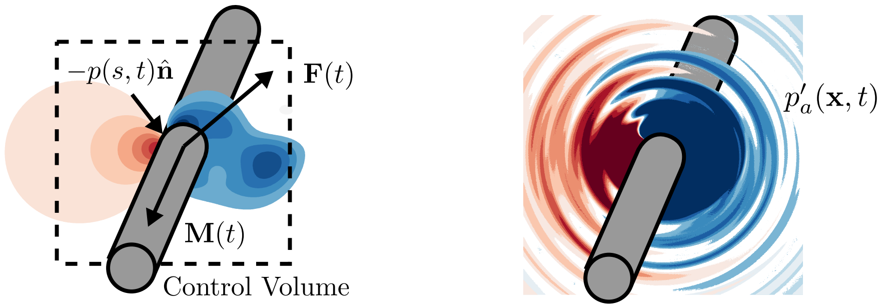

(a) Integral and Surface Load Estimation (b) Acoustic Source Estimation

(c) RANS Turbulence Statistics (d) Vortex Tracking

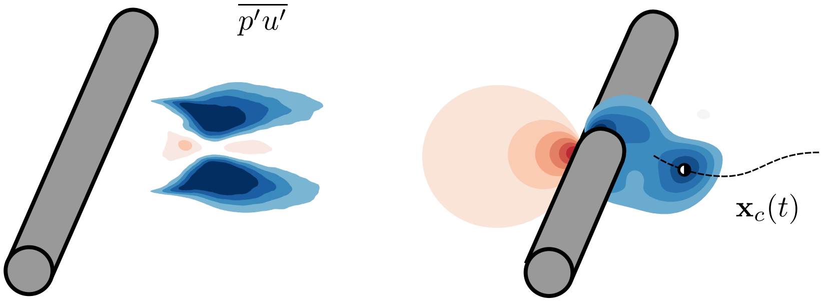

Figure 1.2: Applications of pressure from PIV flow diagnostics.

face pressure transducers reported to be approximately $C_{pp} \approx 0.6 - 0.8$ (e.g., de Kat and van Oudheusden 2012, Ghaemi *et al.* 2012, Azijli *et al.* 2016, Schneiders *et al.* 2016b). Similar magnitudes of errors can be observed in instantaneous structural loading estimates obtained from PIV measurements (Poelma *et al.* 2006, Ragni *et al.* 2009, DeVoria *et al.* 2014), particularly when two-dimensional techniques are applied when strong three-dimensional flows are present (Lucas *et al.* 2017). As a result, there is a need for more clarity on the dominating sources of uncertainty arising when applying time-resolved pressure and load estimations in experiment, as well as methods for their estimation and reduction. The acquisition of PIV-based pressure fields can serve numerous experimental diagnostic goals, a selection of which are summarized in figure 1.2. They may be employed, in conjunction with PIV velocity fields and their derivatives, to estimate time-resolved integral loads and local surface pressure distributions (figure 1.2a), to estimate acoustic sources through aeroacoustic analogies, such as Curle's analogy (Curle 1955), which incorporates scattering and diffraction effects at solid boundaries (figure 1.2b), to construct a statistical analysis of turbulence through the Reynolds-averaged Navier-Stokes equation (RANS) in the entire flow field (figure 1.2c), or to track vortices by identifying the trajectories of pressure minima in the fluid (figure 1.2d). These diagnostics are, for the most part, inaccessible experimentally through traditional measurement techniques, such as surface pressure transducers or probe measurements. So, while the developments in this thesis are primarily targeted towards estimates of instantaneous loads, they serve to bolster a broader range of experimental diagnostics.

Due to the requirement of resolving the entire flow field surrounding the body of interest, planar techniques are significantly more easily deployed than volumetric PIV techniques. Thus, this thesis also explorers low-order modeling to estimate salient features in three-dimensional flows from planar measurements, including total loading estimation.

1.2 Objectives

The work completed in this thesis aims to refine a methodological pipeline for fluid mechanics experiments that infers both time-resolved pressure fields and structural loads surrounding an immersed body. Towards this end, the the following objectives summarize the efforts of the thesis work:

(i) Benchmark most common pressure integration algorithms for use with experimental velocimetry data in bluff body wakes, and select an algorithm for further use through a comparative analysis.
(ii) Determine the limiting and optimal conditions for the use of pressure integration algorithms in experimental bluff body wake measurements.
(iii) Develop a theoretical framework for the analysis of errors in pressure integration from velocimetry data. Determine to what extent these errors may be inferred and corrected for through additional modelling leveraging the governing equations.
(iv) Determine the limiting conditions for the use of control volume-based structural loading estimates in experimental practice.
(v) Unify the methodological developments and benchmark the accuracy of inferring the pressure fields and structural loads from velocimetry data for a challenging experimental scenario of a cylinder undergoing vortex-induced vibration.

1.3 Overview of thesis content

The results chapters of the thesis are a collection of manuscripts published in various journals or conference proceedings, as noted in the acknowledgements section.

Chapters 3-5 deal solely with the acquisition of pressure field data from PIV data. Chapter 3 benchmarks four pressure integration algorithms and develops complementary guidelines for the design of experiments to reduce errors. Chapters 4 and 5 pertain to the development of a physics-based framework for increasing the accuracy of Poisson equation-based pressure integration along with facilitating error estimation.

Chapter 6 investigates the momentum-based control volume analysis employed to estimate instantaneous loads from planar PIV and PIV-based pressure data. The form of the dependence of structural loading estimates based on planar estimates on three-dimensional terms is made explicit and consequent recommendations are made towards minimizing errors due to flow three-dimensionality.

Chapter 7 deals with the analysis of the forcing function in vortex-induced vibrations, leveraging the techniques developed in Chapters 3-6. The methodological developments yield time-resolved forcing estimates from PIV measurements for a stationary and vibrating cylinder in cross-flow.

Chapter 2

Background

A review of the published literature is presented here to frame the motivation for the thesis objectives within the current state-of-the-art, and introduce the reader to mathematical frameworks underlying the areas of research to which the thesis contributes. This serves as an instructive, but not exhaustive, discussion of content built upon in the thesis. Section 2.1 provides an overview of the characteristics and dynamics of the von Kármán wake for the prototypical flow around an infinite, uniform diameter, stationary cylinder in a constant cross-flow. Section 2.2 then reviews the vortex-induced vibrations of elastically supported cylinders in cross-flow. Particular attention is paid to the case of simply supported, one degree-of-freedom vortex-induced vibration, and efforts towards simplified models of the coupled wake and structure dynamics. These sections establish a fundamental basis for the physical analysis of the flows encountered in the thesis. Following that, section 2.3 introduces particle image velocimetry as a measurement technique, and sections 2.4 and 2.5 review the current state-of-the art in the estimation of pressure fields and structural loads from particle image velocimetry measurements, thereby establishing a basis for the methodological development and comparisons explored in the thesis.

2.1 Cylinder wake

Flow past a circular cylinder in a cross-flow configuration is fundamental to the study of bluff body aerodynamics. The configuration is depicted in figure 2.1, where a long cylinder of constant diameter, D, is immersed in a uniform free stream of fluid of density, ρ, and dynamic viscosity, μ, with a constant free stream velocity, U_0. Features of the incompressible wake development are dependant exclusively on Reynolds number ($\mathrm{Re_D} = \rho U_0 D/\mu$) for an infinite, smooth cylinder in undisturbed cross-flow, and von Kármán vortex shedding is present over a wide range of $\mathrm{Re_D}$ encompassing various practical applications (Provansal *et al.* 1987). The unsteady wake vortex dynamics influence the mean and fluctuating structural loads on the cylinder. Critically, wake induced pressure fluctuations at the cylinder surface may lead to the emergence of significant structural vibrations (Zdravkovich 1981, Blevins 1985, Bearman 2011) and acoustic noise (Blevins 1984). The cylinder wake is receptive to both passive (Bearman 1965, Zdravkovich and Volk 1972, Zdravkovich 1981, Bouak and Lemay 1998, Sueki *et al.* 2010, Morton and Yarusevych 2014, McClure *et al.* 2015) and active control methods (Fransson *et al.* 2004, Choi *et al.* 2008, Jukes and Choi 2009), motivating the need for a detailed quantitative understanding of the wake structure through laminar and turbulent flow regimes.

For $\mathrm{Re_D} \gtrsim 50$, the flow development in the wake of a circular cylinder is dominated by vortex shedding, which is initiated by a global instability in the flow (Williamson 1996c) where opposite signed vortices form in the near wake and advect downstream to form an asymmetric vortex street. Incoming flow stagnates at the front of the cylinder and is redirected around the sides forming a boundary layer at the surface. The boundary

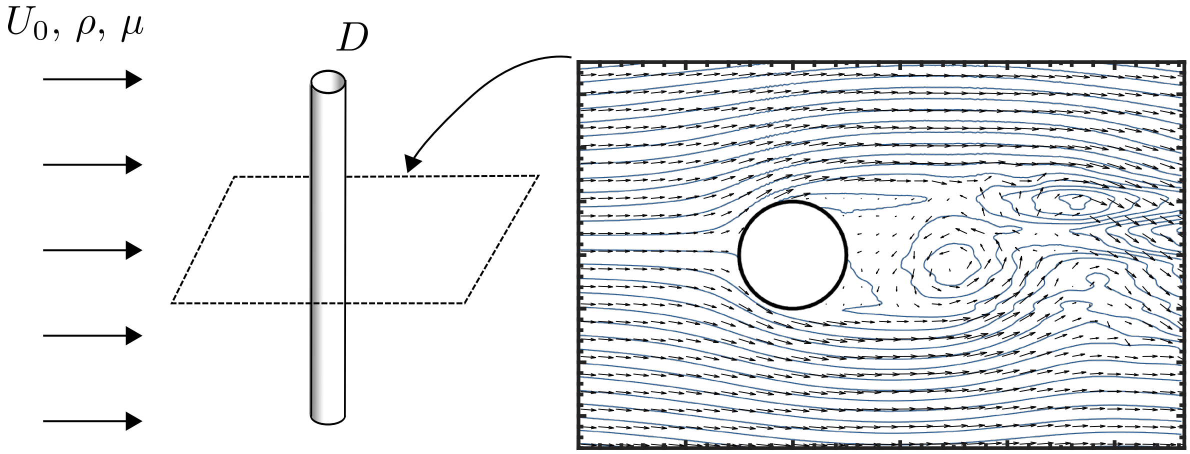

Figure 2.1: (left) Configuration of circular cylinder in cross-flow and (right) instantaneous streamlines (blue lines) and velocity vectors (black vectors) in the cylinder wake at $\mathrm{Re_D} = 4100$.

layer separates at a point within approximately 80 − 130° from the front stagnation point due to the presence of an adverse pressure gradient, with the exact position dependent on the Reynolds number (Wu *et al.* 2004). The separated shear layers roll-up into vortices in the near wake alternately, and the vortices detach into the wake when the supply of vorticity from each shear layer is cut-off by the shear layer roll-up from the opposing side of the cylinder (Bearman 1967, Gerrard 1978, Roshko 1993, Williamson 1996c). The vortices are shed quasi-periodically in a narrow frequency range, and the wake expands due to momentum diffusion as the vortices are carried downstream in a stable configuration (Kármán 1911). The shedding frequency (f_s) is commonly expressed in non-dimensional form as the Strouhal number ($\mathrm{St_D} = f_s D/U_0$), which remains approximately $\mathrm{St_D} \approx 0.2$ over a wide range of Reynolds numbers (Williamson 1996c, McClure and Yarusevych 2016b).

Knowledge of the spatial distribution of turbulent kinetic energy (TKE) in the flow, with velocity fluctuations being dominated by vortex shedding in the wake, along with the corresponding frequency spectra, is critical to the analysis of the flow. Since pressure and velocity fluctuations near the surface of the cylinder are dominated by various aspects of vortex shedding, a detailed understanding of both the time-averaged and time-resolved structural loads, along with their relation to the flow development in the wake, is necessary to guide structural design.

2.1.1 Effect of Reynolds number on wake vortex shedding

The topology of the vortices in the wake of a circular cylinder changes significantly with Reynolds number. The wake vortices are visualized using the Q-criterion (Hunt *et al.* 1988) in figure 2.2 for a range of $\mathrm{Re_D}$ spanning the transition to turbulence. The Q-criterion is the second invariant of the velocity gradient tensor $\boldsymbol{\nabla}\mathbf{u}$ and is defined according to equation 2.1.

$$Q = \frac{1}{2}(||\boldsymbol{\Omega}||^2 - ||\boldsymbol{S}||^2) \tag{2.1}$$

$$\Omega_{ij} = \frac{1}{2}\left(\frac{\partial u_i}{\partial x_j} - \frac{\partial u_j}{\partial x_i}\right) \tag{2.2}$$

$$S_{ij} = \frac{1}{2}\left(\frac{\partial u_i}{\partial x_j} + \frac{\partial u_j}{\partial x_i}\right) \tag{2.3}$$

For $\mathrm{Re_D} \gtrsim 50$ (Provansal *et al.* 1987, Williamson 1989, Williamson 1996c), vortex shedding is initiated by a global instability, leading to the alternate roll-up of the shear layers in the near wake and the development of two-dimensional wake vortices. Three-dimensional vortex structures first appear for $190 \lesssim \mathrm{Re_D} \lesssim 260$, where an elliptic instability (mode A) of the primary vortex cores causes secondary streamwise vortex loops between subsequent primary spanwise rollers (Williamson 1996a). For $230 \lesssim \mathrm{Re_D} \lesssim 250$, a hyperbolic instability (mode B) develops intermittently in the saddle point region between the primary rollers, characterized by smaller scale streamwise vortex pairs (Williamson 1996b). Further increases in $\mathrm{Re_D}$ for $260 \lesssim \mathrm{Re_D} \lesssim 1000$ lead to increased three-dimensionality and fine scale streamwise vortices forming in the wake region. Tomographic PIV measurements in Scarano and Poelma (2009) show the existence of sustained rhombus shaped vortex cells for $\mathrm{Re_D} = 360$, which share similarities to vortex dislocations identified in transitional flows (Williamson 1992). For $1.0 \times 10^3 \lesssim \mathrm{Re_D} \lesssim 2.0 \times 10^5$, the convective Kelvin-Helmholtz instability is amplified sufficiently in the separated shear layer, causing smaller scale vortex roll-up in the separated shear layers before the formation of wake vortices, and primary vortices are fully turbulent during their formation. Beyond $\mathrm{Re_D} \approx 2.0 \times 10^5$, the separated shear layer may reattach on one or both sides of the cylinder after undergoing transition, leading to separation bubble formation and a drastic narrowing of the wake. This regime is the so-called critical regime, or drag crisis (Zdravkovich 1981), where flow reattachment leads to a large reduction in the form drag ($C_{D,p}$) on the cylinder. Above $\mathrm{Re_D} \approx 1.0 \times 10^6$, in the post-critical regime, transition occurs in the boundary layer before separation and eliminates the presence of separation bubbles (Williamson 1996c).

The streamwise wavelength of the von Kármán vortex street ($\lambda_x = U_c/f_s \approx 4D$) is characterized by the frequency of vortex shedding and the convective speed of the wake vortices (Huang *et al.* 2006). The mode A instabilities occur with spanwise wavelengths of $\lambda_z = 3 - 4D$ which decrease with increasing Reynolds number (Williamson 1996b). The mode B instabilities occur with spanwise wavelengths of approximately $\lambda_z = 1$, scaling with the thickness of the vorticity layer in the braid region between vortex cores, yielding a relatively constant wavelength for $\mathrm{Re_D} = 300 - 5540$ (Williamson 1996b, Scarano and Poelma 2009, McClure *et al.* 2019). Measurements of the spanwise wavelengths of the three-dimensional structures have been obtained based on flow visualization images (Wu *et al.* 1994a, Wu *et al.* 1994b, Zhang *et al.* 1995, Williamson 1996a), as well as cross correlation of the streamwise velocity signal along the span (Mansy *et al.* 1994). Spanwise wavelengths based on spatial cross correlations of the spanwise vorticity suggest the existence of two characteristic wavelengths for the three-dimensional vortices (Scarano and Poelma 2009), a smaller wavelength defined by twice the distance between cores of vortex pairs ($2\lambda_{zl} = 0.5 - 0.75$), and a larger wavelength defined by the distance between pairs ($\lambda_z = 0.8 - 1.3$). In the shear layer transition regime ($\mathrm{Re_D} \gtrsim 1000$), the streamwise wavelength of the shear layer vortices varies significantly with $\mathrm{Re_D}$, as their formation frequency relative to the von Kármán shedding frequency increases proportional to $\mathrm{Re_D^{0.67}}$ (Prasad and Williamson 1997). Following formation, the shear layer vortices deform substantially (Bays-Muchmore and Ahmed 1993) and either amalgamate into the von Kármán rollers or are tilted and strained further in the regions between the rollers (Wei and Smith 1986).

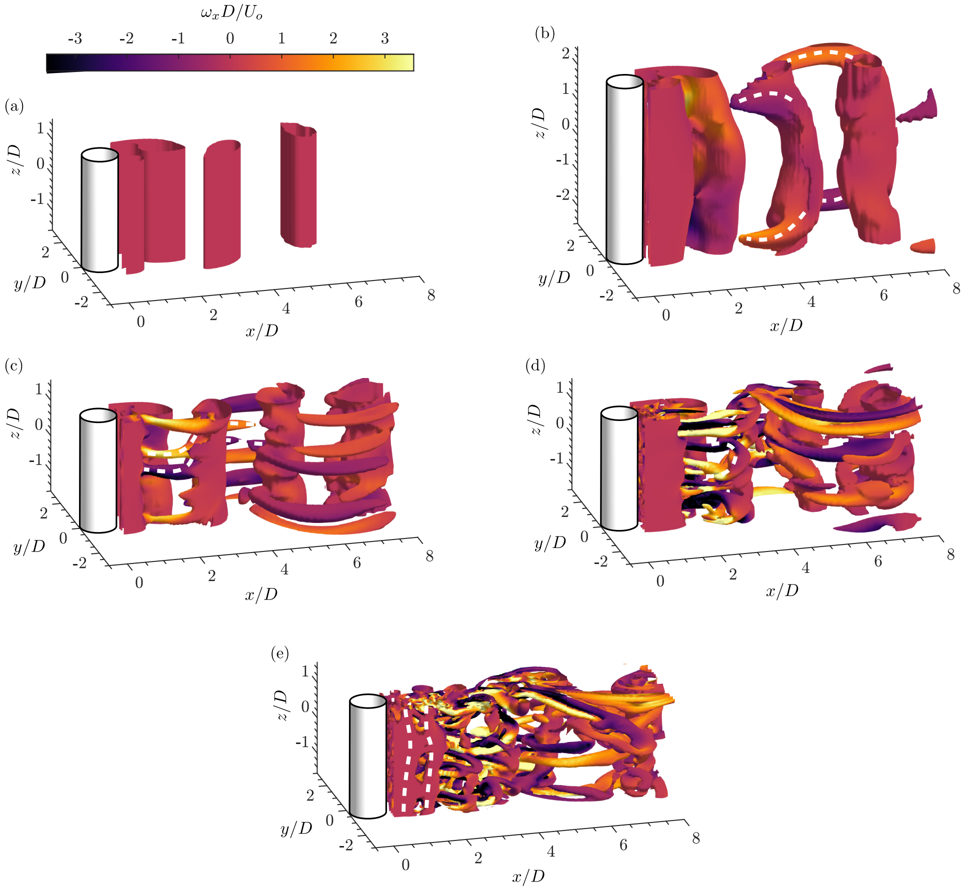

Figure 2.2: Vortex shedding topological regimes for (a) $\mathrm{Re_D} = 100$, (b) $\mathrm{Re_D} = 220$, (c) $\mathrm{Re_D} = 300$, (d) $\mathrm{Re_D} = 800$, and (e) $\mathrm{Re_D} = 1575$. Vortices are visualized using the Q-criterion ($Q = 0.01\ s^{-1}$) (Hunt *et al.* 1988), coloured by the streamwise vorticity.. Prominent secondary vortex structures are highlighted with white dashes (McClure *et al.* 2019).

2.1.2 Structural loading

A mean drag force and instantaneous fluctuating lift and drag components act on a cylinder in uniform cross-flow (Wieselseberger 1922, Norberg 2003). The magnitudes and instantaneous characteristics of the forces acting on the cylinder vary considerably with Reynolds number, as the related vortex topology in the wake undergoes significant changes (Wieselseberger 1922, Williamson 1996c, Norberg 2003).

Wieselseberger (1922) performed drag measurements covering a considerable Reynolds number range ($5 < \mathrm{Re_D} < 5\times10^5$), and the results are corroborated by multiple subsequent studies (Thom 1928, Tritton 1959). In laminar flow regimes, the drag coefficient shows exponential decay with Reynolds number (Wieselseberger 1922, Tritton 1959, McClure and Yarusevych 2016b, McClure *et al.* 2019), as the viscous stresses lose their dominance. Thereafter, the drag coefficient levels off to $C_D \approx 1$ over a wide range of Reynolds numbers

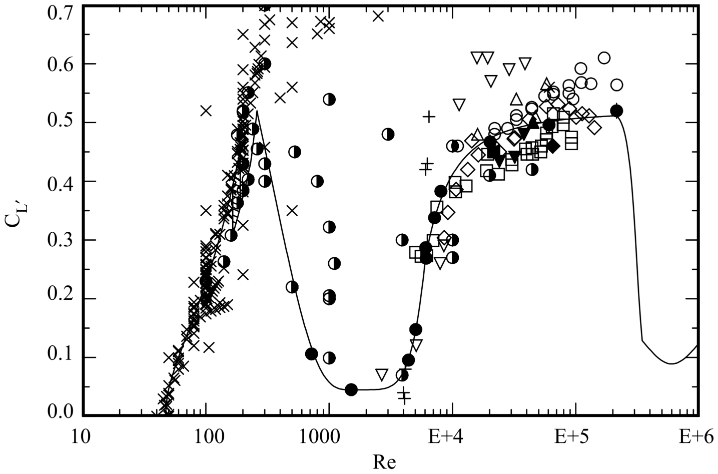

Figure 2.3: Compilation of experimental and numerical measurements of the sectional fluctuating lift coefficient with varying Reynolds number. Figure reprinted from Norberg (2003).

in the sub-critical flow regimes ($200 < \mathrm{Re_D} < 2.0 \times 10^5$). Once critical Reynolds numbers ($\mathrm{Re_D} > 2.0 \times 10^5$) are reached, shear layer reattachment occurs and leads to a reduction of over 50% in the mean drag coefficient (Wieselseberger 1922).

Periodic vortex shedding leads to out of phase fluctuating side pressures, and is the dominant contributor to the fluctuating lift and drag forces (Norberg 2003). The RMS fluctuating lift coefficient (C'_L) is concentrated at the vortex shedding frequency (f_S), while the RMS fluctuating drag coefficient (C'_D) has significantly smaller amplitude and is concentrated at twice the vortex shedding frequency ($2f_S$) along with low frequency pulsations (Davies 1976). Figure 2.3 illustrates the variation of the sectional fluctuating lift coefficient with Reynolds number. From the onset of vortex shedding, the lift coefficient increases monotonically with Reynolds number up to the onset of three-dimensionalities ($\mathrm{Re_D} \approx 190$). Following this, the fluctuating lift decreases rapidly and settles into a so called lift-trough within the shear layer transition regime ($500 < \mathrm{Re_D} < 0.6 \times 10^4$, figure 2.3). Following the onset of the shear layer transition regime, a distinct change in flow development occurs for $\mathrm{Re_D} \geq 0.5 \times 10^4$ (Norberg 1987, Lin *et al.* 1995), characterized by a steady increase in the magnitude of surface pressure fluctuations and fluctuating lift with increasing Reynolds number. This is accompanied by a decrease in base pressure (C_{bp}), due to a reduction in the vortex formation length (l_f). The change in formation length is the primary cause of the increased surface pressure and lift fluctuations, with the forming vortices inducing stronger periodically impinging flow on the aft portion of the cylinder (Norberg and Sunden 1987). For increasing $\mathrm{Re_D}$ in this regime, the bandwidth of the shedding frequency spectral peak also increases by an order of magnitude (Norberg and Sunden 1987).

The total RMS lift acting on a finite cylinder length ($C_{L',T}$) is related to the sectional lift coefficient (C'_L), however, the three-dimensionality of the vortex shedding across the cylinder span means cancellations of forcing occur due to phase differences across the length. The relationship between the sectional lift RMS and the lift on a finite span segment of length L may be expressed exactly by utilizing a two-point spanwise correlation function $R_{LL}(s)$ of the lift force (Equation 2.4). In practise, the spanwise lift two-point correlation can be approximated using a spanwise pressure two-point correlation at a constant surface angle near separation (R_{pp}), or a wake velocity survey (R_{uu}) near the separated shear layer (Ribeiro 1992)

$$C_{L',T}/C_{L'} = \frac{1}{L}\left[2\int_0^L (L-s)R_{LL}(s)ds\right]^{1/2}. \tag{2.4}$$

It can be deduced from wake measurements of the flow across the Reynolds number range that primary factors affecting the fluctuating sectional loading on a cylinder are (i) the vortex formation length (l_f) (Norberg 1987, McClure *et al.* 2015, McClure and Yarusevych 2016a), (ii) the zero-delay cross correlation of fluctuating pressures on opposing sides of the cylinder (Norberg 2003), and (iii) the circulation of the wake vortices (McClure and Yarusevych 2016b). A decreased formation length increases the magnitude of the induced pressure fluctuations at the surface since the vortex formation is closer to the surface, higher asymmetry between the fluctuating side pressures results in higher net lift fluctuations, and higher strength vortex shedding will naturally lead to higher induced pressure fluctuations at the surface. Increases in the base pressure (C_{bp}) are known to correlate with increases in vortex formation length (l_f) (Roshko 1993, McClure *et al.* 2015, McClure and Yarusevych 2016a), and with the base pressure proportional to the total pressure drag, the magnitudes of the mean and fluctuating loads are hence related, both reaching minimums for $500 \leq \mathrm{Re_D} \leq 5000$. The relationships inferred in the discussion are hence $C_D \propto 1/C_{bp}$, $C_{bp} \propto l_f$, and $C_{L'} \propto 1/l_f$.

2.2 Vortex-induced vibrations

The results of investigations in vortex-induced vibration of bluff bodies has been compiled in a number of comprehensive reviews, including Sarpkaya (1979), Bearman (1984), Khalak and Williamson (1999), Leonard and Roshko (2001), Sarpkaya (2004), Williamson and Govardhan (2004), Williamson and Govardhan (2008), Bearman (2011), and Wu *et al.* (2012), and the associated modeling perspectives discussed in Parkinson (1989), Facchinetti *et al.* (2004), and Gabbai and Benaroya (2005).

Due to the induced fluctuating loads, vortex shedding in the wakes of cylindrical bluff-bodies may excite structural vibrations (Zdravkovich 1981, Blevins 1985, Bearman 2011). The characteristics of the vibration response and the fluid forcing are primarily dependent on the following four parameters (Sarpkaya 2004): (i) the reduced velocity $Uj = U_0/f_nD$, which describes the ratio of the vortex shedding frequency for a stationary cylinder ($f_s \approx 0.2U_0/D$) to the structural natural frequency, (ii) the mass ratio

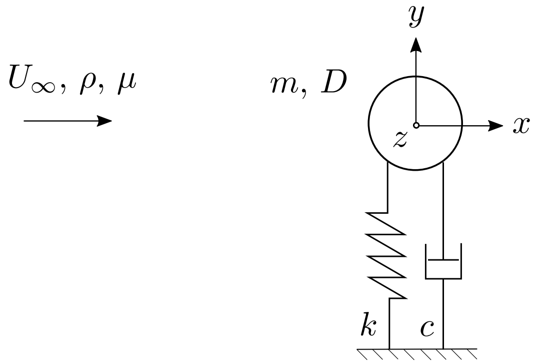

Figure 2.4: Definition of structural and fluid parameters.

$m^* = m_{sys}/m_d$, which is the ratio between the mass of the system and the mass of fluid it displaces when immersed, has influence on inertial forces resulting from the oscillation of the cylinder, (iii) the damping ratio ζ, which dictates the energy dissipated structurally, and (iv) the Reynolds number $\mathrm{Re_D} = U_0 D/\nu$.

2.2.1 One degree-of-freedom cylinder vortex-induced vibration

Since the amplitude of the response of a cylinder undergoing VIV is typically much higher in the transverse direction (Bearman 2011), a large number of studies are confined to an elastically supported cylinder which only allows transverse vibration, eliminating any in-line direction response. For a rigid cylinder constrained to oscillate only in the direction transverse of the flow direction, the physical parameters are defined in figure 2.4. In this work, the convention of Khalak and Williamson (1999) is adapted for the non-dimensional response, forcing, and physical parameters, which is included in table 2.1 for easy reference.

In general, the problem of VIV assumes the structural and physical properties of the cylinder and fluid are known beforehand. That is, the cylinder diameter (D), mass (m), damping (c) and stiffness (k), and the fluid free-stream velocity (U_0), fluid density (ρ), and fluid viscosity (μ) are known. The task is then to predict VIV response ($y(t)$) and fluid-induced forcing ($\mathbf{F}(t)$) characteristics, in particular, their amplitudes and spectral distribution. The associated governing equation of the forced oscillator is given by equation 2.5.

$$m\ddot{y} + c\ddot{y} + ky = F \tag{2.5}$$

The first studies of the VIV of cylinders were conducted at high mass ratios in air and high mass damping ($m^*\zeta$), and found that a response was excited in a band of reduced velocities of $5 < U^* < 8$ (Feng 1968), where the Strouhal frequency nears the structural natural frequency. Generally, the combined mass damping parameter has been

Group	Notation	Equation
Mass ratio	$m^\star$	$\dfrac{m}{\pi\rho D^2 L/4}$
Damping ratio	ζ	$\dfrac{c}{2\sqrt{k(m+m_A)}}$
Reduced Velocity	$U^\star$	$\dfrac{U_0}{f_n D}$
Amplitude ratio	$A^\star$	$\dfrac{y_0}{D}$
Frequency ratio	$f^\star$	$\dfrac{f}{f_n}$
Streamwise force coefficient	C_X	$\dfrac{F_X}{\frac{1}{2}\rho U_0^2 DL}$
Transverse force coefficient	C_Y	$\dfrac{F_Y}{\frac{1}{2}\rho U_0^2 DL}$
Reynolds number	Re	$\dfrac{\rho U_0 D}{\mu}$

† When the subscript denoting streamwise of transverse direction is absent, transverse direction is to be assumed.

Table 2.1: Non-dimensional groups in VIV.

shown to govern the peak amplitude response, with a functional relationship often shown on a so-called Griffin plot (Williamson and Govardhan 2008). However, while peak amplitude is predicted well by $m^*\zeta$, subsequent study of vibrations at low mass ratio (Khalak and Williamson 1999) found that the band of reduced velocities where VIV occurs can be widened by decreasing the mass ratio while maintaining constant mass damping, extending the synchronization regime (Williamson and Govardhan 2008). In addition, the characteristics of the amplitude response changed for a cylinder with low mass ratio and low mass damping. Figure 2.6 shows the amplitude response as a function of the reduced velocity. For high mass damping, the response consists of two branches, an initial excitation branch and a lower branch (Khalak and Williamson 1997, Govardhan and Williamson 2000). The transition between branches exhibits hysteresis (Khalak and Williamson 1999). For low mass damping, the amplitude response is characterized by higher magnitudes and is excited over a wider range of U^*. Moreover, an additional upper branch is observed. The upper branch shows hysteresis with the initial excitation branch, but the change to the lower branch instead is characterized by intermittent switching between the vibration modes (Khalak and Williamson 1999, Williamson and Govardhan 2008). The transition from the initial to upper branch of responses is related to a switching of vortex shedding mode, from 2S to 2P (Khalak and Williamson 1999), where 2S refers to a traditional von

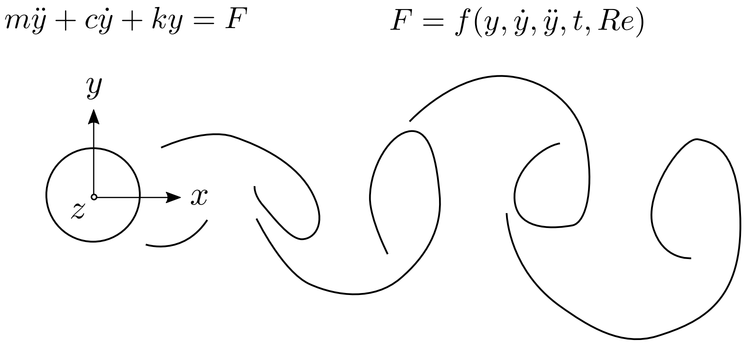

Figure 2.5: Structural response and fluid forcing.

Kármán vortex street, and 2P refers to the formation of two pairs of counter-rotating vortices during a single shedding cycle. The transition to the lower branch, however, maintains the 2P mode, or switches to a non-synchronized shedding pattern. The jump in response amplitude is related to a significant change in shedding timing relative to the response, thus altering the energy transfer from the fluid forcing to the structure (Williamson and Govardhan 2008).

In the region of excited vibrations, the frequency response may lock in to the natural frequency of the structure over a range of reduced velocities in the lower branch (Govardhan and Williamson 2000, Williamson and Govardhan 2008). As a result, the vortex shedding frequency breaks the Strouhal number relationship for stationary cylinders significantly in this region. However, the lock-in reduced frequency only matches the natural frequency $f^* \approx 1$ when the mass ratio is significantly large. For lower mass ratios, the frequency is shown to lock in up to $f^* \approx 1.4$ and remain constant over a range of reduced velocities (Khalak and Williamson 1997, Gabbai and Benaroya 2005). The region where the response frequency and shedding frequency are matched is referred to as the synchronization region. In this region, a dramatic increase in correlation of the shedding along the span is observed when $A^* > 0.05$. Additionally, the strength of the shed vortices in the synchronization region increases significantly when reduced velocity is increased above the resonant point, as the shedding frequency remains relatively constant while the free-stream velocity is increased (Bearman 1984). The dependence of the maximum lock-in frequency attainable on m^* in the synchronization region is described well by $f^* = \sqrt{(m^* + 1)/(m^* - 0.54)}$, defining a nearly constant frequency in the lower response branch (Govardhan and Williamson 2000). The formulation indicates that, when a critical mass is reached, the synchronization region becomes infinite, hence for $m^* < 0.54$, large amplitude vibrations occur even when reduced velocities tend to infinity, and the lower branch is never attained (Williamson and Govardhan 2008). Instead, the response frequency continues to increase linearly with U^* according to the Strouhal relationship as in the upper branch before synchronization (Govardhan and Williamson 2000). For reduced velocities preceding the synchronization

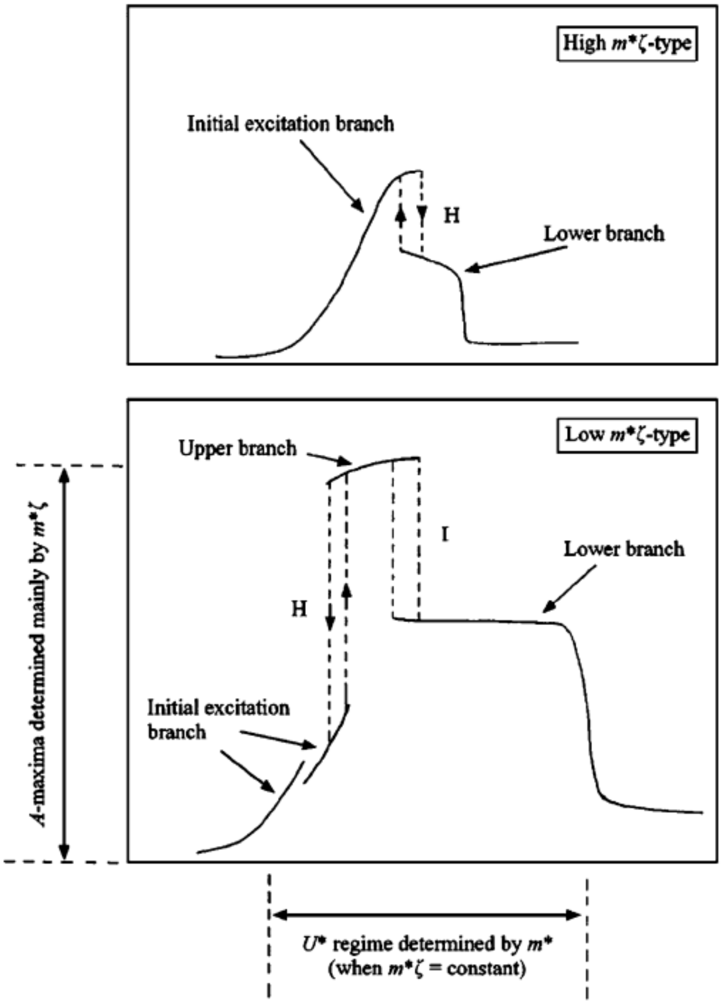

Figure 2.6: Amplitude response for cylinder undergoing transverse vibrations with high (upper) and low (lower) mass damping. Figure reprinted from Govardhan and Williamson (2000).

region, the response is dictated by both the shedding frequency f_s and natural frequency f_n (Khalak and Williamson 1999).

2.2.2 In-line and transverse vortex induced vibration of a cylinder

For a wide range of parameters, the results of previous studies indicate that the addition of in-line vibrations does not affect the system response branches significantly (Jauvtis and Williamson 2004, Williamson and Govardhan 2008). However, at low mass ratios $m^* < 6$, a unique mode appears yielding a super-upper branch with $A_y^* \approx 1.5$ and $A_x^* \approx 0.3$, corresponding to a 2T mode of shedding where a triplet of vortices is shed each half cycle (Williamson and Govardhan 2008).

For the initial branch, the in-line response amplitudes are negligible, besides a region corresponding to when the dominant frequency of the drag forcing function approaches the cylinder natural frequency. Since the drag force fluctuations are centred at twice the vortex shedding frequency, this region is centred around a reduced velocity of $U^* \approx 2.5$, compared to $U^* \approx 5$ for the dominant transverse response caused by the lift force fluctuations centred at the shedding frequency. In this region, the in-line amplitude response may reach appreciable amplitude, and alterations in the shedding mode are observed for $1.25 < U^* < 2.5$, where symmetric shedding occurs, and $2.7 < U^* < 3.8$, where asymmetric shedding occurs (Sarpkaya 2004). At higher reduced velocities in the initial branch, a near negligible in-line amplitude response is observed; however, in both upper and lower response branches, significant in-line vibrations can be observed (Jauvtis and Williamson 2004).

2.2.3 Modelling of Vortex-induced vibration

Due to the vast parameter range underlying the dynamics of VIV reviewed previously, i.e., the dependence on four non-dimensional parameters in just the simplest one degree-of-freedom case, considerable effort has been made in dynamics modelling to better synthesize the available experimental data for predictive use in a wider range of operating conditions. A selection of these models along with their utility and limitations are discussed herein.

Single harmonic assumption

The equations of motion for one-degree of freedom VIV can be simplified greatly by assuming both the response of the cylinder ($y(t)$) and the fluid-induced forcing acting on the cylinder ($F(t)$) are single harmonic functions (Khalak and Williamson 1999) of the same angular frequency (ω), offset by a phase difference (ϕ).

$$y(t) = y_0 sin(\omega t) \tag{2.6}$$

$$F(t) = F_0 sin(\omega t + \phi) \tag{2.7}$$

Substituting the harmonic ansatz into the governing equation 2.5 leads a separation into two coefficient equations for the response amplitude and frequency:

$$y_0 = \frac{F_0 \sin\phi}{c\omega} \tag{2.8}$$

$$\omega = \sqrt{\frac{ky_0}{\frac{F_0 \cos\phi}{\omega^2} + my_0}} \tag{2.9}$$

Non-dimensionalization of equations 2.8 and 2.9 leads to the amplitude and frequency equations of Khalak and Williamson (1999):

$$A^\star = \frac{1}{4\pi^3} \frac{C_Y \sin\phi}{(m^\star + C_A)\zeta} \left(\frac{U^\star}{f^\star}\right)^2 f^\star \tag{2.10}$$

$$f^\star = \sqrt{\frac{m^\star + C_A}{m^\star + C_{EA}}} \tag{2.11}$$

where C_{EA} is an effective added mass coefficient (equation 2.12), which includes the total fluid-induced forcing acting in phase with the cylinder acceleration $\ddot{y}$.

$$C_{EA} = \frac{1}{2\pi^3} \frac{C_Y \cos\phi}{A^\star} \left(\frac{U^\star}{f^\star}\right)^2 \tag{2.12}$$

The effective added mass coefficient does not have direct relation to the added mass coefficient C_A ($C_A = 1$ in inviscid flow), which is fundamental to the alteration of the structural natural frequency when a cylinder is immersed in fluid mediums of varying density, since it contains components from the wake vortex force. While equations 2.10 and 2.11 do not yield direct a-priori predictive power, it will be shown they contain explanatory utility for a number of phenomena encountered in VIV. The effective added mass acts to augment the resonant frequency of the cylinder according to equation 2.11, while the forcing component in-phase with the cylinder velocity ($C_Y \sin\phi$) determines the maximum amplitude of VIV according to equation 2.10. This result has been used to propose widely used collapses of VIV amplitude data. The peak VIV response occurs when the cylinder natural frequency (f_n) and wake vortex shedding frequency (f_s) coincide, resulting in resonance conditions where $f \approx f_s \approx f_n$. At resonance, $f^\star \approx 1$ and $U^\star \approx 5$ can be assumed constants, and according to equation 2.10, the peak amplitude response is inversely dependent on mass ratio and damping structural parameters.

$$A^\star \propto \frac{C_Y \sin\phi}{(m^\star + C_A)\zeta} \tag{2.13}$$

It is assumed that the forcing $C_Y \sin\phi$ is only a function of the amplitude, at resonance conditions, and therefore an appropriate mass-damping parameter may be used to collapse data over a wide range of operating conditions. A number of mass-damping terms have been utilized, including, the stability parameter $K_S = \pi^2 m^\star \zeta$ (Vickery and Watkins 1964), Scruton number $Sc = \pi m^\star \zeta/2$ (Scruton 1965), and the Skip-Griffin parameter $S_G = 2\pi^3 \mathrm{St}^2 m^\star \zeta$ (Skop and Griffin 1973). The Skop-Griffin is typically favoured in rigid body VIV due to its ability to encompass effects of varying natural Strouhal number (St) for different bluff bodies and Re. Various curve fits have been proposed based on collated data (Sarpkaya 1979) of peak amplitudes against S_G; however, their use is complicated by the existence of multiple amplitudes for a given S_G based on which response branch is active, corresponding to different vortex dynamics, and hence, a different functional relationship between amplitude $A^\star$ and the excitation forcing $C_Y \sin\phi$. The difference is most pronounced for low values of mass-damping (Khalak and Williamson 1999). It is also expected that there are certain regimes where independent variations of mass-ratio $m^\star$ will cause $A^\star$ to vary by augmenting the frequency of vibration through equation 2.11 (Bearman 1984), violating the $f^\star \approx 1$ approximation utilized in the derivation of the mass-damping proportionality argument. It has been demonstrated by experiments (Govardhan and Williamson 2006) that the peak amplitude is determined uniquely by $m^\star\zeta$ for $m^\star > 1$. Also, in turbulent regimes, increases in $\mathrm{Re_D}$ increase peak amplitude response (Govardhan and Williamson 2006). These effects can be incorporated in a modified Griffin plot which provides a functional relationship which collapses peak amplitude data at a given $\mathrm{Re_D}$, along with a renormalization parameter which scales the functional relationship based on $\mathrm{Re_D}$.

Interestingly, the single harmonic assumption also implies that, if structural parameters are known, measuring the amplitude and frequency of a cylinder undergoing VIV is sufficient to predict both the phase-lead and magnitude of the fluid-induced forcing, ϕ and C_Y, respectively, using equations 2.14 and 2.15. However, agreement in experiment using those equations to back calculate forcing characteristics is lacking, particularly at high $m^\star$, presumably due to the associated amplification of errors in measurements of the frequency $f^\star$ or other parameters (Khalak and Williamson 1999) or applicability of the single harmonic assumption in single DOF VIV.

$$C_Y \sin\phi = \frac{4\pi^3 A^\star (m^\star + C_A)\zeta}{(U^\star/f^\star)^2 f^\star} \tag{2.14}$$

$$C_Y \cos\phi = \frac{2\pi^3 A^\star}{(U^\star/f^\star)^2} C_{EA} \tag{2.15}$$

2.3 Particle Image Velocimetry

The utility of the Particle Image Velocimetry (PIV) technique is primarily derived from the ability to measure instantaneous velocities in a flow region of interest (Westerweel *et al.* 2013). Depending on the laser and camera configurations, it is possible to measure two or three components of the velocity field in planar or volumetric regions of the flow (Elsinga *et al.* 2006), and for many flows, acquisition times are now fast enough to resolve the temporal evolution of the flow. PIV measurements hence directly permit the calculation of instantaneous vorticity, rate of strain, other derivative-based metrics, and spatial/temporal correlations. This yields a wealth of diagnostic capability compared to popular single-point velocimetry techniques such as hot-wire anemometry (HWA) and laser-Doppler velocimetry (LDV), leading to PIV's dominant adoption in experimental fluid mechanics in the last 30

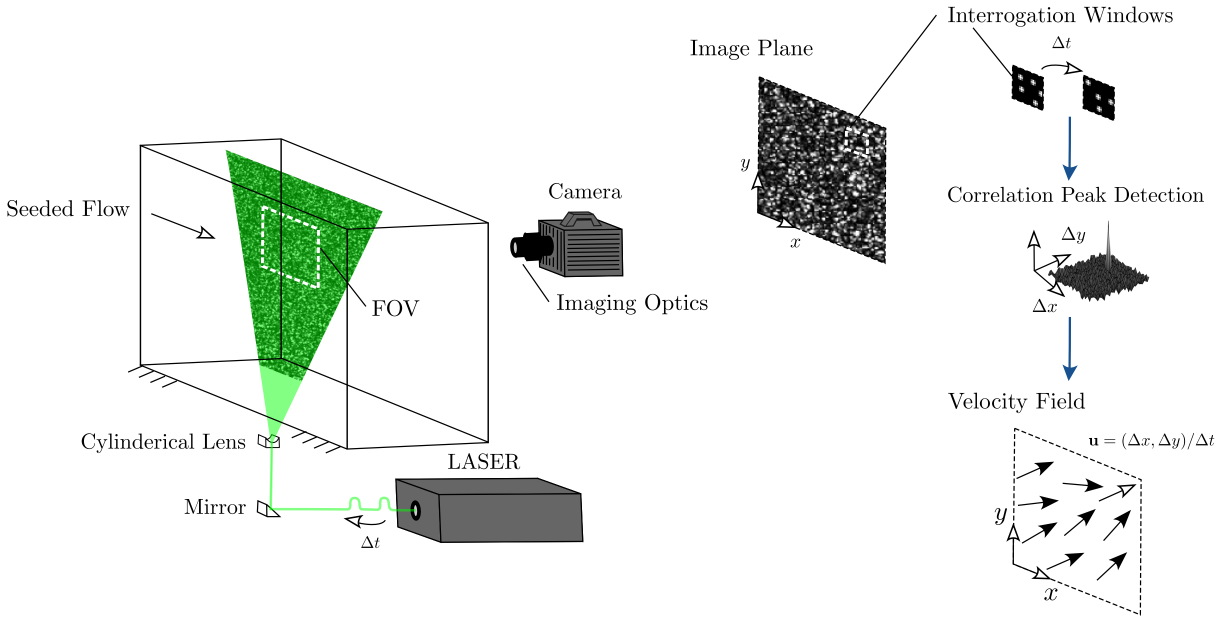

Figure 2.7: Particle Image Velocimetry: principle of operation.

years (Westerweel *et al.* 2013).

The working principle of the PIV technique is described schematically in figure 2.7 using a planar, two-component measurement configuration. The idea is to measure the fluid velocity by estimating the local displacements of tracer particles inserted into the fluid. In a conventional application, the tracer particles (e.g., $\approx 10\mu m$ glass spheres in water, or $\approx 1\mu m$ atomized liquid drops in air) are illuminated by two laser pulses with a pulse separation, Δt_p, and images of the scattered light from the particles are recorded in two separate frames by a digital camera (Raffel 2007). The displacement data of the tracer particles can be measured by algorithms which track the displacement of individual particles, or the image can be partitioned into interrogation areas containing multiple particles, where the average displacements of the particles is evaluated on a statistical basis. The former approach is typically denoted Particle Tracking Velocimetry (PTV), while the latter is typically denoted Particle Image Velocimetry. The use of PTV typically requires significantly decreased tracer seeding densities in order to avoid ambiguity in the identification of matching tracer particles, resulting in decreased instantaneous spatial resolution. On the other hand, PIV introduces spatial filtering effects over the size of the interrogation areas, which affect velocity statistics.

Special care must be taken that the tracer particles faithfully track the fluid motion (Melling 1997). This typically places significant constraints on the admissible size or liquid of solid seeding particles, particularly in gas glows ($\approx 1\mu m$) Helium soap bubbles circumvent this in air flows by closer density matching with the fluid medium, allowing larger tracer sizes suitable for larger scale experiments (Kühn *et al.* 2011, Scarano *et al.* 2015). The same is true for typical seeding in water flows, such as hollow glass and polyethylene spheres in water flows, where the bulk tracer material density is comparable to water density.

2.4 PIV-based Pressure

The common definition of pressure for a fluid continuum is found as an isotropic stress in the constitutive relation for the stress tensor acting on a fluid element,

$$\sigma_{ij} = -p\delta_{ij} + \tau_{ij} = -p\delta_{ij} + \mu\left(\frac{\partial u_i}{\partial x_j} + \frac{\partial u_j}{\partial x_i}\right) + \delta_{ij}\lambda\frac{\partial u_k}{\partial x_k} \tag{2.16}$$

where local thermal equilibrium is assumed and a two-parameter linear model is employed relating the viscous stresses to velocity gradients in the fluid. The mechanical pressure ($\bar{p}$) is defined in equation 2.17 as the negative one-third of the average compressive stress acting on a fluid element and is hence invariant under coordinate rotations (White 2006).

$$\bar{p} = -\frac{1}{3}(\sigma_{xx} + \sigma_{yy} + \sigma_{zz}) = p - (\lambda + 2/3\mu)\frac{\partial u_k}{\partial x_k} \tag{2.17}$$

The mechanical pressure is equivalent to the thermodynamic pressure only when either the fluid is incompressible ($\partial u_k/\partial x_k = 0$) or Stoke's hypothesis is satisfied ($\lambda + 2/3\mu = 0$). Stoke's hypothesis is valid provided the fluid is Newtonian and the rates of expansion and compression are small (Tavoularis 2005, Kundu *et al.* 2012). The flows encountered in this thesis approximately satisfy both of these requirements, so mechanical and thermodynamic pressures can be considered equivalent. Similarly, the incompressibility condition eliminates any dependence of the stress tensor on the bulk viscosity (λ) in equation 2.16.

Substituting the stress tensor into the equation of motion for a fluid continuum in a graviational field yields the familiar Navier-Stokes equation for an incompressible, Newtonian fluid, expressed in tensor notation in equation 2.18 and vector calculus notation in 2.19.

$$\frac{\partial p}{\partial x_i} = -\rho\frac{Du_i}{Dt} + \rho g_i + \mu\frac{\partial^2 u_i}{\partial x_j^2} \tag{2.18}$$

$$\boldsymbol{\nabla} p = -\rho\frac{D\mathbf{u}}{Dt} + \rho\mathbf{g} + \mu\boldsymbol{\nabla}^2\mathbf{u} \tag{2.19}$$

By applying the divergence operator to both sides of the Navier-Stokes equations, the Poisson equation for pressure may be arrived at, shown in equation 2.20. Expanding the terms on the RHS of equation 2.20 and applying the zero velocity divergence condition ($\boldsymbol{\nabla}\cdot\mathbf{u} = 0$) for incompressible flow yields an alternate formulation of the Poisson equation shown in 2.21,

$$\boldsymbol{\nabla}^2 p = f(\mathbf{u}) = \boldsymbol{\nabla} \cdot (-\rho \frac{D\mathbf{u}}{Dt} + \rho \mathbf{g} + \mu \boldsymbol{\nabla}^2 \mathbf{u}) \tag{2.20}$$

$$\boldsymbol{\nabla}^2 p = -\rho \boldsymbol{\nabla} \cdot (\mathbf{u} \cdot \boldsymbol{\nabla}) \mathbf{u} \tag{2.21}$$

where $\boldsymbol{\nabla}^2$ is the Laplacian differential operator and is defined according to equation 2.22 in $\mathbb{R}^n$.

$$\boldsymbol{\nabla}^2 = \frac{\partial^2}{\partial x_n^2} + \frac{\partial^2}{\partial x_{n-1}^2} + \dots \frac{\partial^2}{\partial x_2^2} + \frac{\partial^2}{\partial x_1^2} \tag{2.22}$$

Importantly, inspection of both the Navier-Stokes equations and the Poisson equation reveals that the velocity field and its derivatives are the only dynamic variables needed to specify the pressure gradients (equation 2.18) or the Poisson equation source term (equation 2.20. Therefore, the ability of PIV systems to measure the spatio-temporal evolution of the fluid velocity field allows the inference of pressure fields through the governing equations.

The utility of spatio-temporally resolved fluid pressure estimations from Time-Resolved Particle Image Velocimetry (TR-PIV) measurements has been demonstrated in a variety of flows, including turbulent boundary layers (Ghaemi *et al.* 2012, Pröbsting *et al.* 2013, Laskari *et al.* 2016, Schneiders *et al.* 2016a, Van der Kindere *et al.* 2019), jets (de Kat and Ganapathisubramani 2013, Huhn *et al.* 2018, Sakib *et al.* 2021), bluff-body wakes (Fujisawa *et al.* 2005, van Oudheusden *et al.* 2007, de Kat and van Oudheusden 2012, Dabiri *et al.* 2014, McClure and Yarusevych 2016a, McClure and Yarusevych 2016b, Pirnia *et al.* 2020, Pallas and Bouris 2022), subsonic (van Oudheusden *et al.* 2006, van Oudheusden *et al.* 2007, Violato *et al.* 2011, Auteri *et al.* 2015, Jeon *et al.* 2018) and supersonic aerofoils (van Oudheusden *et al.* 2007), aircraft propellers (Ragni *et al.* 2012), pulsatile diffusers (Charonko *et al.* 2010), bubbles (Hosokawa *et al.* 2003), turbulent cavities (Liu and Katz 2006), and Savonius turbines (Murai *et al.* 2007). The estimation of pressure from PIV data can be done in a number of ways, and many methodologies have emerged from the results of various studies (Charonko *et al.* 2010, van Oudheusden 2013) to integrate either the Navier-Stokes equations (equation 2.19) or the Poisson equation for pressure (equation 2.20) with appropriate boundary conditions. A detailed discussion of these methodologies is left to the appropriate results sections in this thesis.

Regardless of the approach employed, accurate estimation of the material acceleration ($D\mathbf{u}/Dt$) is vital to each method, and often the viscous terms in equation 2.19 are neglected (Ghaemi *et al.* 2012) for large $\mathrm{Re} > 1000$ (van Oudheusden 2013). Random error reduction in material acceleration estimates can be achieved by reconstructing the fluid parcel trajectories over multiple time realizations (Violato *et al.* 2011, Novara and Scarano 2013, Pröbsting *et al.* 2013), filtering the velocity fields in a variety of ways (Charonko *et al.* 2010, Dabiri *et al.* 2014), or using a Taylor's frozen field hypothesis for highly convective flows (de Kat and Ganapathisubramani 2013, Laskari *et al.* 2016).

2.5 PIV-based Load Estimation

A number of velocimetry-based methods have been applied in various investigations for the indirect measurement of fluid forces on a body in place of traditional force balance measurements (Unal *et al.* 1997, van Dam 1999). The majority can be classified as momentum integral methods, which are based on conservation of linear momentum within a control volume encompassing the model. Conservation of linear momentum for a fixed control volume is given by equation 2.23 (van Oudheusden *et al.* 2007)

$$\mathbf{F}(t) = -\iiint_V \frac{\partial \rho \mathbf{u}}{\partial t} dV - \iint_S \rho(\mathbf{u}\cdot\mathbf{n})\mathbf{u} dS + \iint_S (-p\mathbf{n} + \tau\cdot\mathbf{n}) dS \tag{2.23}$$

where V is the interior of the three-dimensional control volume, S is the outer boundary of the control volume, and $\mathbf{n}$ is the unit normal vector on the boundary S.

Mean forces

For mean loading quantities, only boundary data are required for the pressure, velocity, and velocity gradients (van Oudheusden *et al.* 2007), according to equation 2.24, which assumes undisturbed free-stream quantities of a uniform streamwise velocity U_0 at free-stream static pressure p_0. If the control volume is taken sufficiently large, some of the boundary integral segments in equation 2.24 will evaluate to zero, such as the upstream boundary terms, and the momentum flux integral at the transverse boundaries.

$$\overline{\mathbf{F}}(t) = \iint_S \rho(\overline{\mathbf{u}}\cdot\mathbf{n})(\mathbf{U_0} - \overline{\mathbf{u}}) dS + \iint_S ((p_0 - \overline{p})\mathbf{n} + \overline{\tau}\cdot\mathbf{n}) dS \tag{2.24}$$

The pioneering applications of this approach utilized wake surveys (Taylor 1938) and were used primarily for mean drag computation on streamlined bodies. Such estimations utilized a quadrilateral control volume with significant simplifications to Equation 2.23. The incoming flow boundary is assumed to be uniform flow at U_0 and the side boundaries are either assumed to be at U_0 or else a correction is applied to account for the boundary momentum flux (Bohl and Koochesfahani 2009), or the CV shape is adjusted such that side boundaries follow the mean streamlines of the flow (Neatby and Yarusevych 2012). At the downstream boundaries, where complex wake interactions result in mean wake velocity and pressure deficits, more careful validation of simplifying assumptions is required.

Instantaneous forces

In recent years, the development of time-resolved PIV measurements (Raffel 2007) and pressure estimations from such measurements (Baur and Köngeter 1999, Gurka *et al.* 1999) allowed the application of control volume analysis with minimal simplifying assumptions.

In general, the instantaneous loads can be evaluated by using the full control volume formulation of the momentum equation (Equation 2.23). This is complicated by the addition of a volume integral term, which can be challenging to measure accurately over an entire domain, particularly near a surface, as well as a measure of the instantaneous pressure at the boundary. The studies of Noca *et al.* (1999) and Unal *et al.* (1997) were pioneering studies for load estimation from PIV data before pressure estimation techniques were introduced. They utilized a velocity field quadrature in order to eliminate the pressure term (Noca *et al.* 1999) from the control volume formulation or else explicitly calculated it from the momentum equation (Unal *et al.* 1997) and utilized the entirety of the velocity field information, including the volume integrated quantities, in order to estimate time-resolved loads. Although sensitive to high random errors in experimental data, such techniques employed with appropriate filtering showed promise in predicting the force on a forced oscillating cylinder in quiescent and free-stream conditions (Unal *et al.* 1997, Noca *et al.* 1999).

Examples of more recent applications of control volume formulation for load estimation include, but are not limited to, the following studies. Kurtulus *et al.* (2007) performed time-resolved PIV measurements in order to calculate the unsteady loadings on a square-section cylinder at a Reynolds number of 4890. Jardin *et al.* (2009) compared the unsteady-force estimation acting on a hovering airfoil at low Reynolds numbers using both control volume and vortex-parameterization methods. David *et al.* (2009) applied the classic control-volume method to both experimental and synthetic flow fields so as to identify the effect of various parameters such as spatial and temporal resolutions, as well as the out-of-plane velocity component on the accuracy of forces estimation. In order to model fish swimming dynamics, Lucas *et al.* (2017) utilized a PIV-based pressure solver and estimate the forces and torques on a flapping foil by integrating the surface forces. Spoelstra *et al.* (2019) capture the wake velocity deficit behind a passing cyclist with PIV measurements in a two-dimensional plane in order to estimate mean drag forces.

Alternative formulations for time-resolved loading include a derivative-moment transformation proposed in Mohebbian and Rival (2012) which replaces the volume integral term in Equation 2.23, which is difficult to determine accurately near body surfaces in PIV experiments, with a surface integral (equation 2.25).

$$\mathbf{F}(t) = -\rho\frac{\partial}{\partial t}\iint_S \mathbf{x}(\mathbf{u}\cdot\mathbf{n})dS - \rho\iint_S \mathbf{u}(\mathbf{u}\cdot\mathbf{n})dS - \iint_S p\mathbf{n}dS + \iint_S(\tau\cdot\mathbf{n})dS \tag{2.25}$$

Alternatively, if the surface pressure distribution on the immersed structure is available, the pressure loading can be determined from the surface integral:

$$\mathbf{F}(t) = \oint_S p\mathbf{n}dS \tag{2.26}$$

With pressure loading being dominant over viscous loading for $\mathrm{Re_D} > 20$ (Wieselseberger

1922, Thom 1928) for cross-flows over circular cylinders, it is a viable approach, although care must be taken experimentally in order to measure near wall velocities accurately.

Chapter 3

Optimization of Planar PIV-based Eulerian Pressure Estimates in Laminar and Turbulent Wakes

To survey the alternatives for obtaining pressure estimations from Particle Image Velocimetry (PIV) data, the performance of four pressure estimation techniques were evaluated in a bluff body wake. The results identified optimal temporal and spatial resolutions that minimize the propagation of random and truncation errors to the pressure field estimates. For pressure integration based on planar PIV, the effect of flow three-dimensionality was also quantified, and shown to be most pronounced at higher Reynolds numbers downstream of the vortex formation region, where dominant vortices undergo substantial three-dimensional deformations. The results of the present study provide a priori recommendations for the use of pressure estimation techniques from experimental PIV measurements in vortex dominated laminar and turbulent wake flows.

This chapter is based on the journal article: McClure, J., and Yarusevych, S. (2017) “Optimization of planar PIV-based pressure estimation in laminar and turbulent wakes,” *Experiments in Fluids*, 58(5), 62.

3.1 Introduction

The utility of spatio-temporally resolved fluid pressure estimations from Time-Resolved Particle Image Velocimetry (TR-PIV) measurements (van Oudheusden 2013) has been demonstrated in turbulent boundary layers (Ghaemi *et al.* 2012, Pröbsting *et al.* 2013, Laskari *et al.* 2016, Schneiders *et al.* 2016a), jets (de Kat and Ganapathisubramani 2013), bluff-body wakes (Fujisawa *et al.* 2005, van Oudheusden *et al.* 2007, de Kat and van Oudheusden 2012, Dabiri *et al.* 2014, McClure and Yarusevych 2016b), subsonic (van Oudheusden *et al.* 2006, van Oudheusden *et al.* 2007, Violato *et al.* 2011, Auteri *et al.* 2015) and supersonic aerofoils (van Oudheusden *et al.* 2007), aircraft propellers (Ragni *et al.* 2012), pulsatile diffusers (Charonko *et al.* 2010), the region surrounding a rising bubble (Hosokawa *et al.* 2003), cavity flows (Liu and Katz 2006), and other flow configurations (Murai *et al.* 2007). Estimated pressure fields can be used in conjunction with measured velocity fields to extract time-resolved loadings on immersed structures (van Oudheusden *et al.* 2007, Tronchin *et al.* 2015), establishing a minimally intrusive methodology for the measurement of both fluid pressure and structural loading. A number of methodologies have emerged from the results of individual studies, however, a clear consensus on an optimum has not yet been reached, and is flow and setup dependent (Charonko *et al.* 2010, van Oudheusden 2013, Pan *et al.* 2016).

In order to estimate fluid pressure ($p(x,y,t)$), the instantaneous velocity fields ($u_i(x,y,t)$) obtained from two-component TR-PIV measurements are used to calculate the planar pressure gradients from the Navier-Stokes equations:

$$\frac{\partial p}{\partial x} = -\rho\left(\frac{\partial u}{\partial t} + u\frac{\partial u}{\partial x} + v\frac{\partial u}{\partial y} + w\frac{\partial u}{\partial z}\right) + \mu\left(\frac{\partial^2 u}{\partial x^2} + \frac{\partial^2 u}{\partial y^2} + \frac{\partial^2 u}{\partial z^2}\right) \tag{3.1}$$

$$\frac{\partial p}{\partial y} = -\rho\left(\frac{\partial v}{\partial t} + u\frac{\partial v}{\partial x} + v\frac{\partial v}{\partial y} + w\frac{\partial v}{\partial z}\right) + \mu\left(\frac{\partial^2 v}{\partial x^2} + \frac{\partial^2 v}{\partial y^2} + \frac{\partial^2 v}{\partial z^2}\right) \tag{3.2}$$

Since only two velocity components are measured in planar PIV (u, v), terms containing the out-of-plane velocity (w) or out-of-plane derivatives ($\partial/\partial z$) are not evaluated, resulting in an associated error in estimated pressure fields (Baur and Köngeter 1999, Charonko *et al.* 2010, de Kat and van Oudheusden 2012, Ghaemi *et al.* 2012). For stereoscopic PIV measurements, three velocity components (u, v, w) are measured, however, the out-of-plane derivatives cannot be evaluated. In more general terms, the pressure gradient is related to forces arising from viscous stresses and material acceleration (equation 3.3).

$$\frac{\partial p}{\partial x_i} = \mu\frac{\partial^2 u_i}{\partial x_i^2} - \rho\frac{Du_i}{Dt} \tag{3.3}$$

The pressure gradient field may then be integrated, using for example one of the following methods proposed in previous studies: (i) Baur and Köngeter (1999) utilized a spatial marching scheme, (ii) Liu and Katz (2006) developed an omni-directional line integration technique, (iii) Dabiri *et al.* (2014) proposed an eight-path line integration technique, (iv) multiple authors solved the pressure Poisson equation using a standard 5-point discretization (Gurka *et al.* 1999, Fujisawa *et al.* 2005, de Kat and van Oudheusden 2012, Blinde *et al.* 2016) or with an FFT integration (Huhn *et al.* 2016):

$$\frac{\partial^2 p}{\partial x_i^2} = -\rho \frac{\partial}{\partial x_i} \frac{Du_i}{Dt} \tag{3.4}$$

simultaneously over the domain, (v) Tronchin *et al.* (2015) solved local equations for the least squares approximation of the pressure field using an iterative method and (vi) multiple authors (Hosokawa *et al.* 2003, Jaw *et al.* 2009, Regert *et al.* 2011) have explored coupling the PIV velocity fields with common CFD algorithms to solve the pressure Poisson equation. Recent developments in Tomographic PIV (Elsinga *et al.* 2006) and three-dimensional Particle Tracking Velocimetry (PTV) (Schanz *et al.* 2016) allow three-dimensional velocity field characterization inside a volume, further extending the capacity of pressure estimation (Violato *et al.* 2011, Ghaemi *et al.* 2012, Neeteson and Rival 2015, Laskari *et al.* 2016, Schneiders *et al.* 2016a). For volumetric data, Poisson equation based methods are widely used and are relatively computationally inexpensive (Blinde *et al.* 2016, Huhn *et al.* 2016). However, the majority of prior work on pressure estimation has been focused on planar velocity measurements, and such measurements are still prevalent.

Accurate estimation of the material acceleration (Du_i/Dt) is vital to any method of pressure estimation, since the viscous terms in equation 3.3 can often be neglected or are relatively small for turbulent flows where the inertial terms dominate (Ghaemi *et al.* 2012). The material acceleration is typically estimated in either an Eulerian or Lagrangian frame of reference. In the Eulerian frame, the material acceleration is estimated at each grid point using, for example, second order central differences (Gurka *et al.* 1999) (equation 3.5).

$$\frac{Du_i}{Dt}(x_i,t) = \frac{u_i(x_i,t+\Delta t) - u_i(x_i,t-\Delta t)}{2\Delta t} + u_i(x_i,t)\frac{u_i(x_i+\Delta x,t) - u_i(x_i-\Delta x,t)}{2\Delta x} \tag{3.5}$$

In the Lagrangian frame, pseudo-tracking methods are used to track a fluid element coincident with each grid point at time t. For example, the material acceleration of the tracked element may be estimated by iteratively determining the trajectory of the element backward and forward in time using equations 3.6 and 3.7 (Liu and Katz 2006, de Kat and van Oudheusden 2012, Lynch and Scarano 2014):

$$x_{i,p}^k(t+\Delta t) = x_i + u_i(x_i,t)\Delta t + \frac{Du_i^k}{Dt}(x_i,t)\frac{\Delta t^2}{2} \tag{3.6}$$

$$\frac{Du_i^{k+1}}{Dt}(x_i,t) = \frac{u_i(x_{i,p}^k(t+\Delta t),t+\Delta t) - u_i(x_{i,p}^k(t-\Delta t),t-\Delta t)}{2\Delta t} \tag{3.7}$$

Methods of material acceleration determination have been found to be subject to differing temporal resolution constraints depending on the advective and rotational nature of the flow (Jakobsen *et al.* 1997, Violato *et al.* 2011, de Kat and van Oudheusden 2012, van Oudheusden 2013). Studies of wave phenomena indicated that the Lagrangian approach performs poorly compared to the Eulerian (Jakobsen *et al.* 1997). Violato *et al.* (2011) compared errors associated with Eulerian and Lagrangian techniques for flow over a rod-airfoil and found that the upper bound on Δt required to properly sample the convective structures was lower for the Eulerian method compared to the Lagrangian method ($\Delta t_{Lag,max}/\Delta t_{Eul,max} \approx 3$). When adhering to this guideline, resulting pressure evaluations showed minor differences between the Eulerian and Lagrangian estimations (Violato *et al.* 2011). de Kat and van Oudheusden (2012) studied the peak response characteristics of an advecting vortex flow and suggested that the upper bound for Δt scales according to the advective time-scale of the vortices for the Eulerian method, and according to the vortex turn-over time for the Lagrangian method. Hence, in contrast to the results of Violato *et al.* (2011), de Kat and van Oudheusden (2012) found that, in the wake of a square cylinder, the pressure estimated using the Lagrangian approach leads to a rapid decrease in correlation with surface microphone measurements at significantly smaller Δt ($\Delta t_{Lag,max}/\Delta t_{Eul,max} \approx 0.1$). They recommended bounds on the interrogation window size of $\lambda_x/WS > 5$ and on the acquisition frequency of $f_{acq}/f_{flow} > 10$, where λ_x and f_{flow} are the smallest wavelength and the highest frequency of structures to be resolved in the estimated pressure field.

Important for the experimental application of the techniques are methods to reduce the effect of random error propagation to the material acceleration. Noise reduction in material acceleration estimates can be achieved by reconstructing the fluid parcel trajectories over multiple time realizations (Violato *et al.* 2011, Novara and Scarano 2013, Pröbsting *et al.* 2013, Lynch and Scarano 2014), filtering the velocity fields (Charonko *et al.* 2010, Dabiri *et al.* 2014), or applying Taylor's frozen field hypothesis for highly convective flows (de Kat and Ganapathisubramani 2013, Laskari *et al.* 2016). With the accuracy of the pressure estimation being dependent on the random errors present in the velocity measurements, the sensitivity of pressure estimation to typical measurement errors becomes an important criterion for the identification of an optimal technique. The omni-directional, spatial marching, and Poisson solver techniques were compared by Charonko *et al.* (2010) using analytical solutions for a pulsatile flow and a decaying vortex subject to artificially applied velocity noise. It was concluded that the Poisson equation method performs better for the advective oscillating slot flow, while omni-directional line-integration and spatial marching methods perform better for the rotational vortex flow. Murai *et al.* (2007) superimposed artificial error onto their experimental results and found the Poisson equation method to be relatively insensitive to velocity field noise compared to the line-integration methods for flow around a Savonious turbine. Using an analytical solution for an advecting vortex, de Kat and van Oudheusden (2012) found negligible differences between the omni-directional technique and the pressure Poisson equation, but inhomogeneous propagation of velocity error led to higher overall error values for the spatial marching method. Recently, Blinde *et al.* (2016) compared a number of pressure estimation techniques using synthetic data obtained from a zonal detached eddy simulation (ZDES) of an axisymmetric base flow, and showed the superiority of PTV-based material acceleration estimates for computing pressure fields, as well as the benefit of several techniques which implicitly correct the velocity field in the solution for pressure. Some recent studies have attempted to quantify the uncertainty in pressure estimations (ϵ_p) given uncertainties in the velocity field (ϵ_u) (Violato *et al.* 2011, de Kat and van Oudheusden 2012, de Kat and Ganapathisubramani 2013, Azijli *et al.* 2016, Laskari *et al.* 2016), focusing on the Poisson equation problem.

Although the analytical framework has yet to be developed fully, multiple studies (Charonko *et al.* 2010, Violato *et al.* 2011, Laskari *et al.* 2016) suggest that optimal temporal and spatial resolutions exist which minimize the resulting pressure error by balancing the truncation error (ϵ_{trunc}) of the derivative estimates and the random error propagation (ϵ_{rand}) into the pressure integration. In addition, with optimum methodologies apparently dependent on the flow case (Charonko *et al.* 2010), it is of interest to comprehensively evaluate the performance of common pressure estimation techniques in flows that are representative of practical applications, building on the work performed to date on analytical models of relatively simple flows (Charonko *et al.* 2010, de Kat and van Oudheusden 2012). The present study considers a circular cylinder in cross-flow, which represents a prototypical flow case in bluff-body aerodynamics encountered in a variety of practical applications. The main objective is to determine an optimal pressure estimation method, as well as associated optimum sampling rates (f_{acq}) and spatial resolutions (WS) of acquired velocity data for pressure estimation in vortex dominated wakes. In addition, the errors associated with utilizing planar velocimetry data in a three-dimensional flow will be quantified. Previous studies have compared errors associated with utilizing planar velocimetry data by comparing planar and volumetric evaluations on experimental data (de Kat and van Oudheusden 2012, Ghaemi *et al.* 2012) or by sampling analytical solutions on offset planes (Charonko *et al.* 2010, de Kat and van Oudheusden 2012); however, the error has yet to be globally quantified for a realistic flow case. To provide a reference pressure data for comparison, Direct Numerical Simulations (DNS) are used to simulate experimentally acquired velocity fields. The flows spanning laminar, transitional, and turbulent shedding regimes are subjected to uncorrelated velocity noise to simulate an experimental environment which incurs errors in detecting the correlation peak during image processing (Raffel 2007). The results inform on the errors involved in pressure integration from planar PIV data, obtained by common methodologies, and provide recommendations for optimal experimental parameters for minimizing the errors in estimated pressure fields.

3.2 Methodology

3.2.1 Direct numerical simulations

Pressure estimation techniques were tested with synthetic PIV data sampled from direct numerical simulations of a circular cylinder in cross flow for $\mathrm{Re_D} = 100, 300$, and 1575. The

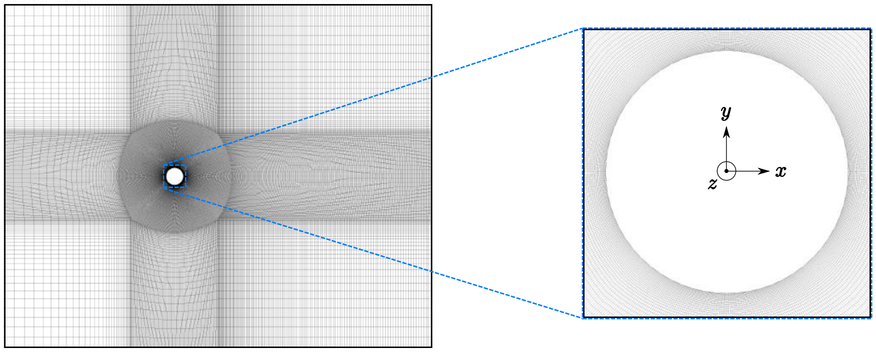

Figure 3.1: Hybrid O-type and H-type structured computational mesh, showing the mesh density utilized for $\mathrm{Re_D} = 1575$.

$\mathrm{Re_D}$	Nodes	$\Delta\theta/\eta \times \Delta r/\eta \times \Delta z/\eta$	L_z/D	$\mathrm{St_D}$	$C_{L'}$	C_D
100	1.2×10^5	$0.53 \times 0.08 \times 0$	0	0.167 **0.16**[1]	0.232 **0.23**[1]	1.35 **1.43**[2]
300	1.1×10^6	$1.21 \times 0.66 \times 4.88$	6	0.199 **0.20**[1]	0.438 **0.46**[1]	1.278 **1.24**[2]
1575	2.9×10^7	$1.59 \times 0.71 \times 2.85$	π	0.217 **0.21**[1]	0.043 **0.045**[1]	0.964 **0.95**[2]

Table 3.1: Mesh parameters alongside experimental (bold) and numerical results for flow around a circular cylinder. [1]Norberg (2003), [2]Wieselseberger (1922)

incompressible Navier-Stokes equations were solved using a finite volume solver (ANSYS CFX 14.0). The solver uses a second-order, blended finite difference spatial discretization scheme and a second-order backwards Euler implicit time marching scheme. The equations were discretized and solved on a two-dimensional mesh for $\mathrm{Re_D} = 100$, since previous experiments and simulations have established that no three dimensional effects are present in the near wake at this Reynolds number (e.g., Persillon and Braza 1998, Williamson 1996a). Three-dimensional meshes were used for $\mathrm{Re_D} = 300$ and 1575 (figure 3.1). The mesh is a structured O-type around the cylinder and a structured H-type mesh in the remaining regions (figure 3.1). Such a hybrid mesh configuration is commonly used in numerical studies on cylindrical geometries (e.g., Inoue and Sakuragi 2008, Morton and Yarusevych 2010, McClure *et al.* 2015). A uniform streamwise velocity ($u = (U_\infty, 0, 0)$) is prescribed at the inlet boundary and an average static pressure of zero is set across the outlet boundary ($\overline{p} = 0$). The no-slip condition ($u = (0, 0, 0)$) is prescribed at the cylinder surface, and the free-slip condition ($u_n = 0, \sigma_t = 0$) is imposed on the remaining domain boundaries. Mesh sizing near the surface of the cylinder (table 3.1) was ensured to be well below sizing recommendations relative to the Kolomogorov scale (η) recommended by Moin and Mahesh (1998) for DNS of common turbulent flows. The mesh sizing can further be compared to the DNS study of Wissink and Rodi (2008), who employed a second order discretization in space for a uniform cylinder at $\mathrm{Re_D} = 3300$ and tested five meshes with various levels of refinement. They achieved good convergence, based on wake statistics, with a mesh containing 1.4×10^8 nodes, and utilized similar relative refinement in the circumferential, radial, and spanwise directions (table 3.1) as those employed in the current study. Assuming the node count scales approximately with $\mathrm{Re_D^{9/4}}$ (Moin and Mahesh 1998), 2.9×10^7 nodes for $\mathrm{Re_D} = 1575$ (table 3.1) was deemed sufficient. The simulations for $\mathrm{Re_D} = 300$ and 1575 were initialized by course mesh simulations which spanned the initial transient of the vortex shedding excitation, and results from the fine mesh simulation were sampled once the fluctuating lift and drag forces reached a quasi-steady state. The instantaneous force data on the cylinder and streamwise velocity data at $x/D = 5$, $y/D = 0.75$ were then collected for a minimum duration of 8 cylinder vortex shedding cycles. The shedding frequency (f_s) was estimated based on a sinusoidal regression of the streamwise velocity data. The results pertaining to the fluctuating lift force ($C_{L'}$), shedding frequency ($\mathrm{St_D} = f_s D/U_\infty$), and mean drag ($C_D$) are summarized in table 3.1 and compared to available experimental data. A comparison with experimental values shows a maximum deviation of 5.6%. The minor deviations between numerical and experimental data in table 3.1 are similar to those found in other DNS studies at similar Reynolds numbers (Marzouk *et al.* 2007, Wissink and Rodi 2008, Zhao and Cheng 2014).

The results are illustrated using iso-surfaces of the λ_2-criterion (Jeong and Hussain 1995), where λ_2 is the second largest negative eigenvalue of $\boldsymbol{S}^2 + \boldsymbol{\Omega}^2$ (equations 2.2 and 2.3), coloured by static pressure in figure 3.2. Note, the results for $\mathrm{Re_D} = 100$ are extruded in the spanwise direction for illustration purposes. It can be seen that, as expected, the near wake development is defined by the formation and evolution of the von Kármán rollers for all Reynolds numbers investigated. The dominant spanwise vortices undergo notable deformations associated with the formation of three-dimensional secondary structures for $\mathrm{Re_D} \geq 300$. For $\mathrm{Re_D} = 300$, a hyperbolic flow instability in the shear regions between primary vortex cores, termed “mode B” instability (Williamson 1996b), leads to the development of secondary streamwise vortices which persist with a spanwise wavelength of $\lambda_z/D \approx 1.0$ (Williamson 1996b, Scarano and Poelma 2009). For $\mathrm{Re_D} = 1575$, turbulent transition occurs in the separated shear layers and precedes primary vortex formation. The wake consists of a plethora of secondary structures interacting with the primary spanwise rollers in a random fashion. As progressively finer scale structures develop with increasing $\mathrm{Re_D}$, characteristic spatial and temporal scales in the wake pressure fields also decrease, as expected, which is the primary reason for selecting these three test cases for the present study.

3.2.2 Synthetic PIV and pressure estimation optimization

Synthetic PIV data were obtained by sampling planar $x - y$ velocity fields from the DNS solutions at $z = 0$ (midspan) on an equispaced Cartesian grid on the domain $-2D < x < 2D$ and $-2D < y < 2D$ for a range of f_{acq} and WS. Similar to the approach employed in previous studies (e.g., Charonko *et al.* 2010, Azijli and Dwight 2015), Gaussian random

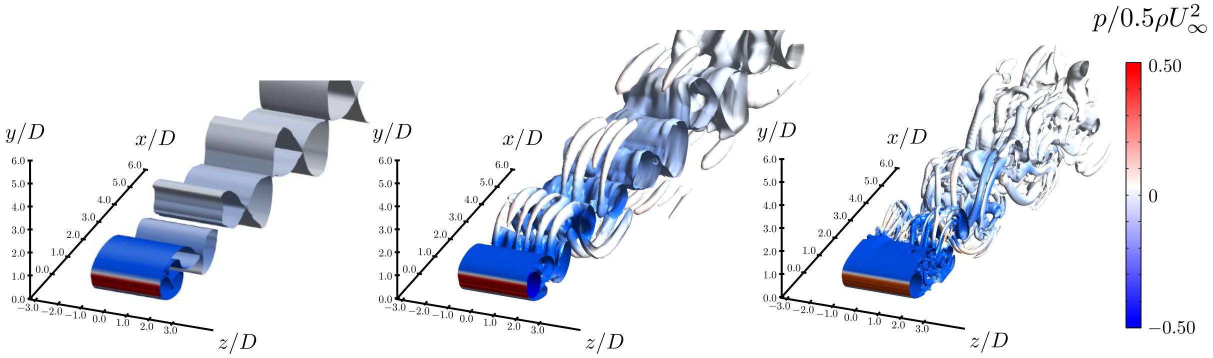

(a) Laminar $Re_D = 100$ (b) Mode B instabilities $Re_D = 300$ (c) Shear layer transition $Re_D = 1575$

Figure 3.2: Vortex visualizations using the λ_2-criterion ($\lambda_2 = 0.01$) (Jeong and Hussain 1995) for (a) laminar vortex shedding at $\mathrm{Re_D} = 100$ (two-dimensional data extruded for comparison), (b) transitional vortex shedding at $\mathrm{Re_D} = 300$, and (c) turbulent vortex shedding at $\mathrm{Re_D} = 1575$.

noise was added to the synthetic velocity fields proportional to the magnitude of each velocity component ($\tilde{u} = u(1 + \epsilon_u)$) to simulate measurement noise. The noise level (ϵ_u) was varied between 0 and 2.5% in 0.25% increments in order to capture the initial error response characteristics, which for a given methodology have been shown to extrapolate to higher noise levels (Charonko *et al.* 2010, de Kat and van Oudheusden 2012). To estimate pressure from the synthetic data, Eulerian spatial and temporal derivatives of the velocity field were calculated with second-order central difference estimators (equation 3.5) and used to estimate the material acceleration and viscous terms in equations 3.3. The viscous terms in the Navier-Stokes equations were found to be non-negligible for $\mathrm{Re_D} = 100$, and hence were included for all $\mathrm{Re_D}$. A parametric study was performed to investigate the effects of Reynolds number ($\mathrm{Re_D}$), spatial resolution (WS), temporal resolution (f_{acq}), velocity field noise level (ϵ_u), and pressure estimation method on the accuracy of instantaneous pressure field estimations (p). The investigated parameters are summarized in table 3.2.

Four common pressure integration techniques were compared: (i) omni-directional line integration (Liu and Katz 2006), (ii) eight-path integration (Dabiri *et al.* 2014), (iii) Poisson equation (Gurka *et al.* 1999), and (iv) local least squares iteration (Tronchin *et al.* 2015). For each temporal resolution (f_{acq}), spatial resolution (WS), and noise level (ϵ_u) investigated in the parametric study, instantaneous velocity fields were sampled at six different phases over half a vortex shedding cycle ($\theta = 0, \pi/6, \pi/3, \pi/2, 2\pi/3, 5\pi/6$) and five refreshed noise profiles were generated at each phase, resulting in a total of 30 unique velocity fields for each combination of parameters investigated, from which pressure is estimated using each integration technique. The error in each estimated pressure field (ϵ_p) was quantified using the spatial standard deviation of the difference between the estimated (p) and DNS (p_{ex}) pressure field (equation 3.8). For a given combination of parameters, the error response was then characterized by the mean ($\bar{\epsilon}_p$) and standard deviation (σ_{ϵ_p}) of this error computed over the 30 pressure estimates.

Estimation methodology	$\mathrm{Re_D}$	ϵ_u	D/WS	f_{acq}/f_S
Omni-directional	$100, 300, 1575$	$0 - 2.5\%$	$5 - 100$	$7.8 - 1000$
Eight-path				
Poisson equation				
Local least squares				

Table 3.2: List of pressure estimation methodologies employed in the current study and ranges of parameters investigated in the parametric study.

$$\overline{\epsilon_p} = \frac{\sqrt{\overline{(p - p_{ex})^2}}}{\frac{1}{2}\rho U_\infty^2} \tag{3.8}$$

The implementation of boundary conditions can have considerable effects on the accuracy of pressure estimates (Pan *et al.* 2016). For the iterative methods (omni-directional, eight-path, and local least squares), the boundary conditions were implemented following the approach employed in the studies that proposed these techniques (Liu and Katz 2006, Dabiri *et al.* 2014, and Tronchin *et al.* 2015), namely, where the domain was initialized to zero pressure before integrating the pressure gradient over the inner domain and boundaries. Additionally, for the omni-directional and eight-path methods, the boundary pressures were initialized by a line integral of the pressure gradient field around the boundary, starting at $p_{1,1} = 0$ at the bottom left corner point. Based on initial convergence tests, a fixed number of pressure gradient integration iterations were performed. Specifically, the omni-directional and eight-path methods used 5 iterations, and the local least squares method used 3000 iterations. For the Poisson equation method, the Laplacian of the pressure field (equation 3.4) was discretized using a 5-point second-order central difference scheme and Neumann boundary conditions were imposed through the use of ghost grid points at the outlet and cylinder boundaries in order to complete the five point scheme where adjacent nodes lie outside the domain. The pressure values at the ghost points were evaluated using the pressure gradient from the Navier-Stokes equation and the nodal pressure on the opposing side of the five point scheme (e.g., $p_{i+1,j} = p_{i-1,j} + 2\Delta x \frac{\partial p}{\partial x}_{i,j}$). Neumann boundary conditions were implemented for the Poisson equation method on all boundaries and an additional constraint equation was added to the system to specify $p_{1,1} = 0$. The resulting system of equations is over-constrained and the solution is the least-squares solution (Trefethen 2000). For each method, the relative pressure field was solved for initially, and a constant value was then added to each field such that the Bernoulli equation extended to irrotational, inviscid, unsteady advective flow with small mean velocity gradients (equation 3.9) (de Kat and van Oudheusden 2012) was satisfied, on average, at the top and bottom boundaries.

$$p + \frac{1}{2}\rho(\overline{u}_i\overline{u}_i + u_i'u_i') = p_\infty + \frac{1}{2}\rho U_\infty^2 \tag{3.9}$$

The parametric study and analytic models developed in the current study use Eulerian estimates for the material acceleration (equation 3.5), since a comparison with a second order Lagrangian scheme for material acceleration estimation (equations 3.6 and 3.7) resulted in minor differences in error levels of the pressure evaluations for $25 \leq f_{acq}/f_S \leq 1000$ when three velocity fields at $t_0 - dt$, t_0, and $t_0 + dt$ were utilized for both methods. However, the extension of the analysis to Lagrangian material acceleration reconstructions over N fields is discussed using second order trajectory estimates (equations 3.6 and 3.7) between fields separated by $\pm Mdt$, $\pm(M-1)dt$, ..., where $N = 2M + 1$, with the material acceleration estimated via a second order polynomial fit to the resulting trajectory (Lynch and Scarano 2014).

3.3 Results

The results of the parametric study yield a data set of about 110,000 pressure field cases. Using this data set, the pressure estimation techniques are compared across a range of spatial resolutions (WS), temporal resolutions (f_{acq}), and velocity noise levels (ϵ_u) in laminar, transitional, and turbulent flows.

3.3.1 Comparison of pressure estimation methodologies

It has been demonstrated in one-dimensional parametric studies (Charonko *et al.* 2010, Violato *et al.* 2011, de Kat and van Oudheusden 2012, Tronchin *et al.* 2015) that optimal temporal ($f_{acq,opt}$) and spatial (WS_{opt}) resolutions can be determined for a given flow such that the combined truncation (ϵ_{trunc}) and random (ϵ_{rand}) uncertainty propagation to the pressure field estimate is minimized. Since the optima may vary based on the pressure integration technique employed, it is necessary to estimate these parameters before a comparison between methods can be carried out. Figure 3.3 shows the variation of the mean pressure error response ($\overline{\epsilon}_p$) with f_{acq} and WS, for each tested technique and Reynolds number, when the synthetic velocity fields are contaminated with 2.0% Gaussian white noise. The magnitude of the mean pressure error is also illustrated by the white to red colormap on the surface, with the optimal sampling parameters identified either by the minima or the whitest region of each surface. The surface sections coloured yellow indicate where pressure estimation is unconverged for the local least squares approach due to insufficient iteration of the solver to mitigate the directional propagation of error for the high spatial resolution calculations ($D/WS \geq 50$). Note that optimal values cannot be strictly defined in every case due to the minima lying on the boundaries of the parametric study. For example, the optima for the eight-path method, for each Reynolds number investigated, likely lies beyond the minimum f_{acq}/f_S investigated, and the optima for the

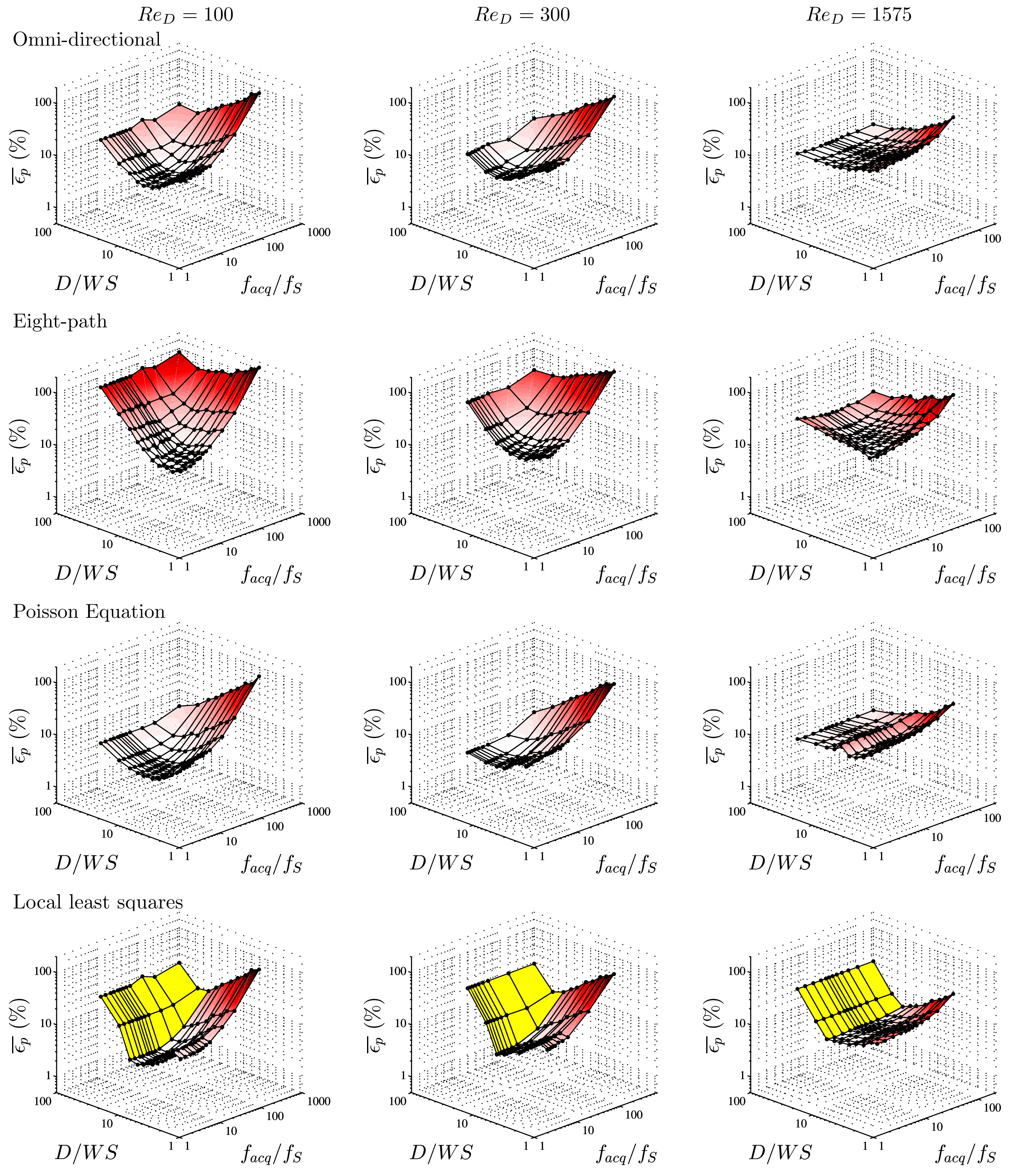

Figure 3.3: Optimization surfaces showing the mean pressure field error ($\bar{\epsilon}_p$) for $\epsilon_u = 2\%$ for the ranges of spatial and temporal resolutions investigated for each Reynolds number and pressure estimation method investigated. Pressure estimations which are not converged are coloured in yellow.

omni-directional method and Poisson equation for $\mathrm{Re_D} = 1575$ is likely located beyond the maximum D/WS investigated. However, the curvature of the optimization surfaces at the boundaries suggest that the optimal values are located not far beyond the boundaries of the parametric study, and that the difference between the pressure error at the optimal point and the boundary point is comparable to the differences due to the resolution of the parametric study. The optimization surfaces exhibit similar topology for $\mathrm{Re_D} = 100$, 300, and 1575 (left to right, respectively in figure 3.3), resembling sections of ellipsoid surfaces, and in most cases, local minima are present within the investigated range of parameters. For higher values of D/WS and f_{acq}/f_S, increasing these parameters causes the error to increase, approximately following a power law. On the other hand, decreasing D/WS and f_{acq}/f_S below the optimal values causes a more gradual increase in the pressure error. Notably, for increasing Reynolds number, the minimum error increases significantly, which is attributed to the increasing three-dimensional error (ϵ_{3D}) caused by neglecting the out of plane velocities and gradients. This causes the random and truncation uncertainty propagation to contribute proportionally less to the RMSE metric utilized, resulting in changes in the temporal and spatial resolution having a less significant effect on the total pressure error in figure 3.3. The values of optimal sampling parameters for $\epsilon_u = 2\%$, identified in figure 3.3, are shown in table 3.3. As expected, the optimal spatial resolutions (WS_{opt}) for each method decrease with increasing Reynolds number as the spatial scales (λ_x) of the flow decrease. On the other hand, the optimal acquisition frequencies ($f_{acq,opt}/f_S$), when normalized by the shedding frequency, do not show a pronounced dependency on the Reynolds number within the uncertainty bounds. This is attributed primarily to two factors. First, the dominant vortical structures shed at f_S dominate the pressure fluctuations. Moreover, the main secondary structures that appear at higher Reynolds numbers are associated with time scales within an order of magnitude of $1/f_S$, and are adequately captured in estimated pressure fields acquired with $f_{acq}/f_S > 10$. Secondly, the error response surfaces in figure 3.3 flatten out near optimal acquisition frequencies making a precise determination of the optimal frequency challenging, which is the main reason for the relatively large uncertainty bounds for this quantity in table 3.3. The development of practical guidelines for the selection of optimal sampling parameters will be discussed further in the next subsection.

To compare the accuracy of the methods at different velocity noise intensities, the mean ($\bar{\epsilon}_p$) and standard deviation (σ_{ϵ_p}) of the pressure error response, extracted at WS_{opt} and $f_{acq,opt}$ for each ϵ_u, are plotted in figure 3.4. It can be seen that the eight-path integration method exhibits consistently higher error sensitivity than the other methods, showing a comparable response for low ϵ_u but a significantly increased response in $\bar{\epsilon}_p$ for more intense noise environments. Inspecting the corresponding pressure integration results (figure 3.5) indicates that the method suffers from high degrees of isotropic noise as the contour topology and pressure magnitudes are, on the average, close to the DNS reference (figure 3.5) but have a high degree of superimposed noise. The high noise sensitivity of the eight-path method is attributed to the lower number of line-integrals used, compared to the omni-directional method, which is a similar method that uses the average of significantly more line-integrals to calculate the fluid pressure at each point. The high noise sensitivity also

Pressure Technique	$\mathrm{Re_D} =$ 100 D/WS_{opt}	$\mathrm{Re_D} =$ 100 $f_{acq,opt}/f_S$	$\mathrm{Re_D} =$ 300 D/WS_{opt}	$\mathrm{Re_D} =$ 300 $f_{acq,opt}/f_S$	$\mathrm{Re_D} =$ 1575 D/WS_{opt}	$\mathrm{Re_D} =$ 1575 $f_{acq,opt}/f_S$
Omni-directional	$20^{+5.0}_{-5.7}$	$25.3^{+6.3}_{-4.2}$	$33.3^{+16.7}_{-8.3}$	$20.4^{+2.6}_{-2.0}$	$100^{+50.0}_{-50.0}$	$15.6^{+20.8}_{-7.81}$
Eight-path	$6.7^{+1.6}_{-4.4}$	$12^{+3.8}_{-3.8}$	$14.3^{+5.7}_{-3.2}$	$20.4^{+2.6}_{-2.0}$	$20^{+5.0}_{-5.7}$	$21.7^{+14.6}_{-6.24}$
Poisson equation	$25^{+8.3}_{-5.0}$	$31.6^{+4.5}_{-6.3}$	$50^{+50.0}_{-16.7}$	$23.0^{+3.3}_{-2.6}$	$100^{+50.0}_{-50.0}$	$10.9^{+32.8}_{-3.1}$
Local least squares	$25^{+8.3}_{-5.0}$	$21.1^{+4.2}_{-5.3}$	$33.3^{+16.7}_{-8.3}$	$20.4^{+2.6}_{-2.0}$	$33.3^{+16.7}_{-8.3}$	$10.9^{+32.8}_{-3.1}$

Table 3.3: Optimal sampling parameters for $\epsilon_u = 2\%$. Uncertainty bounds given by the local resolution of the parametric study at each optimum.

causes the identified optimal sampling parameters for the eight-path method to be shifted relative to the other three tested methods (table 3.3). In contrast, the omni-directional, Poisson equation, and local least squares methods exhibit relatively low sensitivity to the velocity noise environment (ϵ_u), with maximum resulting error levels of $2-5\%$ at $\epsilon_u = 2.5\%$ depending on $\mathrm{Re_D}$ (figure 3.4a-c). In particular, for $\mathrm{Re_D} = 1575$ (figure 3.4c), the pressure error response shows a change of less than 1% across the entire range of velocity noise intensities studied. This insensitivity is due to the relatively high base three-dimensional error present for $\mathrm{Re_D} = 1575$ ($\epsilon_{3D} \approx 4\%$), compared to the lower Reynolds numbers, caused by the two-dimensional assumptions imposed on the three-dimensional flow. This implies that, when significant inaccuracies in pressure estimation exist due to three-dimensional effects, contamination of the pressure gradient field by relatively small random errors in velocity measurements has a smaller additive effect on the pressure error response. The Poisson equation and local least squares method are the least sensitive to velocity fields noise, exhibiting the smallest change in $\bar{\epsilon}_p$ over $\epsilon_u = 0 - 2.5\%$. It should be noted that, since the errors in figure 3.4 are quantified by the standard deviation of the difference between the estimated pressure field and DNS solution (equation 3.8), they pertain to the relative pressure field ($p - p_\infty$). The error associated with establishing the absolute pressure through the application of the modified Bernoulli equation at the side boundaries was approximately 1% for all the pressure estimation methods investigated.

The accuracy of the surface pressure distribution ($C_p(\theta)$) estimation is of particular interest since it may be used to extract instantaneous structural loading (van Oudheusden *et al.* 2007). Figure 3.6 presents a comparison of the surface pressure estimations with the DNS reference for $\mathrm{Re_D} = 100$, 300 and 1575. For each methodology, the pressure integrations were performed with a velocity noise level of $\epsilon_u = 2\%$ and sampled at each method's WS_{opt} and $f_{acq,opt}$. The results indicate that the Poisson equation method estimates the surface pressures best across all the Reynolds numbers investigated, though the omni-directional and local least squares methods perform favourably as well. In comparison, surface pressure distributions resulting from the eight-path method have significant data scatter; however the scatter is approximately centred around the DNS pressure solution, so that its detrimental effect on structural loads is expected to be lower than the

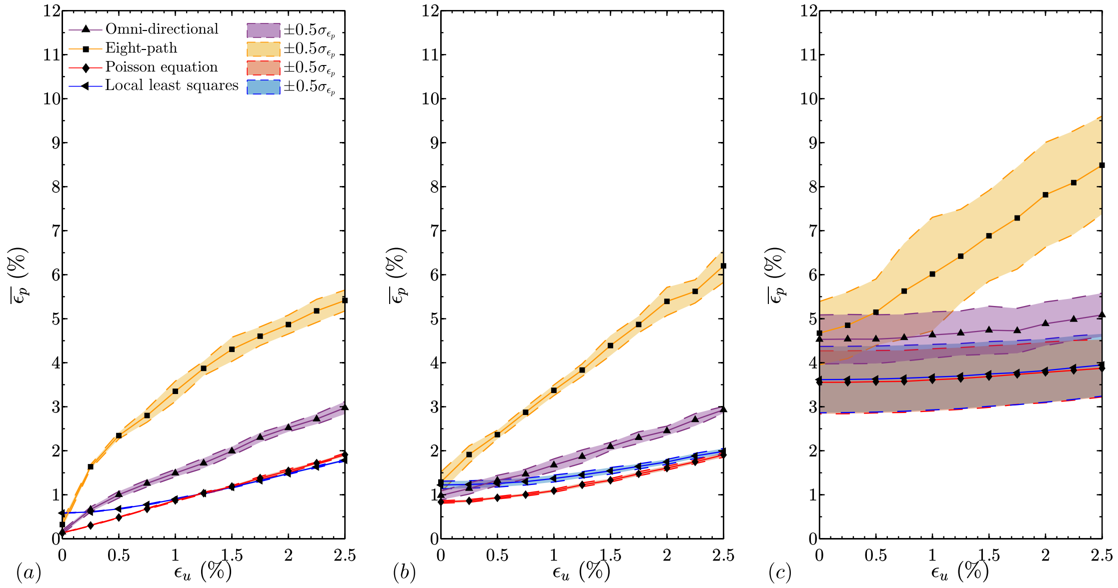

Figure 3.4: Mean pressure field error (ϵ_p) versus velocity field error (ϵ_u) from each pressure integration method investigated for (a) $\mathrm{Re_D} = 100$, (b) $\mathrm{Re_D} = 300$, and (c) $\mathrm{Re_D} = 1575$. Filled regions indicate one standard deviation of the pressure field error. For each ϵ_u, optimal WS_{opt} and $f_{acq,opt}$ were used for the pressure estimation.

associated surface pressure errors. The utilization of the planar results for the extraction of surface pressure loading is deemed acceptable for all Reynolds numbers investigated, as the omni-directional, Poisson equation, and local least squares methods show remarkable agreement with the DNS solver pressures, even for relatively high $\epsilon_u = 2\%$, as well as in turbulent shedding regimes (figure 3.6c). Despite average pressure field errors reaching approximately $\bar{\epsilon}_p = 3 - 5\%$ for $\epsilon_u = 2\%$ and $\mathrm{Re_D} = 1575$ (figure 3.4c), the surface pressures rarely deviated from the DNS reference by more than 1%. The most significant pressure field errors are concentrated in the wake regions where flow three-dimensionalities and complex vortex development occur.

3.3.2 Pressure PIV uncertainty minimization

The results of the parametric study indicate the existence of optimal f_{acq} and WS_{opt} for various ϵ_u, $\mathrm{Re_D}$, and pressure integration methodology which minimize the RMS pressure field error (figure 3.3, and table 3.3). It is of interest to develop a model that can be employed to estimate optimal data acquisition parameters in experimental studies where pressure estimation is of interest. Such a model is developed here based on the following uncertainty propagation analysis.

Neglecting viscous terms, the uncertainty in the determination of the pressure gradient ($\epsilon_{\nabla p}$, equation 3.10) can be expressed by the contributions of the propagation of the ve-

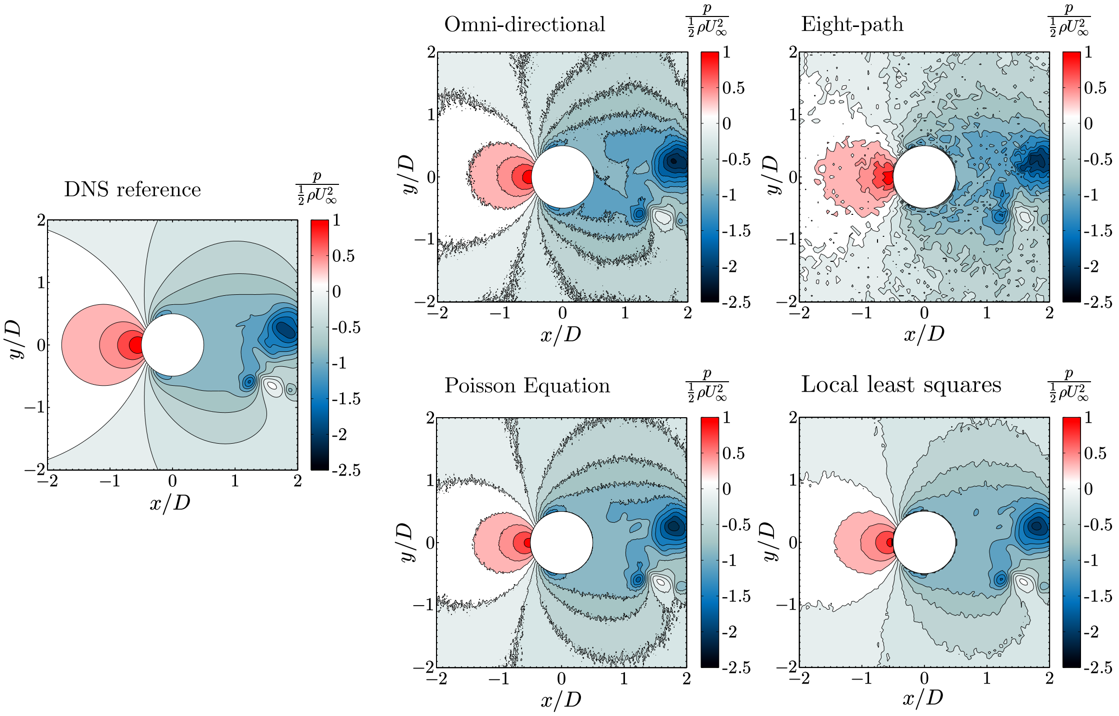

Figure 3.5: Reference pressure from DNS data, along with pressure estimations at respective optimal $D/WS_{opt} = 100$ and $f_{acq,opt}/f_s = 10.9$ for $\epsilon_u = 2\%$ for each method at $\mathrm{Re_D} = 1575$.

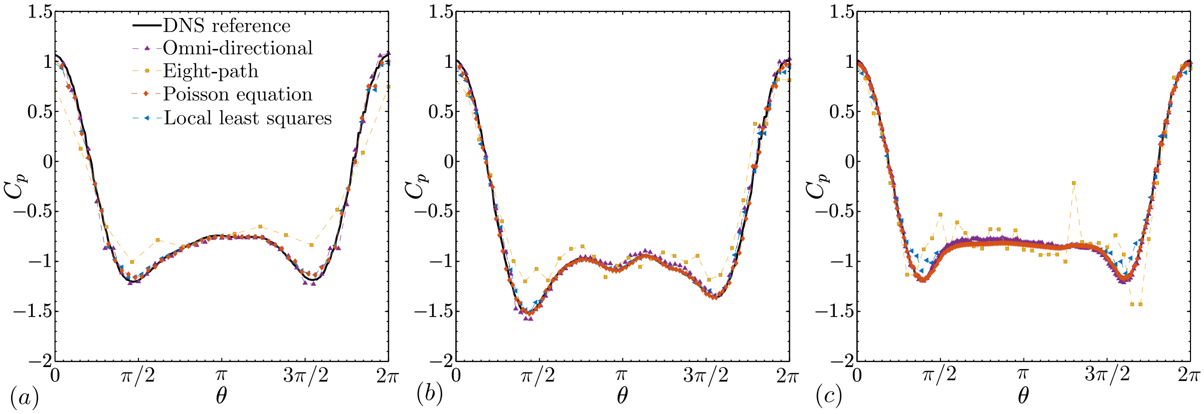

Figure 3.6: Instantaneous surface pressure distributions from each method investigated, contaminated with $\epsilon_u = 2\%$ velocity field error, for (a) $\mathrm{Re_D} = 100$, (b) $\mathrm{Re_D} = 300$, and (c) $\mathrm{Re_D} = 1575$. $C_p(\theta)$ is nearest neighbour interpolated from the pressure evaluations sampled at identified optimal WS_{opt} and $f_{acq,opt}$.

locity error (ϵ_u, equation 3.11, de Kat and van Oudheusden 2012) through the derivative estimators, and the truncation error terms arising from finite resolution of the derivative estimators (Etebari and Vlachos 2005) (ϵ_{trunc}, equation 3.12).

$$\epsilon_{\nabla p}^2 \approx \rho \epsilon_{Du/Dt}^2 \approx \rho \epsilon_u^2 |u|^2 \left(\frac{f_{acq}^2}{2} + \frac{|u|^2}{2WS^2} + |\nabla u|^2 \right) + \frac{WS^4}{36} \left(\nabla^3 u \right)^2 |u|^2 + \frac{1}{36 f_{acq}^4} \left(\frac{\partial^3 u}{\partial t^3} \right)^2 \tag{3.10}$$

$$\epsilon_{rand} = \rho \epsilon_u |u| \sqrt{\frac{f_{acq}^2}{2} + \frac{|u|^2}{2WS^2} + |\nabla u|^2} \tag{3.11}$$

$$\epsilon_{trunc} = \rho \sqrt{\frac{WS^4}{36} (\nabla^3 u)^2 |u|^2 + \frac{1}{36 f_{acq}^4} \left(\frac{\partial^3 u}{\partial t^3} \right)^2} \tag{3.12}$$

Equations 3.10-3.12 suggest minimizing the pressure gradient uncertainty requires balancing between the propagation of random error, which decreases for increasing WS and decreasing f_{acq}, and the truncation error, which decreases for decreasing WS and increasing f_{acq}. In order to model how the pressure gradient uncertainty propagates to pressure field uncertainty, a line-integration serves as a suitable approximation for the techniques employed in this study. In particular, at a single time-step, the omni-directional, eight-path, and local least squares methods rely on a sequential integration of ∇p over a finite number of WS in order to estimate p on the domain. Similarly, although the Poisson equation solves local equations simultaneously across the domain, the solution can nevertheless be cast as an integral of the pressure gradient field using Green's functions. Hence, assuming uncorrelated pressure gradient error, the resulting pressure field uncertainty (ϵ_p) relates to the pressure gradient uncertainty ($\epsilon_{\nabla p}$) according to:

$$\epsilon_p^2 = \sum^{\gamma/WS} \epsilon_{\nabla p}^2 (WS)^2 \approx \gamma \epsilon_{\nabla p}^2 WS \tag{3.13}$$

where γ is the characteristic length scale of a single line-integration (e.g., domain length). An optimization problem $min \left\{ \epsilon_p^2 : f_{acq} > 0, WS > 0 \right\}$ can now be solved for equation 3.13 with respect to f_{acq} and WS through a critical point analysis. The solution is given by equations 3.14 and 3.15.

$$f_{acq,opt} = \left(\frac{(\partial^3 u / \partial t^3)^2}{9 \epsilon_u^2 |u|^2} \right)^{1/6} \tag{3.14}$$

$$WS_{opt}^6 \frac{7 (\nabla^3 u)^2 |u|^2}{36} + WS_{opt}^2 \left(\frac{3}{2} (\epsilon_u f_{acq})^2 + 3 \epsilon_u^2 |\nabla u|^2 + \frac{3}{36 f_{acq}^4} \frac{\partial^3 u}{\partial t^3}^2 \right) + \epsilon_u^2 |u|^2 / 2 = 0 \tag{3.15}$$

The result decouples the solution for the optimal temporal resolution (f_{acq}) from the dependence on the spatial resolution (equation 3.14). However, the solution for the optimal spatial resolution retains temporal terms (equation 3.15). This is due to the coupling caused by the propagation of $\epsilon_{\nabla p}$ through the line-integrations which is $\propto \epsilon_{\nabla p} WS$, resulting in a 6th order polynomial for WS_{opt}. For planning experiments, the solution remain intractable a priori due to its dependence on unknown velocity gradients. However, temporal and spatial derivatives of the flow may be approximated assuming the characteristic velocity (U_∞) varies periodically (i.e., sinusoidally) with the time scales ($1/f_{flow}$) and selecting appropriate spatial scales (λ_x) for a given vortex dominated flow. Substituting these approximations into equations 3.14 and 3.15 simplifies them to:

$$f_{acq,opt} \approx \frac{2\pi f_{flow}}{(3\epsilon_u)^{1/3}} \tag{3.16}$$

$$\frac{7}{18\epsilon_u^2}\left(\frac{2\pi WS_{opt}}{\lambda_x}\right)^6 + 6\left(\frac{2\pi WS_{opt}}{\lambda_x}\right)^2 + 1 = 0 \tag{3.17}$$

Inspection of equation 3.17 reveals that, for $\epsilon_u = 0-3\%$ typically found in PIV experimentation, the leading, 6^{th} order term dominates and the 2^{nd} order term in the polynomial is negligible. Hence the model for the optimal spatial resolution can be simplified further to:

$$WS_{opt} \approx \left(\frac{18\epsilon_u^2}{7}\right)^{1/6} \frac{\lambda_x}{2\pi} \tag{3.18}$$

where WS_{opt} is independent of f_{acq} for small ϵ_u. This can also be inferred from the optimization surfaces presented in figure 3.3, which conform to, on the average, ellipsoid sections with major and minor axes aligned with the temporal and spatial axes. This result implies that the optimal temporal and spatial resolutions obtained from one-dimensional parametric studies in Charonko *et al.* (2010) and Violato *et al.* (2011) are valid as absolute optimums for the respective intensity of the noise environment, and may be compared to the data in the present study. It is important to note that the derivation of equations 3.16 and 3.18 is insensitive to reformulating equation 3.13 as an average of multiple line integrations or incorporating terms representing the boundary error at the start of each line integration. The presented formulation also assumes uncorrelated velocity field error, which will not be the case if interrogation windows are overlapped during PIV processing (Sciacchitano and Wieneke 2016), and does not account for the spatial filtering implicit in the use of finite interrogation windows in PIV processing. However, it was verified that adding correlated velocity field errors after smoothing the velocity field with a 3×3 kernel had minimal effect on the results pertaining to the locations of the optimal sampling parameters and comparison of methods presented in Figs. 3.4 - 3.6.

To validate the derived model (equations 3.16 and 3.18), it is applied to the flow cases considered in the current study. For circular cylinders in cross-flow, the characteristic frequency scale (f_{flow}) is approximated as the frequency of vortex shedding $f_S = \mathrm{St_D} D/U_\infty$ and the characteristic spatial wavelength (λ_x) is approximated as twice the shear layer

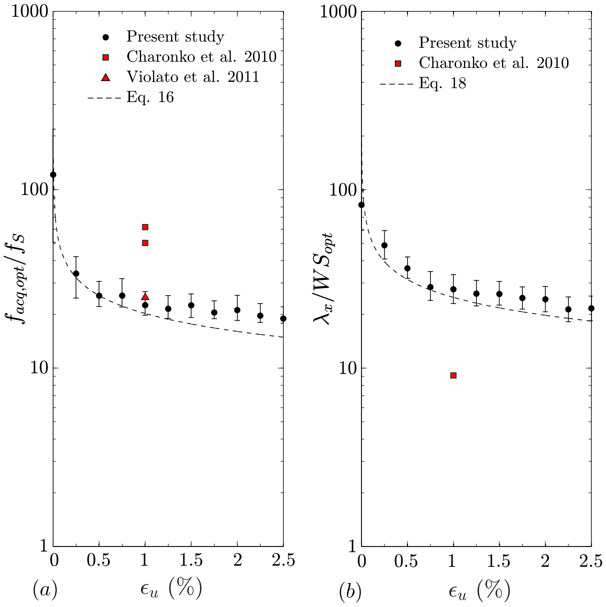

Figure 3.7: (a) Optimal temporal resolutions $f_{acq,opt}$ normalized by the shedding frequency f_s amalgamated from all Reynolds numbers and methodologies tested and compared to available optimal data from other studies and (b) optimal spatial resolution WS_{opt} normalized by the spatial wavelength λ_x of the flow

thickness, approximated according to $\delta_{sl} = 7.5D/\mathrm{Re}_\mathrm{D}^{1/2}$ (Roshko 1993, Williamson 1996c). The optimal temporal and spatial resolutions for pressure evaluation in flow over a circular cylinder may now be calculated using equations 3.16 and 3.18, respectively. It can be seen from equations 3.16 and 3.18 that a universal scaling for the $f_{acq,opt}$, and WS_{opt} is achieved in the form $f_S/f_{aqc,opt}$ and λ_x/WS_{opt}. The results from the present study cast in this form are presented in figures 3.7a and 3.7b, along with relevant data found in the literature for a decaying vortex (Charonko *et al.* 2010), pulsatile flow (Charonko *et al.* 2010), and a rod airfoil (Violato *et al.* 2011). The present data show good collapse, and the model shows close agreement with the parametric data as well as optima reported in other investigations on different flow topologies. Based on the results, a general recommendation can be made for a range of optimal data acquisitions parameters as $f_{acq}/f_{flow} = 18 - 30$ and $\lambda_x/WS = 14.3 - 25$ for the range of velocity error levels expected in a typical PIV experiment when Eulerian material acceleration estimation methods are applied. These results are in agreement with the resolution limitations suggested by de Kat and van Oudheusden (2012) of $\lambda_x/WS > 5$ and $f_{acq}/f_{flow} > 10$, who were primarily concerned with the effects on pressure peak response in the resulting fields. The current results suggest that utilizing resolutions up to twice the minimum limits on the acquisition frequency and four times the minimum limits on the spatial resolution recommended by de Kat and van Oudheusden (2012) will result in optimal performance, minimizing the spatial filtering effects caused by inadequate spatial or temporal resolutions without oversampling to an extent that random error effects become significant.

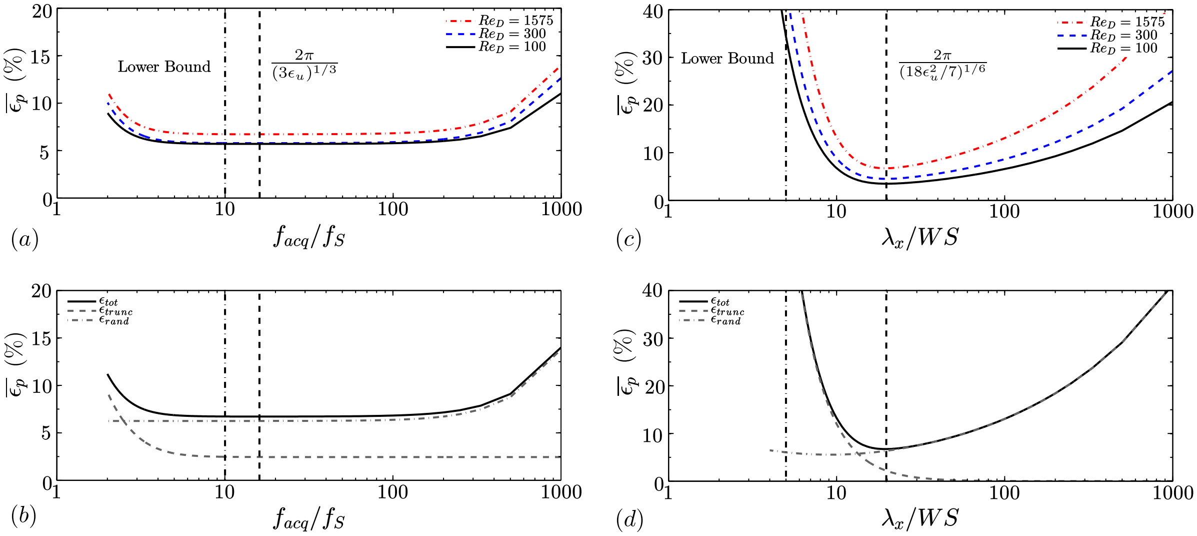

Figure 3.8: Pressure field uncertainty predicted from equation 3.13 with $\epsilon_u = 2\%$ exhibiting Reynolds number similarity across (a) temporal resolution at fixed $D/WS = 100$ and (b) spatial resolution at fixed $f_{acq}/f_s = 50$ compared to bounds proposed by (de Kat and van Oudheusden 2012). The uncertainty is decomposed into random and truncation components according to equation 3.13 using f_S and λ_x estimates, and the variation with (c) spatial and (d) temporal resolutions for $\mathrm{Re_D} = 1575$ is shown.

Figures 3.8a-d elucidate the relation between the data acquisition parameters and the pressure uncertainty predicted by equation 3.13. The identified minima, which stem from equations 3.16 and 3.18, for λ_x/WS and f_{acq}/f_S, respectively, can be seen to be independent of the the Reynolds number, indicating the three-dimensional error contributes independently from the truncation and random error propagation. The pressure uncertainty remains within 1% of the minimum uncertainty for a relatively wide range of acquisition frequencies from $3 \leq f_{acq}/f_s \leq 200$ (figure 3.8a). In contrast, the requirements on the spatial resolution to remain within the same range of the minimum uncertainty are more stringent, namely $\lambda_x/WS = 14.3-33.3$ (figure 3.8c). Figures 3.8b and d decompose the total pressure uncertainty from equation 3.13 for $\mathrm{Re_D} = 1575$ into contributions from truncation (ϵ_{trunc}) and random (ϵ_{rand}) error components. The results illustrate the regions where spatial or temporal resolutions become too fine, and propagation of random error dominates, and where they become too coarse and the truncation error term dominates. Comparing the current formulation to the bounds on the spatial and temporal resolution recommended by de Kat and van Oudheusden (2012), indicated by a dash-dotted line in figures 3.8b and d, it can be seen that the recommended spatial resolution bound corresponds to a region where the truncation error dominates, while the temporal resolution bound corresponds to a region with still acceptable uncertainty levels, beyond which truncation error begins to dominate.

It is important to note that when data is over-sampled temporally (i.e., $f_{acq} > f_{acq,opt}$), Lagrangian trajectory reconstructions over multiple velocity fields (e.g., Lynch and Scarano 2014) can be employed for more accurate estimation of pressure, as low order trajectory reconstructions over longer kernels mitigates random error propagation. Figure 3.9 illustrates how average error levels change with respect to temporal and spatial resolution for

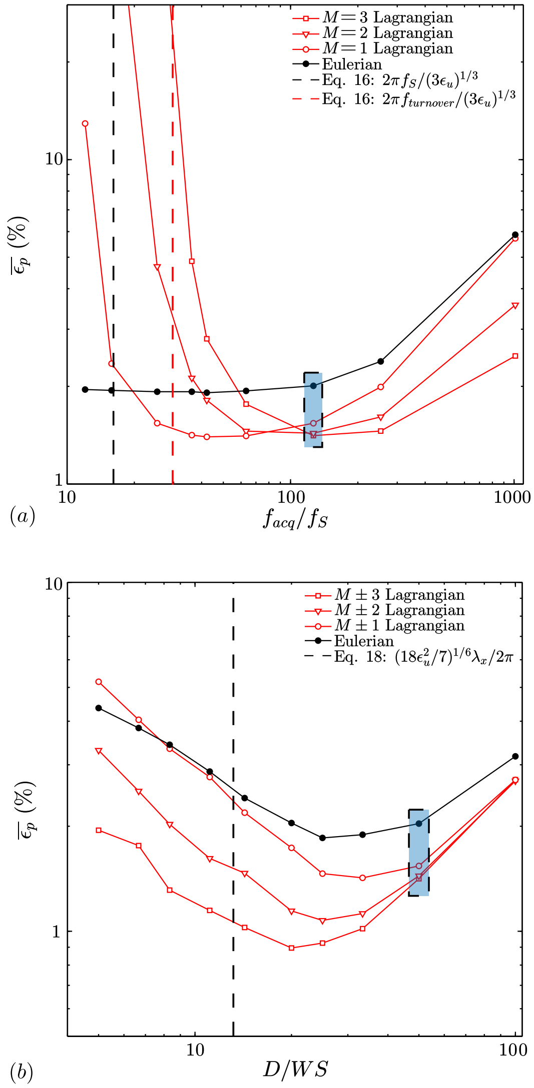

Figure 3.9: Comparison of pressure estimation error using Eulerian and Lagrangian material acceleration estimates reconstructed over 3 ($M = 1$), 5 ($M = 2$), and 7 ($M = 3$) velocity fields using the Poisson equation for $\mathrm{Re_D} = 100$ and $\epsilon_u = 2\%$ for (a) varying acquisition frequency with a constant spatial resolution $D/WS = 50$, and (b) varying spatial resolution with a constant acquisition frequency $f_{acq}/f_S = 123$. The common points where the one-dimensional parametric studies intersect are highlighted in blue.

the Eulerian methods used for the parametric study compared to Lagrangian material acceleration estimates over multiple velocity fields. For the Lagrangian estimates, the fluid trajectories are computed iteratively using a second order trajectory reconstruction (equations 3.6, 3.7) at times $t_0 - Mdt$, $t_0 - (M-1)dt$, ..., t_0, ..., $t_0 + (M-1)dt$, $t_0 + Mdt$, employing a second order polynomial fit function following the method by Lynch and Scarano (2014). The results show that the use of Lagrangian techniques for material acceleration estimation changes substantially the shapes of the optimization curves with respect to temporal resolution (figure 3.9a), while the changes for the spatial resolution (figure 3.9b) are less significant. For the temporal resolution, using the vortex turn over time ($f_{turnover} = U_\infty / \pi D$) (de Kat and van Oudheusden 2012) gives a reasonable estimate of the optimal acquisition frequency for the Lagrangian method with $M = 1$. However, as the kernel for material acceleration estimation is increased to $M = 2$ and $M = 3$, the optimum acquisition frequency increases proportionally, with $f_{acq}/f_S = 50$ for $M = 1$, $f_{acq}/f_S = 100$ for $M = 2$, and $f_{acq}/f_S = 150$ for $M = 3$. This implies that when Lagrangian material acceleration estimates are employed for pressure estimation, velocity acquisition at $Mf_{acq,opt}$ is recommended, where $f_{acq,opt}$ is predicted from equation 3.16. If the data is under-sampled relative to the predicted optimum ($f_{acq} < f_{acq,opt}$), a significant increase in error levels can be observed for the Lagrangian estimates. If such a sub-optimal condition is dictated by limitations of the experiment, one may employ pressure estimation techniques which attempt to operate on temporally sparse data, such as VIC codes (Schneiders and Scarano 2016) or Taylor Hypothesis substitutions (de Kat and Ganapathisubramani 2013, Laskari *et al.* 2016). In contrast to the temporal resolution results (figure 3.9a), the shape of the optimization curves for the spatial resolution (figure 3.9b) does not change significantly when different Lagrangian evaluations are employed, with the optimum shifting to coarser spatial resolutions as the kernel size for material acceleration estimation is increased.

3.3.3 Effect of three-dimensional flow structures

Besides the truncation and random error propagation varying with $\mathrm{Re_D}$ due to associated changes in the spatial and temporal scales of the flow, the onset of three-dimensional flow structures in transitional and turbulent wake regimes (Bloor 1964, Williamson 1989) will lead to addition errors (ϵ_{3D}) due to two-dimensional flow assumptions used for pressure estimation. For two-component, planar PIV, estimation of the pressure gradient from the two-dimensiona Navier-Stokes equations neglects out-of-plane velocities and gradients, and assumes $\nabla_{xy} \cdot \mathbf{u} = 0$. However, the onset of secondary instabilities in transitional flow regimes (Williamson 1989) (figure 3.2b) and turbulent regimes (Bloor 1964) (figure 3.2c) is associated with three-dimensional vortex development, bound to result in errors in planar pressure estimations.

To evaluate the error in the pressure field caused by the presence of three-dimensional structures and decouple it from ϵ_{trunc}, a comparison is carried out between pressure estimations obtained from 2D planar and 3D volumetric velocity data using the Poisson equation method for pressure estimation. The 3D volumetric velocity data are sampled from DNS at three equispaced $x - y$ planes with the spatial resolution in the spanwise direction (z) matching that in the $x - y$ plane. The difference between the integration from the planar data and the integration from the volumetric data serves as a measure of the three-dimensional error ($\epsilon_{3D} = ||p_{3D} - p_{2D}||$). For studies employing planar measurements, it is also of interest to estimate the uncertainty in the pressure estimates caused by neglecting terms containing out of plane velocity and gradients. The x and y momentum equations from which the pressure gradient field is estimated are shown in equations 3.1 and 3.2, including the three-dimensional terms. The additional terms are $w\frac{\partial u}{\partial z}$ and $w\frac{\partial v}{\partial z}$ for the x and y pressure gradients, respectively. When two-component, planar velocity measurements are performed, both the out of plane velocity and gradients in these terms are unknowns. However, in a developed turbulent wake, the spanwise gradients of each velocity component are similar in magnitude ($\frac{\partial w}{\partial z} \approx \frac{\partial v}{\partial z} \approx \frac{\partial u}{\partial z}$), since spanwise gradients in the flow are induced by randomly oriented vortex structures. This implies that the three-dimensional terms can be approximately related to the magnitude of $\frac{\partial w}{\partial z}$, which can be estimated by applying the continuity equation to the planar measurements in incompressible flow as $\frac{\partial w}{\partial z} = \frac{\partial u}{\partial x} + \frac{\partial v}{\partial y}$. Since the out of plane velocity w is expected to act as a pseudo-random variable in a spanwise homogeneous flow, a correlation between the magnitude of $w\frac{\partial u}{\partial z}$ or $w\frac{\partial v}{\partial z}$ (i.e., the neglected three-dimensional terms in equations 3.1 and 3.2) and the planar divergence should be possible. With the use of stereoscopic PIV measurements, the w component could be explicitly resolved in combination with the planar divergence to increase the accuracy of the analysis.

Figures 3.10a-c plot the instantaneous three-dimensional pressure field error ($\epsilon_{3D} = ||p_{3D} - p_{2D}||$) based on a comparison between planar and volumetric pressure estimations for $\mathrm{Re_D} = 100$, 300, and 1575, respectively, and figures 3.10d-f plot the corresponding planar divergence of the velocity field. The figures show that the three-dimensional pressure estimation errors develop locally with some minor propagation to neighbouring regions, and the regions of elevated pressure errors correlate with regions of higher planar divergence. Figure 3.11 presents the two-dimensional correlation maps of the standard deviation of the planar divergence field and the standard deviation of the three-dimensional error field for $\mathrm{Re_D} = 300$, and $\mathrm{Re_D} = 1575$. In both cases, the maximal peak is at zero spatial shift, indicating that the regions of three-dimensional error and planar divergence are well correlated. The correlation maps experience rapid drop off from zero spatial shift, indicating that quantities are strongly correlated in space. The exception is negative streamwise shifts, that exhibit slow drop off due to the error and divergence concentrating in the wake region which extends in the streamwise direction.

Figure 3.12 presents the variation in the standard deviation of the planar divergence in the wake with the three-dimensional error caused by the planar assumptions. An empirical fit is provided, and can be used to estimate local uncertainty of the pressure estimations caused by utilizing planar data in a three-dimensional flow, by calculating the local planar divergence of the velocity data. The form of the fit is based on a trigonometric relation between the out of plane gradient ($\partial w/\partial z = \nabla_{xy} \cdot \mathbf{u}$) and characteristic values for the in plane gradients (U_∞/D). Figure 3.12a shows a significant increase in characteristic planar diver-

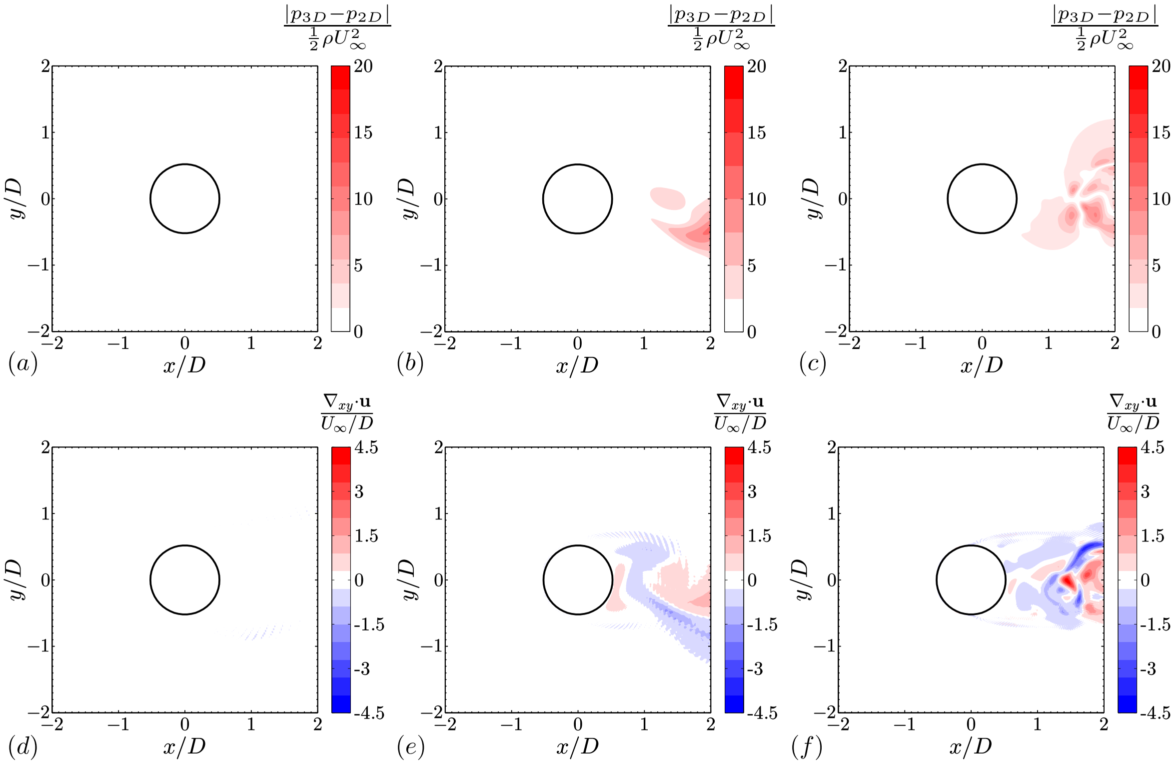

Figure 3.10: Instantaneous pressure field error for (a) $\mathrm{Re_D} = 100$, (b) $\mathrm{Re_D} = 300$, and (c) $\mathrm{Re_D} = 1575$. Instantaneous planar divergence for (d) $\mathrm{Re_D} = 100$, (e) $\mathrm{Re_D} = 300$, and (f) $\mathrm{Re_D} = 1575$. Velocity data sampled at $D/WS = 100$ and $f_{acq}/f_s = 63 - 73$ and pressure field estimated using the Poisson equation method.

gence magnitudes from $\mathrm{Re_D} = 300$ to $\mathrm{Re_D} = 1575$, which directly results in a significant increase in the three-dimensional error in the wake. The increased three-dimensionality for $\mathrm{Re_D} = 1575$ (figures 3.2c and 3.10c,f) is associated with stronger secondary vortex formation at finer scales compared to $\mathrm{Re_D} = 300$. Localized pressure errors can exceed 20% of the dynamic pressure when using planar evaluation techniques (figure 3.10c). In contrast, local errors in pressure estimates from volumetric velocity data are within 1.2% of the DNS solution (not shown for brevity). For $\mathrm{Re_D} = 300$, in a transitional regime, the induced three-dimensional flow of the mode B instability vortices is substantially weaker than that found for fully turbulent Reynolds numbers, and the three-dimensional errors are less pronounced ($< 15\%$). These results can be compared to those of Charonko *et al.* (2010), who found that three-dimensional errors using planar techniques did not grow to significant levels until the measurement plane was misaligned over 30° from the planar velocity field (i.e., when the out-of-plane velocity gradients reaches 50% of the $x - y$ local values). Similarly in the present results, pressure errors become significant ($> 5\%$) when the normalized divergence is greater than 0.5 (i.e., 50% of typical planar gradient values associated with the global vortex shedding).

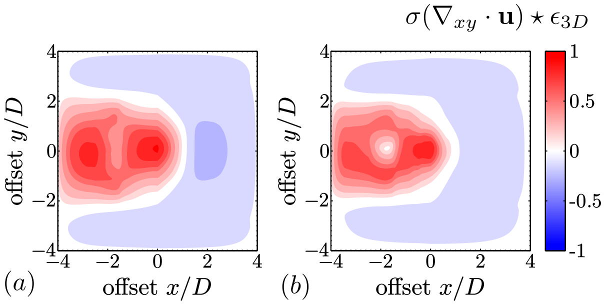

Figure 3.11: Correlation maps of the standard deviation of the planar divergences with the three-dimensional pressure error for (a) $\mathrm{Re_D} = 300$, and (b) $\mathrm{Re_D} = 1575$.

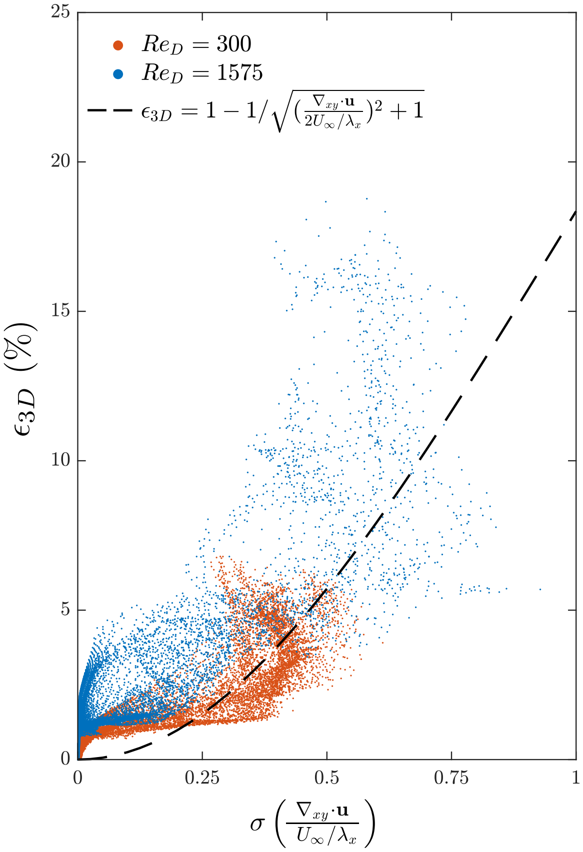

Figure 3.12: RMS of the three-dimensional error related to the standard deviation of the planar divergence of the velocity field.

In order to compare the relative magnitude of the three-dimensional errors to other errors affecting pressure estimation, figure 3.13 plots the base truncation error, three-dimensional error, and random error variation with Reynolds numbers spanning laminar ($\mathrm{Re_D} = 100$), transitional ($\mathrm{Re_D} = 300$) and turbulent ($\mathrm{Re_D} = 1575$) regimes. The errors were decomposed based on evaluations of the pressure field using the omni-directional method at a fixed spatial and temporal resolution. Successive pressure fields were estimated for each $\mathrm{Re_D}$ using two-dimensional and three-dimensional calculations of the pressure gradient with and without velocity noise applied ($\epsilon_u = 0\%$ or 2%). For $\mathrm{Re_D} = 100$, the near wake development is essentially two-dimensional and the pressure error is due primarily to ϵ_u and ϵ_{trunc}, i.e., due to random error propagation and truncation error from the finite sampling resolution. For $\mathrm{Re_D} = 300$, ϵ_{3D} becomes comparable to the other two errors due to the onset of mode B instabilities. For $\mathrm{Re_D} = 1575$, ϵ_{3D} is dominant over the ϵ_{truc} and ϵ_{rand}. The truncation error shows little change for $\mathrm{Re_D} = 300 - 1575$, while the random error decreases for increasing $\mathrm{Re_D}$. The substantial decrease in the random error contribution to the total pressure error for increasing $\mathrm{Re_D}$ is attributed to the growth of ϵ_{3D} with $\mathrm{Re_D}$, which acts in a quasi-random manner in the wake, since the out-of-plane velocities and gradients are produced by passing turbulent structures of varying orientations. The addition of $\epsilon_u = 2\%$ artificial random error onto the three-dimensional errors, which can reach over 20% locally (figure 3.10c), has a marginal additive effect on the total integrated pressure errors in the wake. This decreased sensitivity to random error is also seen in the optimization surfaces for $\mathrm{Re_D} = 1575$ in figure 3.3 with respect to WS and f_{acq}. Hence, for turbulent regimes, the use of planar data for pressure reconstruction is shown to lead to significant errors where three-dimensional vortices develop. To resolve the pressure in a developed turbulent wake region with error levels below 5%, volumetric velocity data is required. However, planar techniques retain reasonable accuracy for estimating the surface pressures, since the magnitude of ϵ_{3D} near the cylinder surface is relatively low when transition occurs in the near wake (figures 3.6 and 3.10). This conclusion is further supported by the experimental results of de Kat and van Oudheusden (2012), who find good agreement in their surface pressure transducer measurements with pressure measurements obtained from planar pressure PIV on the side of a square cylinder, where flow is predominantly two-dimensional. On the other hand, as pointed out by Ghaemi *et al.* (2012), volumetric data is required for accurate pressure reconstruction in a fully developed turbulent boundary layer.

3.4 Conclusion

Direct numerical simulations of flow over a circular cylinder in laminar, transitional and turbulent vortex shedding regimes are utilized in order to evaluate various pressure estimation techniques typically applied to PIV measurements. The simulation data are uniformly sampled in time and space in order to mimic experimental PIV data, and a number of common methods are evaluated based on their ability to accurately estimate the wake and surface pressures when the mimicked PIV data is subjected to artificial, uncorrelated noise levels typical of experimentation (ϵ_u). The results indicate that the Poisson equation, omni-directional, and local least squares methods exhibit characteristically lower error sensitivity compared to the eight-path method. Hence, the Poisson equation, omni-directional, and local least squares methods are recommended for use in instantaneous pressure and force evaluation for immersed cylindrical bodies or similar vortex dominated shear flows.

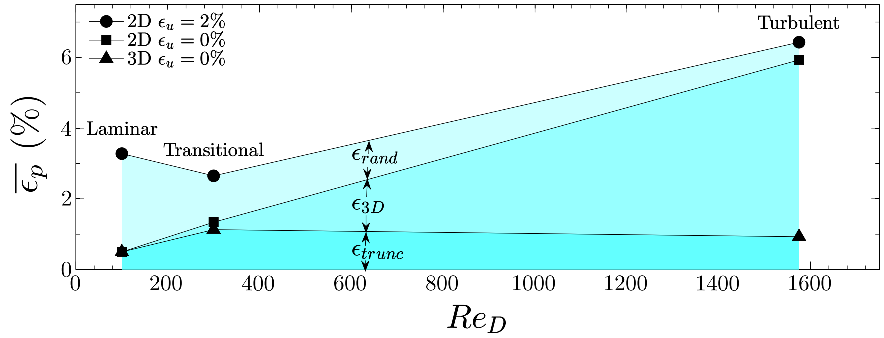

Figure 3.13: Decomposition of the pressure field error into random, truncation, and three-dimensional components. Based on pressure evaluation using the omni-directional integration technique at $D/WS = 20$ and $f_{acq}/f_s = 63-73$. ϵ_{trunc} is the error using 3D NS equations for $\epsilon_u = 0\%$, ϵ_{3D} is the difference between the errors using the 2D NS and 3D NS equations for $\epsilon_u = 0\%$, and ϵ_{rand} is the additional error when using the 2D NS equations for $\epsilon_u = 2\%$

An analytical model for the uncertainty associated with Eulerian pressure estimation from PIV data is developed and is shown to adequately predict the optimal spatial and temporal resolutions to minimize the pressure field uncertainty for a given flow with a given characteristic spatial wavelength (λ_x) and temporal scale (f_{flow}), as well as trends in these optimums with $\mathrm{Re_D}$ and ϵ_u. The model indicates ranges of temporal and spatial resolutions where the random error propagation or the truncation error is amplified significantly. The current study suggests $\lambda_x/WS = 14.3-25$ and $f_{acq}/f_{flow} = 18-30$ for optimal pressure integration, incorporating both the effect of random and truncation error on the resulting fields. For pressure estimations based on material acceleration estimates from Lagrangian trajectory reconstructions over multiple velocity fields, the optimal acquisition frequency increases proportional to the size of the velocity field kernel. The model is validated with a parametric study which computes pressure integrations over a range of spatial and temporal resolutions, velocity error levels, and Reynolds numbers. The resulting minima within the optimization set are extracted and show good agreement with the derived model. The equations for the optimal sampling parameters can be used, in conjunction with estimates of the dominant temporal and spatial scales of the flow, for the selection of experimental sampling parameters to minimize pressure estimation error.

Errors due to three-dimensional vortex structures are evaluated systematically via a comparison of pressure estimations obtained from two-dimensional, planar and three-dimensional, volumetric data. The results show that the increase in flow three-dimensionality moving from transitional ($\mathrm{Re_D} = 300$) to turbulent ($\mathrm{Re_D} = 1575$) shedding regimes leads to substantial local errors ($> 20\%$) in the pressure fields estimated from planar measurements. These errors are reduced substantially (to $\approx 1\%$) when volumetric data is used, and hence volumetric measurements are essential for accurate evaluation of pressures in highly turbulent regions, i.e., in the turbulent wake away from the cylinder surface. On the other hand, when transition occurs in the near wake, surface pressure estimations from planar velocity fields can yield reliable results. Based on the analysis of the planar velocity divergence and three-dimensional error statistics, planar pressure techniques can be expected to produce reliable estimates in regions where the out-of-plane gradients are approximately less than half of in-plane velocity gradients.

Chapter 4

Instantaneous PIV/PTV-based pressure gradient estimation: a framework for error analysis and correction

In the interest of improving the accuracy of PIV-based pressure estimates utilizing a Poisson equation solver, which is the methodology exhibiting the lowest sensitivity to random errors in the results of Chapter 3, the pressure field errors are analyzed through the development of a framework for the exact determination of the pressure gradient estimation error in incompressible flows given erroneous velocimetry data. The framework relies on the calculation of the curl and divergence of the pressure gradient error over the domain, and then the solution of a div-curl system to reconstruct the pressure gradient error field. The results show that the exact form of the pressure gradient error field reconstruction converges onto the exact values, within truncation and round-off errors, except for a small flow field region near the domain boundaries. In practice, a subset of terms required to calculate the source term for the divergence of the pressure gradient error remain unresolved. It is shown that using an approximation for the unresolved terms can retain the fidelity of the reconstruction, even when velocity field errors are generated with substantial spatial variation.

This chapter is based on the journal article: McClure, J., and Yarusevych, S. (2019) “Generalized PIV-based pressure gradient error correction for Lagrangian pseudo-tracking,” *Measurement Science and Technology*, 30(8), 084005.

4.1 Introduction

The estimation of fluid pressure from Particle Image or Tracking Velocimetry (PIV/PTV) measurements serves to broaden significantly flow diagnostic capability for fluid mechanics research. It holds a number of advantages compared to traditional methods for experimental pressure measurement, allowing simultaneous measurement of the time-resolved evolution of the pressure field in up to three spatial dimensions, in essentially non-intrusive fashion (e.g., van Oudheusden 2013), and in potentially sensitive flow regions away from wall boundaries. Moreover, the added benefit from the availability of both the velocity and pressure fields is the ability to estimate time-resolved structural loads on immersed structures (e.g., van Oudheusden *et al.* 2007, Tronchin *et al.* 2015, Rival and Oudheusden 2017), which is of particular importance in flows where direct force measurements are difficult or impossible. Unfortunately, instantaneous pressure estimations are known to suffer from considerable errors due to the propagation of uncertainties from the velocity measurements. For example, correlation coefficients of $C_{pp} \approx 0.7$ between embedded surface microphones and PIV/PTV-based pressure estimates have been reported based on high quality experimental data in fully developed turbulent flows (e.g., Ghaemi *et al.* 2012, de Kat and van Oudheusden 2012, Azijli *et al.* 2016, Schneiders *et al.* 2016a), implying instantaneous errors of approximately 30%, whereas traditional transducers can provide measurement errors on the order of 1% (Tavoularis 2005). Hence, there is a need for more robust time-resolved PIV/PTV-based pressure estimation methodologies, as well as uncertainty characterization.

In general, errors in instantaneous pressure estimation are dependent on a number of parameters (Charonko *et al.* 2010, de Kat and van Oudheusden 2012, Azijli *et al.* 2016, Pan *et al.* 2016, McClure and Yarusevych 2017b). To characterize the sensitivity of pressure estimations to velocity field error, synthetic PIV/PTV data generated from analytical solutions (Charonko *et al.* 2010, de Kat and van Oudheusden 2012) or numerical solutions (Blinde *et al.* 2016, McClure and Yarusevych 2017b) for a wide range of parameters have been analyzed, and theoretical investigations of the error propagation have been performed (Pan *et al.* 2016). The results inform on the dependency of the pressure estimation error magnitude on the spatial and temporal sampling resolution (Charonko *et al.* 2010, de Kat and van Oudheusden 2012, McClure and Yarusevych 2017b), domain size, aspect-ratio, boundary condition type (Pan *et al.* 2016), and the specific flow geometry and physics (Charonko *et al.* 2010), with nearly irrotational and rotational flow regions exhibiting different sensitivities to boundary condition errors (Pan *et al.* 2016, Schneiders *et al.* 2016a). For high quality data with adequate spatial and temporal resolution, minimal bias error in the Poisson solution accumulates (de Kat and van Oudheusden 2012) and time-averaged PIV/PTV-based pressure estimations typically compare favourably with reference values (van Oudheusden *et al.* 2007, McClure and Yarusevych 2016b, Schneiders *et al.* 2016b). However, the instantaneous pressure estimates still contain significant random error, which must result either from random velocity error propagation to the Poisson source term or errors associated with boundary conditions. Compared to the established progress made in recent years towards uncertainty quantification in velocimetry measurements (e.g., Charonko and Vlachos 2013, Sciacchitano 2014, Sciacchitano and Wieneke 2016, Timmins *et al.* 2012), a framework for the uncertainty quantification of PIV/PTV-based pressure estimations from velocimetry data is still in early development. A framework for the linear propagation of velocity uncertainty through material acceleration estimates was developed in (de Kat and van Oudheusden 2012) and formed the basis for extended uncertainty analysis (de Kat and Ganapathisubramani 2013, Laskari *et al.* 2016, McClure and Yarusevych 2017b). Recently, Pan *et al.* (2016) formulated upper bounds on the pressure estimation errors on simply-connected, rectangular domains, with specified Dirichlet boundary, Neumann boundary, and Poisson source term errors. The results provide valuable insight into error propagation through the Poisson equation for pressure. However, the source and boundary errors are assumed values, and are assumed uniform on the boundaries and inside the domain. Azijli *et al.* (2016) formulated a framework for estimating the probability density function of the pressure uncertainty. While the method was deemed more accurate than linear propagation estimates, it retains some limitations which include the reliance on estimates of the velocity field covariance, the assumption of a Gaussian velocity error distribution, and an inability to predict errors on a single instantaneous pressure field.

The propagation of uncertainty from the velocimetry measurement, and that associated with the application of Dirichlet-type boundary conditions (e.g., based on Bernoulli equation) for absolute pressure estimates have been identified as the main sources of errors (Charonko *et al.* 2010, de Kat and van Oudheusden 2012, Azijli *et al.* 2016, McClure and Yarusevych 2016a, McClure and Yarusevych 2016b, Pan *et al.* 2016). In order to characterize the sensitivity of pressure estimations to velocity field error, synthetic PIV/PTV data generated from analytical solutions (Charonko *et al.* 2010, de Kat and van Oudheusden 2012) and numerical solutions (Blinde *et al.* 2016, McClure and Yarusevych 2017b) have been analyzed for a variety of flows. The results inform on differences in pressure estimates sensitivity to velocity field noise in the investigated flows, which are attributed to differences in sampling parameters (de Kat and van Oudheusden 2012, McClure and Yarusevych 2017b), domain size, aspect-ratio, and boundary condition type (Pan *et al.* 2016). For a given velocity error level, the accuracy of pressure estimation also depends on specific flow geometry and physics (Charonko *et al.* 2010), with nearly irrotational and rotational flow regions exhibiting different sensitivities to boundary condition errors (Pan *et al.* 2016, Schneiders *et al.* 2016a). However, compared to the significant progress made in recent years towards uncertainty quantification in velocimetry measurements (e.g., Charonko and Vlachos 2013, Sciacchitano 2014, Sciacchitano and Wieneke 2016, Timmins *et al.* 2012), a framework for uncertainty quantification in PIV/PTV-based pressure estimations from experimental velocity data is yet to be developed fully. Pan *et al.* 2016 formulated upper bounds on the pressure estimation errors on simply-connected, rectangular domains, with specified Dirichlet boundary, Neumann boundary, and Poisson source term errors. The results provide valuable insight into error propagation through the Poisson equation for pressure. However, the source and boundary errors are assumed values, and are assumed uniform on the boundaries and inside the domain. Azijli *et al.* 2016 formulated a framework for the evaluation of the covariance of the pressure uncertainty. While the method certainly has practical utility, its limitations include the reliance on estimates of the velocity field covariance, the assumption of a Gaussian velocity error distribution, and an inability to predict errors on a single instantaneous pressure field.

Due to the effect of velocity error propagation on instantaneous pressure estimates, a number of different techniques have been developed to condition the estimated velocities ($\mathbf{u_m}$) and/or pressure gradient field ($\boldsymbol{\nabla} p_m$) before the pressure is estimated. The first studies on PIV-based pressure estimates utilized Eulerian central differences to estimate velocity derivatives in the Navier-Stokes (NS) equations based on measured velocity data. The computed pressure gradient field was then integrated over the domain (Baur and Köngeter 1999, Gurka *et al.* 1999). Later on, Lagrangian estimates for the material acceleration, based on pseudo-tracking approaches for PIV (e.g., Liu and Katz 2006, Violato *et al.* 2011, de Kat and van Oudheusden 2012, Pröbsting *et al.* 2013, Lynch and Scarano 2014) or directly from PTV (e.g., Neeteson and Rival 2015, Blinde *et al.* 2016), were employed to estimate $\boldsymbol{\nabla} p$ and exhibited lower sensitivity to random errors in velocity measurements compared to the Eulerian formulation. The Lagrangian estimates could also leverage over-sampled data in time to reconstruct least square trajectories over kernels of multiple time separations in order to increase accuracy (e.g, Lynch and Scarano 2014, Pröbsting *et al.* 2013). For both methods, measured velocity field conditioning has been considered to reduce error propagation into pressure gradient estimates. The techniques considered in different studies included low-pass (Charonko *et al.* 2010, Dabiri *et al.* 2014), Proper Orthogonal Decomposition (POD) (Charonko *et al.* 2010), and solenoidal filtering (Azijli and Dwight 2015) of the velocity field, with the latter two approaches typically showing better results. Furthermore, once the pressure gradient field is estimated, the irrotationality condition on the pressure gradient field has been used to correct for directional propagation of error in line-integration based pressure estimation techniques (Wang *et al.* 2016), or the Navier-Stokes equations have been used in conjunction with the solenoidal constraint on the velocity field in a configurable weighted correction scheme for preconditioning the velocity field (Gesemann *et al.* 2016)

The present study serves two purposes. The first is to develop a method for reducing pressure gradient estimation errors in order to increase the fidelity of PIV/PTV-based pressure gradient and pressure estimations. The second is to develop a method for quantifying errors in instantaneous pressure estimations from measured PIV/PTV data which is simple, robust, and requires minimal approximations. Both objectives require the reconstruction of the instantaneous pressure gradient error field ($\boldsymbol{\epsilon}_{\boldsymbol{\nabla} p}$) over the domain, and the framework from which it may be reconstructed exactly based on measured velocity data is presented. The proposed formulation relies exclusively on error propagation through the governing equations of fluid motion. The terms that can be evaluated based on measured velocity field data are identified and the significance of the remaining terms is comprehensively evaluated. The analysis is applied to synthetic velocity data generated from analytical and direct numerical simulation flow test cases, and the exact pressure field information is used to assess the accuracy of pressure gradient/pressure error estimation and performance of the proposed error correction approach.

4.2 Methodology

4.2.1 Pressure from Velocimetry

The Poisson formulation (equation 4.1) is employed to estimate pressure from a measured velocity field (e.g., Gurka *et al.* 1999).

$$\begin{cases} \boldsymbol{\nabla}^2 p_m = \boldsymbol{\nabla} \cdot \boldsymbol{\nabla} p_m, & \text{in } \Omega \\ \boldsymbol{\nabla} p_m \cdot \mathbf{n} = f, & \text{on } \Gamma_i \\ p_m = g, & \text{on } \Gamma_j \end{cases} \tag{4.1}$$

where $\boldsymbol{\nabla} p_m$ is the estimated pressure gradient in the domain (Ω), with Neumann ($f = \boldsymbol{\nabla} p_m$) and/or Dirichlet-type ($g = p_{bernoulli}$) boundary conditions prescribed at domain boundaries Γ_i and Γ_j, respectively, based on PIV/PTV velocity data.

Pressure specified on the boundaries, Γ_j, can be estimated from the steady Bernoulli equation, or from an extended formulation (de Kat and van Oudheusden 2012) valid for unsteady, irrotational flow with small mean velocity gradients. The pressure gradient ($\boldsymbol{\nabla} p_m$) in equation 4.1 is obtained from the Navier-Stokes equations (equation 4.2) using the measured velocity field ($\mathbf{u_m}$). The material derivative in equation 2 is estimated using either an Eulerian (equation 4.3) or Lagrangian (equation 4.4) formulation. The Eulerian evaluation involves the discretization of the terms in equation 4.3 by central differences. The Lagrangian evaluation is a least squares trajectory reconstruction, where $\Delta\mathbf{t} = [-M\Delta t, -(M-1)\Delta t, ..., M\Delta t]$ is a vector of time differentials and $\Delta\mathbf{u}$ contains corresponding velocity differentials based on regressive first order trajectory estimations from t_0 to $t_0 + \Delta\mathbf{t}$, i.e., $\Delta\mathbf{u}(\Delta\mathbf{t}) = \mathbf{u}(\mathbf{x}(\mathbf{t}), \mathbf{t}) - \mathbf{u}(\mathbf{x}(t_0), t_0)$, where t_0 and $\mathbf{x}(t_0)$ are the time and the particle positions at the central time and $\mathbf{x}(\mathbf{t})$ are the positions at time $t_o + \Delta\mathbf{t}$ (e.g, Pröbsting *et al.* 2013). Bi-cubic interpolation is employed for the calculation of velocities at $\mathbf{x}(\mathbf{t})$, and trajectories leaving the domain are not included in the least squares estimate. The evaluation of the viscous term in equation 4.2 relies on central differences; however, the relative magnitude of this term is often small, and the term can be neglected if the Reynolds number is sufficiently high (e.g., Ghaemi *et al.* 2012).

$$\boldsymbol{\nabla} p_m = -\rho \frac{D\mathbf{u_m}}{Dt} + \mu \boldsymbol{\nabla}^2 \mathbf{u_m} \tag{4.2}$$

$$\frac{D\mathbf{u_m}}{Dt} = \frac{\partial \mathbf{u_m}}{\partial t} + (\mathbf{u_m} \cdot \boldsymbol{\nabla})\mathbf{u_m} \tag{4.3}$$

$$\frac{D\mathbf{u_m}}{Dt} = (\Delta\mathbf{t}^T \Delta\mathbf{t})^{-1} \Delta\mathbf{t}^T \Delta\mathbf{u_m} \tag{4.4}$$

4.2.2 Pressure Gradient Error

The measured velocity field ($\mathbf{u_m}$) and estimated pressure gradient field ($\boldsymbol{\nabla} p_m$) can be decomposed into exact fields ($\mathbf{u_{ex}}$ and $\boldsymbol{\nabla} p_{ex}$) and error fields ($\boldsymbol{\epsilon}_u$ and $\boldsymbol{\epsilon}_{\boldsymbol{\nabla} p}$) as follows:

$$\mathbf{u_m} = \mathbf{u_{ex}} + \boldsymbol{\epsilon}_u \tag{4.5}$$

$$\boldsymbol{\nabla} p_m = \boldsymbol{\nabla} p_{ex} + \boldsymbol{\epsilon}_{\boldsymbol{\nabla} p} \tag{4.6}$$

The characteristics of the pressure gradient error field $\boldsymbol{\epsilon}_{\boldsymbol{\nabla} p}$ are of interest for both uncertainty estimation and pressure gradient correction. If $\boldsymbol{\epsilon}_{\boldsymbol{\nabla} p}$ is known, precise pressure estimations can be obtained by solving equation 4.1 with the corrected gradient field. The following analysis will show how $\boldsymbol{\epsilon}_{\boldsymbol{\nabla} p}$ can be determined precisely from erroneous velocity data in an incompressible flow given the divergence of the measured velocity fields, $\boldsymbol{\nabla} \cdot \mathbf{u_m}$, and the curl of the estimated pressure gradient fields, $\boldsymbol{\nabla} \times \boldsymbol{\nabla} p_m$.

First, the divergence of the velocity field error ($\boldsymbol{\epsilon}_u$) and the curl of the pressure gradient field error are calculated by taking the divergence of equation 4.5 and curl of equation 4.6. This leads to equations 4.7 and 4.8, where incompressibility of the exact velocity field and irrotationality of the exact pressure gradient field are invoked.

$$\boldsymbol{\nabla} \cdot \boldsymbol{\epsilon}_u = \boldsymbol{\nabla} \cdot \mathbf{u_m} \tag{4.7}$$

$$\boldsymbol{\nabla} \times \boldsymbol{\epsilon}_{\boldsymbol{\nabla} p} = \boldsymbol{\nabla} \times \boldsymbol{\nabla} p_m \tag{4.8}$$

The curl of the estimated pressure gradient field has been used by several authors (Lynch and Scarano 2014, McClure and Yarusevych 2016a, Wang *et al.* 2016, Wang *et al.* 2018, Lin and Xu 2023) in order to compare the accuracy of pressure gradient and material acceleration estimates from PIV data, while the divergence of the measured velocity has been employed previously to estimate relative errors in tomographic PIV measurements (e.g., Scarano and Poelma 2009, Atkinson *et al.* 2011). However, analysis of either quantity in equation 4.7 or 4.8 can only serve to evaluate relative errors for similar flow cases, and is insufficient as a universal technique for error estimation, since the velocity error field and pressure gradient error field will generally have significant divergence-free and irrotational components, respectively. In addition, analysis of local statistics of derivative quantities of the error neglects the spatial distribution and correlation of the error, which is important in determining pressure estimation error (Azijli *et al.* 2016).

A more complete description of the pressure gradient error field can be obtained if the divergence of the pressure gradient error ($\boldsymbol{\nabla} \cdot \boldsymbol{\epsilon}_{\boldsymbol{\nabla} p}$) is specified. Combining this information with equation 4.8 forms a deterministic system that can be solved for $\boldsymbol{\epsilon}_{\boldsymbol{\nabla} p}$, as will be shown in section 4.2.3. The divergence of the pressure gradient error can be determined by taking the divergence of the NS equations as follows:

$$\boldsymbol{\nabla}\cdot(\boldsymbol{\nabla}p_{ex}+\boldsymbol{\epsilon}_{\boldsymbol{\nabla}p})=-\rho\boldsymbol{\nabla}\cdot\left(\frac{\partial(\mathbf{u_{ex}}+\boldsymbol{\epsilon}_u)}{\partial t}\right)\\ -\rho\boldsymbol{\nabla}\cdot((\mathbf{u_{ex}}+\boldsymbol{\epsilon}_u)\cdot\boldsymbol{\nabla})(\mathbf{u_{ex}}+\boldsymbol{\epsilon}_u)+\mu\boldsymbol{\nabla}\cdot(\boldsymbol{\nabla}^2(\mathbf{u_{ex}}+\boldsymbol{\epsilon}_u)) \tag{4.9}$$

After expanding the convective term and subtracting $\boldsymbol{\nabla}\cdot\boldsymbol{\nabla}p_{ex}$ from both sides, we obtain:

$$\boldsymbol{\nabla}\cdot(\boldsymbol{\epsilon}_{\boldsymbol{\nabla}p})=-\rho\frac{\partial(\boldsymbol{\nabla}\cdot\boldsymbol{\epsilon}_u)}{\partial t}-\rho\boldsymbol{\nabla}\cdot(\mathbf{u}_m\cdot\boldsymbol{\nabla})\boldsymbol{\epsilon}_u-\rho\boldsymbol{\nabla}(\boldsymbol{\epsilon}_u\cdot\boldsymbol{\nabla})\mathbf{u_{ex}}+\mu\boldsymbol{\nabla}^2(\boldsymbol{\nabla}\cdot\boldsymbol{\epsilon}_u) \tag{4.10}$$

Then, expanding the second and third terms on the right-hand side gives:

$$\boldsymbol{\nabla}\cdot(\boldsymbol{\epsilon}_{\boldsymbol{\nabla}p})=-\rho\frac{\partial(\boldsymbol{\nabla}\cdot\boldsymbol{\epsilon}_u)}{\partial t}-\rho(\mathbf{u}_m\cdot\boldsymbol{\nabla})(\boldsymbol{\nabla}\cdot\boldsymbol{\epsilon}_u)\\ -\rho\boldsymbol{\nabla}\boldsymbol{\epsilon}_u:\boldsymbol{\nabla}^T\mathbf{u}_m-\rho(\boldsymbol{\epsilon}_u\cdot\boldsymbol{\nabla})(\boldsymbol{\nabla}\cdot\mathbf{u_{ex}})-\rho\boldsymbol{\nabla}\boldsymbol{\epsilon}_u:\boldsymbol{\nabla}^T\mathbf{u_{ex}}+\mu\boldsymbol{\nabla}^2(\boldsymbol{\nabla}\cdot\boldsymbol{\epsilon}_u) \tag{4.11}$$

Where the double dot product (:) results in a scalar defined as $\boldsymbol{A}:\boldsymbol{B}=A_{ij}B_{ij}$. Finally, rearranging terms and applying the divergence free condition on the exact velocity field yields:

$$\boldsymbol{\nabla}\cdot(\boldsymbol{\epsilon}_{\boldsymbol{\nabla}p})=-\rho\frac{\partial(\boldsymbol{\nabla}\cdot\boldsymbol{\epsilon}_u)}{\partial t}-\rho(\mathbf{u_m}\cdot\boldsymbol{\nabla})(\boldsymbol{\nabla}\cdot\boldsymbol{\epsilon}_u)+\mu\boldsymbol{\nabla}^2(\boldsymbol{\nabla}\cdot\boldsymbol{\epsilon}_u)-\rho\boldsymbol{\nabla}\boldsymbol{\epsilon}_u:(\boldsymbol{\nabla}^T\mathbf{u_{ex}}+\boldsymbol{\nabla}^T\mathbf{u_m}) \tag{4.12}$$

In this form, the first three terms on the right hand side of equation 4.12 can be evaluated from the measured velocity field ($\mathbf{u_m}$), with $\boldsymbol{\nabla}\cdot\boldsymbol{\epsilon}_u$ computed from equation 4.7. However, the last term on the right hand side, denoted hereafter as $\Lambda=-\rho\boldsymbol{\nabla}\boldsymbol{\epsilon}_u:(\boldsymbol{\nabla}^T\mathbf{u_{ex}}+\boldsymbol{\nabla}^T\mathbf{u_m})$, cannot be evaluated based on measured velocity data, as it contains the unknown exact velocity ($\mathbf{u_{ex}}$) and velocity field error gradient ($\boldsymbol{\nabla}\boldsymbol{\epsilon}_u$). In order to approximate Λ, it may be possible to use advanced PIV error estimation techniques (Sciacchitano *et al.* 2015), if a relationship between the velocity error gradients and measured velocity gradients can be obtained. However, the focus of the present work will be on assessing the significance of this term and approximating its magnitude using measurable quantities. Specifically, using equation 4.5, the following decomposition of Λ is convenient:

$$\Lambda=-2\rho\boldsymbol{\nabla}\boldsymbol{\epsilon}_u:\boldsymbol{\nabla}^T\mathbf{u_{ex}}-\rho\boldsymbol{\nabla}\boldsymbol{\epsilon}_u:\boldsymbol{\nabla}^T\boldsymbol{\epsilon}_u \tag{4.13}$$

While the first term on the right hand side remains unmeasurable, the second term can be approximated as $\boldsymbol{\nabla}\boldsymbol{\epsilon}_u:\boldsymbol{\nabla}^T\boldsymbol{\epsilon}_u\approx(\boldsymbol{\nabla}\cdot\boldsymbol{\epsilon}_u)^2$ and thus can be estimated based on experimental data (equation 4.7). This approximation is based on the assumption that spatial derivatives of the velocity error field do not have strong directional dependence, e.g., $\frac{\partial\epsilon_u^x}{\partial x}\approx\frac{\partial\epsilon_u^x}{\partial y}$, which is reasonable since PIV/PTV velocity measurement errors are typically dominated by random errors (Raffel 2007, Sciacchitano *et al.* 2015). An exception where the measurement errors may no longer be random is if peak locking is present in the velocimetry processing, however, this can be avoided by following recommended experimental practice (Raffel 2007). A more drastic simplification that can be considered is neglecting the lambda term entirely. Thus, the following two approximations to equation 4.13 will be evaluated:

$$\tilde{\Lambda} \approx -\rho(\boldsymbol{\nabla} \cdot \boldsymbol{\epsilon}_u)^2 \tag{4.14}$$

$$\Lambda_0 \approx 0 \tag{4.15}$$

4.2.3 Reconstruction of the Pressure Gradient Error

The previous section described the calculation of the curl and divergence of the pressure gradient error field, $\boldsymbol{\epsilon}_{\boldsymbol{\nabla}p}$ (equations 4.8 and 4.12, respectively). The problem of solving for $\boldsymbol{\epsilon}_{\boldsymbol{\nabla}p}$ thus forms the following div-curl system:

$$\begin{cases} \boldsymbol{\nabla} \times \boldsymbol{\epsilon}_{\boldsymbol{\nabla}p} = \mathbf{J}, & \text{in } \Omega \\ \boldsymbol{\nabla} \cdot \boldsymbol{\epsilon}_{\boldsymbol{\nabla}p} = f, & \text{in } \Omega \\ |\boldsymbol{\epsilon}_{\boldsymbol{\nabla}p} \times \mathbf{n}| = a, & \text{on } \Gamma_i, \\ \boldsymbol{\epsilon}_{\boldsymbol{\nabla}p} \cdot \mathbf{n} = b, & \text{on } \Gamma_j \end{cases} \tag{4.16}$$

where $\mathbf{J}$ and f are given by equations 4.8 and 4.12, respectively. Similar div-curl problems have been explored in previous applied mathematics studies (e.g., Auchmuty and Alexander 2001, Rodríguez *et al.* 2015), and it has been shown that a unique solution exists for a simply-connected domain (Ω) where tangential or normal boundary conditions (a and b) are specified on the boundaries of Ω, Γ_i and Γ_j, respectively (Auchmuty and Alexander 2001). If the domain is multiply-connected, then additional line integrals must be specified on the boundaries in order to maintain uniqueness (Auchmuty and Alexander 2001). Since the boundary conditions for equation 4.16 are typically unknown for $\boldsymbol{\epsilon}_{\boldsymbol{\nabla}p}$, they are assumed to be $a = b = 0$, and Helmholtz's theorem (Abraham *et al.* 1988) provides a solution method if $\boldsymbol{\epsilon}_{\boldsymbol{\nabla}p}$ is smooth and vanishes at infinity. An extension of the Helmholtz decomposition for piecewise continuous functions is given in Tong *et al.* 2003, who show its validity for discrete data. Note, the impact of the simplifying assumption made for the boundary conditions will be assessed later in the chapter.

A numerical solution of equation 4.16 requires the curl and divergence of the pressure gradient error field. First, the estimated pressure gradient is obtained from the velocity data by employing Eulerian central differences to estimate the derivative quantities in equation 4.3. The curl and divergence of the pressure gradient error field can then be estimated either on a regular Cartesian grid using central differences to evaluate the derivative quantities in equations 4.8 and 4.12 (figure 4.1a), or on a staggered grid configuration (figure 4.1b). In the staggered scheme, the estimated pressure gradient and velocity field must

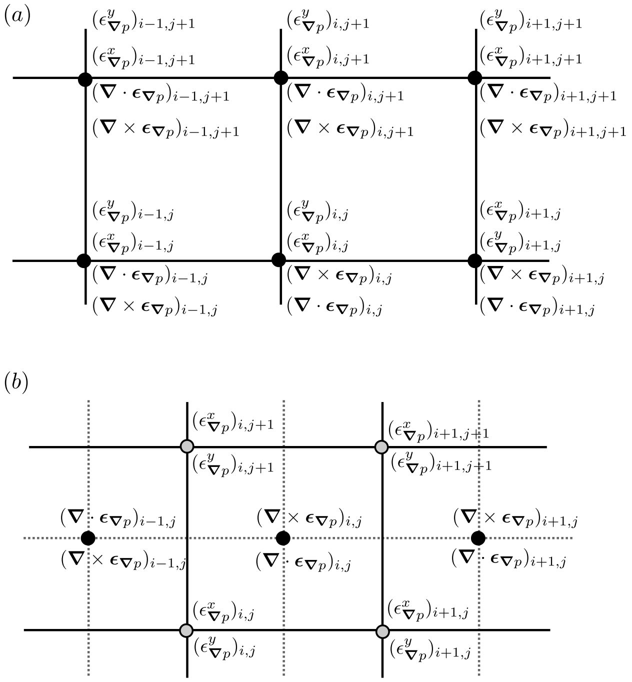

Figure 4.1: (a) Cartesian regular grid and (b) staggered grid for reconstruction of the pressure gradient error field.

be linearly interpolated onto cell centres before staggered differencing schemes are applied to evaluate equations 4.8 and 4.12. The regular and staggered schemes produce nearly identical results in the final pressure reconstruction; however the staggered scheme greatly reduces spurious mode errors (i.e., checker boarding) in the corrected pressure gradient fields.

In general, there are a variety of methods for solving equation 4.16 (Abraham *et al.* 1988, Rodríguez *et al.* 2015, Wang and Wang 2015). For vanishing $\boldsymbol{\epsilon}_{\nabla p}$ at the boundaries, the Helmholtz decomposition of $\boldsymbol{\epsilon}_{\nabla p}$ into curl-free (ϕ) and divergence-free ($\mathbf{A}$) potential fields (Abraham *et al.* 1988, Auchmuty and Alexander 2001) can be employed, as shown in equation 4.17.

$$\boldsymbol{\epsilon}_{\nabla p} = -\nabla\phi + \nabla\times\mathbf{A} \tag{4.17}$$

The potentials ϕ and $\mathbf{A}$ can be determined by using the solenoidal property of $\nabla\times\mathbf{A}$ and irrotationality of $\nabla\phi$ to arrive at separate Poisson-type equations for ϕ and $\mathbf{A}$ (equations 4.18 and 4.19, respectively). The resulting equations can be solved with a 5-point (two-dimensional) or 7-point (three-dimensional) discretization implementation, similar to the Poisson solver used for pressure reconstruction (e.g., Gurka *et al.* 1999).

$$\begin{cases} \nabla^2\phi = -\nabla\cdot\boldsymbol{\epsilon}_{\nabla p}, & \text{in } \Omega \\ \nabla\phi\cdot\mathbf{n} = 0, & \text{on } \Gamma \end{cases} \tag{4.18}$$

$$\begin{cases} \boldsymbol{\nabla}^2 \mathbf{A} = -\boldsymbol{\nabla} \times \boldsymbol{\epsilon}_{\boldsymbol{\nabla} p}, & \text{in } \Omega \\ \boldsymbol{\nabla} \mathbf{A} \cdot \mathbf{n} = \mathbf{0}, & \text{on } \Gamma \end{cases} \tag{4.19}$$

Once $\boldsymbol{\epsilon}_{\boldsymbol{\nabla} p}$ is obtained, corrected pressure gradient fields can be obtained by subtracting $\boldsymbol{\epsilon}_{\boldsymbol{\nabla} p}$ from the pressure gradient field computed based on experimental velocity measurements ($\boldsymbol{\nabla} p_m$). Depending on how the Λ term is determined, i.e., obtained exactly (equation 4.13) or approximated (equations 4.14 and 4.15), the corrected pressure gradient fields are denoted as $\boldsymbol{\nabla} p_\Lambda = \boldsymbol{\nabla} p_m - \boldsymbol{\epsilon}_{\boldsymbol{\nabla} p_\Lambda}$, $\boldsymbol{\nabla} \tilde{p}_{\tilde{\Lambda}} = \boldsymbol{\nabla} p_m - \boldsymbol{\epsilon}_{\boldsymbol{\nabla} \tilde{p}_{\tilde{\Lambda}}}$, and $\boldsymbol{\nabla} \tilde{p}_{\Lambda_0} = \boldsymbol{\nabla} p_m - \boldsymbol{\epsilon}_{\boldsymbol{\nabla} \tilde{p}_{\Lambda_0}}$. The first type of correction is included as a baseline comparison, as it represents the exact correction of the pressure gradient field and requires the exact determination of the Λ term (equation 4.13). On the other hand, the approximate corrections are of particular interest for practical applications. Once the pressure gradient field has been corrected, it can be integrated to obtain the corrected pressure field (p_Λ, $\tilde{p}_{\tilde{\Lambda}}$, or $\tilde{p}_{\Lambda_0}$).

4.2.4 Synthetic PIV Data

To evaluate the effectiveness of the proposed technique, analytical and numerical test cases are employed, where exact pressure fields (p_{ex}) are known. Specifically, the following three flow cases are investigated: the stationary Taylor vortex, the advecting Lamb-Oseen vortex, and the turbulent wake of a circular cylinder for $\mathrm{Re_D} = 1575$. The Taylor vortex (e.g., Panton 2013) and advecting Lamb-Oseen vortex (e.g., Batchelor 2000) are based on two-dimensional analytical solutions for both the velocity and pressure fields, while the cylinder wake data is obtained from the three-dimensional direct numerical simulations presented in McClure and Yarusevych 2017b.

Synthetic velocity data ($\mathbf{u_m}$) are extracted by sampling analytical or numerical velocity field solutions on a regular grid and adding velocity error fields ($\boldsymbol{\epsilon}_u$) to the sampled data. Synthetic data were generated using this methodology in a number of previous studies (Charonko *et al.* 2010, de Kat and van Oudheusden 2012, Azijli *et al.* 2016, Blinde *et al.* 2016, McClure and Yarusevych 2017b), though methods of generating $\boldsymbol{\epsilon}_u$ vary. For the analysis employed herein, the standard deviation (σ_i) of the random error is specified by a two-parameter model, shown in equation 4.20. The first parameter in equation 4.20, α (%), represents an error component proportional to the magnitude of the normalized velocity gradient tensor, reaching a maximum percentage of the peak velocity (αu_{peak}) in the domain. The second parameter, β (px), adds a uniform displacement error for an interrogation window of dimensions $WS \times WS \times WS$ over a time separation of δt for a given scale factor SF (px/mm). For the present study, a 16 × 16 × 16 px interrogation window is assumed, which corresponds to $SF = 16/WS$.

$$\sigma_i = \alpha u_{peak} \frac{|\boldsymbol{\nabla} \mathbf{u_{ex}}|}{\max(|\boldsymbol{\nabla} \mathbf{u_{ex}}|)} + \beta \frac{SF}{\delta t} \tag{4.20}$$

Correlated error is then generated following the method presented by Azijli and Dwight

2015, where the correlation matrix ζ_{ij} is constructed using a triangle function, dropping to zero outside of overlapped regions, modelling the correlation of random errors caused by interrogation window overlap reported in Sciacchitano and Wieneke 2016. The covariance of the velocity error is then $S_{ij} = \sigma_i \zeta_{ij} \sigma_j$, and realizations of correlated random error are generated by computing the Cholesky decomposition, $S_{ij} = L_{ij} L_{ji}$ (Azijli and Dwight 2015) to obtain the velocity error, $(\boldsymbol{\epsilon}_u)_i = L_{ij}\lambda_j$, where λ_j is the vector of samples from a Gaussian distribution with a standard deviation of 1 and a mean of 0. As a result, the synthetically generated errors have zero mean, standard deviations varying in space according to the two-parameter model in equation 4.20, and local correlation depending on the overlap factor.

Results of the synthetic error generation for each flow case investigated herein are illustrated in figure 4.2 for $\alpha = 25\%$ and $\beta = 0.25$ px (equation 4.20). The velocity error levels are exaggerated to approximately double that typically obtained in a carefully controlled experiment to demonstrate the robustness of the error reconstruction methodology. The synthetic fields showcase the local correlation (Sciacchitano and Wieneke 2016) and error concentration in higher gradient regions of the flow (Timmins *et al.* 2012), characteristic of PIV measurement. For each flow case, the time separation is set to $\delta t u_{peak}/WS \approx 0.5$, so that typical particle displacements are over half an interrogation window and the uniform displacement error ($\beta = 0.25$ px), representing typical PIV correlation error in a uniform flow (Raffel 2007) is approximately 3.1% of u_{peak}.

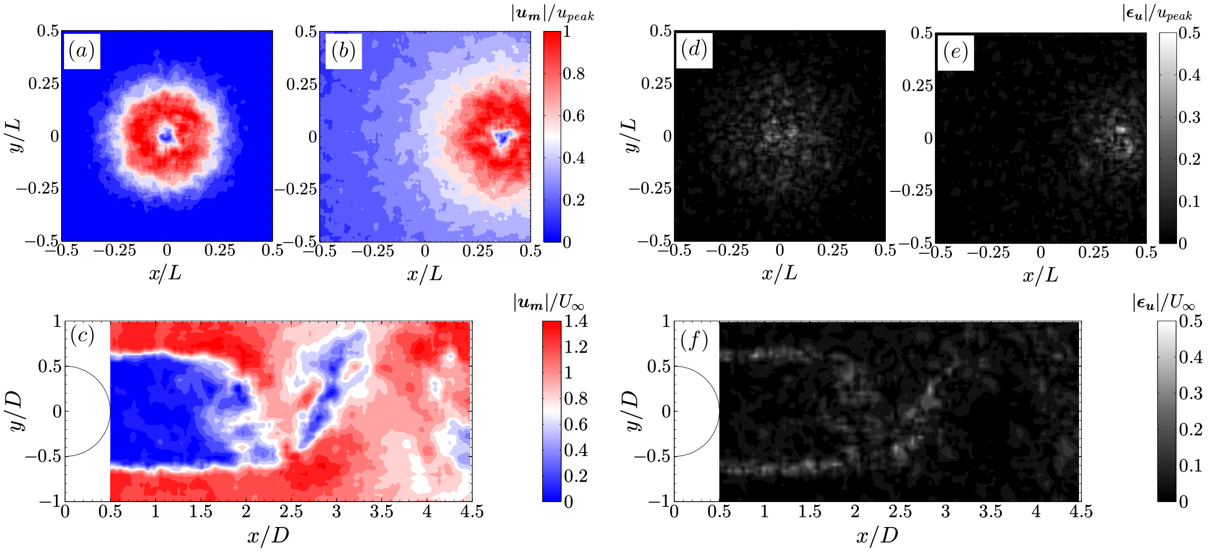

Figure 4.2: Instantaneous synthetic velocimetry data for the three flow cases investigated: (a) stationary Taylor vortex, (b) advecting Lamb-Oseen vortex, and (c) turbulent wake of a cylinder in cross-flow at $\mathrm{Re_D} = 1575$ with (d)-(f) showing their respective added correlated velocity error component generated using equation 4.20 with $\alpha = 25\%$, $\beta = 0.25$ px.

4.3 Results

Pressure gradient error reconstruction is first tested using two analytical test cases. The first one is a stationary Taylor vortex, which is a two-dimensional flow with favourable boundary conditions for evaluating the proposed error reconstruction. The second one is an advecting Lamb-Oseen vortex, which is used to evaluate the effect of boundary errors on the reconstruction. Following that, the reconstruction is tested using synthetic velocity data sampled from the three-dimensional direct numerical simulation of flow over a uniform cylinder at $\mathrm{Re_D} = 1575$. In each case, the pressure estimates were obtained by solution of the Poisson equation (equation 4.1. The Laplacian of the pressure field was discretized using a 5-point scheme (two-dimensional) or a 7-point scheme (three-dimensional), and ghost grid points were used to implement the Neumann boundary conditions to complete the 5- or 7-point scheme employing the estimated pressure gradient at the boundary (e.g., $p_{i+1,j} = p_{i,j} + \Delta x \frac{\partial p}{\partial x}_{i,j}$)

4.3.1 Taylor Vortex

The Taylor vortex (figure 4.2a) is defined in two-dimensions, assuming $p_\infty = 0$, according to Panton 2013 as:

$$u_\theta = \frac{H}{8\pi}\frac{r}{\nu t^2}\exp\left(-\frac{r^2}{4\nu t}\right) \tag{4.21}$$

$$p = \frac{\rho H^2}{64\pi^2 \nu t^3}\exp\left(-\frac{r^2}{2\nu t}\right) \tag{4.22}$$

For the results reported in this section, the following parameters are employed: $H = 7.5 \times 10^{-5}$ m^2, $\nu = 1 \times 10^{-6}$ m^2 s^{-1}, $\rho = 1000$ kg m^{-3}, and $t = 0.5$ s. These parameters were selected to allow sampling at reasonable time separations for a PIV/PTV experiment ($0.1WS/u_{peak} < \delta t < 1WS/u_{peak}$) without a high degree of viscous diffusion occurring over δt. The size of the domain ($L_x = L_y = 8 \times 10^{-3}$ m) is such that pressure and velocity approach zero at the boundaries and Dirichlet boundary conditions based on the steady Bernoulli equation are applied on all boundaries in equation 4.1. This configuration is similar to the approach taken in previous investigations where this flow was employed as a test case (e.g., Azijli and Dwight 2015).

The fidelity of the error reconstruction is first assessed by comparing pressure gradient estimations using exact velocity data (figures 4.3a-b), erroneous velocity data (figures 4.3c-d), and the corrected pressure gradient data (figures 4.3e-g). Figures 4.3a and b present $\partial p/\partial x$ estimated from exact velocity data using the Eulerian method including the viscous term (equation 4.2), and excluding the viscous term (equation 4.3), respectively. The viscous term contributes significantly to the pressure gradient field for this flow; however, since the flow is incompressible, the contribution to the pressure gradient field in the interior of the domain from the viscous term is divergence-free and does effect the pressure field through the Poisson equation source term. The viscous term is highly sensitive to velocity error, and should be neglected when estimating pressure gradients from data containing even minor velocity error (Ghaemi *et al.* 2012, Lynch and Scarano 2014). Hence, for the remainder of the present study, the pressure gradient will be determined based only on the material acceleration (equation 4.3). Figures 4.3c and d present estimates for $\partial p_m/\partial x$ from the erroneous velocity data using Eulerian and Lagrangian ($M = \pm 1$) estimates, respectively, neglecting the viscous term. Significant errors are observed in the pressure gradient estimates for both methods due to the use of a relatively high velocity error magnitude $\boldsymbol{\epsilon}_u \propto \alpha = 25\%$, $\beta = 0.25$ px. Nevertheless, the Lagrangian estimates are smoother in comparison to the Eulerian estimates, agreeing with the results of previous studies (e.g., Violato *et al.* 2011, de Kat and van Oudheusden 2012, Ghaemi *et al.* 2012, Lynch and Scarano 2014). The effect of subtracting the reconstructed error field $\boldsymbol{\epsilon}_{\boldsymbol{\nabla} p}$ from the estimated Eulerian field $\partial p_m/\partial x$ is shown in figures 4.3e-g, corresponding to the three different forms of the Λ-term defined in equation 4.13, $\partial p_\Lambda/\partial x$, $\partial \tilde{p}_{\tilde{\Lambda}}/\partial x$, $\partial \tilde{p}_{\Lambda_0}/\partial x$, respectively. Retaining all terms in Λ (figure 4.3e) or utilizing the approximation $\tilde{\Lambda}$ (figure 4.3f) produce corrected pressure gradient fields that match closely with the exact field (figure 4.3b), even though the viscous term was neglected in the calculation of $\partial p_m/\partial x$ and the reconstruction of $\boldsymbol{\epsilon}_{\boldsymbol{\nabla} p}$. This initial result demonstrates the utility of the pressure

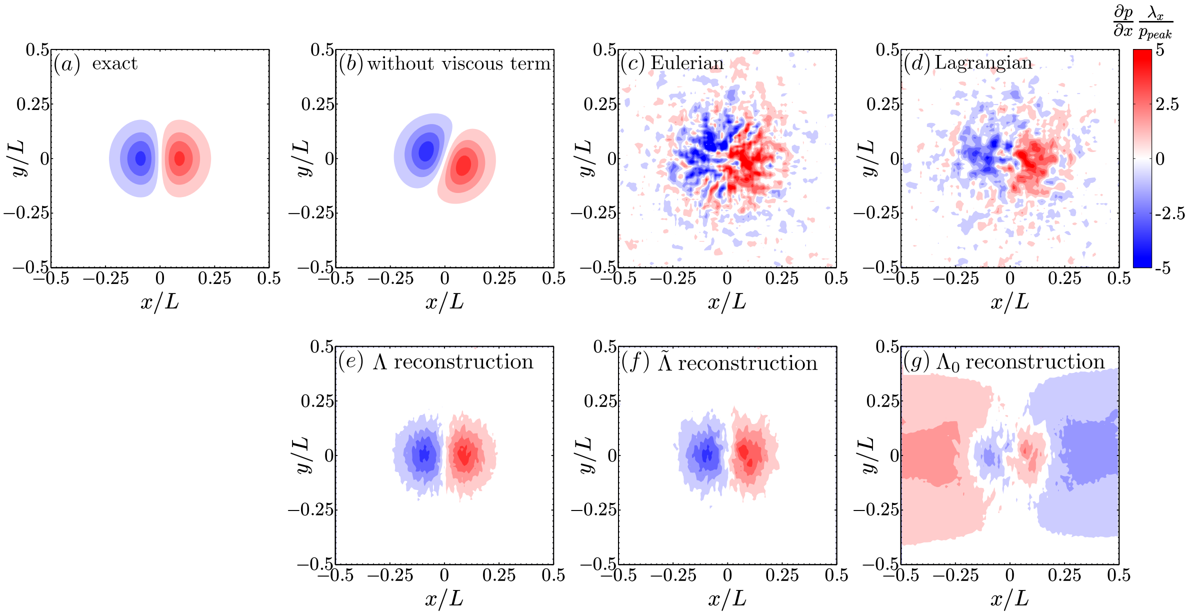

Figure 4.3: Taylor vortex pressure gradient fields sampled at $WS/\lambda_x = 0.08$ with 75% window overlap and $\delta t u_{peak}/WS = 0.50$. (a) Using exact velocity data, (b) using exact velocity data and excluding viscous terms, (c) Eulerian evaluation on erroneous velocity data with $\alpha = 25\%$ and $\beta = 0.25$ px, (d) Lagrangian evaluation on erroneous velocity data, (e) Eulerian evaluation on the same erroneous velocity data with Λ reconstruction, (f) $\tilde{\Lambda}$ reconstruction, and (g) Λ_0 reconstruction.

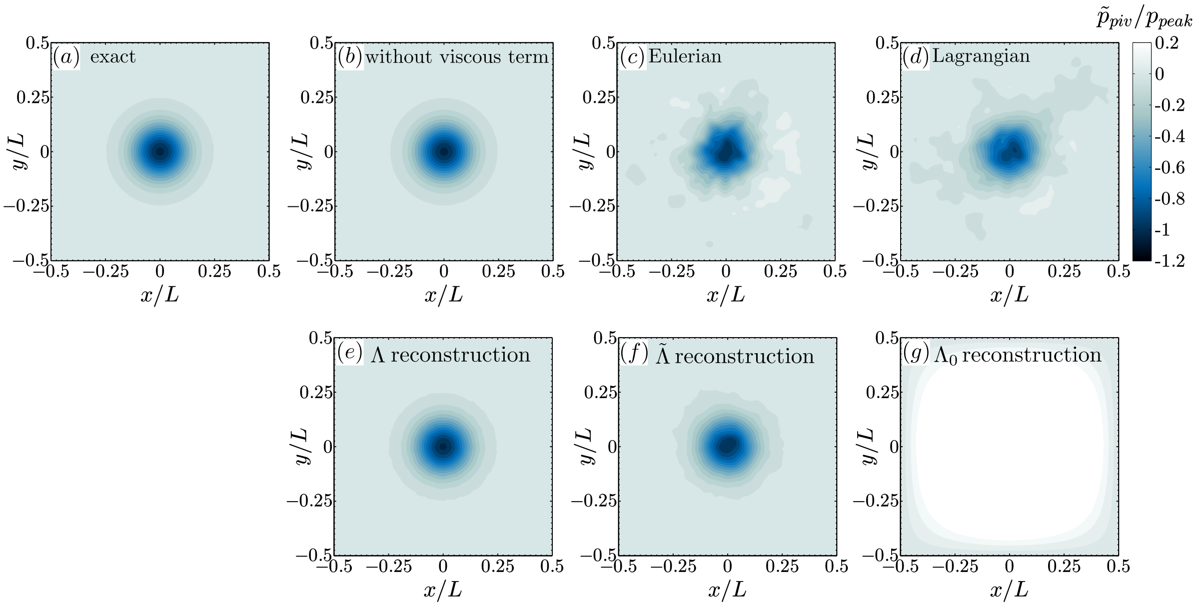

Figure 4.4: Taylor vortex pressure fields computed from solving equation 4.1, sampled at $WS/\lambda_x = 0.08$ with 75% window overlap and $\delta t u_{peak}/WS = 0.50$, (a) using exact data, (b) using exact data and neglecting viscous terms (c) Eulerian evaluation on erroneous velocity data with $\alpha = 25\%$ and $\beta = 0.25$ px, (d) Lagrangian evaluation on erroneous velocity data, (e) Eulerian evaluation on erroneous velocity data with Λ reconstruction, (f) $\tilde{\Lambda}$ reconstruction, and (g) Λ_0 reconstruction.

gradient error reconstruction, with which significantly higher accuracy estimates can be achieved. In contrast, while the corrected field obtained by neglecting the entire Λ term (figure 4.3g) results in a smoother pressure gradient field compared to the Eulerian or Lagrangian estimates and partially resolves the underlying topology, the pressure gradient magnitude differs considerably from the exact field over the majority of the domain.

The pressure gradient estimates presented in figure 4.3 determine the source term in the Poisson problem for pressure (equation 4.1), and figure 4.4 presents the results of pressure estimations from the respective data in figure 4.3. The integration of the exact pressure gradient fields with viscous terms included or neglected results in equivalent pressure fields (figures 4.4a,b), as expected. Figures 4.4c and d show the pressure field determined using Eulerian central differences and Lagrangian trajectory reconstruction, respectively. Both methods resolve the magnitude of the low pressure region adequately, however, the errors seen in the corresponding pressure gradient fields (figures 4.3c and d) have clearly propagated into the pressure estimates. Figure 4.4e plots the corrected pressure field with the error field reconstruction retaining all terms (p_Λ), and the pressure field is reconstructed nearly exactly despite operating on noisy data. Figure 4.4f plots the corrected pressure field with the error field reconstruction which retains terms which are measurable in a typical velocimetry experiment ($p_{\tilde{\Lambda}}$). In this case, the pressure field estimate closely matches the

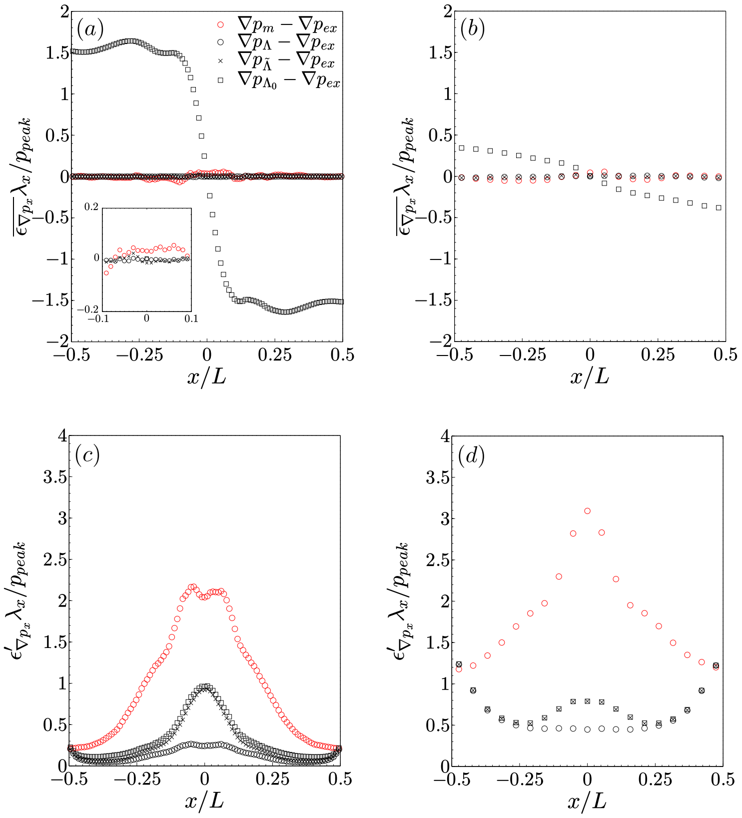

Figure 4.5: Comparing the mean and standard deviation error statistics of uncorrected ($\partial p_m/\partial x$) and corrected ($\partial p_\Lambda/\partial x$, $\partial p_{\tilde{\Lambda}}/\partial x$, $\partial p_{\Lambda_0}/\partial x$) pressure gradient estimations compiled over 3,000 realizations. Refreshed velocity field errors are generated with $\alpha = 25\%$ and $\beta = 0.25$ px and 75% interrogation window overlap for each realization. Evaluated on high spatial resolution data (a,c) with $WS/\lambda_x = 0.08$, $\delta t u_{peak}/WS = 0.50$, and on coarse data (b,d) with $WS/\lambda_x = 0.42$, $\delta t u_{peak}/WS = 0.094$.

exact field as well, showing substantial improvement over estimates from the uncorrected data. On the other hand, the corrected pressure field with the error field reconstruction which neglects Λ entirely (p_{Λ_0}) has pressure growing to high levels in the centre of the domain as a consequence of the pressure gradient offset seen in figure 4.3g.

The corrected fields based on the proposed pressure gradient error reconstruction have been shown to converge close to the exact pressure gradient and pressure fields when either Λ or $\tilde{\Lambda}$ are used in equation 4.12. To statistically characterize the errors of the estimates with respect to the exact fields, a Monte Carlo simulation was performed using 3,000 evaluations of pressure gradient and pressure estimates with refreshed noise profiles. Figure 4.5 plots the bias ($\overline{\boldsymbol{\epsilon}_{\boldsymbol{\nabla} p}}$) and random ($\boldsymbol{\epsilon}'_{\boldsymbol{\nabla} p}$) of the pressure gradient errors along the centre of the domain for data extracted at two different spatial resolutions. The error statistics for the baseline case (shown in red) is compared to that obtained with corrected pressure gradient reconstructions. Figures 4.5a and b demonstrate a notable reduction in the bias

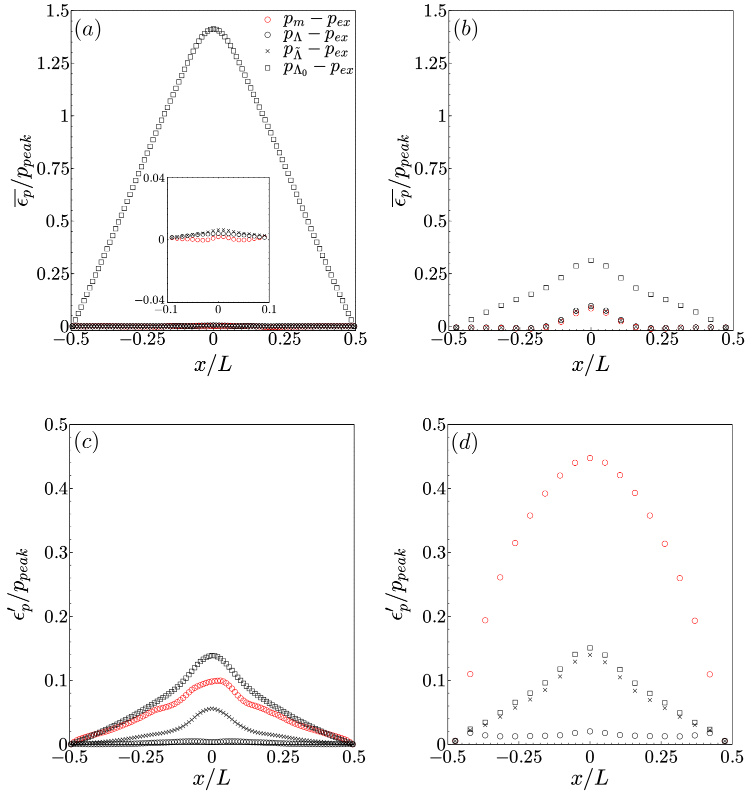

Figure 4.6: Comparing the mean and standard deviation error statistics of uncorrected (p_m) and corrected (p_Λ, $p_{\tilde{\Lambda}}$, p_{Λ_0}) pressure estimations compiled over 3,000 realizations. Refreshed velocity field errors are generated with $\alpha = 25\%$ and $\beta = 0.25$ px and 75% interrogation window overlap for each realization. Evaluated on high spatial resolution data (a,c) with $WS/\lambda_x = 0.08$, $\delta t u_{peak}/WS = 0.50$, and on coarse data (b,d) with $WS/\lambda_x = 0.42$, $\delta t u_{peak}/WS = 0.094$.

errors for the corrected fields $\partial p_\Lambda/\partial x$ and $\partial p_{\tilde{\Lambda}}/\partial x$, while the corrected field $\partial p_{\Lambda_0}/\partial x$ has significantly higher bias errors compared to the uncorrected data, as previously seen in figure 4.3g. As the spatial resolution is decreased (figure 4.5b), the relative reduction of the bias pressure gradient error is increased notably for $\partial p_\Lambda/\partial x$, $\partial p_{\tilde{\Lambda}}/\partial x$ and $\partial p_{\Lambda_0}/\partial x$. The random pressure gradient error, shown in figures 4.5c and d, shows a substantial reduction in the deviation of the local errors when any error reconstruction is used to correct the pressure gradient field. As expected, correcting the field with the error reconstruction retaining the full Λ-term performs best, especially in the high gradient regions near the centre of the domain, while the corrected fields from approximate reconstructions exhibit higher error deviations of similar magnitude. It is of interest to note that the similarity between the standard deviation of the error fields for the $\tilde{\Lambda}$ and the more simplistic Λ_0 correction indicates that the former method may be improved with more advanced modelling.

Figure 4.6 plots the bias ($\overline{\boldsymbol{\epsilon}_p}$) and random ($\boldsymbol{\epsilon}_p'$) components of the pressure error along the same profile intersecting the centre of the Taylor vortex. Inspection of the bias errors in figures 4.6a and b shows that the corrected fields with the Λ and $\tilde{\Lambda}$ error reconstructions exhibit similar bias error as the uncorrected fields, while the Λ_0-based reconstruction leads to substantially higher bias errors. The bias errors seen in the uncorrected results as well as Λ and $\tilde{\Lambda}$ reconstructions are attributed to finite spatial resolution, which has been shown by de Kat and van Oudheusden 2012 to occur in pressure estimates from the Poisson equation. Consequently, these error reconstructions cannot account for truncation error due to under-resolved data. The profiles of random error in figures 4.6c and d show that p_Λ yields a significant decrease in error variations compared to the estimates from uncorrected results, for both fine and coarse spatial resolution data, with the corrected data showing minor deviation from the exact pressure field. Notably, $p_{\tilde{\Lambda}}$ yields a minimum of 50% reduction in random error for each case, while p_{Λ_0} results show a more significant dependence on the spatial resolution. The underlying reason for the changes in performance of the approximate correction methods with spatial resolution can be deduced from inspection of the form of Λ (equation 4.13), whose magnitude depends on a tensor contraction resulting in terms containing spatial derivatives of velocity error such as $(\partial \epsilon_u / \partial x)(\partial u_{ex}/\partial x)$ and $(\partial \epsilon_u/\partial x)^2$. Consequently, the entire magnitude of the Λ term relative to the other terms in equation 4.12 increases with increasing spatial resolution, which explains that the performance of the Λ_0 approximation that neglects this term altogether decreases at finer spatial resolutions. On the other hand, as the spatial resolution is decreased, the Λ_0 reconstruction becomes less erroneous, approaching $\tilde{\Lambda}$. Thus, in the limiting case, $\tilde{\Lambda}$ represents the upper performance limit for the Λ_0 approximation.

Due to their similarity to the exact pressure fields, the corrected fields p_Λ and $p_{\tilde{\Lambda}}$ may also be used to determine instantaneous pressure estimation uncertainties from uncorrected data. In particular, the instantaneous error may be approximated as $p_m - p_\Lambda$ or $p_m - \tilde{p}_{\tilde{\Lambda}}$, with the goal of estimating the exact error value $p_m - p_{ex}$. An integral measure for the pressure error can be obtained by evaluating the RMS ($||\boldsymbol{\epsilon}_p'|| = \sqrt{\sum(p-p_{ex})^2/N}$) of the random instantaneous pressure error on the domain. This measure is evaluated for 100 realizations and averaged for varying velocity field error levels $\alpha = 0-50\%$ and $\beta = 0-0.5$ px and the obtained error response is plotted in figure 4.7. Estimates of the instantaneous pressure field error obtained using either p_Λ or $p_{\tilde{\Lambda}}$ show a remarkable agreement with the exact error values. Such a good agreement is not immediately expected since the p_Λ and $p_{\tilde{\Lambda}}$ results featured some minor deviations from the exact pressure solutions (e.g., figure 4.6). However, the corrected field p_Λ lies in an identical subspace as the exact field p_{ex} where irrotational pressure gradients and solenoidal velocity are satisfied. The Euclidean distance between the measured field (p_m) and the nearest field in this subspace (p_Λ) hence appears to serve as an accurate predictor of instantaneous pressure uncertainty. To confirm this, figure 4.8 plots the normalized covariance of the pressure and velocity field errors from the same evaluations used to tabulate statistics in figures 4.5 and 4.6, which were obtained from 3,000 realizations at $\alpha = 25\%$, $\beta = 0.25$ px, and an overlap factor of 75%. The plotted covariance is that between the point at the centre of the vortex ($x = 0$, $y = 0$) and every other domain point a distance r_{ij} away, fit with a four-term Gaussian curve fit. The dotted red line denotes the velocity error covariance, and shows the expected behaviour

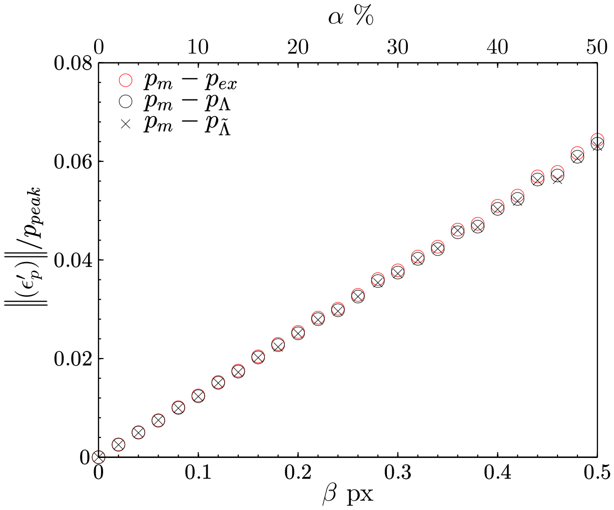

Figure 4.7: Comparison of integral measure of pressure estimation errors, averaged over 100 realizations, for a range of velocity field error levels $\alpha = 0 - 50\%$ and $\beta = 0 - 0.5$ px. Evaluated on high spatial resolution data with $WS/\lambda_x = 0.08$, $\delta tu_{peak}/WS = 0.5$ and 75% overlap.

of a linear function from $0 < r_{ij}/WS < 1$ which is implicit in the correlation matrix ζ_{ij} populated with a triangle function to generate the correlated velocity error fields (Azijli and Dwight 2015, Sciacchitano and Wieneke 2016). A high agreement is seen between the exact pressure error covariance and that estimated from p_Λ and $p_{\tilde{\Lambda}}$, attesting to the high fidelity of these methods in pressure uncertainty estimation. Notably, figure 4.8 shows that, for pressure estimates obtained from erroneous velocity data, the radius of pressure error correlation expands relative to the velocity error correlation, indicating that the propagation of local velocity error through the Poisson equation extends to surrounding regions within $12WS$ in this case. The propagation of local velocity error to surrounding regions in the pressure solution is due to the elliptic nature of the Poisson equation and underlies some of the difficulty in performing accurate PIV/PTV-based pressure estimates in practice, for example, near wall boundaries.

4.3.2 Advecting Lamb-Oseen Vortex

The pressure gradient error reconstructions proposed in the current study neglect errors at the boundaries of the domain. For the Taylor vortex test case, only minor velocity errors were present at the boundary (figure 4.2a); consequently, neglecting the effect of measurement errors at boundaries of the domain had a minimal effect on the accuracy of the error reconstruction. In order to evaluate the effect of this assumption under more strenuous conditions, an advecting Lamb-Oseen vortex (figure 4.2b) is analysed, where the pressure and pressure gradients have a slower rate of decay away from the vortex centre. The Lamb-Oseen vortex (Batchelor 2000) is defined in two-dimensions as:

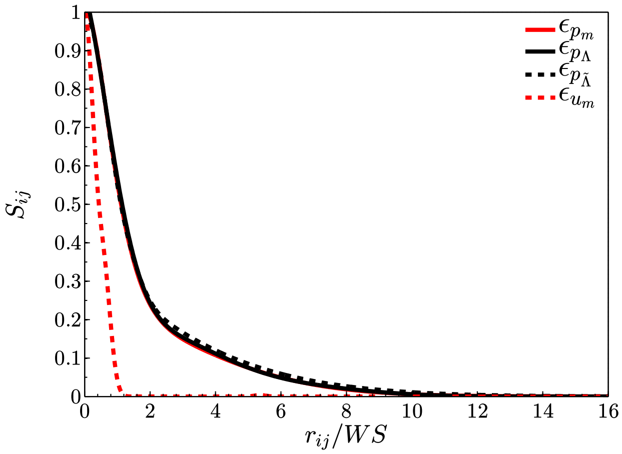

Figure 4.8: Covariance of the exact pressure estimation error ($\boldsymbol{\epsilon}_{p_m}$), that estimated using the Λ reconstructed field as reference ($\boldsymbol{\epsilon}_{p_\Lambda}$), or the $\tilde{\Lambda}$ reconstructed field ($\boldsymbol{\epsilon}_{p_{\tilde{\Lambda}}}$), compared to the covariance of the velocity field error with 75% overlap.

$$u_\theta = \frac{\Gamma}{2\pi r}\left(1 - \exp\left(-\frac{r^2}{r_c^2/\gamma}\right)\right) \tag{4.23}$$

$$p = -\frac{1}{2}\rho\frac{\Gamma^2}{4\pi^2 r^2}\left(1 - \exp\left(-\frac{r^2}{r_c^2/\gamma}\right)\right)^2 - \frac{\rho\Gamma^2}{4\pi^2 r_c^2/\gamma}\left(E_1\left(\frac{r^2}{r_c^2/\gamma}\right) - E_1\left(\frac{2r^2}{r_c^2/\gamma}\right)\right) \tag{4.24}$$

where $E_1(x) = \int_1^\infty e^{-xt}/t\, dt$ is the exponential integral, $\gamma = 1.256431$, and $r^2 = (x - U_a t)^2 + y^2$. For the analysis in this section, the following parameters are used: $\Gamma = 0.001$ m^2 s^{-1}, $r_c = L/8$ m, $\rho = 1000$ kg m^{-3}, $\nu = 1 \times 10^{-6}$ m^2 s^{-1}, $U_a = 0.003$ m s^{-1}. The flow is evaluated on a domain $L_x = L_y = 6 \times 10^{-3}$ m, ensuring flow gradients are of significant magnitude at the boundaries in order to facilitate a higher sensitivity to boundary error. Pressure gradient and pressure estimations are evaluated as the vortex is advected from the centre of the domain ($x/L = 0$) to the right side boundary ($x/L = 0.5$). A Neumann condition for the pressure Poisson equation is enforced on the right boundary, and Dirichlet conditions based on the steady Bernoulli equation are enforced on the remaining boundaries (equation 4.1). This configuration is similar to the approach of de Kat and van Oudheusden 2012 where the same flow was used as a test case.

Figure 4.9 plots the pressure gradient fields in the x direction when the advecting vortex reaches $x/L = 0.375$ and strong pressure gradients are present at the right boundary ($x/L = 0.5$). Figures 4.9a and b present $\partial p/\partial x$ estimated from exact velocity data including the viscous term, and excluding the viscous term, respectively. The resulting pressure gradient fields are nearly identical, indicating that the viscous term is negligible for the parameters chosen for this flow. When correlated error of $\epsilon_u \propto \alpha = 25\%$ and $\beta = 0.25$ px is added to the velocity fields, the pressure gradient estimations using Eulerian (figure 4.9c)

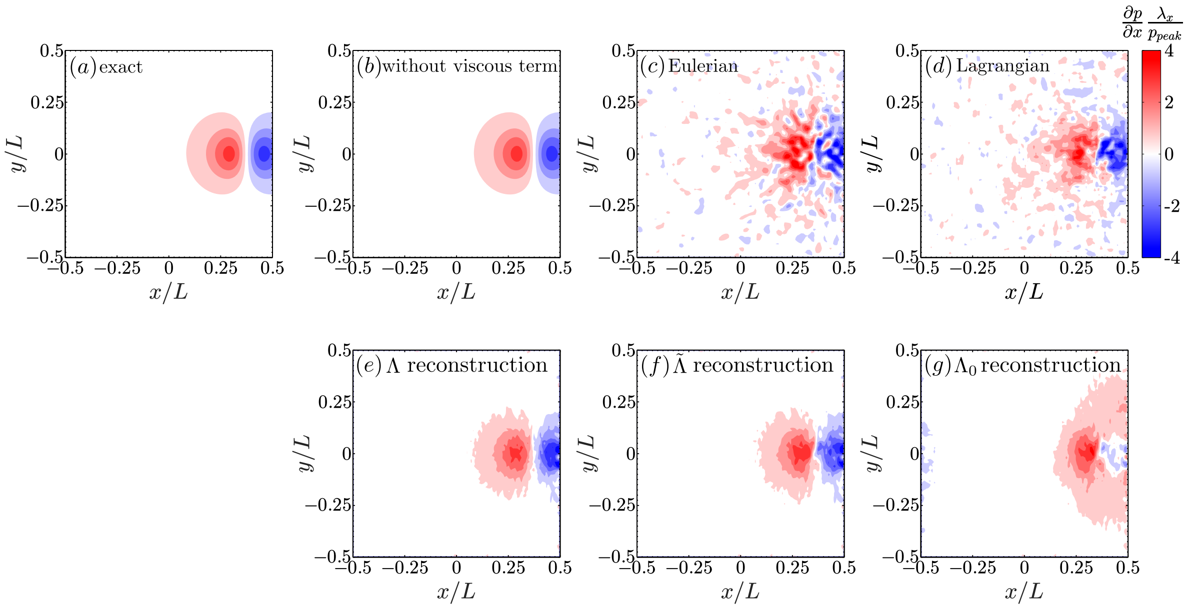

Figure 4.9: Lamb-Oseen vortex pressure gradient fields sampled at $WS/\lambda_x = 0.08$, $\delta t u_{peak}/WS = 0.5$, with its centre at $x/L = 0.375$. (a) exact velocity data neglecting viscosity, (b) exact velocity data including viscosity, (c) Eulerian evaluation on erroneous velocity data with $\alpha = 25\%$ and $\beta = 0.25$ px, (d) Lagrangian evaluation on erroneous velocity data, (e) Eulerian evaluation on erroneous velocity data with Λ reconstruction, (f) $\tilde{\Lambda}$ reconstruction, and (g) Λ_0 reconstruction.

and Lagrangian (figure 4.9d) methods become notably contaminated, similar to the Taylor vortex results. When the pressure gradient error field is reconstructed (equation 4.16), and subtracted from the raw Eulerian estimate (figure 4.9c), a significant reduction in random variations is attained when Λ is retained fully in the reconstruction (figure 4.9e) or approximated by $\tilde{\Lambda}$ (figure 4.9d). Similar to the Taylor vortex test case, estimations which neglect Λ entirely (Λ_0) lead to a significant mean offset in the corrected pressure gradient field. The results show that corrections that employ the Λ or $\tilde{\Lambda}$ error reconstructions perform well even when significant flow dynamics exist at the boundary. In particular, the effect of neglecting errors at the boundaries can be deduced from a careful inspection of figures 4.9e and f. Specifically, boundary errors affect a region near the right boundary ($0.45 < x/L < 0.5$) near the boundary of the pressure gradient field where the reconstructed results retain pressure gradient variations similar to those in the uncorrected results (figure 4.9c). However, away from this region, the effect of boundary errors on $\partial p_{\Lambda}/\partial x$ or $\partial p_{\tilde{\Lambda}}/\partial x$ is minimal.

Pressure field estimations from the gradient fields shown in figure 4.9 are presented in figure 4.10. The results are similar to the previously investigated Taylor vortex case, indicating robustness of the method to boundary errors for the majority of the domain. In comparison to the exact pressure solution (figure 4.10a), pressure estimates on the erro-

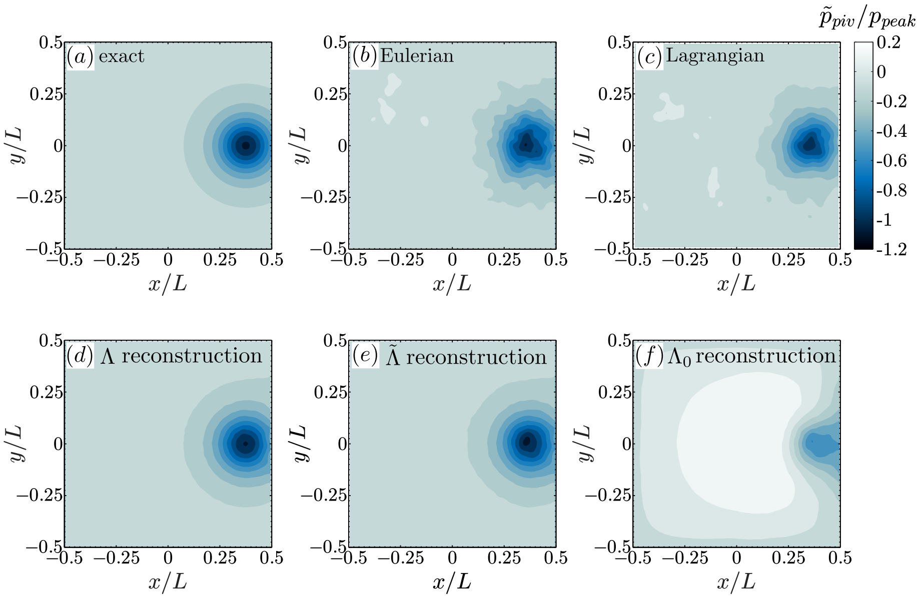

Figure 4.10: Lamb-Oseen vortex pressure fields sampled at $WS/\lambda_x = 0.08$, $\delta t u_{peak}/WS = 0.5$, with its centre at $x/L = 0.375$, (a) exact solution, (b) Eulerian evaluation on erroneous velocity data with $\alpha = 25\%$ and $\beta = 0.25$ px, (c) Lagrangian evaluation on erroneous velocity data, (d) Eulerian evaluation on erroneous velocity data with Λ reconstruction, (e) $\tilde{\Lambda}$ reconstruction, and (f) Λ_0 reconstruction..

neous velocity data using uncorrected Eulerian (figure 4.10b) or Lagrangian (figure 4.10c) techniques leads to appreciable random error propagation, whereas estimates utilizing the error reconstructions retaining Λ (figure 4.10d) or $\tilde{\Lambda}$ (figure 4.10e) terms approach the exact field. Once again, neglecting Λ entirely in the error reconstruction results in erroneous pressure fields (figure 4.10f). A closer inspection of the corrected fields in figures 4.10d and e reveals that corrected pressure estimates share essentially the same boundary values with the uncorrected pressure field (figure 4.10b), indicating that boundary conditions, and any errors present in such, dominate the reconstruction in the immediate vicinity of the boundary. This behaviour is implied in the formulation of the div-curl system used to reconstruct $\boldsymbol{\epsilon}_{\boldsymbol{\nabla} p}$, since the solution is required to equal to zero at the boundaries (equation 4.16).

To statistically characterize the effect of boundary errors on corrected pressure estimates, a Monte Carlo simulation is performed using 3,000 evaluations of pressure estimates with refreshed noise profiles for three positions of the advecting vortex. Figures 4.11a-c plot the random pressure estimation error relative to the exact solution (equation 4.24) when the vortex centre is in three different positions relative to the boundary, $x/L = 0$, $x/L = 0.25$ and $x/L = 0.5$, respectively. The random error in the uncorrected Eulerian estimate (red circles, figure 4.11), the corrected field using the Λ reconstruction (black circles, figure 4.11), and the corrected field using the $\tilde{\Lambda}$ reconstruction (black crosses, figure

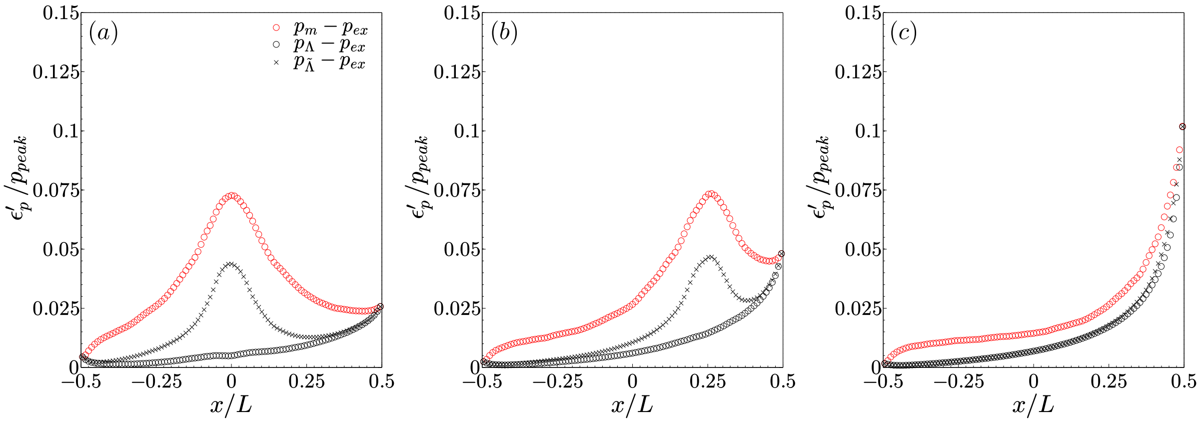

Figure 4.11: Comparison of the standard deviation of exact and estimated pressure errors of the Eulerian estimates, evaluated over 2,000 realizations, for $\alpha = 25\%$ and $\beta = 0.25$ px. Data is sampled at $WS/\lambda_x = 0.08$ and $\delta t u_{peak}/WS = 0.5$, and evaluated when the Lamb-Oseen vortex centre is at (a) $x/L = 0$, (b) $x/L = 0.25$, and (c) $x/L = 0.5$.

4.11), are compared. The bias errors are relatively small for all besides the p_{Λ_0} case, similar to the high resolution case for the Taylor vortex (figure 4.6c), and are omitted here for brevity. As well, the corrected fields using Λ_0 reconstruction have been consistently demonstrated to be significantly erroneous and are omitted from following analysis. The error deviations shown in figure 4.11 indicates that p_Λ and $p_{\tilde{\Lambda}}$ produce a significant reduction in random error sufficiently far from the boundary. For example, when the vortex is in the centre of the domain (figure 4.11a), the results are similar to the Taylor vortex case (figure 4.6a). As the vortex approaches the right side boundary (figure 4.11b), the random error for both the uncorrected and corrected fields increases towards the Neumann boundary; however, this does not affect the performance of the Λ and $\tilde{\Lambda}$ corrections near the centre of the vortex and the remainder of the domain. When the centre of the vortex reaches the boundary (figure 4.11c), the adverse effect of boundary error propagation is the highest, with a notably lower reduction in error deviation attained by the correction schemes. In all the cases, the corrected fields retain the same error statistics as in the uncorrected fields near the boundaries, so that when the pressure gradient error is highest on the boundary and all significant flow features reside in close proximity to the boundary, the accuracy of p_Λ and $p_{\tilde{\Lambda}}$ is diminished. An inspection of the error deviations for the p_Λ fields indicates that the magnitude of the boundary errors is inversely related to the distance from the boundary, which is expected from the form of the boundary terms in the two-dimensional potential function formulation of the div-curl system (equation 4.16) (Aris 1989).

4.3.3 Three-Dimensional Cylinder Wake

The final test case considered in this work is included to model an experimental application of the proposed methodology, in which three-dimensional, volumetric velocity data is acquired. Here, the acquisition of volumetric velocity data in the wake of a circular cylinder in cross-flow at $\mathrm{Re_D} = 1575$ (figure 4.2c) is considered. Since the error reconstruction is only applicable to planar velocity data if the flow is fully two-dimensional, a three-dimensional flow demands volumetric data acquisition. Details regarding the DNS data are reported in McClure and Yarusevych 2017a. Synthetic velocity data are obtained by sampling a volume on an equispaced Cartesian grid spanning $0.5D < x < 3D$, $-0.9D < y < 0.9D$, and $-0.94D < z < 0.94D$, where the origin is defined at the midspan and centre of the cylinder (figure 4.12). The velocity fields are sampled at a time separation of $\delta t u_{peak}/WS = 0.34$ and a vector pitch of $\delta x/D = 0.0375$ or $WS/D = 0.15$, with 75% overlap. A correlated velocity error is added to the sampled velocity fields following equation 4.20, with $\alpha = 25\%$ and $\beta = 0.25$ px. The important flow and geometry parameters are: $\rho = 997$ kg m^{-3}, $\nu = 8.926 \times 10^{-7}$ m^2 s^{-1}, $U_\infty = 0.1406$ m s^{-1}, and $D = 0.01$ m. The iso-surfaces of wake pressure in figure 4.12a highlight the dominant vortical structures in the cylinder wake. These structures pass through the $\pm x$-normal and $\pm z$-normal boundaries, and Neumann conditions are employed on these boundaries to solve the Poisson equation for pressure (equation 4.1). For the $\pm y$-normal boundaries, Dirichlet conditions for pressure are approximated using an extended form of Bernoulli's equation for unsteady irrotational flow (de Kat and van Oudheusden 2012). Viscous terms are neglected in the pressure gradient and pressure estimation (equation 4.2), since the Reynolds number is sufficiently high. It was verified that the effect of viscous terms is negligible, similar to the Lamb-Oseen test case in the previous section.

Figure 4.12 compares exact three-dimensional pressure fields (figure 4.12a) with pressure estimates based on uncorrected erroneous data (figures 4.12b,c), and corrected erroneous data (figures 4.12d,e), along with corresponding two-dimensional slices of the pressure estimates at the midspan of each data set. Due to the close proximity of the $\pm y$-normal boundaries to the wake, implementation of Dirichlet conditions on these boundaries based on the extended Bernoulli equation results in a significant error ($\approx 10\%$) compared to the pressure fields from the DNS solution. Since this Dirichlet boundary error is present in every pressure estimate, pressure estimates obtained from exact velocity fields (figure 4.12a) with the same boundary conditions are used as a reference for comparison instead of the DNS pressure solution. The pressure estimates utilizing Eulerian (figure 4.12b) or Lagrangian (figure 4.12c) methods on the uncorrected erroneous velocity fields are shown to result in significant random errors compared to the reference pressure field, similar to the results presented earlier for the Taylor vortex and Lamb-Oseen vortex. In comparison, pressure estimates which subtract the pressure gradient error reconstructed by retaining all terms in Λ (figure 4.12d), or using the $\tilde{\Lambda}$ (figure 4.12e) approximation, reduce the resulting pressure estimation errors substantially. The minor residual errors in the p_Λ and $\tilde{p}_{\tilde{\Lambda}}$ fields are attributed primarily to the propagation of boundary errors and truncation errors occurring during the reconstruction of the data. Specifically, the observed errors in the (*a*) exact

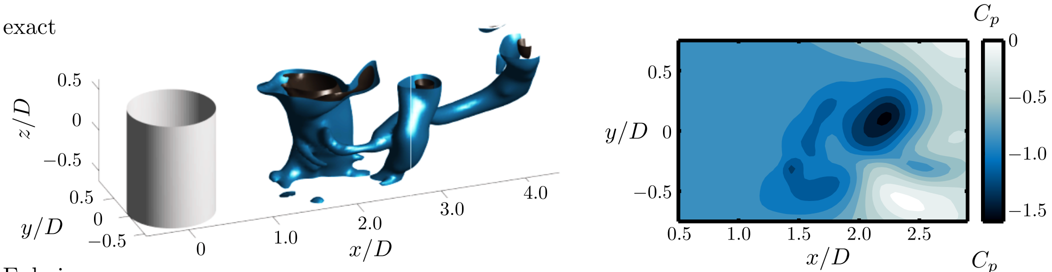

(*b*) Eulerian

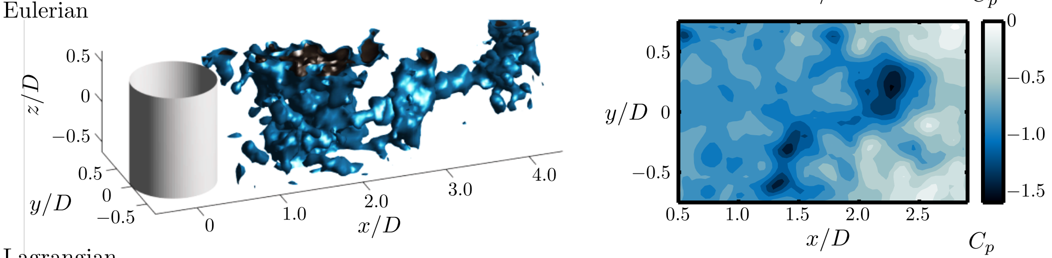

(*c*) Lagrangian

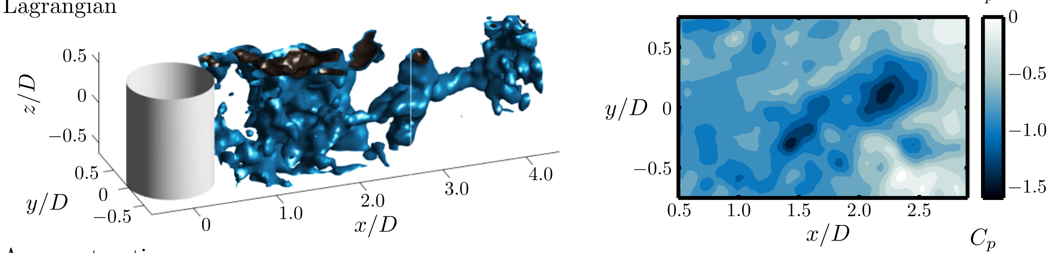

(*d*) Λ reconstruction

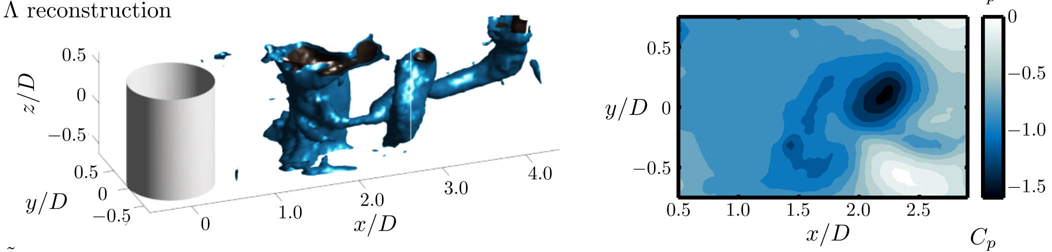

(*e*) $\tilde{\Lambda}$ reconstruction

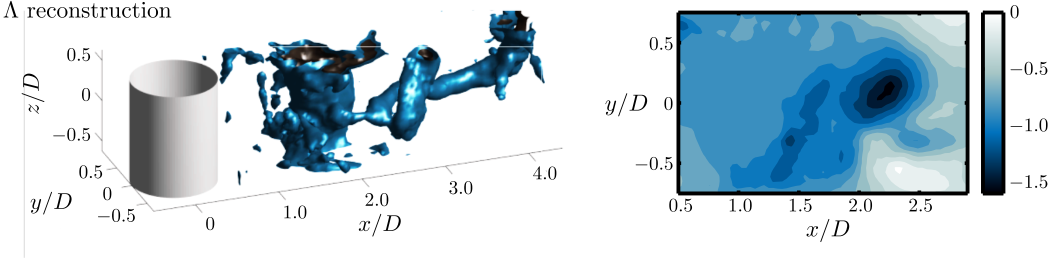

Figure 4.12: Isosurfaces of pressure at $C_p = -1$ (blue) and $C_p = -1.25$ (dark purple) for (a) Eulerian method with exact velocity data, (b) Eulerian method with $\alpha = 25\%$ and $\beta = 0.25$ px correlated errors, (c) Lagrangian method with errors, (d) Eulerian method with Λ reconstruction, and (e) Eulerian method with $\tilde{\Lambda}$ reconstruction. Data sampled at $WS/D = 0.15$ and $\delta tu_{peak}/WS = 0.34$ with contour plots sampled at the midspan ($z/D = 0$).

corrected fields are highest near the Neumann boundaries, but are minimal in the centre of the domain where the results approach the reference pressure contours in the midspan

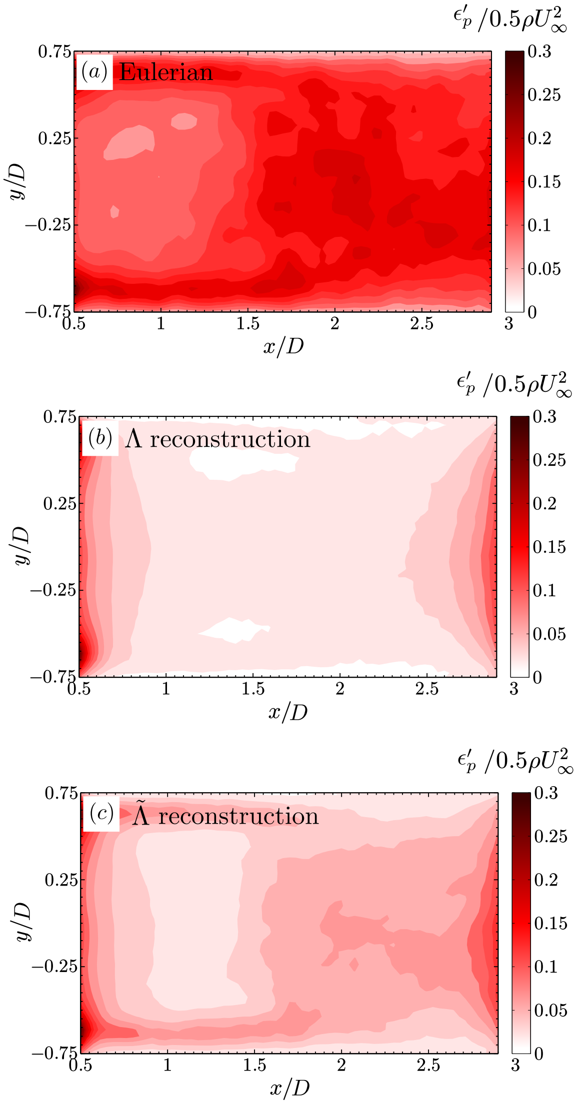

Figure 4.13: Standard deviation of the instantaneous pressure estimation error in and $x - y$ plane at the midspan of the data set over 250 different velocity field realizations. Errors are determined by the differential between the Eulerian estimate of pressure on the exact velocity data and (a) the Eulerian uncorrected estimate on the erroneous data, (b) the pressure estimate with the Λ reconstruction on the erroneous data, and (c) the pressure estimate with the $\tilde{\Lambda}$ reconstruction on the erroneous data.

plane (c.f., figures 4.12d,e and 4.12a).

Figure 4.13 presents the random error ($\boldsymbol{\epsilon}'_p$) of the pressure estimation errors in an $x - y$ plane at the midspan of the data set. The statistics were tabulated over 250 realizations of estimated pressure fields spanning one vortex shedding cycle. The results for the Eulerian estimates are shown in figure 4.13a and indicate that the pressure estimation errors are concentrated predominantly in the separated shear layers and vortex formation region where high spatial gradients occur. This is presumed to be due to a combined effect of truncation errors occurring during pressure estimation (de Kat and van Oudheusden 2012, McClure and Yarusevych 2017b), and strong random error propagation from velocity errors concentrating in the high gradient regions (equation 4.20). Near the $\pm x$ boundaries, error is amplified slightly where the Neumann boundary conditions are applied. In comparison, the boundary errors on the $\pm y$ boundaries are minimal due to the application of Dirichlet boundary conditions which are less sensitive to velocity errors. The random errors for corrected fields p_Λ and $p_{\tilde{\Lambda}}$ (figures 4.13b,c) indicate a substantial reduction over the entire domain, except for the small affected regions near the boundaries with the Neumann boundary conditions. Compared to the p_Λ field, the $p_{\tilde{\Lambda}}$ field reduces errors less substantially in the high gradient regions of the flow, where the terms neglected in the model for Λ become more significant. However, overall, a substantial reduction in random error propagation is achieved by both the exact and approximate correction schemes.

4.4 Conclusion

A mathematical framework for the solution of instantaneous pressure gradient error from PIV/PTV-based measurement has been developed for incompressible flows. The pressure gradient error field ($\boldsymbol{\epsilon}_{\boldsymbol{\nabla} p}$) has been shown to satisfy a div-curl system of equations which requires the calculation of its curl ($\boldsymbol{\nabla} \times \boldsymbol{\epsilon}_{\boldsymbol{\nabla} p}$) and divergence ($\boldsymbol{\nabla} \cdot \boldsymbol{\epsilon}_{\boldsymbol{\nabla} p}$) over the domain. Once $\boldsymbol{\epsilon}_{\boldsymbol{\nabla} p}$ is reconstructed, its subtraction from the estimated fields has been shown to result in a significant increase in the accuracy of both pressure gradient and pressure estimations from erroneous velocity data, and the reconstruction maintains robustness for correlated velocity field error levels in excess of 25% with large spatial variations. For exact determination of the pressure gradient/pressure field, the framework requires two quantities not immediately realizable in experiment (i) the pressure gradient error on the boundaries of the domain, and (ii) certain spatial gradients of the exact velocity and velocity error field. Hence, a simplified methodology has been developed for application in practical settings. The two simplifications are the assumption of error-free boundary conditions, and the approximation of the term containing the unknown error gradients (Λ term). For the latter approximation, the Λ term is either neglected (Λ_0 reconstruction) or approximated ($\tilde{\Lambda}$).

The proposed methodology has been evaluated using three test cases: (i) a stationary Taylor vortex, (ii) an advecting Lamb-Oseen vortex, and (iii) the wake of a circular cylinder in cross-flow. Specifically, three different error reconstructions have been assessed and compared to the exact solutions and uncorrected estimations from synthetic PIV data sampled from the exact solutions with imposed velocity error profiles, (i) the Λ reconstruction which only assumes zero pressure gradient error on the boundaries, but retains the full Λ term from knowledge of the exact velocity and velocity error gradients, (ii) the $\tilde{\Lambda}$ term which estimates the full Λ term using the divergence of the measured velocity field, and (iii) the Λ_0 reconstruction which neglects the Λ term entirely.

The results have shown that subtracting the reconstructions of $\boldsymbol{\epsilon}_{\boldsymbol{\nabla} p}$ from the original pressure gradient estimates results in significant error reduction in pressure gradient and pressure estimates across the inner domain for all the three test flow cases examined. The effect of neglecting the pressure gradient error at the boundaries affects the results in a relatively small region near the boundaries when flow structures are in close proximity. As expected, the Λ reconstruction method performs best, and approaches the exact solution when boundary errors are not significant. The $\tilde{\Lambda}$ method also performs well, leading to a minimum of 50% reduction of pressure gradient and pressure random errors away from the boundaries. The efficacy of the corrections is decreased in the high gradient flow regions where velocity error gradients and velocity gradients are the highest. The Λ_0 reconstruction, on the other hand, leads to significant bias errors in pressure gradient and pressure estimates, rendering it impractical.

In addition to reducing errors in pressure estimation, the Λ and $\tilde{\Lambda}$ pressure gradient error field reconstructions both provide reliable estimates for uncertainty bounds on the uncorrected instantaneous pressure estimates, predicting the integral error levels and covariance of the pressure errors to a high degree of accuracy. While the current results strongly support the effectiveness of the proposed methodology, the technique can be optimized further. Specifically, improved modelling of the Λ term, compared to the simple estimate $\tilde{\Lambda}$, may be considered with the incorporation of established methods for estimation of velocity field uncertainty. The applicability of the method for planar pressure determination in three-dimensional flow remains to be evaluated or treated analytically. The boundary velocity errors are neglected in the present formulation, but may be incorporated through a more complex formulation. Finally, the framework is developed only for Eulerian evaluation over three velocity fields, and can be extended to Lagrangian techniques over multiple velocity fields in time to further improve the accuracy of the reconstructions.

Chapter 5

Generalized framework for PIV-based pressure gradient error field determination

The framework leveraging the governing equations of incompressible flow for the reconstruction and correction of pressure gradient estimation errors from experimental data, previously introduced in Chapter 4, is extended to incorporate non-zero errors on domain boundaries and Lagrangian pseudo-tracking methods for material acceleration estimation. For the selected test case of a cylinder wake flow in turbulent shedding regime, the analysis of simulated three-dimensional, three-component velocity measurements demonstrates that the errors in pressure estimates can be reduced by up to 50% using a basic finite difference implementation.

This chapter is based on the journal article: McClure, J., and Yarusevych, S. (2019) “Generalized PIV-based pressure gradient error correction for Lagrangian pseudo-tracking,” *Measurement Science and Technology*, 30(8), 084005.

5.1 Introduction

The advancement of Particle Image Velocimetry (PIV) and Particle Tracking Velocimetry (PTV) image processing algorithms along with LASER/high-speed camera technology has progressed to a level where volumetric velocity data sets resolving the dominant spatio-temporal kinematics of flow fields are becoming common. Access to the full resolution of the velocity field, $\mathbf{u}(\mathbf{x}, t)$, in a measurement domain, allows an experimentalist to utilize the governing equations to increase the accuracy or extend the fidelity of the experimental data. Resulting developments in this direction include PIV/PTV-based fluid pressure estimates (van Oudheusden 2013, Gesemann *et al.* 2016, Schneiders *et al.* 2016b, van Gent *et al.* 2017, Huhn *et al.* 2018, Schneiders *et al.* 2018, Suzuki *et al.* 2018, Wang *et al.* 2018), instantaneous structural loading estimates (Rival and Oudheusden 2017), and the growing class of variational methods and denoising methodologies (Heitz *et al.* 2010, Azijli and Dwight 2015, Azijli *et al.* 2016, Wang *et al.* 2016, McClure and Yarusevych 2017a). In this view, experimental measurements now may be contextualized by their conformity to the Navier-Stokes equations governing the underlying smooth dynamics of the real flow, and methodologies are developed for measurement problems in order to draw the data closer to conformity.

The current study is concerned with the problem of PIV-based pressure estimation. The pressure may be reconstructed using a number of methods; namely, solution of the pressure Poisson equation (PPE) using finite difference (Gurka *et al.* 1999, van Oudheusden 2013), finite volume (Neeteson and Rival 2015), finite element (Auteri *et al.* 2015, Schiavazzi *et al.* 2017), or spectral (Huhn *et al.* 2016) schemes, the iterative averaging of successive line integrations of the pressure gradient (Baur and Köngeter 1999, Liu and Katz 2006, Dabiri *et al.* 2014, Liu *et al.* 2016), and sequential least square reconstruction (Jeon *et al.* 2018). The full spatio-temporal evolution of both pressure and velocity in a flow gives the experimenter access to the entire kinematics and dynamics of the flow, and is a precursor for estimating time-resolved structural loads on immersed structures using the momentum-integral method (van Oudheusden *et al.* 2007, Tronchin *et al.* 2015, Rival and Oudheusden 2017). Consistent pressure estimates are, in general, challenging due to their sensitivity to velocity measurement error. For example, significant challenges often arise near boundaries when Neumann boundary conditions have to be applied in the pressure solver (e.g., near walls, wake boundaries) (Pan *et al.* 2016, McClure and Yarusevych 2017a). In practise, accurate pressure estimates require high quality data and careful selection of solver boundary locations (Tronchin *et al.* 2015, Van De Meerendonk *et al.* 2018), with the degree to which the error of PIV-based pressure estimates is dominated by error propagation from the boundaries dependent on the specific flow (Charonko *et al.* 2010, Pan *et al.* 2016). As well, minimum requirements on the temporal and spatial resolution of the PIV measurements must be met in order to avoid excessive truncation errors (Charonko *et al.* 2010, de Kat and van Oudheusden 2012, McClure and Yarusevych 2017b, Nie *et al.* 2022). If the data are over-sampled beyond these requirements, down-sampling or employing low-pass filtering can help mitigate random error propagation to the pressure field estimates (Charonko *et al.* 2010, Dabiri *et al.* 2014). An optimum sampling resolution can be selected relative to the flow scales using a simple analytical model (McClure and Yarusevych 2017b, Nie *et al.* 2022) or by considering the effect of varying sampling parameters on the material acceleration estimates during post-processing (van Gent *et al.* 2018).

A common low-pass filtering technique is the curve fitting of pseudo-trajectories following fluid elements over multiple time realizations (Novara and Scarano 2013, Pröbsting *et al.* 2013, Lynch and Scarano 2014, van Gent *et al.* 2017, van Gent *et al.* 2018). For PIV-data, smooth material acceleration estimates can be obtained from these Lagrangian pseudo-tracking approaches. Further, a number of approaches have been developed leveraging physical constraints on the data to reduce error, which correct the velocity field measurement data before material acceleration estimation or include material acceleration estimates as part of the correction scheme. One method for correcting measured velocity fields is solenoidal filtering of the velocity field for incompressible flows (Song *et al.* 1993, de Silva *et al.* 2013, Schiavazzi *et al.* 2014, Azijli and Dwight 2015, Schiavazzi *et al.* 2017). In one approach, the velocity field can be decomposed into its solenoidal and irrotational components by employing a Helmholtz decomposition (Aris 1989), leading to a method of solution for the solenoidal component through solution of a Poisson equation. A similar approach can be formulated for the pressure gradient field that instead enforces pressure gradient estimates from velocity measurements to be irrotational (Wang *et al.* 2016). More advanced methods for correction utilize averaged integrations of the vorticity transport equation (Schneiders and Scarano 2016), the solution of an optimization procedure that penalizes high frequency field components and non-zero residuals of the velocity field divergence and the divergence of the momentum equation (Gesemann *et al.* 2016), and projection methods to form a decoupled iterative correction scheme employed with a weighting parameter that balances the result from the experiment with a corresponding numerical solution of the pressure and velocity fields (Wang *et al.* 2018).

The focus of the present study uniquely considers the pressure gradient field $\boldsymbol{\nabla} p$, which is the primary input into any pressure estimation algorithm and thus forms a direct connection to PIV-based pressure estimation accuracy. Specifically, the problem of determining the pressure gradient error field $\epsilon_{\boldsymbol{\nabla} p}$ is considered, for which the governing equations are employed. The equations governing the exact determination of the error field may then serve to inform uncertainty analysis through a statistical analysis, or closure methods for the equations when working with experimental data may be inferred, with the assumptions and simplifications tracked back to the fully generalized problem. In addition, dealing with the reconstruction of the error field to be subtracted off the measured field ensures that any spatial or temporal modulation introduced by the solution process propagates only to the error fields and not the corrected pressure or pressure gradient fields. This implies that no additional truncation error or smoothing is introduced into the resulting estimates. Building on the previous work presented in (McClure and Yarusevych 2017a), the present study utilizes an equivalent div-curl system that simplifies the solution process for the pressure gradient error field, and allows the prescription of boundary error terms more naturally, while maintaining solvability. In addition, the methodology for use with material acceleration estimates obtained from Lagrangian pseudo-tracking is derived and evaluated on the test case of flow around a circular cylinder.

5.2 Mathematical Development

5.2.1 Pressure gradient estimation

The pressure gradient ($\boldsymbol{\nabla} p_m$) can be estimated from the Navier-Stokes equations using the measured velocity field ($\mathbf{u_m}$) from time-resolved PIV measurements. The material acceleration and viscous term can be estimated using an Eulerian discretization of the terms in equation 5.1 and 5.2 using a central difference scheme.

$$\frac{D\mathbf{u_m}}{Dt} = \frac{\partial \mathbf{u_m}}{\partial t} + (\mathbf{u_m} \cdot \nabla)\mathbf{u_m} \tag{5.1}$$

$$\boldsymbol{\nabla} p_m = -\rho \frac{D\mathbf{u_m}}{Dt} + \mu \nabla^2 \mathbf{u_m} \tag{5.2}$$

Alternatively, an estimate for the material acceleration of a fluid may be obtained from PIV measurements using various pseudo-tracking methods that construct fluid particle trajectories from a set of time-resolved velocity fields. The least squares estimate of the material acceleration over recursive first order trajectories (Pröbsting *et al.* 2013) will be considered in the present study, but the results presented in this work can be easily extended to central difference estimates (Liu and Katz 2006, Violato *et al.* 2011) or estimates using polynomial fits (Wang *et al.* 2017, van Gent *et al.* 2018) from first-order trajectories. Some additional development is required to incorporate second-order trajectories (de Kat and van Oudheusden 2012, Laskari *et al.* 2016, van Gent *et al.* 2018), however the principle is the same. The pseudo-trajectory is constructed over a symmetric time interval centred at the snapshot of interest, $\mathbf{t} = t^0 + \boldsymbol{\Delta}\mathbf{t}$, where $\boldsymbol{\Delta}\mathbf{t} = [-M\Delta t, -(M-1)\Delta t, ..., M\Delta t]$. The trajectory $\mathbf{x}(\mathbf{t})$ is obtained by a recursive first-order relation both forward and backward in time from t^0 (equation 5.3),

$$\mathbf{x}(\mathbf{t}^{\pm i}) = \pm\mathbf{x}(\mathbf{t}^{\pm(i-1)}) \pm \mathbf{u_m}(\mathbf{x}(\mathbf{t}^{\pm(i-1)}), \mathbf{t}^{\pm(i-1)})\Delta t \tag{5.3}$$

and the velocities along each trajectory are computed by bi-cubic interpolation of the corresponding velocity field at the trajectory points at the same snapshot in time. The velocity differentials along the trajectory from t^0 are computed as $\boldsymbol{\Delta}\mathbf{u_m} = \mathbf{u_m}(\mathbf{x}(\mathbf{t}), \mathbf{t}) - \overline{\mathbf{u_m}(\mathbf{x}(\mathbf{t}), \mathbf{t})}$, where $\overline{\mathbf{u_m}(\mathbf{x}(\mathbf{t}), \mathbf{t})}$ is the mean velocity over the trajectory, and the least squares estimate for the material acceleration is (Pröbsting *et al.* 2013):

$$\frac{D\mathbf{u_m}}{Dt} = (\boldsymbol{\Delta}\mathbf{t}^T \boldsymbol{\Delta}\mathbf{t})^{-1} \boldsymbol{\Delta}\mathbf{t}^T \boldsymbol{\Delta}\mathbf{u_m} \tag{5.4}$$

Then, similar to the Eulerian estimate, once the material acceleration is estimated, the pressure gradient may be computed from the Navier-Stokes equation (equation 5.2). Often, unless the Reynolds number is low enough for it to be significant, the viscous term is omitted in order to avoid unnecessary error amplification through the second derivatives (Ghaemi *et al.* 2012).

5.2.2 Pressure Estimation

Once an estimate for the pressure gradient is obtained, a Poisson solver (equation 5.5) is employed to estimate pressure (Gurka *et al.* 1999).

$$\begin{aligned} \boldsymbol{\nabla}^2 p_m = \boldsymbol{\nabla} \cdot \boldsymbol{\nabla} p_m, &\quad \text{in } \Omega \\ \boldsymbol{\nabla} p_m \cdot \mathbf{n} = h, &\quad \text{on } \Gamma_i \\ p_m = g, &\quad \text{on } \Gamma_j \end{aligned} \tag{5.5}$$

where Γ_i denotes boundary sections where the Neumann boundary condition is employed, setting the boundary-normal pressure gradient to that estimated from the Navier-Stokes equation (equation 5.2), and Γ_j denotes boundary sections where the Dirichlet condition is employed, setting the pressure on the boundary using an extended form of the Bernoulli equation, valid for unsteady, irrotational flow with small mean velocity gradients (de Kat and van Oudheusden 2012). For the cylinder flow test case investigated in the current study, the boundary conditions employed are illustrated in figure 5.1a. For the 2D2C test case, the top and bottom boundaries are set to Dirichlet conditions since they reside in regions of irrotational flow, while the left and right boundaries are set to Neumann conditions due to their immersion in rotational flow. For the 3D3C test case, the additional spanwise boundaries are prescribed Neumann conditions. The Laplacian of the pressure field (equation 5.5) is discretized using a 5-point second-order central difference scheme and Neumann boundary conditions were imposed through the use of ghost grid points at the boundaries in order to complete the five point scheme where adjacent nodes lie outside the domain. The pressure values at the ghost points were evaluated using the pressure gradient from the Navier-Stokes equation and the nodal pressure on the opposing side of the five point scheme (e.g., $p_{i+1,j} = p_{i-1,j} + 2\Delta x \frac{\partial p}{\partial x}_{i,j}$).

5.2.3 Error Field Correction

To analyse the equations governing the error fields, the measured velocity field (equation 5.6) and estimated pressure gradient field (equation 5.7) are decomposed into their respective true component and error component as:

$$\mathbf{u_m} = \mathbf{u_{ex}} + \boldsymbol{\epsilon}_u \tag{5.6}$$

$$\boldsymbol{\nabla} p_m = \boldsymbol{\nabla} p_{ex} + \boldsymbol{\epsilon}_{\boldsymbol{\nabla} p} \tag{5.7}$$

Following the development in McClure and Yarusevych (2017a), the following first-order div-curl system governing the pressure gradient error field is considered:

$$\begin{aligned} \boldsymbol{\nabla} \times \boldsymbol{\epsilon}_{\boldsymbol{\nabla} p} &= \mathbf{J}, \quad \text{in } \Omega \\ \boldsymbol{\nabla} \cdot \boldsymbol{\epsilon}_{\boldsymbol{\nabla} p} &= f, \quad \text{in } \Omega \\ |\boldsymbol{\epsilon}_{\boldsymbol{\nabla} p} \times \mathbf{n}| &= a, \quad \text{on } \Gamma_i, \\ \boldsymbol{\epsilon}_{\boldsymbol{\nabla} p} \cdot \mathbf{n} &= b, \quad \text{on } \Gamma_j \end{aligned} \tag{5.8}$$

where the divergence and curl of the pressure gradient error fields can be obtained from a combination of the Navier-Stokes equations and velocity field divergence (McClure and Yarusevych 2017a), and boundary conditions can be chosen to specify either the tangential (Γ_i) or normal (Γ_j) component of the pressure gradient error. Previously, the system was made tractable by assuming zero-errors in the pressure gradient on the boundaries, i.e., $a = 0$ and $b = 0$, and a Helmholtz decomposition of the pressure gradient error field allowed the solution through decoupled Poisson equations for the corresponding Helmholtz potential fields.

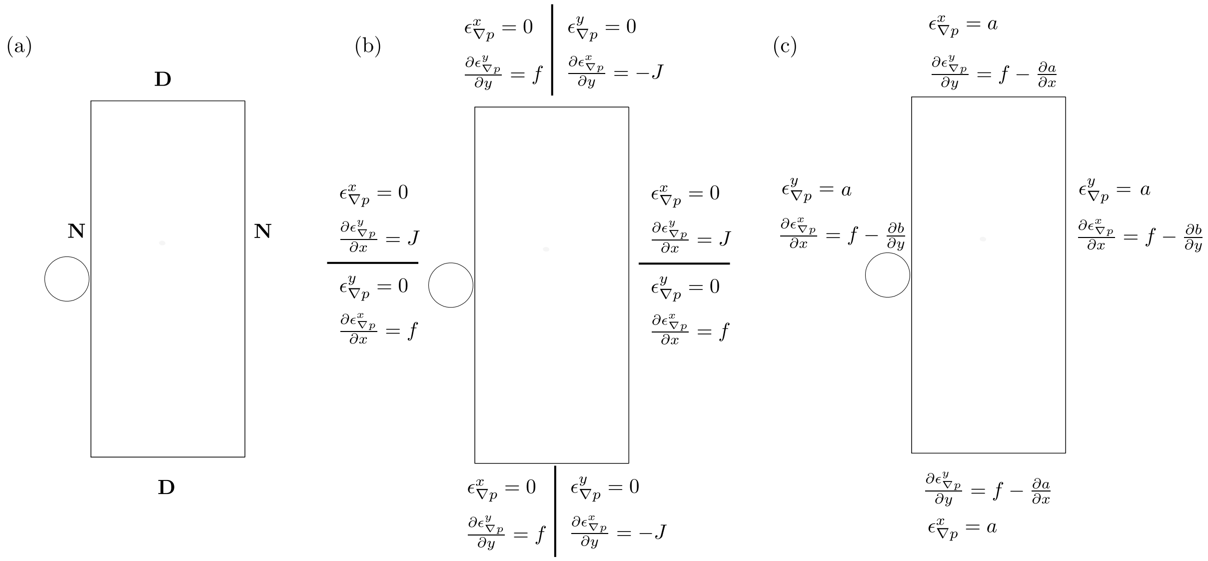

Figure 5.1: (a) Boundary condition implementation for the Poisson equation solver for pressure, with D denoting Dirichlet and N denoting Neumann conditions. (b) Possible boundary conditions for the pressure gradient error field equations where a minimum of one error component is set zero on each boundary, and (c) Boundary conditions used for the pressure gradient error field equations which accept arbitrary errors on the boundaries for both components.

Alternatively, for zero-error boundary conditions, the system in equation 5.8 can be shown to be equivalent to the following second-order system (Jiang 1998):

$$\begin{aligned} \boldsymbol{\nabla}^2 \boldsymbol{\epsilon}_{\boldsymbol{\nabla} p} = -\boldsymbol{\nabla} \times \mathbf{J} + \boldsymbol{\nabla} f, &\quad \text{in } \Omega, \\ \boldsymbol{\nabla} \cdot \boldsymbol{\epsilon}_{\boldsymbol{\nabla} p} = f, &\quad \text{on } \Gamma_i, \\ \mathbf{n} \times \boldsymbol{\epsilon}_{\boldsymbol{\nabla} p} = 0, &\quad \text{on } \Gamma_i, \\ \mathbf{n} \times (\boldsymbol{\nabla} \times \boldsymbol{\epsilon}_{\boldsymbol{\nabla} p}) = \mathbf{n} \times \mathbf{J}, &\quad \text{on } \Gamma_j, \\ \mathbf{n} \cdot \boldsymbol{\epsilon}_{\boldsymbol{\nabla} p} = 0, &\quad \text{on } \Gamma_j \end{aligned} \tag{5.9}$$

Subject to some solvability conditions for a simply connected domain. Namely, $\mathbf{J}$ must satisfy:

$$\boldsymbol{\nabla} \cdot \mathbf{J} = \boldsymbol{\nabla} \cdot (\boldsymbol{\nabla} \times \boldsymbol{\nabla} p_m) = 0 \text{ in } \Omega \tag{5.10}$$

$$\mathbf{n} \cdot \mathbf{J} = \mathbf{n} \cdot (\boldsymbol{\nabla} \times \boldsymbol{\nabla} p_m) = 0 \text{ on } \Gamma_j \tag{5.11}$$

$$\int_\Gamma \mathbf{n} \cdot \mathbf{J} d\Gamma = \int_\Gamma \mathbf{n} \cdot (\boldsymbol{\nabla} \times \boldsymbol{\nabla} p_m)\, d\Gamma = 0 \tag{5.12}$$

for which equation 5.10 holds by vector identity, and equations 5.11 and 5.12 hold automatically for two-dimensional domains, as the curl of the pressure gradient error field ($\mathbf{J}$) is always orthogonal to the boundary normal vector. For three-dimensional domains, equation 5.11 is not satisfied since all three components of the curl of the pressure gradient error field ($\mathbf{J}$) are generally non-zero. In addition, equation 5.12 is not generally satisfied, however the expected value of the integral is zero if $\mathbf{J}$ is dominated by random error with zero mean. If Γ_i is empty, then there are conditions on the divergence source term f for solvability, namely:

$$\int_\Omega f d\Omega = 0 \tag{5.13}$$

This is not generally satisfied, although if f takes the form of a random variable with mean zero, the expected value of the integral is again zero. In any case, if the pressure gradient errors are zero on the boundaries, both solvability conditions are satisfied. However, we will ensure a minimum of one tangential boundary condition is always employed such that Γ_i is always non-empty (McClure and Yarusevych 2017a). In fact, in three-dimensions, all boundaries are prescribed Γ_i conditions in order to avoid potential complications with the constraints implied by equation 5.11. Notably, these solvability constraints only guarantee a unique solution if the domain is simply connected. If the domain is multiply-connected, such as in the case of flow surrounding an immersed body, a useful experimental configuration for load determination from PIV-based pressure estimates, then non-trivial harmonic functions with vanishing divergence and curl on the domain are permitted as solutions, and additional line integrals (Auchmuty and Alexander 2001) may be required in order to fix the solution. The system in equation 5.9 separates into two Poisson equations in two-dimensions and three Poisson equations in three-dimensions, for each component of $\boldsymbol{\epsilon}_{\boldsymbol{\nabla} p}$, with two or three separated boundary conditions to be satisfied on each boundary, corresponding to the two or three separated Poisson equations. Figure 5.1b summarizes the possible boundary condition configurations on each boundary, where a single error component is set to zero, and the respective derivative of the other error component is set to match either the divergence or curl of the pressure gradient error on the boundary to maintain consistency with the source term.

The theory surrounding the system in equation 5.9 is well-developed (Jiang 1998), however it does not completely represent the desired solution since one error component must always take a zero value, which is not a constraint on real error fields. Hence, we make a minor modification of the boundary conditions to conform the system of equations to describing realistic error fields, where both boundary-normal and boundary-tangential components are non-zero. Equation 5.14 splits the pressure gradient error divergence (f) or curl ($\mathbf{J}$) appropriately in order to maintain consistency at the boundaries and to accept arbitrary boundary errors for all components. This is done by specifying the distribution of the error of one component on the boundary in two-dimensions and two components for three-dimensions, and specifying the Neumann condition on the remaining component by constraining it to match the curl or divergence of the error.

$$\begin{aligned}
\boldsymbol{\nabla}^2 \boldsymbol{\epsilon}_{\boldsymbol{\nabla} p} &= -\boldsymbol{\nabla} \times \mathbf{J} + \boldsymbol{\nabla} f, && \text{in } \Omega, \\
\mathbf{n} \times \boldsymbol{\epsilon}_{\boldsymbol{\nabla} p} &= \mathbf{a}, && \text{on } \Gamma_i, \\
\frac{\partial(\boldsymbol{\epsilon}_{\boldsymbol{\nabla} p} \cdot \mathbf{n})}{\partial n} &= f - \boldsymbol{\nabla} \cdot \mathbf{a} && \text{on } \Gamma_i, \\
\mathbf{n} \cdot \boldsymbol{\epsilon}_{\boldsymbol{\nabla} p} &= \mathbf{b}, && \text{on } \Gamma_j, \\
\frac{\partial(\boldsymbol{\epsilon}_{\boldsymbol{\nabla} p} \times \mathbf{n})}{\partial n} &= \mathbf{J} - \boldsymbol{\nabla} \times \mathbf{b} && \text{on } \Gamma_j
\end{aligned} \tag{5.14}$$

Depending on which error field components are prescribed on the boundary, either Γ_i or Γ_j type of boundary conditions may be prescribed, where τ denotes the unit tangential vector. For both the test cases used in the current study, Γ_i boundary conditions are used, shown in figure 5.1c for a two-dimensional domain.

Once the pressure gradient error field ($\boldsymbol{\epsilon}_{\boldsymbol{\nabla} p}$) is solved for using equation 5.14, it is subtracted from the pressure gradient estimate to increase accuracy ($\boldsymbol{\nabla} p_\lambda = \boldsymbol{\nabla} p_m - \boldsymbol{\epsilon}_{\boldsymbol{\nabla} p}$), where the λ subscript denotes the corrected field.

5.2.4 Error correction for Lagrangian pseudo-tracking

The solution of equation 5.14 requires the specification of the divergence and curl of the pressure gradient error over the field in order to provide the source terms and boundary conditions for the Poisson equations. The procedure for incompressible flows and necessary experimental approximations that may be utilized when the pressure gradient is estimated using an Eulerian central difference scheme is included in McClure and Yarusevych (2017a). The procedure is derived here for material acceleration and pressure gradient estimates using least square fitting of Lagrangian pseudo-tracks. The condition on the irrotationality of the pressure gradient field may be invoked to yield that the curl of the pressure gradient error ($\boldsymbol{\epsilon}_{\boldsymbol{\nabla} p}$) is equal to the curl of the estimated pressure gradient field ($\boldsymbol{\nabla} p_m$):

$$\boldsymbol{\nabla} \times \boldsymbol{\epsilon}_{\boldsymbol{\nabla} p} = \boldsymbol{\nabla} \times \boldsymbol{\nabla} p_m \tag{5.15}$$

The second relation we require to form a deterministic set of equations for $\boldsymbol{\epsilon}_{\boldsymbol{\nabla} p}$ is the divergence $\boldsymbol{\nabla} \cdot \boldsymbol{\epsilon}_{\boldsymbol{\nabla} p}$. As an example, for a first order trajectory fundamental to the pseudo-tracking method, the velocity divergence for the trajectories centred at t_0 and $\mathbf{x}_0$ after the trajectory is stepped forward once in time is computed as:

$$\nabla^0 \cdot \mathbf{u_m}(\mathbf{x}^1, t^1) = \boldsymbol{\nabla}^0 \cdot \mathbf{u_m}(\mathbf{x}^0 + \mathbf{u_m}(\mathbf{x}^0, t^0)\Delta t, t^0 + \Delta t) \tag{5.16}$$

which expands to

$$\nabla^0 \cdot \mathbf{u_m}(\mathbf{x}^1, t^1) = \boldsymbol{\nabla}^1 \cdot \mathbf{u_m}(\mathbf{x}^1, t^1) + \nabla^1 \mathbf{u_m} : (\nabla^0 \mathbf{u_m})^T \tag{5.17}$$

where the double dot product (:) of the velocity gradient tensors is defined as $\boldsymbol{\nabla}^1 \mathbf{u} : (\boldsymbol{\nabla}^0 \mathbf{u})^T = u^1_{i,j} u^0_{j,i}$, resulting in a scalar sum of quadratic velocity field derivative terms. The superscripts denote the discrete time stamp along the trajectory where the quantities are evaluated. For example, the computation of $\boldsymbol{\nabla}^1 \cdot \mathbf{u_m}(\mathbf{x}^1, t^1)$ requires the computation of the velocity divergence using central differences on the velocity data at t^1, and the interpolation of the divergence onto the trajectory locations $\mathbf{x}^1$, rather than the standard Cartesian grid that initializes the trajectories at $\mathbf{x}^0$. The accumulation of the terms along the trajectory from the starting position is shown in figure 5.2. Substituting in the decomposition in equation 5.6, making the derivative approximation $\partial u/\partial x \approx \partial u/\partial y \approx \partial u/\partial z$ (McClure and Yarusevych 2017a) for each velocity field component, and using the divergence free condition on the exact velocity field results in:

$$\begin{gathered}\boldsymbol{\nabla}^0 \cdot \boldsymbol{\epsilon}_u(\mathbf{x}^1, t^1) = (\boldsymbol{\nabla}^1 \cdot \boldsymbol{\epsilon}_u^1)(1 + (\boldsymbol{\nabla}^0 \cdot \boldsymbol{\epsilon}_u^0 \Delta t)) \\ +(\boldsymbol{\nabla}^1 \mathbf{u_{ex}}^1 : (\boldsymbol{\nabla}^0 \boldsymbol{\epsilon}_u^0)^T)\Delta t + (\boldsymbol{\nabla}^0 \mathbf{u_{ex}}^0 : (\boldsymbol{\nabla}^1 \boldsymbol{\epsilon}_u^1)^T)\Delta t\end{gathered} \tag{5.18}$$

The divergence of the error field evaluated at a certain time can be obtained by the divergence of the measured velocity field at that time, by invoking incompressibility of the velocity field:

$$\boldsymbol{\nabla}^i \cdot \boldsymbol{\epsilon}_u^i = \boldsymbol{\nabla}^i \cdot \mathbf{u_m}^i \tag{5.19}$$

Hence, to compute the divergence of the pressure gradient computed using the least square estimate in equation 5.4, a least squares estimate for the error divergence over the trajectory must be obtained. The vector of differentials $\Delta(\boldsymbol{\nabla} \cdot \boldsymbol{\epsilon}_u) = \boldsymbol{\nabla} \cdot \boldsymbol{\epsilon}_u(\mathbf{x}(\mathbf{t}), \mathbf{t}) - \overline{\boldsymbol{\nabla} \cdot \boldsymbol{\epsilon}_u(\mathbf{x}(\mathbf{t}), \mathbf{t})}$ is formed, and the following equation computes the divergence of the pressure gradient error field.

$$\boldsymbol{\nabla} \cdot \boldsymbol{\epsilon}_{\boldsymbol{\nabla} p} = -\rho(\Delta \mathbf{t}^T \Delta \mathbf{t})^{-1} \Delta \mathbf{t}^T \Delta(\boldsymbol{\nabla} \cdot \boldsymbol{\epsilon}_u) \tag{5.20}$$

In practise, equation 5.18 cannot be evaluated exactly since the expanded right hand side will contain two terms involving unknown gradients of the velocity error field and exact velocity field. Hence, the computations in the current study omit these two terms, and the effect of this approximation is discussed. Note also that the derivations of equations 5.15 and 5.20 have no explicit treatment of errors incurred by truncation, i.e., higher-order errors resulting from the use of central difference estimators for velocity gradients, and first-order trajectory estimates. Thus, the error correction is only applicable to correcting for random and bias error components of the velocity and pressure gradient field at a given set of measurement points. It cannot correct for bias errors incurred by truncation due to data resolution (McClure and Yarusevych 2017a). The procedure for the error correction involves the solution of equation 5.14 using a finite-difference scheme with a five-point stencil for the pressure gradient error field. The source terms for the Poisson equation, $\mathbf{J}$ and f, are furnished by the curl and divergence of the pressure gradient error field computed from equations 5.15 and 5.20, respectively. The boundary conditions are furnished by the source terms, as well as error estimates for the pressure gradient field determined using knowledge of the erroneous and true velocity fields for validation purposes, and then using the erroneous and filtered erroneous velocity fields for practical demonstration.

5.3 Test Case

In order to validate the methodologies derived within the current study, a two-dimensional, two-component (2D-2C) synthetic PIV test data set is generated by sampling from the direct numerical simulation (DNS) of flow around a circular cylinder for $\mathrm{Re_D} = 100$ (McClure

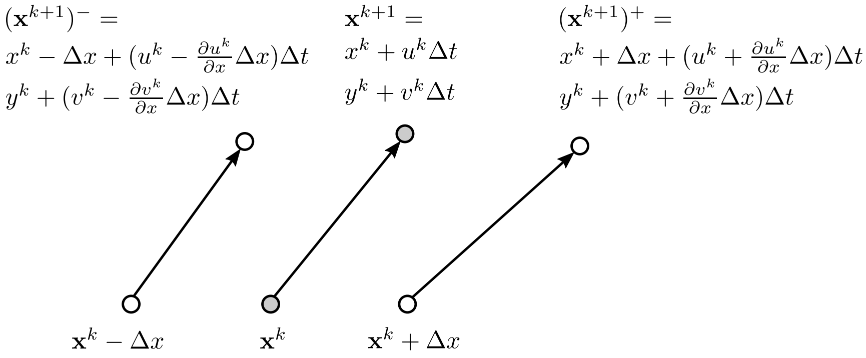

Figure 5.2: Divergence of trajectories from pseudo-tracking due to spatial variation in trajectory starting position.

and Yarusevych 2017b). The data are obtained by sampling 545 velocity fields through time from the DNS solution on an equispaced Cartesian grid on the domain $0.5D < x < 4D$ and $-4D < y < 4D$ at a temporal resolution of $f_{acq}/f_S = 54.9$ and a spatial resolution of $\delta x/D = 0.02$. To mimic experimental error associated with PIV algorithms, a synthetic error distribution is added to the sampled velocity fields from DNS. The standard deviation (σ_i) of the random error is specified by a two-parameter model, shown in equation 5.21. The first parameter in equation 5.21, α (%), represents an error component proportional to the magnitude of the normalized velocity gradient tensor, reaching a maximum percentage of the peak velocity (αu_{peak}) in the domain. The second parameter, β (px), adds a uniform displacement error for an interrogation window of dimensions $WS \times WS \times WS$ over a time separation of δt for a given scale factor SF (mm/px). For the present study, a 16 × 16 px interrogation windows or 16 × 16 × 16 px interrogation volumes are assumed, which corresponds to $SF = WS/16$.

$$\sigma_i = \alpha u_{peak} || \frac{\partial u_i}{\partial x_j} || / || \frac{\partial u_i}{\partial x_j} ||_{peak} + SF \frac{\beta}{\delta t} \tag{5.21}$$

In addition, the errors are generated to be correlated locally in space by constructing a correlation matrix with a triangle function $\zeta_{ij} = (1 - |r_{ij}|/(0.75WS))$ when $|r_{ij}| < 0.75WS$ and zero otherwise, to mimic the correlation of random errors when 75% window overlap is utilized in PIV processing (Sciacchitano and Wieneke 2016), giving a sampled vector pitch of $\delta x = WS/4$. The covariance of the velocity error, $S_{ij} = \sigma_i \zeta_{ij} \sigma_j$, is factored using the Cholesky decomposition, $S_{ij} = L_{ij} L_{ji}$ (Azijli and Dwight 2015) and independent velocity error field realizations are generated by constructing λ_j, a vector of samples from a Gaussian distribution with a standard deviation of 1 and a mean of 0 and computing $(\boldsymbol{\epsilon}_u)_i = L_{ij} \lambda_j$.

Figure 5.3 depicts the composition of a single instantaneous streamwise velocity field for the 2D-2C data set at $\mathrm{Re_D} = 100$. Figure 5.3a shows the exact data directly sampled from DNS, figure 5.3b shows the added synthetic error, and figure 5.3c shows the resulting erroneous instantaneous streamwise velocity field. The added error field is more intense in the wake region, where velocity gradients are higher, leading to increased PIV velocity error. The standard deviation of the velocity error (figure 5.3d) is just under 1% in the free-stream, irrotational flow area, and reaches a maximum of nearly 4% of the free-stream velocity in the wake region. The spatial autocorrelation of the errors is shown to reproduce the triangle function relationship (figure 5.3e), associated with the localized correlation caused by an interrogation window overlap of 75% (Sciacchitano and Wieneke 2016).

To complement the 2D-2C test case, a 3D-3C test case of flow around a circular cylinder at $\mathrm{Re_D} = 1575$ from DNS (McClure and Yarusevych 2017b) is utilized for demonstrating the practical implementation of the methodology to the three-dimensional flow encountered in this turbulent vortex shedding regime (Williamson 1996c). The data is obtained by sampling 85 fields through time on a three-dimensional equispaced Cartesian grid on the domain $0.5D < x < 4D$, $-2D < y < 2D$, and $-1D < z < 1D$ at a temporal resolution of $f_{acq}/f_S = 115.3$ and a spatial resolution of $\delta x/D = 0.05$. The same procedure for

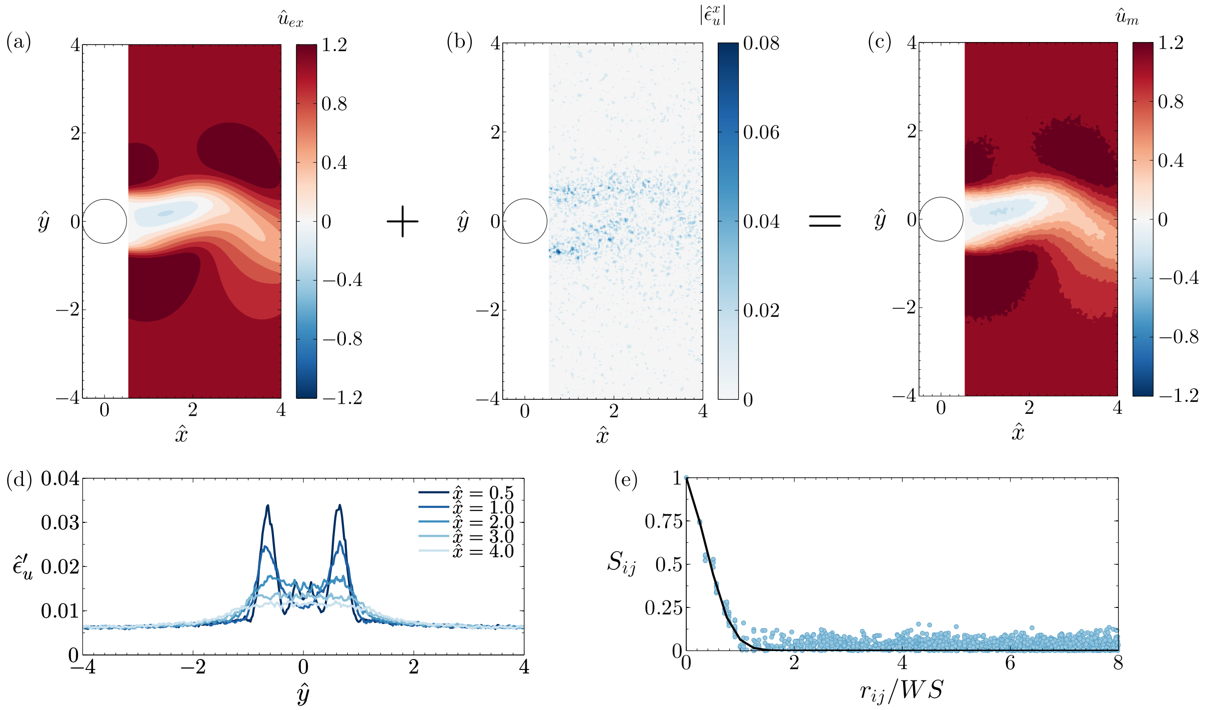

Figure 5.3: 2D-2C test case. (a) The exact streamwise velocity field sampled directly from DNS, (b) the synthetic velocity error added, and (c) the resulting erroneous streamwise velocity field. Statistics of the synthetic velocity error: (d) distribution of the standard deviation of the error, and (e) the spatial autocorrelation of the error from the domain centre.

generating synthetic error is utilized, modelling an interrogation window overlap of 50%, for this case. Figure 5.4 plots iso-surfaces of instantaneous vorticity for the 3D-3C data set at $\mathrm{Re_D} = 1575$. Both the exact (figure 5.4a) and erroneous (figure 5.3b) fields show the alternate shedding of vortices in the wake, with small scale three-dimensional deformations and secondary vortices. For the 3D-3C data set, the standard deviation of the velocity errors (figure 5.4c) indicates the free-stream error reaches approximately 2% the free-stream velocity, and reaches approximately 7% the free-stream velocity in the wake region. The spatial autocorrelation of the error (figure 5.4d) levels off after half an interrogation window size, modelling the 50% window overlap in PIV processing.

For presentation of the data, normalized variables are denoted with a hat $\hat{(.)}$, including: $\hat{u} = u/U_\infty$, $\hat{x} = x/D$, $\hat{y} = y/D$, $\hat{\omega} = \omega D/U_\infty$, $\hat{p} = 2p/\rho U_\infty^2$, and $\boldsymbol{\nabla}\hat{p} = 2\boldsymbol{\nabla} pD/\rho U_\infty^2$. The error metrics used are the L2-norm integral measure of error over the entire domain. For example, for a pressure estimation it is given as:

$$||\epsilon_{p_m}|| = \sqrt{\sum^{N} \frac{(p_m - p_{ex})^2}{N}} \tag{5.22}$$

where the subscript “m" denotes the estimated field, subscript “ex" denotes the exact field,

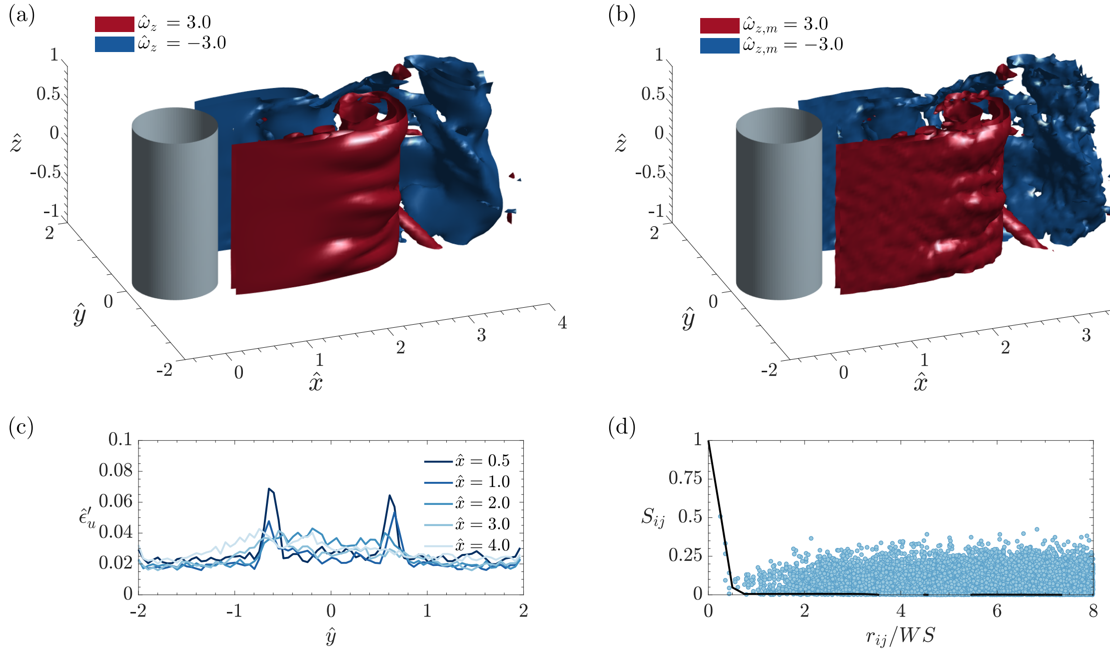

Figure 5.4: 3D-3C test case. (a) Iso-surfaces of the exact vorticity field sampled directly from DNS, (b) iso-surfaces of the resulting erroneous vorticity field after the addition of synthetic error. Statistics of the synthetic velocity error: (c) distribution of the standard deviation of the error, and (d) the spatial autocorrelation of the error from the domain centre.

and N denotes the number of discrete points in the domain. Alternatively, to express the spatial distribution of errors, ϵ'_{p_m} denotes the RMS error of the pressure estimation evaluated over the entire time sample. The error metrics are subsequently normalized according to: $\hat{\epsilon}_p = 2\epsilon_p D/\rho U_\infty^2$.

5.4 Results

5.4.1 Verification of solver

First, the capability of the solver for the system of equations in equation 5.14 is evaluated using the exact and erroneous 2D-2C PIV data set in the cylinder wake at $\mathrm{Re}_\mathrm{D} = 100$ (figure 5.3. For verification purposes, the source and boundary terms in equation 5.8 are computed using knowledge of both the exact and erroneous fields, with an Eulerian second-order central difference scheme, and hence are computed without approximation up to the limitations of the numerical implementation. In following sections, practical methods to close the system of equations in experiment utilizing the Lagrangian pseudo-tracking formulation will be discussed.

Figure 5.5 shows the exact pressure field (figure 5.5a), alongside the raw estimate (figure 5.5b) obtained from the erroneous set, and the estimate obtained after solving equation 5.8 (figure 5.5c) to correct the pressure gradient field before input into the Poisson solver for pressure. The distributions of the RMS of the pressure errors for the erroneous data set (red profiles, figure 5.5d) and the corrected fields (blue profiles, figure 5.5d) can be compared, and show a reduction in the error over 90% when the system of equations in equation 5.14 is solved to correct the pressure gradient estimates. The raw data exhibits the expected increased sensitivity to error on the boundaries, shown by elevated error level for the $\hat{x} = 0.5$ and $\hat{x} = 4.0$ profiles (Pan *et al.* 2016), where Neumann boundary conditions are employed, while the regions near the application of the Bernoulli equation at $\hat{y} = -4.0$ and $\hat{y} = 4.0$ show relatively low errors. In the corrected fields, the errors on the boundaries are significantly reduced, demonstrating that the current formulation is valid and more effective compared to the zero error assumption employed in previous studies (McClure and Yarusevych 2017a). The spatial autocorrelation of the pressure errors for the raw (red data points, figure 5.5e) and corrected (blue data points, figure 5.5e) fields show that the pressure estimation errors of the uncorrected, raw fields are correlated over the entirety of the domain, whereas the corrected fields only retain a local correlation, similar to the velocity field errors shown in figure 5.3. The global correlation behaviour is due to the error propagation from the errors in the pressure gradient applied at the Neumann boundaries, which lead to a global error over the domain for each time instant (Pan *et al.* 2016). Hence, when the pressure gradient errors are corrected on the boundaries and in the domain, this global correlation is eliminated completely.

In theory, equation 5.14 is exact, and ideally should be able to correct for errors completely, yielding 0% error in the reconstructed field. However, the practical implementation of the finite difference method introduces numerical limitations. To probe the numerical artefacts, deterministic, sinusoidal errors are introduced to the exact velocity fields of varying wavelength, and the integral error statistics are plotted in figure 5.6. As expected, when the wavelength of the error component is larger, more of the pressure gradient error field can be faithfully reconstructed. For $\Lambda/\delta x = 2$, i.e., point-to-point oscillations, the reconstruction performs better than slightly longer wavelength errors due to beneficial effects of the second-order central difference operators used to discretize the system of equations. On the whole, figure 5.6 indicates the limitations of the current numerical implementations, in which small wavelength error components may only be resolved up to 75%.

5.4.2 Lagrangian Pseudo-Tracking Formulation

The fidelity of the error correction formulation is tested using the 3D-3C data set with the approximations required for calculation of the divergence of the pressure gradient error using the Lagrangian pseudo-tracking formulation (equation 5.20). Similar to the previous analysis, the exact correction formulation, where the source terms and boundary terms in equation 5.14 are computed using knowledge of the exact and erroneous velocity fields and their derivatives, is considered along with an approximate correction formulation.

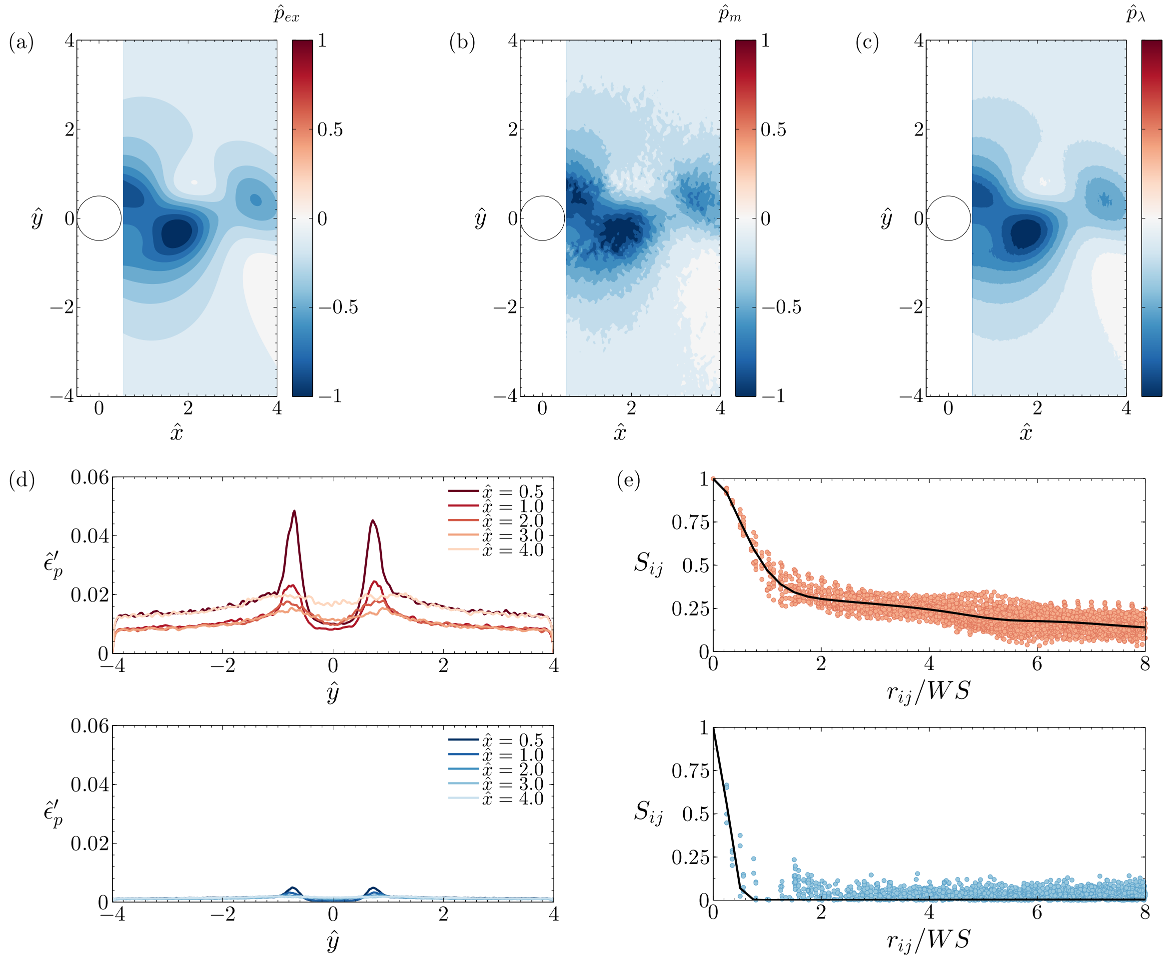

Figure 5.5: (a) Exact pressure field, (b) raw pressure estimate, and (c) corrected pressure estimate using the solution of equation 5.14. (d) The spatial autocorrelation of the pressure error from the centre of the domain, and (e) traverse profiles of the RMS of the pressure error for (red) the raw estimate and (blue) the corrected pressure estimate.

The approximate formulation neglects terms requiring knowledge of the exact velocity field and its derivatives in equation 5.20, and, for the boundary conditions, filters the velocity fields in time using a 6th order butterworth low-pass filter with a cut-off frequency of $6f_S$. This simple filter is employed for the sole purpose of obtaining estimates for the error distributions on the boundaries required to solve equation 5.14. The pressure gradient estimate based on the filtered field is subtracted from the raw estimate in order to obtain an approximation for the pressure gradient error on the boundaries for the two boundary-tangential directions, which are prescribed as Dirichlet conditions in the Poisson solver for the appropriate pressure gradient error component. A Neumann condition for the boundary-normal component of the pressure gradient error is then determined by the appropriate derivatives of these tangential error components and the divergence of the pressure gradient error field (equation 5.14, on Γ_i).

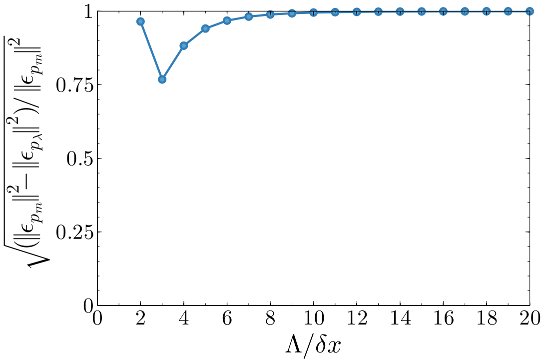

Figure 5.6: Fraction of the pressure gradient error field that is reconstructed versus the spatial wavelength of the error field (Λ) component, normalized by the vector pitch (δx).

Figure 5.7 plots isosurfaces of the pressure field estimates at $\hat{p} = -0.4$ (light blue isosurface, figure 5.7) and $\hat{p} = -0.9$ (dark blue isosurface, figure 5.7). figure 5.7a is the estimate from the exact velocity field data sampled from DNS, figure 5.7b is the raw estimate from the erroneous velocity data set, figure 5.7c is the corrected estimate using exact data in the formulation, and figure 5.7d is the corrected estimate using approximate boundary and source terms. A significant propagation of error into the raw pressure estimate on the erroneous data set is observed, and temporal continuity of the pressure estimate is poor, especially near the Neumann boundary conditions. In both the corrected pressure estimates using exact data and approximate data, there is a high degree of spatial correspondence with the field obtained using exact data (figure 5.7a), besides the minor low wavelength error components remaining due to the limitations of the numerical methodology (figure 5.6).

Figure 5.8 shows both the spatial autocorrelation and distribution of the RMS of the pressure estimation errors for the raw erroneous estimates (figure 5.8a and b), corrected estimates using exact data (figure 5.8c and d), and corrected estimates using approximate data (figure 5.8e and f). The RMS of the pressure errors reaches characteristic values of 15% of the dynamic pressure for the raw erroneous estimates (figure 5.8b), and the high spatial autocorrelation of the errors (figure 5.8a) over the entire domain indicates that a large proportion of the error is propagating from errors on the boundary conditions. This behaviour of the pressure errors leads to deteriorating temporal continuity of the pressure estimates. For the corrected pressure estimates using the exact formulation (figure 5.8c and d), the RMS of the pressure errors shows similar reductions of approximately 90% as the verification study on the previously discussed 2D-2C data set (figure 5.5), and the spatial autocorrelation of the errors drops off quickly (figure 5.8c), although it does not level off at zero due to the use of a limited sampling of 85 fields in time for computation of the statistics. For the corrected fields using the approximate formulation (figure 5.8e and f), the RMS of the pressure errors is characteristically approximately half that of the raw erroneous estimates, and the high spatial correlation of the errors over the domain indicates that these errors predominantly propagate from the boundary conditions. This indicates

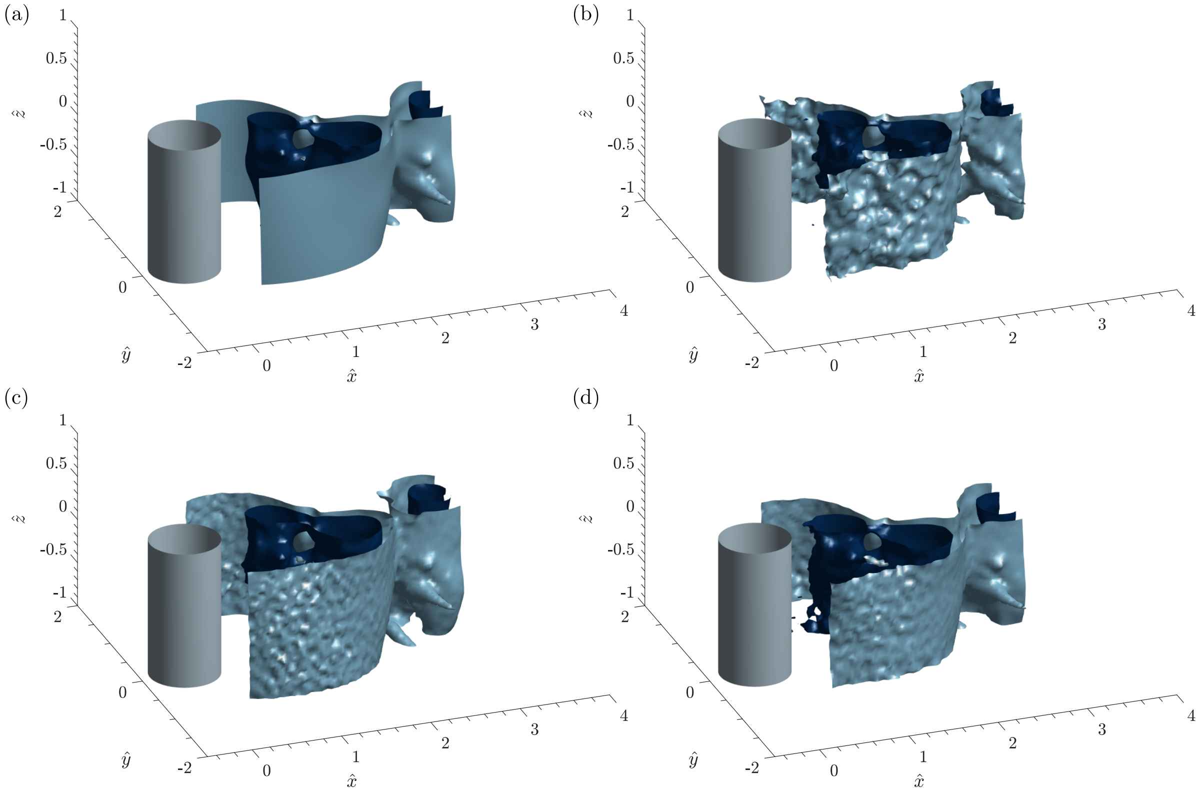

Figure 5.7: Comparison of pressure field estimates using Lagrangian pseudo-tracking for $M = 1$: (a) exact, (b) erroneous, (c) corrected with exact formulation, and (d) corrected with approximate formulation.

that the filtering of the velocity fields for use in approximating the boundary conditions for the system of equations used to correct the pressure gradient field is introducing the dominant remaining error. It is possible to improve the accuracy of the corrected pressure field estimates using an optimized filter design, or an alternate technique for obtaining a more accurate estimate of the pressure gradient error on the boundaries.

Figure 5.9 shows the effect of varying the cut-off frequency (f_c) of the 6th order butterworth filter, which was applied forward and backward in time to yield a zero-phase filter. The filtered data was used exclusively on the boundaries to give the required error estimates, e.g., $\epsilon_{\boldsymbol{\nabla} p} = \boldsymbol{\nabla} p_m - \boldsymbol{\nabla} p_m^{filt}$, and close the approximate method. The time-averaged integral pressure error is shown to vary with the cut-off frequency. Specifically, the error levels of the approximate method begin to increase sharply when the cut-off frequency is decreased towards the lower range of frequencies associated with real velocity fluctuations present in the flow, i.e., partially filtering out real flow events. On the other hand, as the cut-off frequency increases to its maximum near the Nyquist frequency (f_N), the results approach those obtained with the assumption of zero error boundary conditions, e.g., $\epsilon_{\boldsymbol{\nabla} p} = 0$. Here, only a minor correction of errors over the domain is attained, since

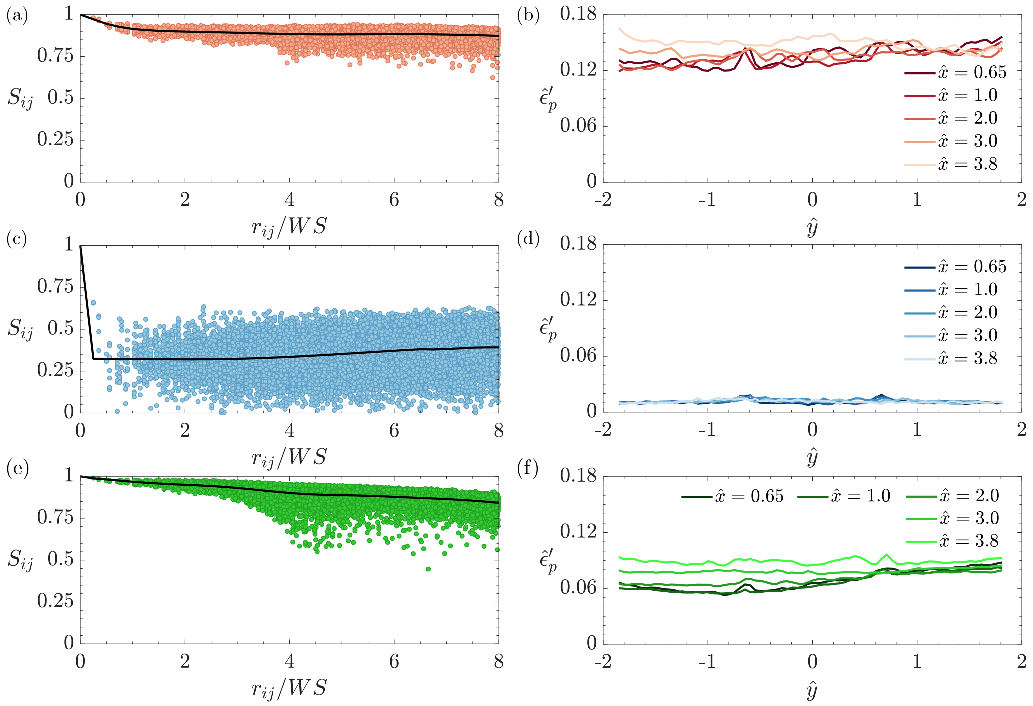

Figure 5.8: Spatial autocorrelation of the pressure error from the centre of the domain for (a) raw erroneous estimate, (c) corrected estimate using exact formulation, and (e) corrected estimate using approximate formulation. Transverse profiles of the RMS of the pressure error for (b) raw erroneous estimate, (d) corrected estimate using exact formulation, and (f) corrected estimate using approximate formulation.

errors in the pressure field propagating from the Neumann boundary conditions dominate in this specific flow case. However, between these two extremes, there is an intermediate range of cut-off frequencies where the filter is most effective for estimating errors on the boundaries. Hence, for use in an experimental setting, it is required to judicially choose the cut-off frequency of the filter used for approximating boundary errors, ensuring the filter does not attenuate frequencies associated with the real flow dynamics. The correction scheme will also perform best when the Bernoulli equation can be employed on the boundaries for a Dirichlet-type boundary condition. The Dirichlet conditions are less sensitive to random errors (Pan *et al.* 2016, McClure and Yarusevych 2017a), so that the correction methodology will be less dependent on estimates of boundary errors.

In order to evaluate the practical effectiveness of the correction scheme in experiment, where systematic errors may lead to different behaviour compared to the performance shown so far using synthetic random errors, a common PIV/PTV calibration bias error is considered by scaling the entire velocity and coordinate fields by a constant factor A, such that $\mathbf{u_{bias}} = A\mathbf{u_m}$ and $\mathbf{x_{bias}} = A\mathbf{x}$. Figure 5.10 shows the average RMS error of the pressure estimations over the domain using the raw erroneous velocity fields, compared to the pressure estimations using the correction procedure subjected to the scaling parameter

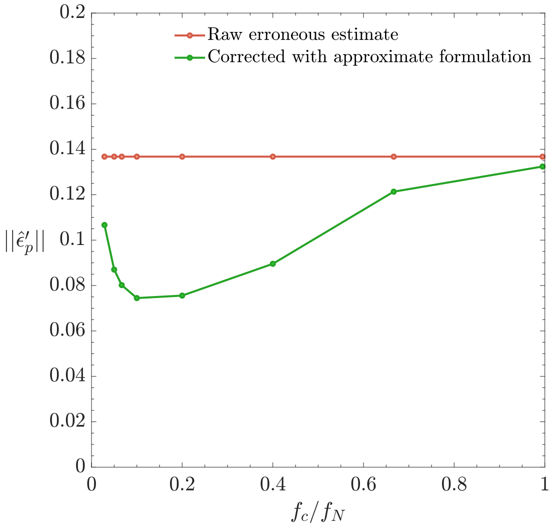

Figure 5.9: Dependence of the time-averaged integral pressure error of the corrected fields using the approximate formulation on the cut-off frequency for the filtered boundary data.

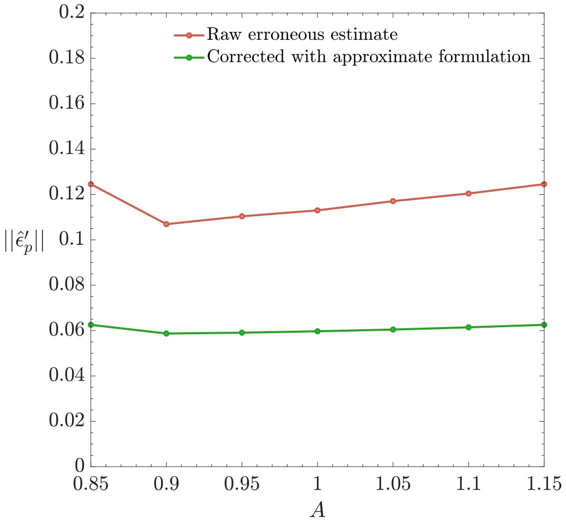

Figure 5.10: Dependence of the time-averaged integral pressure error of the corrected fields using the approximate formulation on bias due to scaling errors in calibration causing a uniform scaling of the velocity field by factor A.

A within $0.85 < A < 1.15$. The results show only minor sensitivity of the errors to the scaling parameter for the pseudo-tracking material acceleration estimates, particularly for the corrected estimates.

5.5 Conclusion

A methodology for correcting material acceleration estimates based on Lagrangian pseudo-tracking methods from PIV data is derived and tested on both 2D-2C and 3D-3C test cases of flow around a circular cylinder for $\mathrm{Re_D} = 100$ and 1575, respectively. The method leverages the governing equations to extract a div-curl system of equations for the error fields based on the deviations of the measured velocity field data from the divergence-free condition of the velocity field for incompressible flow, and the curl-free condition for the pressure gradient field. The mathematical formulation is shown to have the capability of specifying non-zero errors on the domain boundaries, a vital requirement for accurate pressure from PIV estimation. However, the error equations cannot be solved exactly due to unknown gradients of the error field and exact velocity field remaining in the formulation, and approximation must be applied. The results show that application of the correction with the current numerical implementations yields a reduction of errors in the pressure estimation by about 90% for a known error field. In practise, the use of a basic approximate formulation involving the neglection of terms associated with exact velocity and velocity gradients in the formulation for the divergence of the pressure gradient error field, and a temporal filtering of the boundary data in order to prescribe an estimate for a subset of the boundary errors, reduces pressure estimation errors by approximately 50% for the 3D-3C test case studied. The main cause for deviation of the corrected data using the approximate formulation from the ideal formulation, is propagation of errors on the boundaries shown by reduced temporal continuity in the pressure estimates and non-zero spatial auto-correlation of the errors over the entirety of the domain. This indicates that improved accuracy of the corrected estimates may be achieved through the development of optimized, physics based filters on the boundary data. Future studies should aim to validate the developed methodology in an experimental setting using volumetric velocity data and compare its effectiveness to other physics-based correction techniques.

Chapter 6

Planar momentum balance in three-dimensional flows: applications to load estimation

The acquisition of pressure field estimates from PIV measurements, explored in detail in Chapters 3-5, enables the capability to estimate loads on immersed structures with the integral form of the momentum equation. In particular, load estimation based on the momentum balance for a planar control volume is investigated, a configuration which is ubiquitous in experimental fluid mechanics. A formulation required for the exact momentum balance over the planar control volume is derived here, involving often neglected terms related to the three-dimensional momentum fluxes and viscous forces. The main result is the demonstration of the significance of area integrals involving out-of-plane velocity and velocity gradients, which are shown to be required for accurate estimation of instantaneous sectional loads and cause a sensitivity to experimental conditions for mean sectional load estimates. The findings highlight common issues responsible for inconsistent estimates of instantaneous and mean sectional loads for three-dimensional flows using control volume methods, and offer practical recipes for detecting and minimizing errors due to flow three-dimensionality.

This chapter is based on the journal article: McClure, J., and Yarusevych, S. (2019) "On the planar momentum balance in three-dimensional flow: applications to load estimation," *Experiments in Fluids*, 60(3), 41.

6.1 Introduction

The measurement of flow-induced loading is a fundamental component of aerodynamic testing, as the reliable estimation of structural loads is of primary interest for engineering design. There are three common approaches to measuring loads, namely, (i) full-body, direct measurements with a force balance, (ii) integration of surface stresses (i.e., pressure and/or wall shear stress), and (iii) analysis of field measurements, e.g., control volume (CV)-based methods (Unal *et al.* 1997, van Dam 1999, Rival and Oudheusden 2017). Each approach can offer an advantage in simplicity or accuracy depending on the experimental context, and each poses specific challenges and limitations. The present study is focused on load estimation from CV analysis, which is a minimally intrusive approach particularly useful in: flows over bodies undergoing complex motion (e.g., flow-induced vibration, bio-inspired propulsion), low-speed flows, microfluidics, and two-phase flows (e.g., loads on bubbles and droplets).

A variety of load estimation formulations are possible starting from classical CV analysis. For instantaneous loading estimates, time-resolved velocimetry is required in order to evaluate the unsteady terms within the CV. Analytically, the simplest method is the classical integral momentum balance, (Unal *et al.* 1997), where the pressure term is typically estimated from pressure fields obtained using measured velocity fields (van Oudheusden 2013). If near-wall velocity data are unavailable or significantly erroneous, and the flow is incompressible, the derivative-moment transform may be applied to the unsteady volume integral term to replace it by a contour integral (Wu *et al.* 2005); however, the resulting unsteady contour integral demands increased spatial resolution to maintain accuracy (Mohebbian and Rival 2012). These two formulations for instantaneous load estimation may be widely grouped as integral momentum equation approaches, and have been applied in numerous studies (Unal *et al.* 1997, van Oudheusden *et al.* 2006, Kurtulus *et al.* 2007, van Oudheusden *et al.* 2007, David *et al.* 2009, Spedding and Hedenström 2009, Kotsonis *et al.* 2011, Ragni *et al.* 2012, Gharali and Johnson 2014, Villegas and Diez 2014, Tronchin *et al.* 2015, Terra *et al.* 2017). Alternatively, loading estimates may be derived from the concept of hydrodynamic impulse (Lin and Rockwell 1996, Poelma *et al.* 2006), which eliminates the need for pressure field estimates at the expense of vorticity field estimates (Saffman and Schatzman 1982, Noca *et al.* 1999, Wu *et al.* 2006, DeVoria *et al.* 2014, Kriegseis and Rival 2014, Graham *et al.* 2017, Guissart *et al.* 2017, Rival and Oudheusden 2017, Limacher *et al.* 2018). Another alternative to the classical integral momentum balance and hydrodynamic impulse methods utilizes the concept of a drift volume to estimate unsteady loads for added mass dominated flows (Darwin 1953, Dabiri 2006, McPhaden and Rival 2018).

The present study focuses on the integral momentum equation methods for the evaluation of instantaneous loads; however, the integral momentum equation is also commonly utilized in a Reynolds averaged Navier-Stokes (RANS) form, in conjunction with wake traverse measurements, to estimate mean drag forces (Betz 1925, Jones 1936, van Dam 1999). In the RANS formulation, all necessary terms can, in principle, be measured on a contour surrounding the body using a combination of velocity and pressure measurements; however, it is more common and expedient to only perform a wake traverse at a single streamwise location downstream of the body, and appropriate free-stream assumptions are made on the upstream and side boundaries (van Dam 1999). To further simplify the measurements, the need for pressure measurements can be eliminated by replacing the mean pressure along the cross flow contour with an integration of the transverse Reynolds stress $\overline{v'^2}$. Such an approximation is only valid where the cross Reynolds stress $\overline{u'v'}$ has decayed to zero (Antonia and Rajagopalan 1990, van Dam 1999). A correction to mean drag estimates can also be employed based on the residual mass flux deficit over the CV, in order to increase accuracy (van Oudheusden *et al.* 2007, Ragni *et al.* 2009). Alternatively, the integral momentum equation can be formulated in terms of total and static pressure measurements, eliminating the need for direct velocity measurements (Betz 1925). The use of the wake-traverse method is common in aerodynamic testing, however, a high degree of scatter may be present dependent on the experimental set-up, flow configuration, and methodology employed (van Dam 1999, van Oudheusden *et al.* 2006, van Oudheusden *et al.* 2007, Neatby and Yarusevych 2012), and deviations from surface pressure and force balance measurements have been noted by multiple authors (Kurtulus *et al.* 2007, Zaman and Culley 2008, Neatby and Yarusevych 2012). A root-cause error analysis pointing towards the dominating source of error is not explored directly in the literature and uncertainty analysis is complicated by the large number of simplifying assumptions employed in varying formulations (Takahashi 1997, Méheut and Bailly 2008, Zaman and Culley 2008, Bohl and Koochesfahani 2009), resulting in varying methodological suggestions and corrective measures in the literature (van Dam 1999, Neatby and Yarusevych 2012).

Despite the wide-spread use of CV-based methods for load estimation, concrete experimental methodology guidelines remain largely unresolved. As a consequence, while some authors report consistent measurement accuracy from wake-traverse measurements (Antonia and Rajagopalan 1990, Spedding and Hedenström 2009), the source of bias and random errors in load estimates is not always completely clear (van Dam 1999, Kurtulus *et al.* 2007, van Oudheusden *et al.* 2007, Zaman and Culley 2008, Bohl and Koochesfahani 2009). In contrast, verification studies for CV-based instantaneous and mean load estimations from *two-dimensional* direct numerical simulations (DNS) give close agreement with solver values (Noca *et al.* 1999, David *et al.* 2009, Mohebbian and Rival 2012), and experimental studies utilizing a three-dimensional control volume to capture the entirety of the wake deficit report good accuracy (Méheut and Bailly 2008, Terra *et al.* 2017). In the present study, a general CV formulation for three-dimensional flows is considered and the effect of flow three-dimensionality is investigated. The exact formulation for sectional load estimation on a planar CV is derived, and the dependency of the associated instantaneous and mean load estimates on flow three-dimensionality is deduced for a synthetic PIV data set sampled from DNS data and a matching PIV experiment for cross-flow over a circular cylinder.

6.2 Mathematical Development

6.2.1 Conservation of linear momentum

The conservation of linear momentum over $V \subset \mathbb{R}^3$ for a stationary, non-deforming control volume in a single-phase flow with velocity $\boldsymbol{u}(\boldsymbol{x},t) = (u(\boldsymbol{x},t), v(\boldsymbol{x},t), w(\boldsymbol{x},t))$, density $\rho(\boldsymbol{x},t)$ and pressure $p(\boldsymbol{x},t)$ fields is:

$$\sum \boldsymbol{F}_{CV} = \frac{d}{dt}\left(\int_V \rho \boldsymbol{u} dV\right) + \int_{\partial V} \rho \boldsymbol{u}(\boldsymbol{u} \cdot d\boldsymbol{A}) \tag{6.1}$$

where V denotes the fluid volume and ∂V denotes the boundaries of V. For the case of a single stationary body inside the control volume, the force vector $\boldsymbol{F} = (F_x(t), F_y(t), F_z(t))$ acting on the body is:

$$\boldsymbol{F} = -\frac{d}{dt}\left(\int_V \rho \boldsymbol{u} dV\right) - \int_S \rho \boldsymbol{u}(\boldsymbol{u} \cdot \boldsymbol{n}) dS - \int_S p \boldsymbol{n} dS + \int_S (\tau \cdot \boldsymbol{n}) dS + \int_V \rho \boldsymbol{f} dV \tag{6.2}$$

where $\boldsymbol{f}$ denotes an arbitrary body force, τ denotes the viscous stress tensor field, and S denotes the outer boundary of the doubly-connected domain, V.

6.2.2 Conservation of linear momentum for a planar CV

Consider the momentum balance over a two-dimensional Euclidean plane $S_1 \subset \mathbb{R}^3$. To formulate the appropriate conservation law over S_1, when the velocity field remains evolving in three-dimensional space, consider a thin three-dimensional CV formed by extruding S_1 in the $+z$ direction by a length δz (figure 6.1a). Applying equation 6.2 to this CV yields:

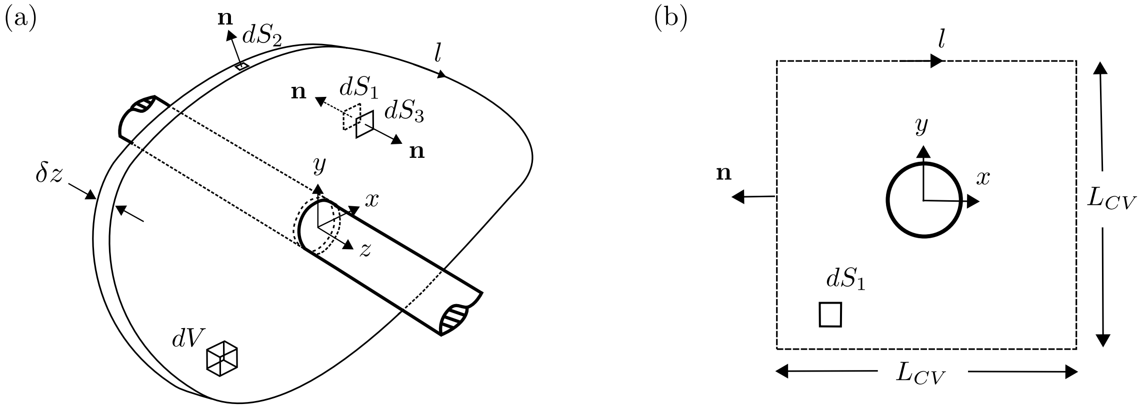

Figure 6.1: (a) Thin, three-dimensional control volume and (b) planar control volume.

$$\begin{aligned}\boldsymbol{F_S}\delta z = -\frac{d}{dt}\left(\int_{S_1} \rho\boldsymbol{u}dS\right)\delta z - \left(\int_l \rho\boldsymbol{u}(\boldsymbol{u}\cdot\boldsymbol{n})dl\right)\delta z + \int_{S_1}(\rho\boldsymbol{u}w)\,dS \\ - \int_{S_3}(\rho\boldsymbol{u}w)\,dS - \left(\int_l p\boldsymbol{n}dl\right)\delta z + \left(\int_l(\tau\cdot\boldsymbol{n})dl\right)\delta z - \int_{S_1}(\tau_{zi})dS \\ + \int_{S_3}(\tau_{zi})dS + \left(\int_{S_1}\rho\boldsymbol{f}dS\right)\delta z \end{aligned} \tag{6.3}$$

where the outer surface is partitioned as $S = S_1 \cup S_2 \cup S_3$ (figure 6.1a) and $S_1 \subset \mathbb{R}^2$ is bounded by the closed contour l. In moving to equation 6.3, attention is restricted to only the x, y components of the momentum balance, such that the planar sectional force vector is defined as $\boldsymbol{F_S} = (F_x(t)/\delta z, F_y(t)/\delta z)$. The integrals over S_3, related to flow three-dimensionality, can be expressed as integrals over S_1 through a first order Taylor series expansion of the integrand variables over $+\delta z$, leading to:

$$\begin{aligned}\boldsymbol{F_S}\delta z = -\frac{d}{dt}\left(\int_{S_1} \rho\boldsymbol{u}dS\right)\delta z - \left(\int_l \rho\boldsymbol{u}(\boldsymbol{u}\cdot\boldsymbol{n})dl\right)\delta z - \left(\int_{S_1}\frac{\partial}{\partial z}(\rho\boldsymbol{u}w)\,dS\right)\delta z \\ - \left(\int_l p\boldsymbol{n}dl\right)\delta z + \left(\int_l(\tau\cdot\boldsymbol{n})dl\right)\delta z + \left(\int_{S_1}\frac{\partial}{\partial z}(\tau_{zi})dS\right)\delta z + \left(\int_{S_1}\rho\boldsymbol{f}dS\right)\delta z + O(\delta z^2)\end{aligned} \tag{6.4}$$

Dividing both sides by δz and taking the limit as $\delta z \to 0$ yields the following:

$$\begin{aligned}\boldsymbol{F_S} = -\frac{d}{dt}\left(\int_{S_1} \rho\boldsymbol{u}dS\right) - \int_l \rho\boldsymbol{u}(\boldsymbol{u}\cdot\boldsymbol{n})dl - \int_{S_1}\frac{\partial}{\partial z}(\rho\boldsymbol{u}w)\,dS \\ - \int_l p\boldsymbol{n}dl + \left(\int_l(\tau\cdot\boldsymbol{n})dl\right) + \int_{S_1}\frac{\partial}{\partial z}(\tau_{zi})dS + \int_{S_1}\rho\boldsymbol{f}dS\end{aligned} \tag{6.5}$$

Hence, the momentum balance on a plane (S_1 in this case) does not map simply onto the momentum balance for the projected two-dimensional flow, and area integrals of the terms $\frac{\partial}{\partial z}(\rho\boldsymbol{u}w)$ and $\frac{\partial}{\partial z}(\tau_{zi})$ are necessary for momentum conservation. Practically, this implies that volumetric measurements surrounding an immersed body are required for sectional load estimation, which may not be feasible in practice. To increase load estimation accuracy for planar, two-component measurement configurations in incompressible flow, the three-dimensional terms can be expanded and made partially tractable with planar measurements through the application of the divergence-free constraint on the velocity field $\frac{\partial w}{\partial z} = -\frac{\partial u}{\partial x} - \frac{\partial v}{\partial y} = -\boldsymbol{\nabla}_{xy}\cdot\boldsymbol{u}$:

$$\frac{\partial}{\partial z}(\rho\boldsymbol{u}w) = \rho w\frac{\partial\boldsymbol{u}}{\partial z} + \rho\boldsymbol{u}\frac{\partial w}{\partial z} = \rho w\frac{\partial\boldsymbol{u}}{\partial z} - \rho\boldsymbol{u}\left(\boldsymbol{\nabla}_{xy}\cdot\boldsymbol{u}\right) \tag{6.6}$$

$$\frac{\partial}{\partial z}\tau_{zi} = \mu\frac{\partial^2 \boldsymbol{u}}{\partial z^2} + \mu\boldsymbol{\nabla}\left(\frac{\partial w}{\partial z}\right) = \mu\frac{\partial^2 \boldsymbol{u}}{\partial z^2} - \mu\boldsymbol{\nabla}\left(\boldsymbol{\nabla}_{xy}\cdot\boldsymbol{u}\right) \tag{6.7}$$

To benchmark the accuracy of different possible measurement methodologies, the following three formulations, with the body force term neglected, are compared in the present study and evaluated on the control volume depicted in figure 6.1b.

$$\begin{aligned}\boldsymbol{F_S} = &-\frac{d}{dt}\left(\int_{S_1}\rho\boldsymbol{u}dS\right) - \int_l \rho\boldsymbol{u}(\boldsymbol{u}\cdot\boldsymbol{n})dl - \int_{S_1}\left(\rho w\frac{\partial\boldsymbol{u}}{\partial z} + \rho\boldsymbol{u}\frac{\partial w}{\partial z}\right)dS \\ &-\int_l p\boldsymbol{n}dl + \left(\int_l(\tau\cdot\boldsymbol{n})dl\right) + \int_{S_1}\mu\left(\frac{\partial^2\boldsymbol{u}}{\partial z^2} + \mu\boldsymbol{\nabla}\left(\frac{\partial w}{\partial z}\right)\right)dS\end{aligned} \tag{6.8}$$

$$\begin{aligned}\boldsymbol{F_S} = &-\frac{d}{dt}\left(\int_{S_1}\rho\boldsymbol{u}dS\right) - \int_l \rho\boldsymbol{u}(\boldsymbol{u}\cdot\boldsymbol{n})dl + \int_{S_1}\rho\boldsymbol{u}\left(\boldsymbol{\nabla}_{xy}\cdot\boldsymbol{u}\right)dS \\ &-\int_l p\boldsymbol{n}dl + \left(\int_l(\tau\cdot\boldsymbol{n})dl\right) - \int_{S_1}\mu\boldsymbol{\nabla}\left(\boldsymbol{\nabla}_{xy}\cdot\boldsymbol{u}\right)dS\end{aligned} \tag{6.9}$$

$$\boldsymbol{F_S} = -\frac{d}{dt}\left(\int_{S_1}\rho\boldsymbol{u}dS\right) - \int_l \rho\boldsymbol{u}(\boldsymbol{u}\cdot\boldsymbol{n})dl - \int_l p\boldsymbol{n}dl + \left(\int_l(\tau\cdot\boldsymbol{n})dl\right) \tag{6.10}$$

Equations 6.8 and 6.9 are referred to as the exact and approximate formulations, respectively, and represent volumetric measurement and planar measurement in incompressible flow. The viscous terms are often neglected in practise, however, they may have a non-negligible contribution to the instantaneous loading estimates to merit inclusion. The approximation involved in equation 6.9 is the omission of the three-dimensional momentum flux and viscous stresses associated with the terms containing $w\partial\boldsymbol{u}/\partial z$ and $\partial^2\boldsymbol{u}/\partial z^2$ in equation 6.8, respectively. Equation 6.10 is representative of the classical planar CV formulation. It is often cast in the Reynolds averaged form to estimate mean drag from wake traverses, where the pressure term can be expressed in terms of fluctuating velocity components (Antonia and Rajagopalan 1990, Takahashi 1997, van Dam 1999). However, in the present study, both instantaneous and mean loading are considered.

6.3 Test Cases

The derived sectional force formulations were validated and compared for the load estimation on a circular cylinder in a turbulent vortex shedding regime. Two data-sets were

Nodes	$\frac{\Delta\theta}{\eta} \times \frac{\Delta r}{\eta} \times \frac{\Delta z}{\eta}$	$\frac{\Delta t}{\tau}$	$\frac{L_x}{D}$	$\frac{L_y}{D}$	$\frac{L_z}{D}$
2.9×10^7	$1.59 \times 0.71 \times 2.85$	0.17	24	35	3.1

Table 6.1: Computational domain and grid parameters.

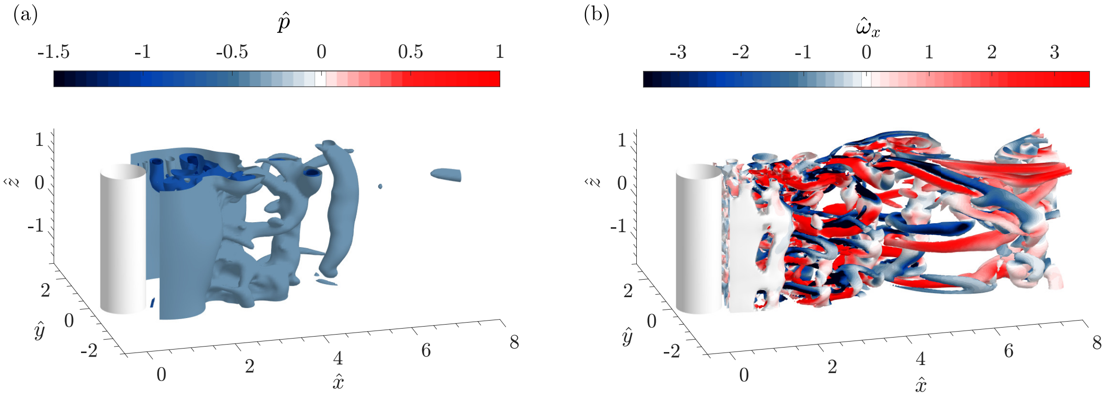

Figure 6.2: Three-dimensional DNS of a cylinder in cross-flow at $\mathrm{Re_D} = 1575$. Iso-surfaces of (a) pressure, and (b) $Q = 0.2$ s^{-1} coloured by streamwise vorticity.

employed, namely, three-dimensional DNS results at $\mathrm{Re_D} = 1575$, and experimental planar, two-component PIV data for $\mathrm{Re_D} = 1900$, where $\mathrm{Re_D} = U_0 D/\nu$.

For the DNS results, the computational mesh is a hybrid mesh configuration with a structured O-type section around the cylinder surface and a structured H-type mesh in the remaining regions, allowing for local grid refinement around the cylinder surface. The domain sizing and mesh spacing parameters around the cylinder surface are summarized in table 6.1, where L_x, L_y, and L_z are the streamwise, transverse and spanwise domain lengths, respectively. The mesh sizing was ensured to be below recommendations of Moin and Mahesh 1998 for finite volume solvers (ANSYS 14.0). The simulations were run until a periodic steady state was reached in the lift and drag fluctuation history, before results were sampled over a time length of 16 shedding cycles. More specific details of the DNS are included in McClure and Yarusevych 2017b. The three-dimensional wake topology is visualized in figure 6.2 by iso-surfaces of $Q = 0.2$ s^{-1}, coloured by streamwise vorticity and iso-surfaces of pressure. The data were sampled in two ways to facilitate the analysis. First, a fully three-dimensional, three-component data set (3D3C) was sampled, where both pressure and velocity fields were directly interpolated from the DNS solver results onto a three-dimensional Cartesian grid with spatial resolution $0.01D$ and temporal resolution of $f_{acq}/f_S = 217.4$, where D and f_S are the cylinder diameter and the vortex shedding frequency, respectively. Second, a noisy, two-dimensional, two-component planar data set (2D2C) was constructed, where the velocity data were interpolated onto a two-dimensional grid with spatial resolution $0.03D$ and temporal resolution of $f_{acq}/f_S = 15.4$, and synthetic

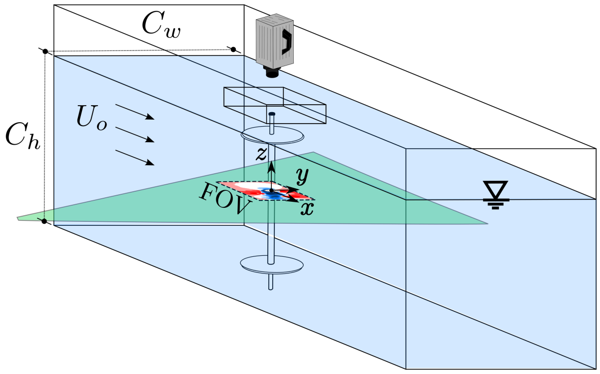

Figure 6.3: Experimental PIV configuration.

Parameters	Symbol	Value
Focal Ratio	$f\#$	$f/5.6$
Interrogation Window	WS	16×16 px $(0.12D \times 0.12D)$
Acquisition Frequency	f_{acq}	100 Hz
Field of View	FOV/D	3.8×3.8
Vector Pitch	dx/D	0.03
Overlap	OV	75%

Table 6.2: PIV acquisition parameters.

errors were added to the interpolated velocity fields according to the two parameter model presented in McClure and Yarusevych 2017a. The model prescribed error proportional to the local norm of the velocity gradient tensor, up to a maximum standard deviation of $0.25U_0$, along with flow independent error, with a standard deviation of $0.036U_0$, representative of PIV errors caused by high shear and correlation peak detection, respectively. The errors were correlated locally in space to model a PIV interrogation window overlap of 75% (Azijli and Dwight 2015). The corresponding pressure fields were then computed by inputting the noisy planar fields into a Poisson solver. Hence, the first data set forms the "ground-truth" test using exact velocity and pressure sampled from the DNS solution, while the second data set is representative of a planar, two-component PIV experiment with noisy velocity fields and pressure obtained through the Poisson equation solution corresponding to the noisy, planar velocity fields.

The experimental two-dimensional, two-component (2D2C) PIV measurements were obtained in the water flume facility at the University of Waterloo on a 1 inch diameter acrylic cylinder model at $\mathrm{Re_D} = 1900$ (figure 6.3). The acrylic model allowed penetration of laser light through the model, such that high quality particle images could be obtained near the body surface without shadowed regions and significant surface reflections. The

Data Set:	DNS	DNS+Noise	EXP
$\mathrm{Re_D}$	1575	1575	1900
$\Delta x/D$	0.01	0.03	0.03
f_{acq}/f_S	217.4	15.4	13.4
Number of Samples	645	645	5446
Shedding cycles	16	16	37
Field of View	$4D \times 4D$	$4D \times 4D$	$3.8D \times 3.8D$
Dimensionality	3D3C	2D2C	2D2C

Table 6.3: Data set parameters.

free surface was cut with an acrylic box above the mounting point of the cylinder in order to facilitate imaging from the camera mounted above the free-surface coaxial with the cylinder axis. The test section dimensions were 1.2 m wide (C_w), 2.4 m long (C_l) with a constant water level height of 0.8 m (C_h). The free-stream turbulence intensity was characterized to be less than 1% and mean flow non-uniformity less than 4% within the empty test section. The free-stream velocity was measured to be 74.4 mm s^{-1} (U_0) from the mean velocity obtained from the upstream PIV data acquired during the experiment. The cylindrical model was positioned between two acrylic circular endplates with diameter $14D$, and positioned $2D$ upstream of the end-plate centre, following the recommendations of Stansby 1974 and Fox and West 1990 to improve flow two-dimensionality surrounding the model. The aspect ratio of the model was $L/D = 16$. The PIV system comprised of a single high-speed, 1024 × 1024 px Photron SA4 camera equipped with a 50 mm Nikkor lens with the numerical aperture set to $f/5.6$ and a Photonics high repetition rate Nd:YLF laser. The flow was seeded with 10 μm diameter hollow glass spheres, with specific gravity of 1.05. The particle images were acquired in single-frame mode at $f_{acq} = 100$ Hz ($147 f_S$), and were processed in DaVis 8.2 using an iterative, multi-grid cross-correlation algorithm with window deformation. The final interrogation window size was 16 × 16 px, overlapped by 75%, and yielded a vector pitch of approximately $0.03D$. Details of the final acquisition and processing parameters are summarized in table 6.2. The PIV uncertainty was assessed using the particle disparity method (Sciacchitano *et al.* 2015) and mean instantaneous velocity uncertainties reached a maximum of $0.13U_0$, within 95% confidence, in the turbulent wake region. Direct lift and drag measurements were performed with a two-component force balance, with experimental uncertainty associated with mean drag and RMS lift measurements less than 5% (McClure and Yarusevych 2016b). A Poisson equation solver (equation 6.11) was employed to estimate instantaneous pressure from both the PIV and planar, noisy DNS velocity fields (e.g., Gurka *et al.* 1999).

$$\left.\begin{aligned}
\boldsymbol{\nabla}_{xy}^2 p = \boldsymbol{\nabla}_{xy} \cdot \left(-\rho \frac{D\boldsymbol{u}}{Dt} + \mu \boldsymbol{\nabla}_{xy}^2 \boldsymbol{u}\right) \quad &\text{in} \quad S_1, \\
\boldsymbol{\nabla}_{xy} p \cdot \boldsymbol{n} = \left(-\rho \frac{D\boldsymbol{u}}{Dt} + \mu \boldsymbol{\nabla}_{xy}^2 \boldsymbol{u}\right) \cdot \boldsymbol{n} \quad &\text{on} \quad \Gamma_i, \\
p = \frac{1}{2}\rho U_0^2 - \frac{1}{2}\rho \left(\overline{\boldsymbol{u}} \cdot \overline{\boldsymbol{u}} + \boldsymbol{u}' \cdot \boldsymbol{u}'\right) \quad &\text{on} \quad \Gamma_j,
\end{aligned}\right\} \qquad (6.11)$$

The pressure gradient was estimated from the Navier-Stokes equations using the velocity field and its derivatives with a central difference approximation. Neumann-type boundary conditions were prescribed at the outflow domain boundary and the cylinder surface based on the boundary-normal projection of the pressure gradient estimate. An extended form of Bernoulli's equation (de Kat and van Oudheusden 2012) was used on the inflow and top/bottom side boundaries, where the flow was approximately steady and irrotational. The relative spatial resolution of the PIV data was $13.6\lambda_x$, where λ_x is twice the shear layer thickness. For the calculation of temporal derivatives, the PIV data were downsampled to a relative temporal resolution of $f_{acq}/f_S = 13.4$. The relative resolutions were chosen to coincide with optimal ranges identified in McClure and Yarusevych 2017b which minimize the propagation of random and truncation error to the pressure solution. Furthermore, the sensitivity of the pressure estimates to a number of user chosen parameters was investigated to validate their consistency. The temporal resolution of the data was varied an order of magnitude above and below the selected $f_{acq}/f_S = 13.4$, resulting in amplification of the pressure RMS statistics, predominantly near the domain and cylinder wall boundaries, indicating more pronounced propagation of random and truncation error into the solution when sampled away from optimal values (McClure and Yarusevych 2017b). The circular boundary condition surrounding the cylinder wall was expanded over a range of diameters from $1D$ to $1.6D$, and the outer extents of the domain were truncated up to $2D$. It was found that varying the boundary locations in this manner resulted in nearly identical mean and RMS statistics in the solved regions. Temporal filtering of the velocity data using median filtering resulted in a minor reduction of erroneous pressure fluctuations near the inflow boundary and stagnation point, but was not employed for the sake of clarity, though a temporal filtering operation (Dabiri *et al.* 2014, Schiavazzi *et al.* 2017) is useful and recommended in noisier data sets. A summary of the sampling parameters for the three data sets employed in the present study is included in table 6.3. The data sets are denoted DNS, DNS+Noise and EXP for the 3D3C directly sampled DNS data, 2D2C down sampled DNS data with synthetic noise introduced, and 2D2C experimental PIV data, respectively.

Figures 6.4(a)-(c) present instantaneous snapshots of the vorticity and pressure fields during similar shedding phases obtained directly from three-dimensional DNS (figure 6.4a), obtained from the noisy planar DNS and the corresponding planar Poisson equation solution (figure 6.4b), and obtained from the experimental planar PIV data and its corresponding planar Poisson equation solution (figure 6.4c). Variables with a hat denote normalized

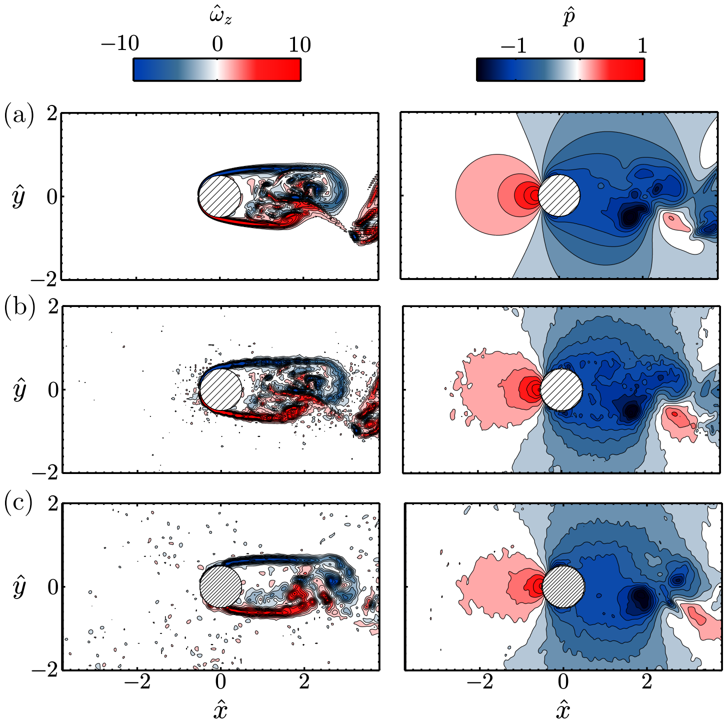

Figure 6.4: Instantaneous spanwise vorticity ($\hat{\omega}_z = \omega_z D/U_0$) and pressure fields ($\hat{p} = 2p/\rho U_0^2$) for (a) direct interpolation of the DNS solver pressure, (b) Poisson solution on the downsampled DNS velocity fields with synthetic noise, and (c) Poisson solution on the PIV velocity fields.

variables, namely, $\hat{\omega}_z = \omega_z D/U_0$, $\hat{p} = 2p/\rho U_0^2$, $\hat{t} = tf_s$, $\hat{x} = x/D$, and $\hat{y} = y/D$. Inspection of the instantaneous fields indicates that vortex formation occurs between $\hat{x} = 1.8 - 2.0$ for each case, and no distinct topological changes in the flow occur between the cases; hence, a close correspondence between the noisy DNS data set and experiment is expected. Figure 6.5 plots transverse profiles of the mean pressure, RMS pressure, and pressure-velocity correlations along the wake centreline. The pressure statistics show a good agreement between the three cases, indicating the minor $\mathrm{Re_D}$ difference does not have a significant effect on the comparison between the DNS and experimental results. The average RMS error (RMSE) of the DNS+Noise mean and RMS pressure statistics are $0.022C_p$ and $0.020C_p$, respectively, and the RMSE of the EXP mean and RMS pressure statistics are $0.044C_p$ and $0.021C_p$, respectively. Minor deviations of the estimated pressure fields from the direct DNS pressure are attributed to systematic errors in the planar Poisson solutions due to truncation errors and omitted three-dimensional terms (Baur and Köngeter 1999, Violato *et al.* 2011, Ghaemi *et al.* 2012, McClure and Yarusevych 2017b), with the most pronounced differences confined to regions of pronounced three-dimensional flow ($\hat{x} > 2$).

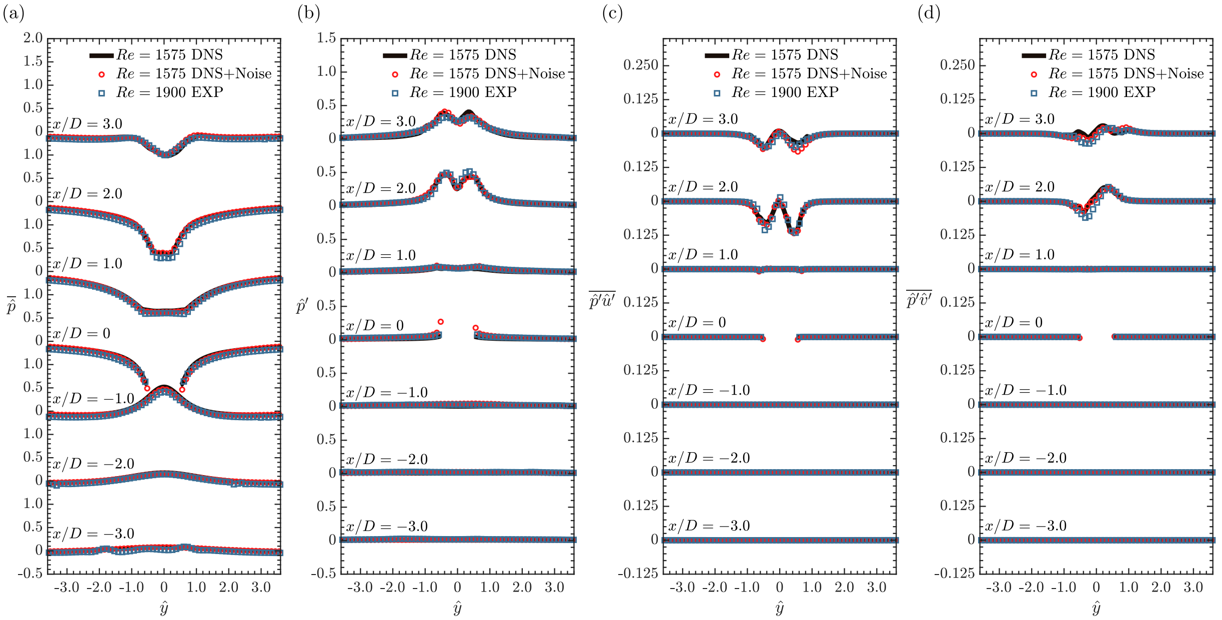

Figure 6.5: Comparison of pressure field statistics using transverse profiles at varying streamwise locations of (a) mean pressure, (b) pressure RMS, (c) pressure-streamwise velocity correlation, and (d) pressure-transverse velocity correlation.

6.4 Results

6.4.1 Instantaneous load estimation

A comparison of CV formulations given by equations 6.8-6.10 predicts the sensitivity of the approximate (equation 6.9) and classical (equation 6.10) control volume formulations to flow three-dimensionality. It may be conjectured from figure 6.4 that three-dimensionality becomes significant for $\hat{x} > 2$, with turbulent transition beginning in the separated shear layers a proceeding during the formation and shedding of turbulent von Kármán vortices downstream of the cylinder. To demonstrate the importance of three-dimensional effects, figure 6.6 presents the time history of the sectional drag and lift coefficients, obtained by applying the exact (equation 6.8), approximate (equation 6.9) and classical (equation 6.10) formulations to the direct DNS data set for two control volume sizes. The first CV (figure 6.6a, $L_{CV}/D = 1.34$) is representative of a situation where the CV includes only regions of predominantly two-dimensional flow, which is in contrast to the second CV (figure 6.6b, $L_{CV}/D = 4.0$) that includes regions of significant three-dimensional flow, where L_{CV} is a parameter defining the control volume size (figure 6.1b). The results demonstrate that the exact CV formulation derived here (equation 6.8) is the correct linear momentum conservation law for the planar control volume, with force estimates matching the surface integrated results from the DNS solver for both CVs. On the other hand, when three-dimensional flow regions are present within the CV, simplified formulations (equation 6.9 and 6.10) can lead to significant errors in instantaneous force estimates. Specifically, the

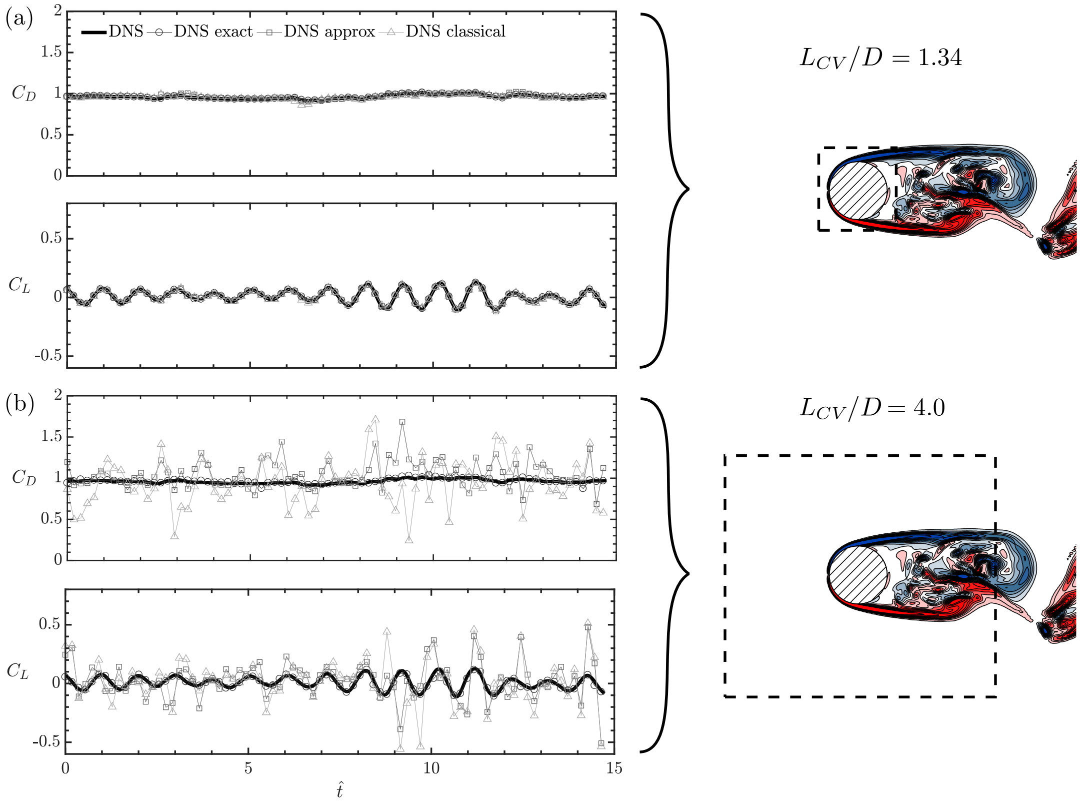

Figure 6.6: Time evolution of the control volume load estimates for sectional drag coefficient $C_D(t) = 2F_x(t)/\rho U_0^2 D$ and sectional lift coefficient $C_L(t) = 2F_y(t)/\rho U_0^2 D$, using equations 6.8, 6.9, and 6.10 on the exact DNS data, compared to surface integrated loads from the DNS solver (a) using a small CV of size $L_{CV}/D = 1.34$, and (b) using a larger CV of size $L_{CV}/D = 4.0$.

classical formulation (equation 6.10) yields instantaneous results for both the lift and drag with errors over $0.5C_D$ ($0.5C_L$) for the control volume bounding three-dimensional flow (figure 6.6b). The use of the approximate form (equation 6.9) appears to yield a minor overall improvement over the classical formulation; however, instantaneous deviations up to $0.5C_D$ ($0.5C_L$) remain. As expected, when the CV is constructed to bound minimal flow three-dimensionality (figure 6.6a), the approximate and classical formulations provide more reliable estimations.

6.4.2 Mean and RMS loading statistics

To more comprehensively characterize and quantify the accuracy of the CV formulations in the presence of three-dimensional flow and experimental errors, the CV size (L_{CV}) is systematically varied, and estimates obtained by applying the different formulations to instantaneous fields from the test data sets are compiled. Figures 6.7 and 6.8 present the mean drag and RMS lift statistics, respectively. The error bars are determined by

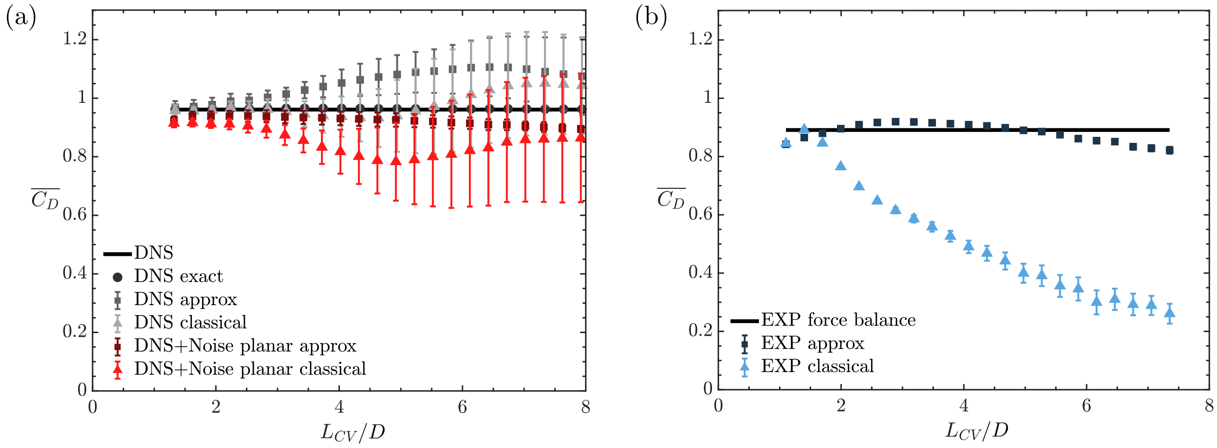

Figure 6.7: Mean drag forces evaluated using equations (6.8), (6.9), and (6.10) for variable control volume size (L_{CV}) for (a) direct DNS and noisy, planar DNS at $\mathrm{Re_D} = 1575$, and (b) PIV experiment at $\mathrm{Re_D} = 1900$.

estimators for the uncertainty of the mean and RMS, respectively, using an effective number of samples based on the integral time scale of the signals (Sciacchitano and Wieneke 2016). All estimates from DNS are compared to the surface integrated forces from the DNS solver, while all estimates from PIV data are compared to sectional forces derived from force balance measurements (McClure and Yarusevych 2016b).

Figure 6.7a plots estimates of mean drag for the three-dimensional and planar DNS data sets, while figure 6.7b plots mean drag estimates from the PIV data. In general, mean drag estimates using simplified formulations achieve their highest accuracy for small CV sizes, and the approximate formulation shows improved accuracy over the classical formulation for the experimental data (figure 6.7b), but not for the numerical data (figure 6.7a). In both the numerical and experimental data sets (figures 6.7a,b), the classical and approximate CV formulations exhibit a dependency on CV size, while the exact formulation is insensitive to CV size and exhibits universal agreement with the DNS solver drag (figure 6.7a). In the numerical case (figure 6.7a), the flow should be statistically two-dimensional, and the three-dimensional terms in equation 6.8 cancel when Reynolds averaged. However, the convergence of the second order statistics needed for the three-dimensional terms to cancel is slow, relative to the time sample of the DNS data used here and numerical results in general, and their instantaneous magnitude is substantial (figure 6.6). Hence, the mean drag estimates using the approximate and classical formulations deviate from the exact forcing but are within the uncertainty of the mean. Using approximate and classical formulations applied to the coarser resolution, planar, noisy DNS data causes under prediction of the mean drag, even for small CV sizes (figure 6.7a). This is ascribed to truncation error accumulation due to the lower spatial resolution employed, which can be observed in a minor, but systematic under prediction of the stagnation pressure in the Poisson solutions for pressure in figure 6.5a. A similar trend is seen for the experimental case (figure 6.7b); however, the disparity between the mean drag estimates becomes more pronounced with increasing CV size compared to the numerical case. Since the PIV experiment allowed sufficient independent samples to achieve statistical convergence of the estimates, the decreased accuracy of the classical formulation for the experimental case is instead attributed to a high sensitivity of the CV momentum flux terms to small misalignments in the PIV set-up or minor mean flow/model non-uniformities characteristic of experimental facilities, which is discussed in more depth in Section 4.3.

Figures 6.8a and 6.8b compare the results for the RMS lift statistics (C_L') for DNS and experimental data, respectively. Similar to the drag estimates, the results from the exact formulation based on three-dimensional DNS data match the direct force results. Furthermore, all formulations exhibit close agreement to the DNS solver RMS lift if the CV size is small (figure 6.8a), but the approximate and classical formulations yield erroneous growth of the RMS lift when L_{CV} becomes large enough to encompass three-dimensional flow regions. For each case, the RMS drag statistics show similar behaviour, as can be deduced from figure 6.6, while the mean lifts are zero within the convergence of the statistics and are omitted for brevity. In the cases of the planar DNS and PIV data, the propagation of random error from the velocity fields through the CV formulation is also significant, even for small CV sizes. The influence of the random error on the instantaneous force estimates motivates the use of zero-phase temporal low-pass filtering for each term in the formulation for the estimations from the PIV data set (figure 6.8b). Here, a low-pass, equiripple finite-impulse response filter with a pass band at $1.5f_S$ and a 60 dB stop band at $15f_S$ is employed, and the results in figure 6.8(b) show the improved accuracy that filtering provides for the estimate. The results demonstrate that, for the planar CV configuration, failure to account for flow three-dimensionality can result in significantly erroneous instantaneous loading estimates and care must be employed in selecting the CV boundaries, such that they bound minimal three-dimensional flow regions. To ensure this, the experimentalist should systematically vary the CV boundaries in a similar manner, and select a CV size in a converged region where loading estimates are insensitive to changes in CV size (e.g, $L_{CV}/D < 2.5$ in figure 6.8).

To elucidate on the trends observed in the mean drag and RMS lift statistics derived from CV formulations, figure 6.9 plots the relative magnitude of the individual terms appearing in the momentum balance (equation 6.8) for varying L_{CV} for the three-dimensional DNS data (figure 6.9a, b) and the PIV experiment (figure 6.9c, d). For the mean drag, the mean time derivative term, $\frac{d}{dt}(\int_{S_1} \rho u dS)$ and viscous terms are negligible. Instead, figures 6.9a and 6.9b show that the mean drag is primarily determined by the difference between the mean boundary momentum flux, $\int_l \rho u(\boldsymbol{u}\cdot\boldsymbol{n})dl$, and the mean boundary pressure force, $\int_l p\boldsymbol{n}dl$. The magnitudes of the three-dimensional terms reach up to relative magnitudes of $0.1\overline{C}_D$ for certain L_{CV}/D, but generally cancel each other out for the resulting mean drag estimate. However, due to the finite convergence of the statistics, the area integrals of the correlations $w'\frac{\partial u'}{\partial z}$ and $u'\frac{\partial w'}{\partial z}$ do not converge to zero for each data set, and combine to give rise to a minor force contribution when equation 6.8 is averaged. On the other hand, the three-dimensional momentum flux term $\int_{S_1}(\rho\boldsymbol{u}\frac{\partial w}{\partial z})dS$ attains a larger magnitude in experiment compared to the DNS data set (figure 6.9b), despite increased statistical

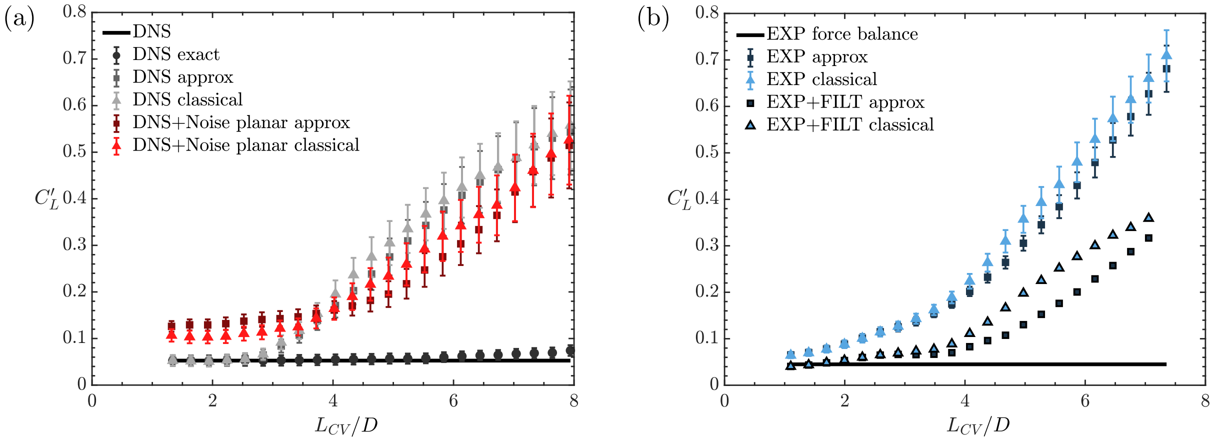

Figure 6.8: RMS lift forces evaluated using equations 6.8, 6.9, and 6.10 for variable control volume size (L_{CV}) for (a) direct DNS and noisy, planar DNS at $\mathrm{Re_D} = 1575$ and (b) PIV experiment at $\mathrm{Re_D} = 1900$.

convergence, indicating its persistence in the experiment.

For the RMS lift statistics (figures 6.9c,d), only one of the three-dimensional viscous terms, $\int_{S_1} \mu(\frac{\partial^2 \boldsymbol{w}}{\partial y \partial z})dS$, is negligible. The force is determined primarily by the difference between the time derivative term, $\frac{d}{dt}(\int_{S_1} \rho v dS)$, and the boundary momentum flux, $\int_l \rho v(\boldsymbol{u} \cdot \boldsymbol{n})dl$, for larger CVs ($L_{CV}/D > 3$), while the boundary pressure force, $\int_l p\boldsymbol{n}dl$, is dominant for smaller CVs. Both of the three-dimensional momentum fluxes, and the three-dimensional viscous force, $\int_{S_1} \mu(\frac{\partial^2 \boldsymbol{v}}{\partial z^2})dS$, become increasingly more significant for $L_{CV}/D > 3$ and contribute significantly to the instantaneous forcing (figure 6.9c). The growth of these three-dimensional terms for $L_{CV}/D > 3$ explains the significant errors encountered in figures 6.6 and 6.8 for the instantaneous forces when they are neglected in the classical (equation 6.10) and approximate (equation 6.9) formulations.

6.4.3 Diagnosing estimation sensitivity to out-of-plane statistics

The sensitivity of instantaneous loading estimates to flow three-dimensionality has been demonstrated for the planar CV configuration in the present flow case. Such a sensitivity can be expected in other classes of separated, unsteady, transitional or turbulent flows over stationary bodies, however, in the case of accelerating bodies, the added mass term may dominate the instantaneous loading fluctuations to such a degree that omission of three-dimensional terms is less noticeable. The present analysis implies that, to retain accuracy when working with planar velocity measurements, one must construct a CV which bounds minimal regions of 3D flow (figure 6.6). This is a straightforward recommendation based on the results of the instantaneous load estimations, however, the dependency of the mean loading estimates on flow three-dimensionality is obfuscated in the analysis due to the numerical and experimental data sets encountering two differing sensitivities related to the three-dimensional terms in the momentum balance. The numerical data set converges

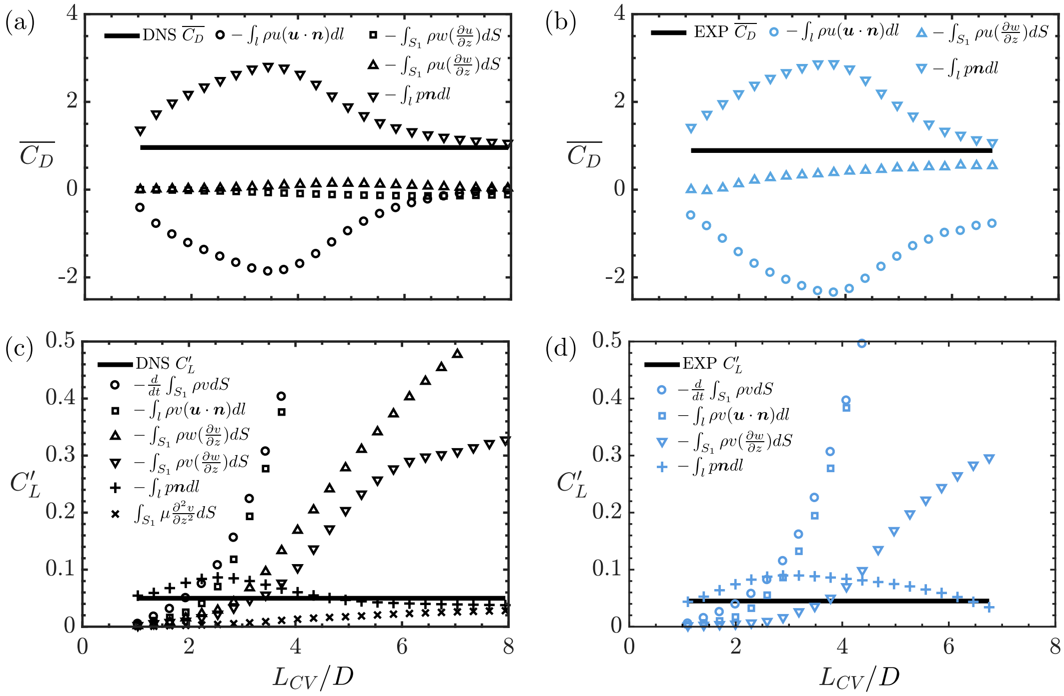

Figure 6.9: Relative magnitudes of momentum balance terms for variable control volume size (L_{CV}) for (a) mean drag for direct DNS at $\mathrm{Re_D} = 1575$, (b) mean drag for PIV experiment at $\mathrm{Re_D} = 1900$, (c) RMS lift for direct DNS at $\mathrm{Re_D} = 1575$, and (d) RMS lift for PIV experiment at $\mathrm{Re_D} = 1900$.

towards two-dimensional flow statistics, however the relatively short time sample of the DNS limits the statistical convergence of the three-dimensional terms. Since the magnitude of the instantaneous three-dimensional momentum fluxes can reach above 100% the mean drag, and strong streamwise structures in the cylinder wake may induce formation of repeating streamwise structures at the same spanwise position on subsequent shedding cycles (Williamson 1996c), the statistical convergence of the mean drag for the classical and approximate momentum equations formulations suffers (figure 6.7a). On the other hand, the experimental data set is sampled over a long enough period to allow adequate convergence of the mean drag statistics (figure 6.7b), and, instead, the inaccuracies of the classical and approximate momentum equation formulations are due to three-dimensional statistics present in the converged fields. In either case, minimizing the size of the control volume to mitigate the space over which three-dimensional area integral terms are active is found to increase accuracy (figure 6.7b). Hence, one can diagnose sensitivities to flow three-dimensionality in a simple manner by observing if the load estimate statistics show dependency on the size of the CV, as shown in figures 6.7 and 6.8, with estimates deemed reliable only if one can establish a region where the estimates are sufficiently independent of changes in CV geometry (e.g., $L_{CV}/D < 2.5$ in the current flow).

To investigate the source of the sensitivity of flow three-dimensionality for the mean drag estimates, figure 6.10 quantifies the development of the mean flow three-dimensionality present in the flow by computing the mass residual ratio when varying the normalized streamwise location of the downstream CV boundary ($\hat{x}_{CV}$), with the upstream CV boundary fixed at $\hat{x} = -3.6$ and top and bottom CV boundaries fixed at $\hat{y} = \pm 3.6$. The mass residual ratio is defined here by the residual in the mass balance (equation 6.12) computed over the CV, normalized by the mass flow rate through the upstream boundary of the CV ($\rho U_o L_{CV}$). Figure 6.10a computes the mass residual ratio including the area integral $\iint \rho \partial w/\partial z dS$ accounting for the mass flux due to the flow three-dimensionality, while figure 6.10b computes only the mass fluxes from the contour integrals at the CV boundaries. The mass residual ratio reduces to zero when all terms are accounted for in figure 6.10a, for both data sets, indicating that the measurement and DNS data are conforming to the governing equations. In contrast, the deviations of the mass residual ratio from zero in figure 6.10b give an indication of the magnitude and character of the flow three-dimensionality for the numerical and experimental data sets. For the numerical data set, the mass residual ratio is small, and deviations from zero occur only in the wake region, due to convergence of the mean statistics in the three-dimensional wake. On the other hand, for the experimental data set, the mass residual ratio systematically increases as the CV boundary is moved further downstream, reaching a maximum of nearly 5% of the incoming mass flow rate. This is indicative of a persistent three-dimensionality over the entire CV area due to free-stream flow non-uniformity or laser sheet alignment. For a mass residual ratio of 5%, the corresponding local mean variation of the spanwise velocity is approximately $0.7\% U_0$ per diameter, which is a feasible non-uniformity characteristic of an experimental facility.

$$\dot{M}_{res} = -\int_l \rho(\overline{\boldsymbol{u}} \cdot \boldsymbol{n}) dl + \int_{S_1} \rho \left(\boldsymbol{\nabla}_{xy} \cdot \overline{\boldsymbol{u}} \right) dS \tag{6.12}$$

To test the sensitivity of the loading estimates to laser sheet misalignment, the exact DNS data set was utilized, and the data were sampled in a plane with small rotations about the x and y axes. The mean drag estimates for several sampling plane angles about the y-axis are shown in figure 6.11a; with the plane angle within the investigated range producing a minor effect on loading estimates. The exact pressure fields were interpolated from the exact fields at a 0° plane angle for comparison, but also computed by solving the pressure Poisson equation from the sampled velocity data on the misaligned planes for 0°, 5°, and 10°. Measurement plane misalignment is shown to not affect the planar mass residual ratio significantly (figure 6.11b) when omitting the three-dimensional term, hence it is not the cause of the trend observed in the experimental data in figure 6.10b, which shows a progressive deviation of the mass residual ratio with increasing CV size. Therefore, the failure of the classical method to accurately predict the mean drag for large CVs for the experimental data set in the current study (figure 6.7b) is attributed to statistical three-dimensionalities in the flow, rather than alignment error. The approximate method provides a significant correction to the mean drag estimates in the experiment due to the dominating influence of the computable three-dimensional flux term (figure 6.9b), associated with a significant mass imbalance in the CV (figure 6.10b). Therefore, the analysis

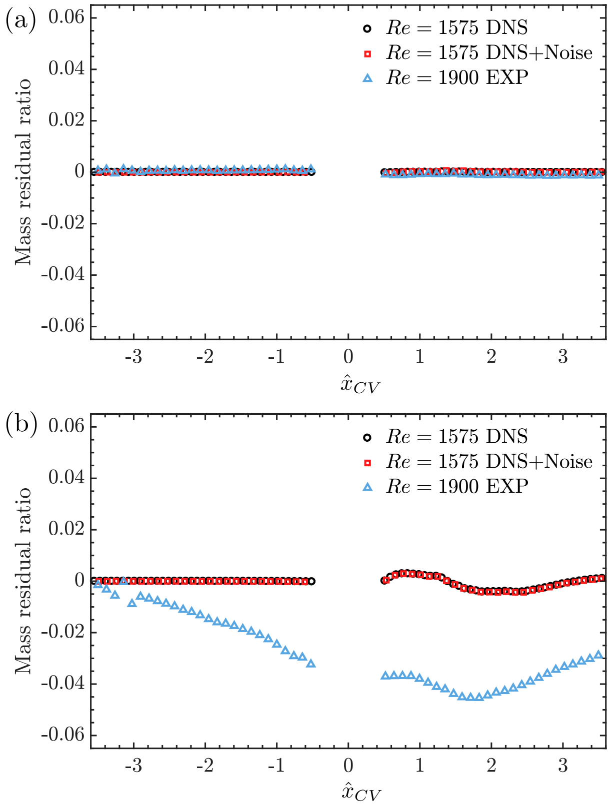

Figure 6.10: Mass residual ratio in the CV based on (a) the planar mass balance including the three-dimensional mass flux term (equation 6.12) and (b) the planar mass balance omitting the three-dimensional term.

indicates a high sensitivity of the mean drag estimates to statistical three-dimensionalities in the flow when using the classical formulation, highlighting the importance of ensuring low free-stream non-uniformity and carefully controlling model boundary conditions when using this formulation. On the other hand, the estimates are insensitive to three-dimensionality associated with measurement plane alignment. The use of the approximate formulation corrects for flow three-dimensionalities associated with mass imbalance in the CV and is hence less sensitive to experimental conditions. For instantaneous loading estimates, only minimal flow three-dimensionality may be tolerated, and the approximate formulation provides only minor compensations. To ensure instantaneous accuracy, establishing the independence of the CV estimates from CV size is vital in order to ensure flow three-dimensionalities are not a dominating error source.

To increase the accuracy of mean drag estimates from wake integrals, the momentum fluxes are often corrected to account for conservation of mass over the CV (van Dam 1999, van Oudheusden *et al.* 2007) by subtracting out the equivalent momentum deficit incurred by the residual mass flow out of the domain at the free-stream velocity (equation 6.13).

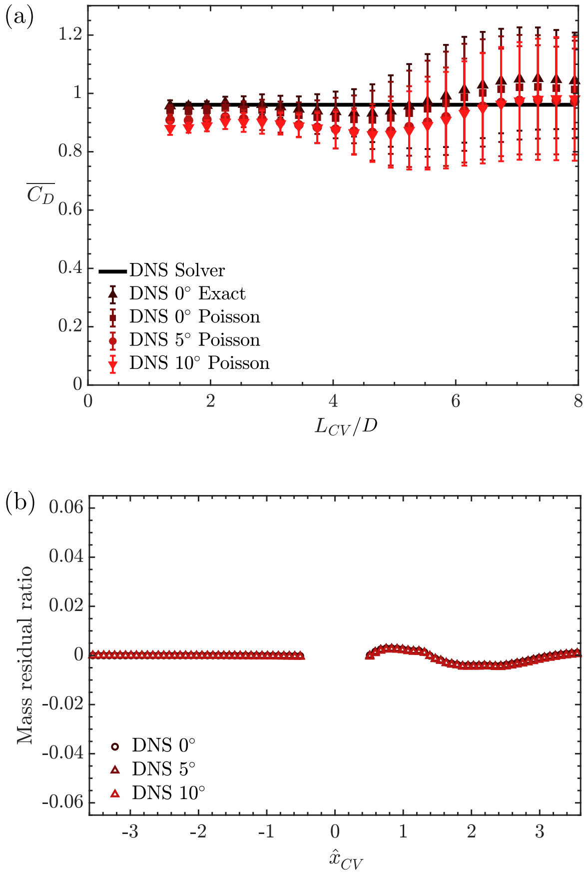

Figure 6.11: When the sampling plane is misaligned by rotation about the y-axis: (a) variation of the mean drag coefficient, and (b) variation of the mass residual ratio.

CV Formulation:	Exact	Approximate	Classical
$\overline{C_D}$ ($L_{CV} = 1.34$)	0.076%	0.83%	0.37%
$\overline{C_D}$ ($L_{CV} = 6.14$)	0.22%	15%	5.5%
C'_D ($L_{CV} = 1.34$)	0.22%	16%	3.6%
C'_D ($L_{CV} = 6.14$)	59%	1300%	2100%
C'_L ($L_{CV} = 1.34$)	0.14%	0.49%	0.071%
C'_L ($L_{CV} = 6.14$)	18%	680%	710%

Table 6.4: Summary of error metrics for DNS data.

$$\overline{F_D} = \int_{l_{wake}} \rho(U_o - \overline{u})\overline{u}dl - \int_{l_{wake}} \rho\overline{u'^2}dl + \int_{l_{wake}} (p_o - \overline{p})dl + \int_{l_{wake}} (\overline{\tau} \cdot \boldsymbol{n})dl \tag{6.13}$$

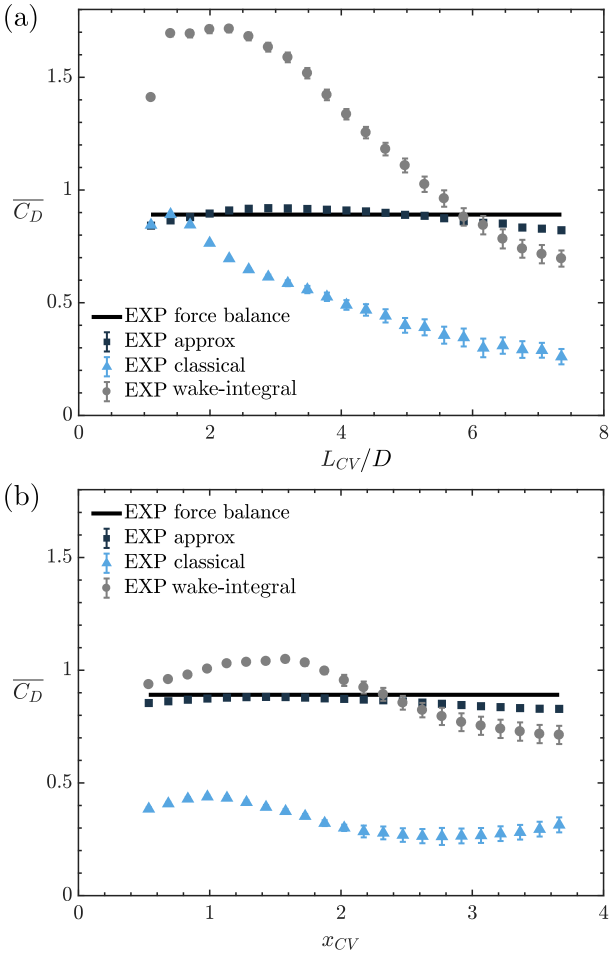

Figure 6.12: Comparison of the wake-integral equation (equation 6.13) with the classical (equation 6.10) and approximate (equation 6.9) forms of the momentum integral equation using the experiment PIV data set, (a) for a square CV centred at the cylinder centre with side length L_{CV} and (b) a traditional CV with inflow boundary at $x = -3.5D$ and transverse height $7D$ with varying outflow boundary position from $x = 0.5 - 3.7D$.

It is of interest to compare this wake integral formulation with the approximate formulation derived in the present study, which utilizes an area integral of the momentum flux associated with the planar divergence of the velocity field over the CV. Figure 6.12 compares the wake-integral approach to the three formulations compared previously using the same square CV which expands larger in all direction with increasing L_{CV}. Not surprisingly, the wake-integral method performs poorly in this case for small L_{CV}, as the momentum fluxes out the top and bottom CV boundaries are significant and are in accelerated flow regions. In practice, one would utilize the wake-integral method by encompassing the largest possible extent of the wake data, hence figure 6.12b gives a more realistic comparison of a CV with its inflow boundary fixed at $x = -3.5D$, transverse boundaries fixed at $y = -3.5D$ and $y = 3.5D$, and only the downstream boundary location in the wake is being varied.

The result shows the wake-integral approach to be superior to the classical formulation, which does not correct for mass flow imbalance for all CV boundary locations, however, the approximate formulation derived in the present study is shown to enable higher accuracy for this test case. The higher accuracy of the approximate formulation here should not be treated as universal, since it relies on the approximated three-dimensional momentum flux dominating the neglected term. It also appears to benefit in this case by counteracting the slight under prediction in mean drag estimates caused by the lower spatial resolution of the PIV data, a trend observed in figure 6.7a. To summarize the results, table 6.4 includes the error metrics for the loading statistics using the ideal DNS data set for relevant loading statistics.

6.5 Conclusion

The conservation of linear momentum in a planar control volume is derived for the general case of three-dimensional flow. In comparison to the classical, two-dimensional formulation (equation 6.10), the derived formulation (equation 6.8) includes area integrals involving the out-of-plane velocities and gradients associated with the out-of-plane momentum flux and viscous stresses. The formulation is validated on a prototypical cylinder wake flow in a turbulent shedding regime using a combined analysis of DNS data and experimental PIV data. The results reveal significant implications flow three-dimensionality can have on both instantaneous and mean sectional load estimation methodologies common in fluid mechanic testing. Failure to account for the three-dimensional terms can lead to instantaneous and mean errors on the order of 50%, and the results will show dependence on control-volume location. Invoking a divergence-free condition for incompressible flow allows the estimation of a subset of the expanded three-dimensional terms, yielding an increase in accuracy over the classical two-dimensional formulation for the test case considered. The improvement is most significant in the mean drag estimates from the PIV experiment, where the statistical three-dimensionality of the flow caused significant errors in the classical estimates, while the instantaneous improvement of the loading estimates was relatively minor. The cumulative results suggest that, when only planar velocity measurements are possible, it is best to strategically select a CV to avoid encompassing three-dimensional flow regions, employ temporal filtering on individual CV terms to mitigate random error propagation, and use the approximate CV formulation (equation 6.9) to enable instantaneous loading estimates with the highest precision. Regions of three-dimensional flow can be identified in planar measurement, for example, through a comparative analysis of the planar divergence statistics over the domain.

Chapter 7

Flow-induced force distribution for a cylindrical body undergoing VIV

With a methodology for both pressure and load estimation from time-resolved PIV data determined, an experimental test case in now performed. The method is applied to a stationary cylinder in cross flow, and two forced vibration cases corresponding to $2S$ and $2P_0$ modes of vortex-induced vibrations. The resulting estimates of instantaneous fluid forcing are compared to simultaneously acquired force balance data, and are shown to capture the low frequency modulation of the fluctuating lift force associated with shedding phase variation along the span for the uniform stationary cylinder.

This chapter is based on the conference proceedings: McClure, J., Morton, C., and Yarusevych, S. (2019) “Forcing function and volumetric flow field estimation for a cylinder undergoing VIV,” *13th International Symposium on Particle Image Velocimetry*, 22-24 July, Munich, Germany.

7.1 Introduction

Within the wide-spread deployment of Particle Image Velocimetry (PIV) and Particle Tracking Velocimetry (PTV) systems for application in industrial and research laboratory settings, it is of interest to extract time-resolved load estimates ($\mathbf{F}(t)$) from such measurements (Rival and Oudheusden 2017). A challenging case which that the current study will focus on, is an immersed body undergoing motion in a fluid flow (e.g., Morse and Williamson 2009). There are a few candidate formulations to choose from for evaluating forcing from velocimetry data: (i) the pressure-velocity formulation (Unal *et al.* 1997, Wu *et al.* 2005, McClure and Yarusevych 2019) (i.e., momentum methods) , (ii) the vorticity-velocity formulation (Noca *et al.* 1999, Graham *et al.* 2017, Guissart *et al.* 2017, Limacher *et al.* 2018) (i.e., impulse methods), and (iii) the Lagrangian drift volume formulation (Dabiri 2006, McPhaden and Rival 2018). For flows with significant contributions from added mass and vortex force components, a complete force estimate can only be obtained from the momentum and impulse methods. The classical momentum formulation is selected for consideration in the current study, due to its characteristically lower error sensitivity (Noca *et al.* 1999, Limacher *et al.* 2019, Limacher *et al.* 2020) compared to impulse methods for finite domains. In addition, the concomitant resolution of the pressure field facilitates advanced diagnostics for applications involving flexible structures and aeroacoustics.

A limitation of time-resolved PIV-based loading estimates is their application in three-dimensional flows with salient dynamics occurring outside the PIV measurement plane or volume. Since, in general, the flow completely surrounding the body must be resolved for time-resolved force estimation, this poses an experimental challenge for both resolution and illumination. Specifically, tomographic camera set-ups have limited ability to resolve the flow near highly curved geometries, and mitigation of optical shadowing, encountered when the measurements domain encompasses a solid body, requires a drastic increase in complexity of the measurement. In addition, the light budget limitations often restrict the size of the measurement volume, making illuminating the flow surrounding the entire immersed body infeasible in most cases. (Spoelstra *et al.* 2019) circumvent this issue for evaluation of time-resolved drag force by utilizing a single measurement volume downstream of a cyclist, aimed at capturing the entire extent of the time-resolved evolution of the trailing wake permitting the use of a simplified control volume analysis.

The approach in this study is primarily aimed at measuring the fluctuating lift force utilizing a pseudo-instantaneous three-dimensional flow reconstruction technique derived from a minimum of two independent time-resolved, planar Particle Image Velocimetry (TR-PIV) measurements to estimate time-resolved fluid pressure and loads for a stationary and oscillating cylinder in cross flow at a Reynolds of approximately 4100. The study serves as a validation case of the proposed methodology, with the TR-PIV measurements accompanied by reference force balance data to benchmark the accuracy of the proposed methods.

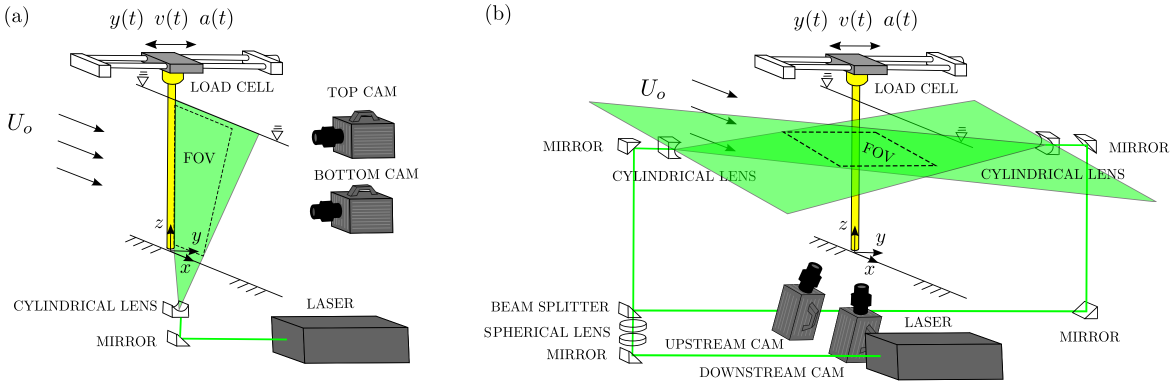

Figure 7.1: Experimental configuration for (a) vertical plane (x-z) and (b) horizontal plane (x-y) PIV measurements.

7.2 Experimental Methodology

Experiments were performed in a closed-loop water tunnel facility at the University of Calgary. The tunnel test section width and free surface height were $0.385m$ and $0.431m$, respectively. The free-stream velocity was set to $U_0 = 0.21m/s$, and was monitored by a Dynasonics TFX ultrasonic flow meter. The experimental configuration is depicted in figure 7.1. A cylinder model was mounted vertically on an actuated platform capable of linear motion over a range of amplitudes (A) and frequencies (f) in the cross-flow direction to replicate one-degree-of-freedom Vortex-Induced Vibrations (VIV). The cylinder model had diameter $D = 19.05mm$, resulting in solid blockage of 5%, and was made hollow to enhance PIV laser light penetration and minimize inertial loading during motion, with a total mass of 0.167 kg. The aspect ratio of the immersed portion of the cylinder was $L/D = 22.62$, and the free end of the cylinder extended to within 1 mm of the test section floor. The Reynolds number based on cylinder diameter was approximately 4100. Three cases were investigated: (i) a stationary cylinder, (ii) forced VIV at normalized amplitude $A^* = A/D = 0.45$ and wavelength $\lambda^* = U_0/fD = 5$ resulting in 2S shedding, and (iii) forced VIV at $A^* = 0.8$ and $\lambda^* = 7$ resulting in $2P_0$ shedding (Morse and Williamson 2009). Time-resolved, two-component, planar PIV-measurements in $x-y$ and $x-z$ planes are obtained in sync with force and cylinder position measurements from a load cell and encoder, respectively.

The sinusoidal trajectory of the cylinder is actuated by a motorized traverse above the free surface of the water channel. The traverse is driven by a digital brushless servomotor (ClearPath MCVC-2341P) through a timing belt attached to a moving carriage mounted between two v-slot linear rails aligned in the transverse direction, ensuring motion in only one degree-of-freedom. The position of the carriage is monitored by an optical encoder with 800 counts per revolution resulting in a resolution of $0.002D$ in position measurement. A homing procedure was used to consistently centre the cylinder position in the test section with an uncertainty within $\pm 0.016D$. Coaxially mounted to the bottom of the carriage are the load cell and acrylic cylinder model. A detailed description of the control system

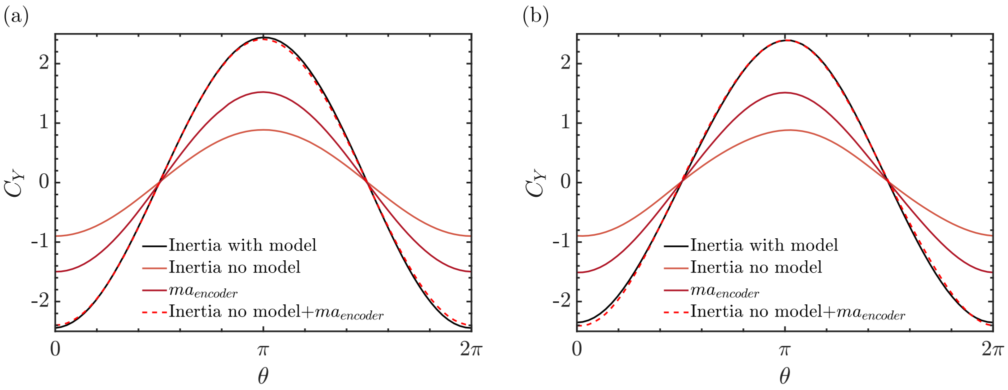

Figure 7.2: Phase-averaged inertial lift force subtraction for oscillating cylinder cases (a) $A^* = 0.45$ and $\lambda^* = 5.0$ and (b) $A^* = 0.8$ and $\lambda^* = 7.0$.

implemented to follow the input sinusoidal trajectories is included in Riches and Morton (2018). In the current work, the desired trajectory is prescribed as a sinusoid with a given amplitude and frequency $y = A\sin(2\pi f t)$.

Instantaneous forces were measured using an ATI Mini40 six-component load cell. The load cell force resolution is 0.005 N. In the oscillating cylinder cases, the inertial force on the load cell associated with accelerating/decelerating the cylinder model assembly must be quantified and subtracted from transverse lift force measurements. To do so, the prescribed motion for the two oscillating cases was repeated in air, and the resulting filtered lift data was phase averaged using the phase of the cylinder position computed by the Hilbert transform (Khalak and Williamson 1999) providing an estimate for the phase-averaged inertial force (black line, figure 7.2). The result was then subtracted from the forces obtained in the current experiments based on the phase of the cylinder position. The inertial subtraction was further validated by repeating the prescribed motion in air with the cylinder model detached from the load cell. The resulting phase averaged inertial force when added to the additional inertial force computed by the measured mass of the cylinder model undergoing acceleration measured by the second derivative of the filtered encoder data ($ma_{encoder}$) matches the previously obtained inertial subtraction with the entire assembly actuated (figure 7.2). The correspondence of the two signals suggests no secondary inertial effects, e.g., due to deflection of the cylinder model, are significant.

Velocity measurements were obtained in six independent planes using two-component, time-resolved PIV, comprising of three vertical $x - z$ planes (figure 7.1a) at transverse positions $y/D = 0$, 0.5, and 1.0, and three horizontal $x - y$ planes (figure 7.1b) at spanwise positions $z/D = 5$, 11.9 and 17.7. The flow was seeded with 10 μm hollow glass spheres, with specific gravity 1.05, illuminated by a high repetition rate Photonics DM30 Nd:YLF laser. Particle images were acquired with two 2560×1600 px Phantom Miro 340 high-speed cameras equipped with 60 mm lenses. Scheinpflug adapters were affixed to the lenses for the horizontal plane measurements, and the cameras rotated 20 deg from the vertical axis to facilitate resolution of the velocity field surrounding the entire cylinder surface. For

Parameters	Symbol	Value
Focal Ratio	$f\#$	$f/5.6$
Acquisition frequency	f_{acq}	400 Hz
Number of samples	N	1000×10
Field of view	FOV/D	3.8×3.8

Table 7.1: PIV acquisition parameters.

Parameters	Symbol	Value
Interrogation window	WS	24×24 px
Acquisition frequency	f_{acq}	400 Hz
Field of view (horz)	FOV_h/D	7.2×3.8
Field of view (vert)	FOV_v/D	4.0×20.3
Vector pitch (horz)	dx_h	$0.016D$
Vector pitch (vert)	dx_v	$0.029D$
Overlap	OV	75%

Table 7.2: PIV processing parameters.

each measurement plane and set of parameters, 10000 images were acquired at $f_{acq} = 400$ Hz in single frame mode, approximately 200 times the Strouhal shedding frequency of the stationary cylinder. The velocity fields were processed in DaVis 8.4.0 using an iterative multigrid algorithm with window deformation at a final interrogation window size of 24×24 px with 75% overlap. Erroneous vectors were eliminated by employing a median temporal filter over a sliding kernel of 7 velocity fields. After stitching the resulting vector fields from two cameras in a minor $< 0.5D$ overlap region with a linear weighting factor, the final $x - y$ Field of View (FOV) was $-3.6 < x/D < 3.6$, $-1.9 < y/D < 1.9$, and $x - z$ FOV was $0 < x/D < 4.0$, $0.1 < z/D < 20.2$, with a vector pitch of 0.55 mm ($0.029D$) and 0.31 mm ($0.016D$) in the $x - z$ and $x - y$ planes, respectively.

The PIV laser Q-switch, encoder, and load cell force signals were acquired simultaneously at $f_{acq} = 50$ kHz with an Advantech PCI1716L DAQ card. The encoder and force balance signals were synchronized with the PIV velocity measurements through resampling the acquired data at the mid point between rising edges of the Q-switch corresponding to the timing of laser pulses. In the oscillating cylinder cases, data acquisition was initiated only after a minimum of 10 oscillation periods to ensure transients in the controls and flow dynamics did not influence the results.

7.2.1 Pressure and Force Estimation

A Poisson equation solver was employed to estimate pressure from the horizontal plane PIV measurements based on the numerical solution of equation 7.1 (e.g., Gurka *et al.* 1999).

$$
\begin{aligned}
\nabla^2 p &= \nabla \cdot \left(-\rho \frac{D\mathbf{u}}{Dt} + \mu \nabla^2 \mathbf{u}\right), \quad \text{in } \Omega \\
\nabla p \cdot \mathbf{n} &= \left(-\rho \frac{D\mathbf{u}}{Dt} + \mu \nabla^2 \mathbf{u}\right) \cdot \mathbf{n}, \quad \text{on } \Gamma_i \\
p &= \frac{1}{2}\rho U_0^2 - \frac{1}{2}\rho \left(\overline{\mathbf{u}} \cdot \overline{\mathbf{u}} + \mathbf{u}' \cdot \mathbf{u}'\right), \quad \text{on } \Gamma_j
\end{aligned}
\tag{7.1}
$$

where Γ_i denotes boundary sections where Neumann boundary conditions are employed, setting the pressure gradient to that estimated from the Navier-Stokes equation, and Γ_j denotes boundary sections where the Dirichlet condition is employed, setting the pressure on the boundary using an extended form of the Bernoulli equation, valid for unsteady, irrotational flow with small mean velocity gradients (de Kat and van Oudheusden 2012). Dirichlet condition were prescribed on the inflow boundary, where the flow was deemed approximately steady and irrotational for all cases, and Neumann conditions were prescribed on the remaining top, bottom, outflow boundaries and on a circular contour surrounding the cylinder. The contour around the cylinder had a diameter of $1.2D$, moving with the cylinder's position, in order to avoid amplified errors in near wall regions. For computation of sectional loads, $\mathbf{F_S} = (F_x, F_y)$, from the horizontal plane PIV measurements, a small control volume was selected surrounding the cylinder ($-1.05 < x/D < 1.05$, $-1.05 < y/D < 1.05$), to avoid regions of flow three-dimensionality. The mathematical formulation used is given in equation 7.2, which represents the approximate momentum balance for a planar control volume in three-dimensional flow (McClure and Yarusevych 2019), with viscous terms neglected.

$$
\mathbf{F_S} = -\frac{d}{dt}\left(\int_S \rho \mathbf{u} dxdy\right) - \oint_l \rho \mathbf{u}(\mathbf{u}\cdot\mathbf{n})dl + \int_S \rho \mathbf{u}\left(\nabla_{xy}\cdot\mathbf{u}\right)dxdy - \oint_l p\mathbf{n}dl \tag{7.2}
$$

7.2.2 Pseudo-Instantaneous Three-Dimensional Reconstruction

Since planar PIV measurements are only capable of yielding sectional estimates of the flow induced loading, it is necessary to employ a reconstruction of the flow along the entire span of the cylinder model in order to accurately characterize the forcing. This is done by leveraging instantaneous, vertical plane PIV measurements located at a transverse position $y = 0.5D$. At each spanwise location, streamwise velocity data in the overlapping region between the vertical and horizontal plane PIV measurements is used to obtain an estimation for horizontal velocity fields, pressure fields, and sectional forces. This estimate is computed

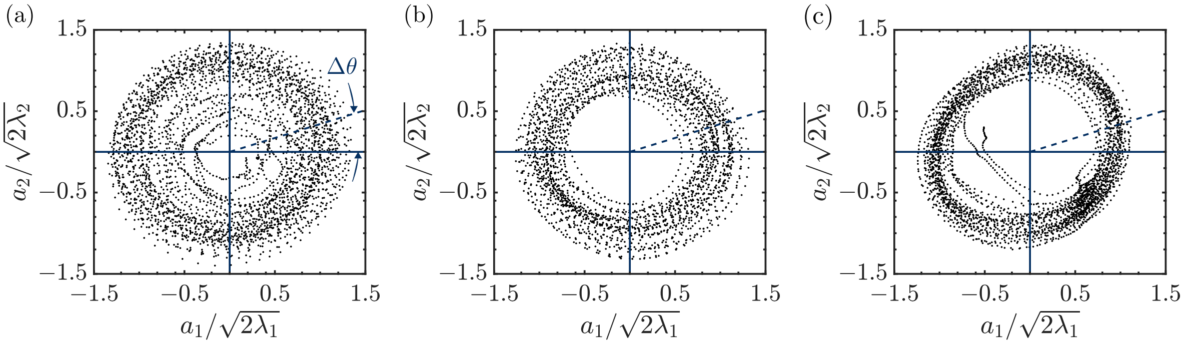

Figure 7.3: First two temporal coefficients of the POD for (a) stationary cylinder, (b) oscillating cylinder $A^* = 0.45$, $\lambda^* = 5.0$, and (c) oscillating cylinder $A^* = 0.8$, $\lambda^* = 7.0$.

in two ways: (i) phase-averaging the horizontal plane measurements and correlating a line of streamwise velocity data at every spanwise location (z_k) in the instantaneous vertical plane velocity field, $u(x, y_v, z_k)$, to identify the shedding phase at every spanwise position ($\theta(z_k)$), and (ii) phase-averaging the horizontal plane measurements and projecting the same line of velocity data $u(x, y_v, z_k)$ onto the horizontal POD-basis modes to estimate the temporal coefficients $\{a_1(z_k), a_2(z_k), \ldots\}$ at every spanwise position, the temporal coefficients can then be leveraged to compute the spanwise distribution of shedding phase.

To phase average the horizontal plane PIV measurements, Proper Orthogonal Decomposition (POD) is employed (Sirovich 1987), which decomposes the velocity fields into deterministic spatial modes, $\phi_i(x, y)$, with corresponding time varying temporal coefficients, $a_i(t)$. Figures 7.3a-c plot the values of the first two temporal coefficients for the horizontal plane PIV data acquired at $\hat{z} = 11.9$ for the stationary and oscillating cylinder cases. The first two temporal coefficients define the dominant dynamics of the primary shedding instability (Noack and Eckelmann 1994), and the shedding phase can be identified by $\theta = \arctan \sqrt{\lambda_2/\lambda_1} a_1/a_2$ (Oudheusden *et al.* 2005). Notably, figure 7.3a indicates a larger spread of temporal coefficient data for the stationary case, indicative of larger variations in planar wake dynamics, while the data for the oscillating cylinder case at $A^* = 0.8$ and $\lambda^* = 7.0$ has a slightly skewed distribution, presumably associated with the asymmetric wake dynamics for the observed $2P_0$ shedding regime (Morse and Williamson 2009). Once the shedding phase is identified for the acquired data during the horizontal plane PIV measurements, the corresponding phase averages of the velocity fields, pressure fields, PIV-based sectional loads, and total loads measured by the force balance are computed by binning the data into phase bins of $\Delta\theta = 20°$.

To estimate the spanwise distribution of shedding phase from the vertical plane data at a given time, the streamwise velocity data at each spanwise position is either correlated with the corresponding line of data from each phase averaged streamwise velocity field, or the streamwise data is projected onto the corresponding line of data from the first two $x-y$ plane POD modes ($\phi_1(x, y_v)$, $\phi_2(x, y_v)$) according to $a_i(z_k, t) =< u(x, y_v, z_k), \phi_i(x, y_v) > /||\phi_i(x, y_v)||^2$ to recover the temporal coefficients at each spanwise position which can be

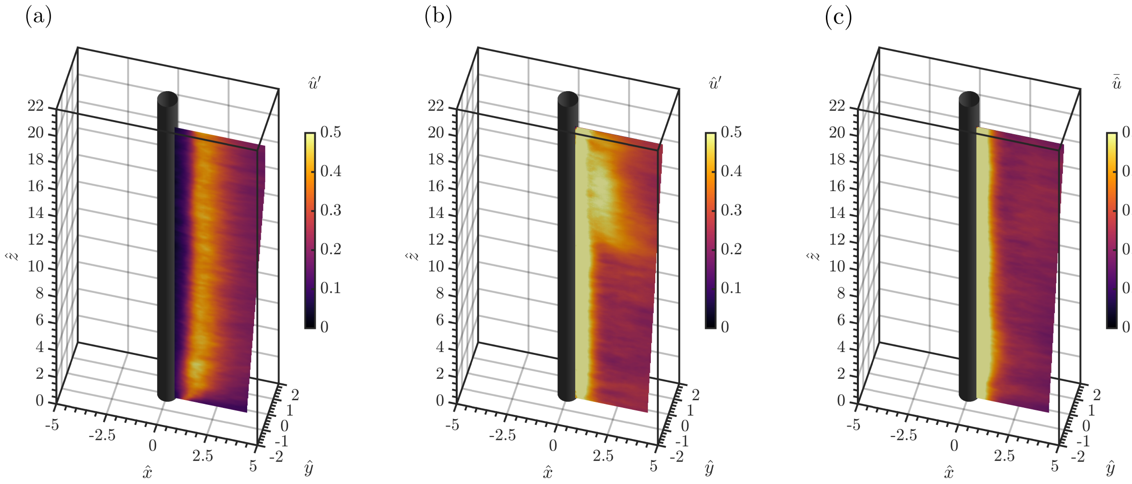

Figure 7.4: RMS streamwise velocity contours in a transverse plane at $\hat{y} = 9.5$ for (a) stationary cylinder, (b) oscillating cylinder $A^* = 0.45$, $\lambda^* = 5.0$, and (c) oscillating cylinder $A^* = 0.8$, $\lambda^* = 7.0$.

used to estimate the phase according to figure 7.3. For each case, a low order representation of the instantaneous flow field can be constructed according to $u_{POD}(x, y, z, t) = \bar{u}(x, y, z) + \sum_i a_i(z, t)\phi_i(x, y)$ and $u_{PA}(x, y, z, t) = u_\theta(x, y, z, \theta(z, t))$, and the shedding phase along the span of the cylinder is used in conjunction with the phase-averaged sectional force data to estimates the total forcing.

7.3 Results

7.3.1 Sectional Results

The main results of the analysis of the sectional PIV data acquired in the three horizontal planes at $z/D = 5$, 11.9, and 17.7 are summarized in figures 7.5, 7.6 and 7.7 for the stationary cylinder, oscillating cylinder in a $2S$ shedding regime, and oscillating cylinder in a $2P_0$ shedding regime, respectively.

For the stationary cylinder, the total lift coefficient fluctuations are characteristically lower than the simultaneously acquired PIV-based estimates at $\hat{z} = 11.9$, and exhibit differences in phase with one another for the majority of the time sample. This result is expected since the spanwise variation of the shedding phase, unaccounted for in the sectional force estimates, acts to reduce the resultant force experienced by the cylinder model. There are several instances where the sectional and total lift coefficient data show high correspondence in phase and amplitude (e.g., $0 < \hat{t} < 1.5$ and $5 < \hat{t} < 6$ in figure 7.5a) indicating times when the phase of shedding happens to be highly correlated along

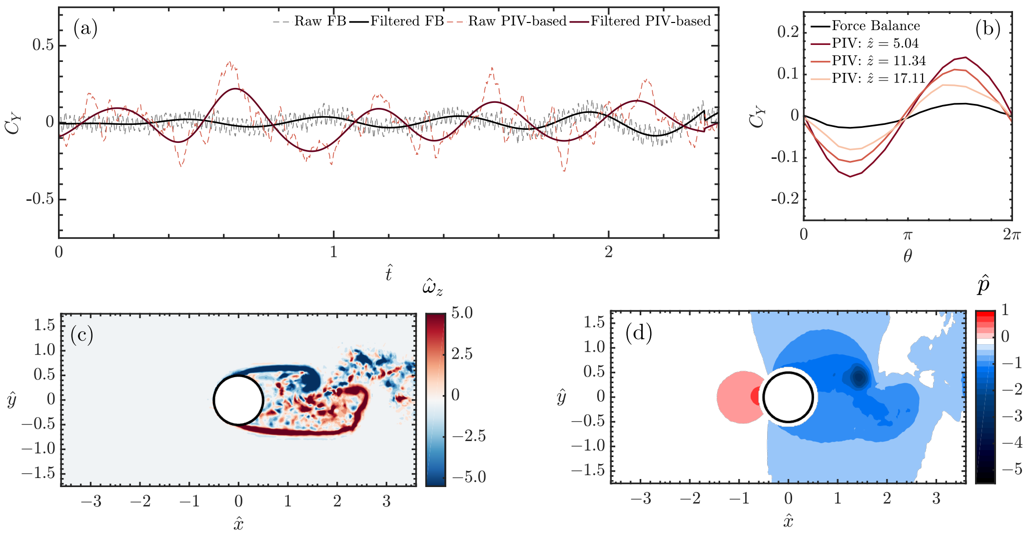

Figure 7.5: Sectional results for the stationary cylinder. (a) Total lift coefficient force balance data compared to PIV-based sectional lift coefficient data, (b) phase averages of these data for each spanwise plane investigated, (c) instantaneous spanwise vorticity field and (d) instantaneous PIV-based pressure field.

the span. The resulting phase averages of instantaneous force measurements and PIV-based estimates based on the POD coefficient data in the sectional horizontal planes are shown in figure 7.5. The sectional lift coefficient data indicate the sectional fluctuating lift force increases as the measurement plane transverses downward in z.

For the oscillating case at $A^* = 0.45$ and $\lambda^* = 5.0$, the total and sectional lift coefficient data are highly correlated in each horizontal plane and exhibit nearly matching amplitude (figure 7.6a,b). This is indicative of the lock-in of shedding phase along the span of the cylinder, typical for high amplitude vortex-induced vibrations (Bearman 1984). The flow regime is denoted “2S” due to the shedding of two vortices per oscillation cycle (figures 7.6c,d), similar to the natural von Kármán wake for the stationary cylinder (figures 7.5c,d). For the oscillating case at $A^* = 0.8$ and $\lambda^* = 7.0$, the total and sectional lift coefficient data are again highly correlated in each horizontal plane and exhibit nearly matching amplitude (figure 7.7a,b), though the minor deviations are more substantial than for the “2S” shedding case. Notably, the phase averaged estimates of the sectional loads exhibit variations in their peak location dependent on the spanwise position of the measurement plane (figure 7.7b). This indicates possible spanwise variations of the wake dynamics, on the average, though the correspondence of the phases of the sectional and total force coefficient data indicates that the shedding remains largely locked-in along the span.

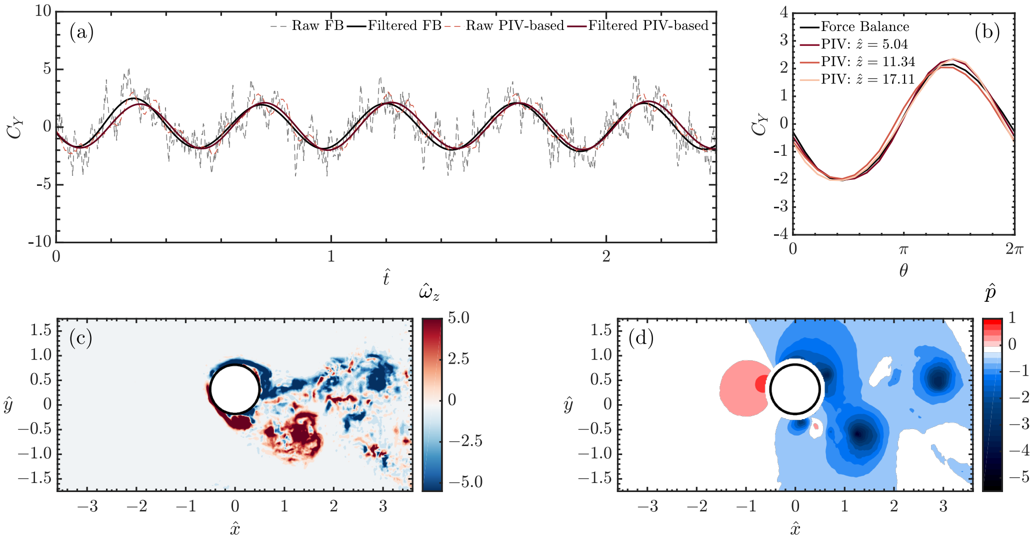

Figure 7.6: Sectional results for the oscillating cylinder at $A^* = 0.45$, $\lambda^* = 5.0$. (a) Total lift coefficient force balance data compared to PIV-based sectional lift coefficient data, (b) phase averages of these data for each spanwise plane investigated, (c) instantaneous spanwise vorticity field and (d) instantaneous PIV-based pressure field.

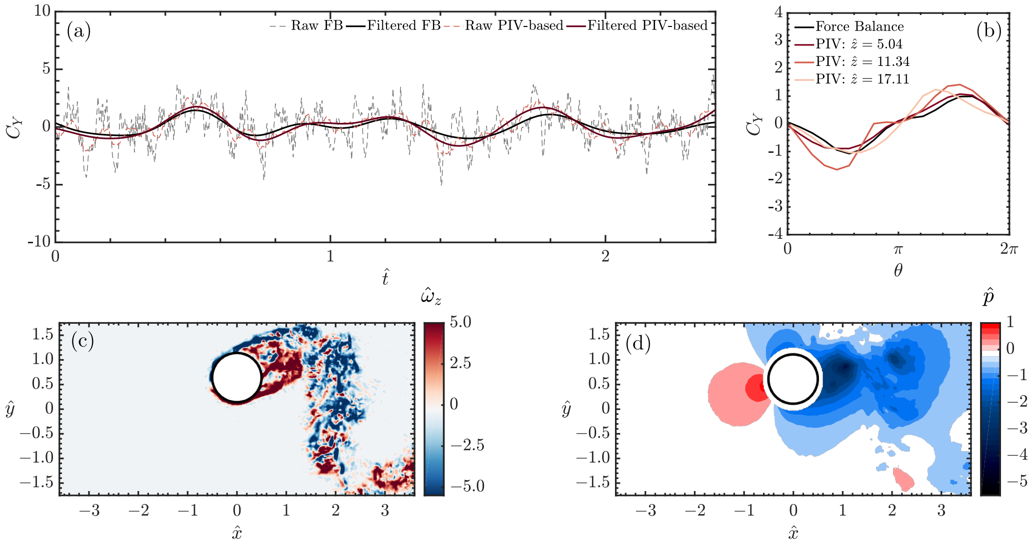

Figure 7.7: Sectional results for the oscillating cylinder at $A^* = 0.8$, $\lambda^* = 7.0$. (a) Total lift coefficient force balance data compared to PIV-based sectional lift coefficient data, (b) phase averages of these data for each spanwise plane investigated, (c) instantaneous spanwise vorticity field and (d) instantaneous PIV-based pressure field.

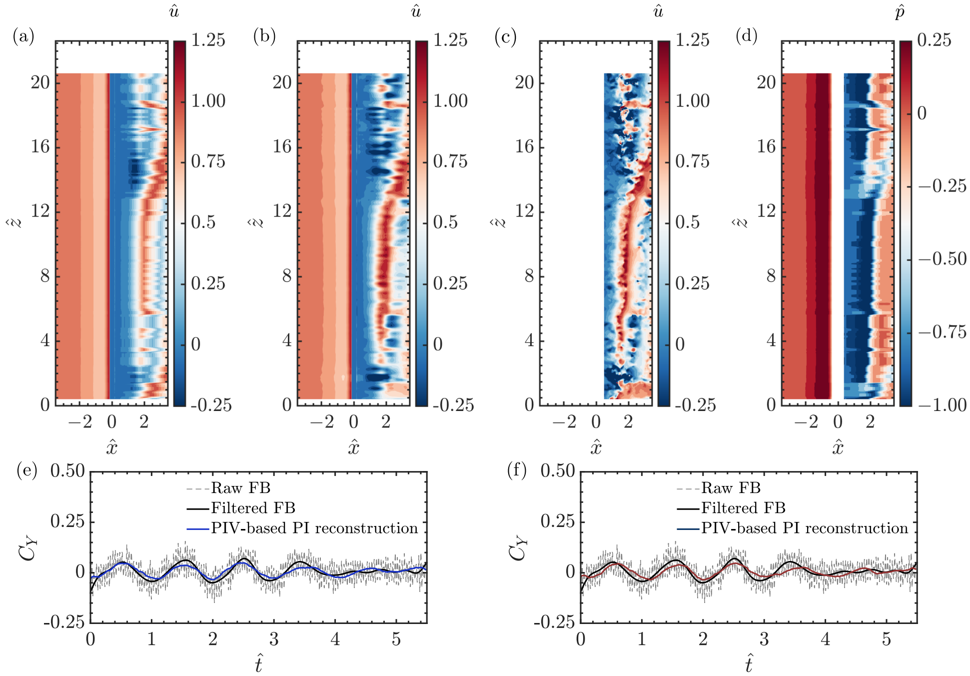

Figure 7.8: Stationary cylinder: reconstruction of instantaneous streamwise velocity at $\hat{y} = 0.5$ using (a) phase-averaged method, (b) POD-based method, compared to (c) measured streamwise velocity data. (d) Reconstructed pressure at $\hat{y} = 0.5$ using phase-averaged method. PIV-based total force reconstruction with (e) phase-averaged method and (f) POD-based method, compared to force balance data.

7.3.2 Three-Dimensional Results

The disagreement of the total force data with the sectional estimates for the stationary cylinder highlights the need for a three-dimensional flow estimation procedure for full characterization of the forcing function acting on the cylinder. Figures 7.8, 7.9, and 7.10, summarise the results of the pseudo-instantaneous reconstructions for the stationary, $2S$, and $2P_0$ cases, respectively. The methods are evaluated for their ability to estimate the instantaneous shedding phase variation along the span towards more accurate evaluation of total lift coefficient data from the PIV-based estimates.

Figures 7.8a, 7.9a, 7.10a, plot the reconstructed streamwise velocity fields at $\hat{y} = 0.5$ by correlating the phase averaged velocity fields, obtained at the midspan of the cylinder ($\hat{z} = 11.9$), to the instantaneous data, while figures 7.8b, 7.9b, and 7.10b plot the reconstructed streamwise velocity field at the same plane by projecting the instantaneous data onto the first 5 spatial POD modes to estimate the horizontal plane temporal coefficient data. When compared to the instantaneous vertical plane velocity field from which the reconstructions were derived (figures 7.8c, 7.9c, 7.10c), it can be observed that the low order representation constructed by projecting onto the first 5 spatial POD modes reconstructs the original field with a higher fidelity. When the shedding phase data ($\theta(z, t)$) are estimated from the three-dimensional reconstructions using either the phase-averaged (figure

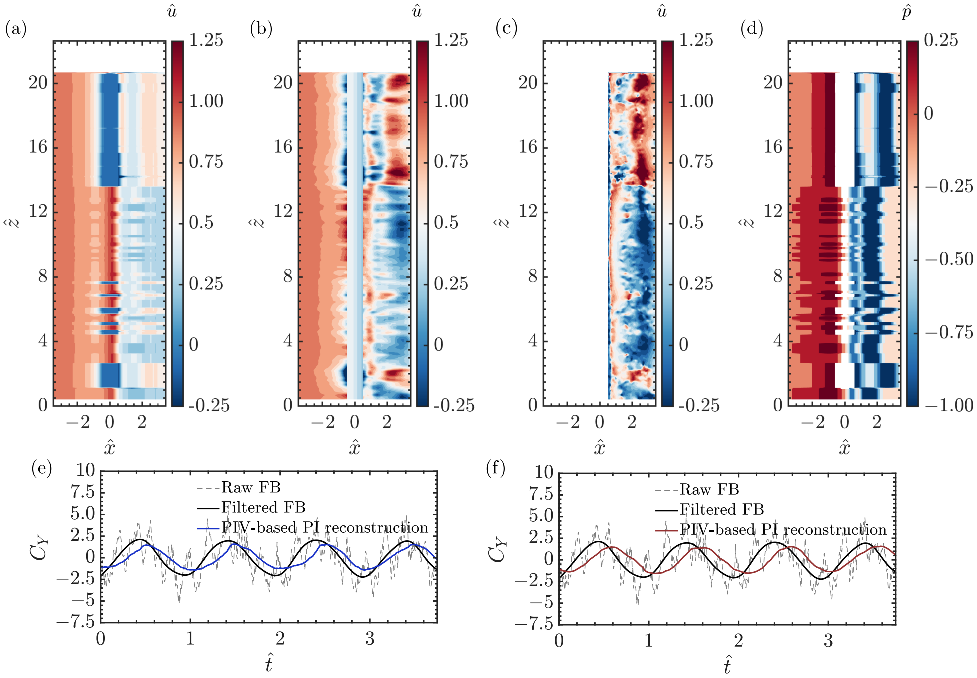

Figure 7.9: Oscillating cylinder at $A^* = 0.45$, $\lambda^* = 5.0$: reconstruction of instantaneous streamwise velocity at $\hat{y} = 0.5$ using (a) phase-averaged method, (b) POD-based method, compared to (c) measured streamwise velocity data. (d) Reconstructed pressure at $\hat{y} = 0.5$ using phase-averaged method. PIV-based total force reconstruction with (e) phase-averaged method and (f) POD-based method, compared to force balance data.

7.8e) or POD-based (figure 7.8f) methods for the stationary cylinder case, a substantial improvement in the alignment of both the phase and amplitude of the lift coefficient data between the force balance and PIV-based measurements is achieved compared to the previously discussed sectional measurements (figure 7.5a). Based on the reconstruction of the volumetric pressure field (figure 7.8d), the shedding of the vortex cores can be seen to vary in phase considerably over the length of the cylinder, resulting in the earlier observed changes in the phase of planar forcing along the span. However, in the sectional loading estimates discussed previously, significant modulations of the sectional fluctuating lift may occur on a cycle-to-cycle basis, indicating a more complex reconstruction may be required to correctly capture the dynamics associated with this modulation effect of the amplitude of the fluctuating lift at each spanwise location, instead of relying on a simple phase average based on the primary instability.

For the 2S and $2P_0$ cases, the force reconstructions shows less agreement for both the phase-average and POD-based methods, with the POD-based method deteriorating substantially in the $2P_0$ case. This appears to be due to the violation of the spanwise homogeneity of the data relied upon in order to apply the phase averaged fields or POD spatial modes corresponding to $\hat{z} = 11.9$ at every spanwise position. Analysis of the instantaneous fields for the 2S case (figures 7.9a-d) reveals that, although the shedding

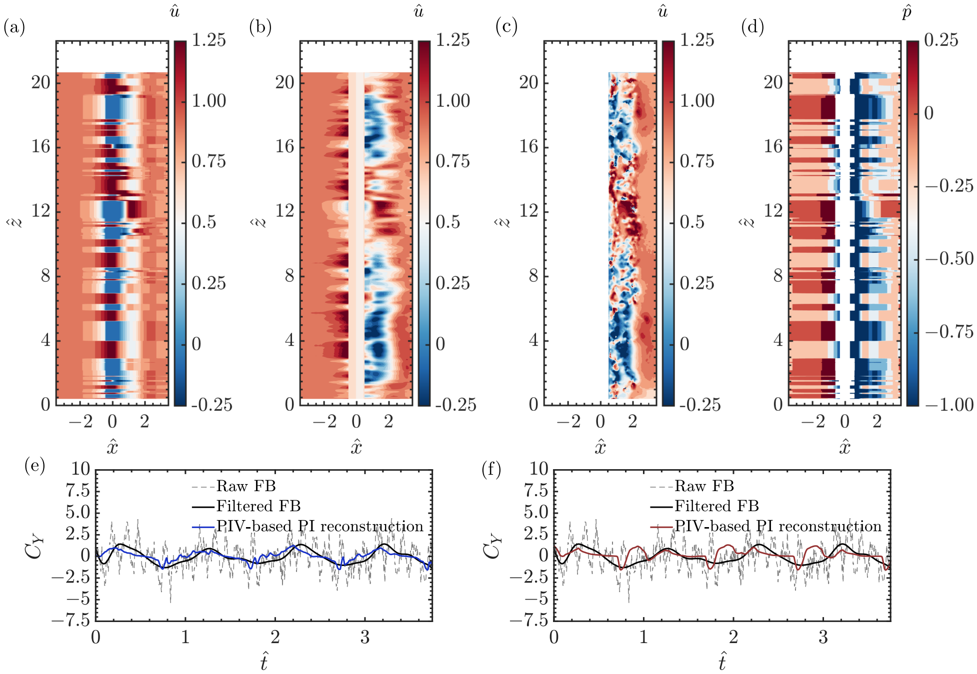

Figure 7.10: Oscillating cylinder at $A^* = 0.8$, $\lambda^* = 7.0$: reconstruction of instantaneous streamwise velocity at $\hat{y} = 0.5$ using (a) phase-averaged method, (b) POD-based method, compared to (c) measured streamwise velocity data. (d) Reconstructed pressure at $\hat{y} = 0.5$ using phase-averaged method. PIV-based total force reconstruction with (e) phase-averaged method and (f) POD-based method, compared to force balance data.

remains locked in phase along the span, the vertical plane measurement gives drastically different streamwise velocity signatures at different spanwise locations. This is due to the expansion of the wake width with decreasing $\hat{z}$, such that the measurement plane cuts into the vortex core at some locations, but remains in the accelerated flow region outside the vortex core at other locations (i.e., $\hat{z} > 14$). This causes both methods to erroneously detect a phase switching in the shedding, resulting in an under prediction of the total lift coefficient amplitude and phase misalignment (figures 7.9e-f), compared to the previously observed good sectional force agreement. Similar issues are prevalent in the $2P_0$ case, however, the wake width appears instead more narrow approaching the midspan. The resulting PIV-based total force reconstruction based on matching to sectional phase averaged fields maintains its phase relationship, however erroneous detection of phases contributes to higher noise levels (figure 7.10e).

7.4 Conclusion

A POD-based flow reconstruction technique is compared to a phase-averaged reconstruction technique for estimating total forcing on a three-dimensional bluff body from planar TR-PIV measurements for the case of a stationary, circular cylinder, and two oscillating cylinder case in 2S and $2P_0$ shedding regimes in uniform cross flows. For the stationary cylinder case, the three-dimensional reconstruction techniques yield a substantial increase in correspondence with reference force balance measurements for determining the total instantaneous lift forcing acting on the cylinder, compared to corresponding PIV-based sectional force estimates. However, for the oscillating cylinder cases, the opposite is true. Since the phase of shedding is largely locked in along the span of the periodically oscillating cylinders, the sectional estimates instead show high correspondence with the reference force balance measurements, whereas the total force estimates based on the three-dimensional reconstructions are contaminated by errors associated with violations of the assumption of spanwise homogeneity of the flow statistics used to reconstruct the velocity fields. However, it is expected that more complex reconstruction methodologies will remedy these issues, such as linearly combining the POD modes and phase averaged fields from all three horizontal planes measured in order to best match the mean and fluctuating statistics at each spanwise position where the reconstruction and shedding phase is evaluated. In addition, reduction of the raw instantaneous vertical-plane fields using a reduced order model before use in reconstruction could yield some reduction in noise.

Chapter 8

Conclusions

This thesis presented a series of manuscripts relating the determinants of fluid forcing on immersed structural bluff bodies to aspects of the flow development. Contributions were made to the state-of-the-art by improving and optimizing the experimental methodologies to extract pressure and force data from spatio-temporally resolved velocimetry data, the analysis of computation fluid dynamics results to relate the properties of the vorticity evolution surrounding the structures to fluid forcing, and the application of the methodologies in an experiment of forced vortex-induced vibrations.

A model was derived from linear uncertainty propagation to select optimal sampling parameters for pressure from PIV measurements. Of the pressure integration techniques compared (Poisson equation, spatial marching, omnidirectional, and eight-path), there were minimal differences in error sensitively, though the eight-path technique consistently produced higher errors. A mathematical framework was developed based on the governing equations to analyse the error terms in the Poisson equation approach to pressure from PIV measurements. It was found that a subset of the error terms could be resolved after leveraging the governing equations, resulting in a more accurate solution. However, pressure gradient errors on the boundaries of the domain lack a method of estimation, and certain terms in the pressure gradient divergence remain and must be estimated or neglected.

The momentum equation-based method for deriving structural loads from PIV measurements is approached, and the dependency of sectional loading estimates derived from planar measurements on an often neglected three-dimensional term is highlighted. In order to avoid excessive errors due to flow three-dimensionality, a small field of view surrounding the structure is recommended, where the flow is nominally two-dimensional. As a matter of methodology, one should check the dependency of the forcing estimates on the field of view size. If the loading estimates are insensitive to changes in field of view, then errors due to three-dimensionality are likely mitigated.

The pressure and structural loading estimation methodologies developed herein were applied to an experiment of a cylinder undergoing forced vortex-induced vibration. Utilizing a set of independent planar PIV measurements in orthogonal planes, a pseudo-instantaneous force reconstruction is possible. A set of horizontal plane measurements characterize the flow development along the span of the body, while instantaneous vertical plane measurements allow the identification of the shedding phase across the span of the body at every instant in time. The pseudo-instantaneous force reconstruction shows good agreement with the lift force signal derived from load cell measurements, while the drag force reconstruction is systematically underestimated.

Chapter 9

Recommendations

Uncertainty estimation for PIV-based pressure estimates. The pressure gradient error correction framework developed in this thesis provides a methodology for increasing the accuracy of PIV-based pressure estimates, despite the inability to satisfy the exact formulation with typical instantaneous measurements. However, on a statistical basis, the equations can be analyzed precisely with the use of modern uncertainty estimation algorithms for velocity fields in PIV which yield the temporal and spatial distributions of the velocity uncertainty, along with their local non-zero covariance due to the overlap of particle images within interrogation windows. A robust and fast method for computing uncertainty in PIV-based pressure mean and RMS estimations should be feasible. Instantaneous PIV-based pressure uncertainty is subject to the same limitations as the correction framework, however. As well, neither method can currently account for errors due to truncation error effects arising from spatial or temporal under resolution of the flow scales.

Effect of three-dimensionality on reconstruction framework. Notably, for planar PIV measurements, the accuracy of PIV-based pressure estimates deteriorates rapidly in regions of three-dimensional flow. However, within the reconstruction framework, regions of three-dimensionality will register sharply as errors in the source terms of the formulation through the propagation of non-zero velocity divergence and pressure gradient curl. A systematic study of the use of the planar reconstruction configuration in three-dimensional flows will characterize its performance in these flows. As well, the possibility of reconstructing errors in the pressure gradient field induced by the presence of three-dimensional flow can be explored. In particular, the specific form that three-dimensional errors take $\epsilon_{u,3D} = (0, 0, -w)$, $\epsilon_{\nabla p,3D} = (w\partial u/\partial z, w\partial v/\partial x, 0)$ has potential to be exploited.

Stereo three-dimensional reconstruction. The use of stereo PIV measurements in conjunction with the reconstruction methods utilized in this thesis will allow for a reduced order representation of the entire three-dimensional flow field. Use of the reconstructed field in PIV-based pressure solvers will overcome the limitations of using stereo and planar PIV data in three-dimensional flows. In addition, the reconstruction of all three velocity components opens up the possibility of utilizing the governing equations to inform a physics-based reconstruction.

Single degree of freedom VIV. The degree to which secondary harmonics contribute to the response in free vibrations remains an open question, along with their appropriate modelling. An analytic framework which incorporates the ability of the forcing function and cylinder response to have two harmonics is necessary for characterization of the VIV response across the entire operating range, particularly outside of lock-in.

Vortex Force in VIV. In this thesis, the generation and advection of the added vorticity due to body acceleration in vortex-induced vibration is shown to be a significant contributor to the amplification of the forcing function in the 2S regime. Furthermore, the stability of this mechanism is shown to predict reasonable bounds for the transition between flow regimes. Experimental analysis of transient PIV data during flow regime changes can better characterize the physical mechanisms governing the transfer between regimes and inform on enhanced large amplitude models for the forcing function in VIV.

Pressure-based vortex tracking. The solution of the pressure field through the Poisson equation facilitates a simple decomposition of the flow velocity field into solenoidal and rotational components. The rotational component contributes completely through the source term of the Poisson equation. Hence, pressure minima associated with flow rotation can easily be decomposed and identified for the purpose of vortex tracking. While the commonly used Q-criterion seeks this through analysis of derivative quantities, the spatial integration of the Poisson equation has significant benefits in the mitigation of spatial noise and may be more robust for experimental data.

References

[1] T. Kármán. On the mechanism of the drag a moving body experiences in a fluid. *Progress in Aerospace Sciences*, 59:16–19, May 1911. DOI.

[2] C. Wieselsberger. New data on the laws of fluid resistance. Technical report 84, NACA, 1922. URL.

[3] A. Betz. A method for the direct determination of wing-section drag. Technical report NACA-TM-337, United States. National Advisory Committee for Aeronautics., 1925. URL.

[4] A. Thom. An investigation of fluid flow in two dimensions. Technical report 1194, Aeronautical Research Committee, 1928. URL.

[5] B. Jones. *The Measurement of Profile Drag by the Pitot-traverse Method*, volume Technical Report 1688 of *Aeronautical Research Committee. Reports and Memoranda*. H.M. Stationery Office, 1936. URL.

[6] G. I. Taylor. The spectrum of turbulence. *Proceedings of the Royal Society of London. Series A - Mathematical and Physical Sciences*, 164(919):476–490, 1938. DOI.

[7] C. Darwin. Note on hydrodynamics. *Mathematical Proceedings of the Cambridge Philosophical Society*, 49(2):342–354, 1953. DOI.

[8] N. Curle. The influence of solid boundaries upon aerodynamic sound. *Proceedings of the Royal Society of London. Series A. Mathematical and Physical Sciences*, 231(1187):505–514, 1955. DOI.

[9] A. Roshko. On the wake and drag of bluff bodies. *Journal of the Aeronautical Sciences*, 22(2):124–132, 1955. DOI.

[10] D. J. Tritton. Experiments on the flow past a circular cylinder at low Reynolds numbers. *Journal of Fluid Mechanics*, 6(4):547–567, 1959. DOI.

[11] M. S. Bloor. The transition to turbulence in the wake of a circular cylinder. *Journal of Fluid Mechanics*, 19(02):290, 1964. DOI.

[12] B. Vickery and R. Watkins. Flow-induced vibrations of cylindrical structures. In *Hydraulics and Fluid Mechanics*, Proceedings of the First Australasian Conference, pages 213–241. Elsevier, University of Western Australia, 1964. DOI.

[13] P. W. Bearman. Investigation of the flow behind a two-dimensional model with a blunt trailing edge and fitted with splitter plates. *Journal of Fluid Mechanics*, 21(02):241, 1965. DOI.

[14] C. Scruton. On the wind-excited oscillations of towers, stacks and masts. In *Proceedings of the Symposium Wind Effects on Buildings and Structures*, volume 16, pages 798–836, London. HMSO, 1965

[15] P. W. Bearman. On vortex street wakes. *Journal of Fluid Mechanics*, 28(4):625–641, 1967. DOI.

[16] G. H. Koopmann. The vortex wakes of vibrating cylinders at low Reynolds numbers. *Journal of Fluid Mechanics*, 28(03):501, 1967. DOI.

[17] C. C. Feng. *The measurement of vortex induced effects in flow past stationary and oscillating circular and D-section cylinders*. MASc Thesis, University of British Columbia, 1968. URL.

[18] Y. N. Chen. Fluctuating lift forces of the Karman vortex streets on single circular cylinders and in tube bundles: Part 2 - lift forces of single cylinders. *Journal of Engineering for Industry*, 94(2):613–618, 1972. DOI.

[19] M. Zdravkovich and J. Volk. Effect of shroud geometry on the pressure distributed around a circular cylinder. *Journal of Sound and Vibration*, 20(4):451–455, 1972. DOI.

[20] R. Skop and O. Griffin. A model for the vortex-excited resonant response of bluff cylinders. *Journal of Sound and Vibration*, 27(2):225–233, 1973. DOI.

[21] S. Kacker, B. Pennington, and R. Hill. Fluctuating lift coefficient for a circular cylinder in cross flows. *Journal of Mechanical Engineering Science*, 16, 4, 1974. DOI.

[22] P. K. Stansby. The effects of end plates on the base pressure coefficient of a circular cylinder. *The Aeronautical Journal*, 78(757):36–37, 1974. DOI.

[23] M. E. Davies. A comparison of the wake structure of a stationary and oscillating bluff body, using a conditional averaging technique. *Journal of Fluid Mechanics*, 75(2):209–231, 1976. DOI.

[24] J. H. Gerrard. The wakes of cylindrical bluff bodies at low Reynolds number. *Philosophical Transactions of the Royal Society of London. Series A, Mathematical and Physical Sciences*, 288(1354):351–382, 1978. URL.

[25] T. Sarpkaya. Vortex-induced oscillations: A selective review. *Journal of Applied Mechanics*, 46(2):241–258, 1979. DOI.

[26] M. Zdravkovich. Review and classification of various aerodynamic and hydrodynamic means for suppressing vortex shedding. *Journal of Wind Engineering and Industrial Aerodynamics*, 7(2):145–189, 1981. DOI.

[27] S. Lloyd. Least squares quantization in PCM. *IEEE Transactions on Information Theory*, 28(2):129–137, 1982. DOI.

[28] P. G. Saffman and J. C. Schatzman. An inviscid model for the vortex-street wake. *Journal of Fluid Mechanics*, 122:467, September 1982. DOI.

[29] P. W. Bearman. Vortex shedding from oscillating bluff bodies. *Annual Review of Fluid Mechanics*, 16(1):195–222, 1984. DOI.

[30] R. Blevins. Review of sound induced by vortex shedding from cylinders. *Journal of Sound and Vibration*, 92(4):455–470, 1984. DOI.

[31] R. D. Blevins. The effect of sound on vortex shedding from cylinders. *Journal of Fluid Mechanics*, 161:217, 1985. DOI.

[32] T. Wei and C. R. Smith. Secondary vortices in the wake of circular cylinders. *Journal of Fluid Mechanics*, 169:513, August 1986. DOI.

[33] C. Norberg and B. Sunden. Turbulence and reynolds number effects on the flow and fluid forces on a single cylinder in cross flow. *Journal of Fluids and Structures*, 1(3):337–357, 1987. DOI.

[34] C. Norberg. Effect of Reynolds number and low-intensity freestream turbulence on the flow around a circular cylinder. Technical report 2, Chalmers University of Technology, 1987, page 55

[35] M. Provansal, C. Mathis, and L. Boyer. Bénard-von Kármán instability: transient and forced regimes. *Journal of Fluid Mechanics*, 182:1, September 1987. DOI.

[36] L. Sirovich. Turbulence and the dynamics of coherent structures. II. Symmetries and transformations. *Quarterly of Applied Mathematics*, 45(3):573–582, 1987. DOI.

[37] R. Abraham, J. E. Marsden, and T. Ratiu. *Manifolds, Tensor Analysis, and Applications*. J. E. Marsden, L. Sirovich, and F. John, editors, volume 75 of *Applied Mathematical Sciences*. Springer New York, New York, NY, 1988. DOI.

[38] J. Hunt, A. Wray, and P. Moin. Eddies streams and convergence zones in turbulent flows. In *Proceedings of the 1988 Summer Program*, December 1988

[39] R. Aris. *Vectors, Tensors, and the Basic Equations of Fluid Mechanics*. Dover books on engineering. Dover Publications, New York, dover ed edition, 1989. ISBN.

[40] G. Parkinson. Phenomena and modelling of flow-induced vibrations of bluff bodies. *Progress in Aerospace Sciences*, 26(2):169–224, 1989. DOI.

[41] C. Williamson. Oblique and parallel modes of vortex shedding in the wake of a circular cylinder at low Reynolds numbers. *Journal of Fluid Mechanics*, 206:579–627, September 1989. DOI.

[42] R. A. Antonia and S. Rajagopalan. Determination of drag of a circular cylinder. *AIAA Journal*, 28(10):1833–1834, 1990. DOI.

[43] T. A. Fox and G. S. West. On the use of end plates with circular cylinders. *Experiments in Fluids*, 9(4):237–239, 1990. DOI.

[44] J. L. D. Ribeiro. Fluctuating lift and its spanwise correlation on a circular cylinder in a smooth and in a turbulent flow: a critical review. *Journal of Wind Engineering and Industrial Aerodynamics*, 40(2):179–198, 1992. DOI.

[45] C. Williamson. The natural and forced formation of spot-like 'vortex dislocations' in the transition of a wake. *Journal of Fluid Mechanics*, 243:393, October 1992. DOI.

[46] B. Bays-Muchmore and A. Ahmed. On streamwise vortices in turbulent wakes of cylinders. *Physics of Fluids A: Fluid Dynamics*, 5(2):387–392, 1993. DOI.

[47] A. Roshko. Perspectives on bluff body aerodynamics. *Journal of Wind Engineering and Industrial Aerodynamics*, 49(1-3):79–100, 1993. DOI.

[48] P. G. Saffman. *Vortex Dynamics*. Cambridge University Press, 1st edition, January 1993. DOI.

[49] S. M. Song, S. Napel, G. H. Glover, and N. J. Pelc. Noise reduction in three-dimensional phase-contrast MR velocity measurementsl. *Journal of Magnetic Resonance Imaging*, 3(4):587–596, 1993. DOI.

[50] H. Mansy, P.-M. Yang, and D. R. Williams. Quantitative measurements of three-dim ensional structures in the wake of a circular cylinder. *Journal of Fluid Mechanics*, 270:277–296, July 1994. DOI.

[51] B. R. Noack and H. Eckelmann. A global stability analysis of the steady and periodic cylinder wake. *Journal of Fluid Mechanics*, 270:297–330, July 1994. DOI.

[52] J. Wu, J. Sheridan, J. Soria, and M. Welsh. An experimental investigation of streamwise vortices in the wake of a bluff body. *Journal of Fluids and Structures*, 8(6):621–625, 1994. DOI.

[53] J. Wu, J. Sheridan, M. C. Welsh, K. Hourigan, and M. Thompson. Longitudinal vortex structures in a cylinder wake. *Physics of Fluids*, 6(9):2883–2885, 1994. DOI.

[54] J. Jeong and F. Hussain. On the identification of a vortex. *Journal of Fluid Mechanics*, 285:69–94, February 1995. DOI.

[55] J.-C. Lin, J. Towfighi, and D. Rockwell. Instantaneous structure of the near-wake of a circular cylinder on the effect of Reynolds number. *Journal of Fluids and Structures*, 9:409–418, 1995

[56] H.-Q. Zhang, U. Fey, B. R. Noack, M. König, and H. Eckelmann. On the transition of the cylinder wake. *Physics of Fluids*, 7(4):779–794, 1995. DOI.

[57] A. Khalak and C. Williamson. Dynamics of a hydroelastic cylinder with very low mass and damping. *Journal of Fluids and Structures*, 10(5):455–472, 1996. DOI.

[58] J.-C. Lin and D. Rockwell. Force identification by vorticity fields: techniques based on flow imaging. *Journal of Fluids and Structures*, 10(6):663–668, 1996. DOI.

[59] C. Williamson. Mode A secondary instability in wake transition. *Physics of Fluids*, 8(6):1680–1682, 1996. DOI.

[60] C. Williamson. Three-dimensional wake transition. *Journal of Fluid Mechanics*, 328:345–407, 1996. DOI.

[61] C. Williamson. Vortex dynamics in the cylinder wake. *Annual Review of Fluid Mechanics*, 28:477–539, 1996. URL.

[62] M. L. Jakobsen, T. P. Dewhirst, and C. A. Greated. Particle image velocimetry for predictions of acceleration fields and force within fluid flows. *Measurement Science and Technology*, 8(12):1502–1516, 1997. DOI.

[63] A. Khalak and C. Williamson. Fluid forces and dynamics of a hydroelastic structure with very low mass and damping. *Journal of Fluids and Structures*, 11(8):973–982, 1997. DOI.

[64] A. Melling. Tracer particles and seeding for particle image velocimetry. *Measurement Science and Technology*, 8(12):1406–1416, 1997. DOI.

[65] A. Prasad and C. Williamson. Three-dimensional effects in turbulent bluff-body wakes. *Journal of Fluid Mechanics*, 343:235–265, 1997. DOI.

[66] T. Takahashi. On the decomposition of drag components from wake flow measurements. In *35th Aerospace Sciences Meeting and Exhibit*, Reno,NV,U.S.A. American Institute of Aeronautics and Astronautics, January 1997. DOI.

[67] M. Unal, J.-C. Lin, and D. Rockwell. Force prediction by PIV imaging: a momentum-based approach. *Journal of Fluids and Structures*, 11(8):965–971, 1997. DOI.

[68] F. Bouak and J. Lemay. Passive control of the aerodynamic forces acting on a circular cylinder. *Experimental Thermal and Fluid Science*, 16(1-2):112–121, 1998. DOI.

[69] B. Jiang. *The Least-Squares Finite Element Method: Theory and Applications in Computational Fluid Dynamics and Electromagnetics*. Scientific Computation. Springer Berlin Heidelberg, Berlin, Heidelberg, 1998. DOI.

[70] P. Moin and K. Mahesh. Direct numerical simulation: a tool in turbulence research. *Annual Review of Fluid Mechanics*, 30(1):539–578, 1998. DOI.

[71] H. Persillon and M. Braza. Physical analysis of the transition to turbulence in the wake of a circular cylinder by three-dimensional Navier–Stokes simulation. *Journal of Fluid Mechanics*, 365:23–88, June 1998. DOI.

[72] J. D. Anderson. *Aircraft Performance and Design*. WCB/McGraw-Hill, Boston, 1999. ISBN.

[73] T. Baur and J. Köngeter. PIV with high temporal resolution for the determination of local pressure reductions from coherent turbulent phenomena. In *3rd Int. Workshop on Particle Image Velocimetry*, pages 101–106, Santa Barbara, 1999

[74] R. Gurka, A. Liberzon, D. Hefetz, D. Rubinstein, and U. Shavit. Computation of pressure distribution using piv velocity data. In *Workshop on particle image velocimetry*, volume 2, pages 1–6, September 1999

[75] A. Khalak and C. Williamson. Motions, forces and mode transitions in vortex-induced vibrations at low mass-damping. *Journal of Fluids and Structures*, 13(7-8):813–851, 1999. DOI.

[76] F. Noca, D. Shiels, and D. Jeon. A comparison of methods for evaluating time-dependent fluid dynamic forces on bodies, using only velocity fields and their derivatives. *Journal of Fluids and Structures*, 13(5):551–578, 1999. DOI.

[77] C. van Dam. Recent experience with different methods of drag prediction. *Progress in Aerospace Sciences*, 35(8):751–798, 1999. DOI.

[78] G. K. Batchelor. *An Introduction to Fluid Dynamics*. Cambridge University Press, Cambridge, 2000. ISBN.

[79] R. Govardhan and C. Williamson. Modes of vortex formation and frequency response of a freely vibrating cylinder. *Journal of Fluid Mechanics*, 420:85–130, October 2000. DOI.

[80] L. N. Trefethen. *Spectral Methods in MATLAB*. Society for Industrial and Applied Mathematics, January 2000. DOI.

[81] G. Auchmuty and J. C. Alexander. L2 well-posedness of planar div-curl systems. *Archive for Rational Mechanics and Analysis*, 160(2):91–134, 2001. DOI.

[82] E. H. Dowell and K. C. Hall. Modeling of fluid-structure interaction. *Annual Review of Fluid Mechanics*, 33(1):445–490, 2001. DOI.

[83] A. Leonard and A. Roshko. Aspects of flow-induced vibration. *Journal of Fluids and Structures*, 15(3-4):415–425, 2001. DOI.

[84] S. Hosokawa, S. Moriyama, A. Tomiyama, and N. Takada. PIV measurement of pressure distributions about single bubbles. *Journal of Nuclear Science and Technology*, 40(10):754–762, 2003. DOI.

[85] C. Norberg. Fluctuating lift on a circular cylinder: review and new measurements. *Journal of Fluids and Structures*, 17(1):57–96, 2003. DOI.

[86] Y. Tong, S. Lombeyda, A. N. Hirani, and M. Desbrun. Discrete multiscale vector field decomposition. *ACM Transactions on Graphics*, 22(3):445–452, 2003. DOI.

[87] M. Facchinetti, E. de Langre, and F. Biolley. Coupling of structure and wake oscillators in vortex-induced vibrations. *Journal of Fluids and Structures*, 19(2):123–140, 2004. DOI.

[88] J. Fransson, P. Konieczny, and P. Alfredsson. Flow around a porous cylinder subject to continuous suction or blowing. *Journal of Fluids and Structures*, 19(8):1031–1048, 2004. DOI.

[89] N. Jauvtis and C. Williamson. The effect of two degrees of freedom on vortex-induced vibration at low mass and damping. *Journal of Fluid Mechanics*, 509:23–62, June 2004. DOI.

[90] T. Sarpkaya. A critical review of the intrinsic nature of vortex-induced vibrations. *Journal of Fluids and Structures*, 19(4):389–447, 2004. DOI.

[91] C. Williamson and R. Govardhan. Vortex-induced vibrations. *Annual Review of Fluid Mechanics*, 36(1):413–455, 2004. DOI.

[92] M.-H. Wu, C.-Y. Wen, R.-H. Yen, M.-C. Weng, and A.-B. Wang. Experimental and numerical study of the separation angle for flow around a circular cylinder at low Reynolds number. *Journal of Fluid Mechanics*, 515:233–260, September 2004. DOI.

[93] A. Etebari and P. P. Vlachos. Improvements on the accuracy of derivative estimation from DPIV velocity measurements. *Experiments in Fluids*, 39(6):1040–1050, 2005. DOI.

[94] N. Fujisawa, S. Tanahashi, and K. Srinivas. Evaluation of pressure field and fluid forces on a circular cylinder with and without rotational oscillation using velocity data from PIV measurement. *Measurement Science and Technology*, 16(4):989–996, 2005. DOI.

[95] R. Gabbai and H. Benaroya. An overview of modeling and experiments of vortex-induced vibration of circular cylinders. *Journal of Sound and Vibration*, 282(3-5):575–616, 2005. DOI.

[96] G. Haller. An objective definition of a vortex. *Journal of Fluid Mechanics*, 525:1–26, February 2005. DOI.

[97] B. W. v. Oudheusden, F. Scarano, N. P. v. Hinsberg, and D. W. Watt. Phase-resolved characterization of vortex shedding in the near wake of a square-section cylinder at incidence. *Experiments in Fluids*, 39(1):86–98, 2005. DOI.

[98] S. Tavoularis. *Measurement in Fluid Mechanics*. Cambridge University Press, Cambridge ; New York, 2005. ISBN.

[99] J.-Z. Wu, Z.-L. Pan, and X.-Y. Lu. Unsteady fluid-dynamic force solely in terms of control-surface integral. *Physics of Fluids*, 17(9):098102, 2005. DOI.

[100] J. O. Dabiri. On the estimation of swimming and flying forces from wake measurements. *Journal of Experimental Biology*, 209(7):1364–1364, 2006. DOI.

[101] J. Dahl, F. Hover, and M. Triantafyllou. Two-degree-of-freedom vortex-induced vibrations using a force assisted apparatus. *Journal of Fluids and Structures*, 22(6-7):807–818, 2006. DOI.

[102] G. E. Elsinga, F. Scarano, B. Wieneke, and B. W. Van Oudheusden. Tomographic particle image velocimetry. *Experiments in Fluids*, 41(6):933–947, 2006. DOI.

[103] R. N. Govardhan and C. Williamson. Defining the ‘modified Griffin plot’ in vortex-induced vibration: revealing the effect of Reynolds number using controlled damping. *Journal of Fluid Mechanics*, 561:147, August 2006. DOI.

[104] J. F. Huang, Y. Zhou, and T. Zhou. Three-dimensional wake structure measurement using a modified PIV technique. *Experiments in Fluids*, 40(6):884–896, 2006. DOI.

[105] X. Liu and J. Katz. Instantaneous pressure and material acceleration measurements using a four-exposure PIV system. *Experiments in Fluids*, 41(2):227–240, 2006. DOI.

[106] C. Poelma, W. B. Dickson, and M. H. Dickinson. Time-resolved reconstruction of the full velocity field around a dynamically-scaled flapping wing. *Experiments in Fluids*, 41(2):213–225, 2006. DOI.

[107] B. W. van Oudheusden, F. Scarano, and E. W. F. Casimiri. Non-intrusive load characterization of an airfoil using PIV. *Experiments in Fluids*, 40(6):988–992, 2006. DOI.

[108] F. M. White. *Viscous Fluid Flow*. McGraw-Hill series in mechanical engineering. McGraw-Hill Higher Education, New York, NY, 3rd ed edition, 2006. ISBN.

[109] J.-Z. Wu, H.-Y. Ma, and M.-D. Zhou. *Vorticity and Vortex Dynamics*. Springer, Berlin ; New York, 2006. ISBN.

[110] D. F. Kurtulus, F. Scarano, and L. David. Unsteady aerodynamic forces estimation on a square cylinder by TR-PIV. *Experiments in Fluids*, 42(2):185–196, 2007. DOI.

[111] O. Marzouk, A. H. Nayfeh, I. Akhtar, and H. N. Arafat. Modeling steady-state and transient forces on a cylinder. *Journal of Vibration and Control*, 13(7):1065–1091, 2007. DOI.

[112] Y. Murai, T. Nakada, T. Suzuki, and F. Yamamoto. Particle tracking velocimetry applied to estimate the pressure field around a Savonius turbine. *Measurement Science and Technology*, 18(8):2491–2503, 2007. DOI.

[113] M. Raffel, editor. *Particle Image Velocimetry: A Practical Guide*. Springer, Heidelberg ; New York, 2nd ed edition, 2007. ISBN.

[114] B. W. van Oudheusden, F. Scarano, E. W. M. Roosenboom, E. W. F. Casimiri, and L. J. Souverein. Evaluation of integral forces and pressure fields from planar velocimetry data for incompressible and compressible flows. *Experiments in Fluids*, 43(2-3):153–162, 2007. DOI.

[115] M. M. Bernitsas, K. Raghavan, Y. Ben-Simon, and E. M. H. Garcia. VIVACE (Vortex Induced Vibration Aquatic Clean Energy): A new concept in generation of clean and renewable energy from fluid flow. *Journal of Offshore Mechanics and Arctic Engineering*, 130(4):041101, 2008. DOI.

[116] H. Choi, W.-P. Jeon, and J. Kim. Control of flow over a bluff body. *Annual Review of Fluid Mechanics*, 40(1):113–139, 2008. DOI.

[117] O. Inoue and A. Sakuragi. Vortex shedding from a circular cylinder of finite length at low Reynolds numbers. *Physics of Fluids*, 20(3):033601, 2008. DOI.

[118] M. Méheut and D. Bailly. Drag-breakdown methods from wake measurements. *AIAA Journal*, 46(4):847–862, 2008. DOI.

[119] T. Morse, R. Govardhan, and C. Williamson. The effect of end conditions on the vortex-induced vibration of cylinders. *Journal of Fluids and Structures*, 24(8):1227–1239, 2008. DOI.

[120] A. Rencher and G. Schaalje. *Linear Models in Statistics*. Wiley-Interscience, Hoboken, New Jersey, 2nd ed edition, 2008. ISBN.

[121] C. Williamson and R. Govardhan. A brief review of recent results in vortex-induced vibrations. *Journal of Wind Engineering and Industrial Aerodynamics*, 96(6-7):713–735, 2008. DOI.

[122] J. Wissink and W. Rodi. Numerical study of the near wake of a circular cylinder. *International Journal of Heat and Fluid Flow*, 29(4):1060–1070, 2008. DOI.

[123] K. Zaman and D. Culley. Flow separation control over an airfoil: implication of wake-deficit reduction. In *4th Flow Control Conference*, Seattle, Washington. American Institute of Aeronautics and Astronautics, June 2008. DOI.

[124] D. G. Bohl and M. M. Koochesfahani. MTV measurements of the vortical field in the wake of an airfoil oscillating at high reduced frequency. *Journal of Fluid Mechanics*, 620:63–88, February 2009. DOI.

[125] L. David, T. Jardin, and A. Farcy. On the non-intrusive evaluation of fluid forces with the momentum equation approach. *Measurement Science and Technology*, 20(9):095401, 2009. DOI.

[126] C. Haigermoser. Application of an acoustic analogy to PIV data from rectangular cavity flows. *Experiments in Fluids*, 47(1):145–157, 2009. DOI.

[127] T. Jardin, L. Chatellier, A. Farcy, and L. David. Correlation between vortex structures and unsteady loads for flapping motion in hover. *Experiments in Fluids*, 47(4-5):655–664, 2009. DOI.

[128] S. Y. Jaw, J. H. Chen, and P. C. Wu. Measurement of pressure distribution from PIV experiments. *Journal of Visualization*, 12(1):27–35, 2009. DOI.

[129] T. N. Jukes and K.-S. Choi. Flow control around a circular cylinder using pulsed dielectric barrier discharge surface plasma. *Physics of Fluids*, 21(8):084103, 2009. DOI.

[130] T. L. Morse and C. Williamson. Prediction of vortex-induced vibration response by employing controlled motion. *Journal of Fluid Mechanics*, 634:5, September 2009. DOI.

[131] D. Ragni, A. Ashok, B. W. Van Oudheusden, and F. Scarano. Surface pressure and aerodynamic loads determination of a transonic airfoil based on particle image velocimetry. *Measurement Science and Technology*, 20(7):074005, 2009. DOI.

[132] F. Scarano and C. Poelma. Three-dimensional vorticity patterns of cylinder wakes. *Experiments in Fluids*, 47(1):69, 2009. DOI.

[133] G. R. Spedding and A. Hedenström. PIV-based investigations of animal flight. *Experiments in Fluids*, 46(5):749–763, 2009. DOI.

[134] J. J. Charonko, C. V. King, B. L. Smith, and P. P. Vlachos. Assessment of pressure field calculations from particle image velocimetry measurements. *Measurement Science and Technology*, 21(10):105401, 2010. DOI.

[135] D. Heitz, E. Mémin, and C. Schnörr. Variational fluid flow measurements from image sequences: synopsis and perspectives. *Experiments in Fluids*, 48(3):369–393, 2010. DOI.

[136] C. Morton and S. Yarusevych. Vortex shedding in the wake of a step cylinder. *Physics of Fluids*, 22(8):083602, 2010. DOI.

[137] T. Sueki, T. Takaishi, M. Ikeda, and N. Arai. Application of porous material to reduce aerodynamic sound from bluff bodies. *Fluid Dynamics Research*, 42(1):015004, 2010. DOI.

[138] J. D. Anderson. *Fundamentals of Aerodynamics*. Anderson series. McGraw-Hill, New York, 6th ed edition, 2011. ISBN.

[139] C. Atkinson, S. Coudert, J.-M. Foucaut, M. Stanislas, and J. Soria. The accuracy of tomographic particle image velocimetry for measurements of a turbulent boundary layer. *Experiments in Fluids*, 50(4):1031–1056, 2011. DOI.

[140] P. Bearman. Circular cylinder wakes and vortex-induced vibrations. *Journal of Fluids and Structures*, 27(5-6):648–658, 2011. DOI.

[141] M. Kotsonis, S. Ghaemi, L. Veldhuis, and F. Scarano. Measurement of the body force field of plasma actuators. *Journal of Physics D: Applied Physics*, 44(4):045204, 2011. DOI.

[142] M. Kühn, K. Ehrenfried, J. Bosbach, and C. Wagner. Large-scale tomographic particle image velocimetry using helium-filled soap bubbles. *Experiments in Fluids*, 50(4):929–948, 2011. DOI.

[143] T. Regert, L. Chatellier, B. Tremblais, and L. David. Determination of Pressure Fields from Time-Resolved data. In *9th International Symposium on Particle Image Velocimetry*, page 5, Tsukubu, Japan, July 2011

[144] M. A. Stremler, A. Salmanzadeh, S. Basu, and C. Williamson. A mathematical model of 2P and 2C vortex wakes. *Journal of Fluids and Structures*, 27(5-6):774–783, 2011. DOI.

[145] D. Violato, P. Moore, and F. Scarano. Lagrangian and Eulerian pressure field evaluation of rod-airfoil flow from time-resolved tomographic PIV. *Experiments in Fluids*, 50(4):1057–1070, 2011. DOI.

[146] R. de Kat and B. W. van Oudheusden. Instantaneous planar pressure determination from PIV in turbulent flow. *Experiments in Fluids*, 52(5):1089–1106, 2012. DOI.

[147] S. Ghaemi, D. Ragni, and F. Scarano. PIV-based pressure fluctuations in the turbulent boundary layer. *Experiments in Fluids*, 53(6):1823–1840, 2012. DOI.

[148] P. K. Kundu, I. M. Cohen, and D. R. Dowling. *Fluid Mechanics*. Academic Press, Waltham, MA, 5th ed edition, 2012. ISBN.

[149] A. Mohebbian and D. E. Rival. Assessment of the derivative-moment transformation method for unsteady-load estimation. *Experiments in Fluids*, 53(2):319–330, 2012. DOI.

[150] H. Neatby and S. Yarusevych. Towards reliable experimental drag measurements on an airfoil at low Reynolds numbers. In *42nd AIAA Fluid Dynamics Conference and Exhibit*, New Orleans, Louisiana. American Institute of Aeronautics and Astronautics, June 2012. DOI.

[151] D. Ragni, B. W. van Oudheusden, and F. Scarano. 3D pressure imaging of an aircraft propeller blade-tip flow by phase-locked stereoscopic PIV. *Experiments in Fluids*, 52(2):463–477, 2012. DOI.

[152] B. H. Timmins, B. W. Wilson, B. L. Smith, and P. P. Vlachos. A method for automatic estimation of instantaneous local uncertainty in particle image velocimetry measurements. *Experiments in Fluids*, 53(4):1133–1147, 2012. DOI.

[153] X. Wu, F. Ge, and Y. Hong. A review of recent studies on vortex-induced vibrations of long slender cylinders. *Journal of Fluids and Structures*, 28:292–308, January 2012. DOI.

[154] J. J. Charonko and P. P. Vlachos. Estimation of uncertainty bounds for individual particle image velocimetry measurements from cross-correlation peak ratio. *Measurement Science and Technology*, 24(6):065301, 2013. DOI.

[155] R. de Kat and B. Ganapathisubramani. Pressure from particle image velocimetry for convective flows: a Taylor's hypothesis approach. *Measurement Science and Technology*, 24(2):024002, 2013. DOI.

[156] C. M. de Silva, J. Philip, and I. Marusic. Minimization of divergence error in volumetric velocity measurements and implications for turbulence statistics. *Experiments in Fluids*, 54(7):1557, 2013. DOI.

[157] M. Novara and F. Scarano. A particle-tracking approach for accurate material derivative measurements with tomographic PIV. *Experiments in Fluids*, 54(8):1584, 2013. DOI.

[158] R. L. Panton. *Incompressible Flow*. Wiley, 1st edition, July 2013. DOI.

[159] S. Pröbsting, F. Scarano, M. Bernardini, and S. Pirozzoli. On the estimation of wall pressure coherence using time-resolved tomographic PIV. *Experiments in Fluids*, 54(7):1567, 2013. DOI.

[160] B. W. van Oudheusden. PIV-based pressure measurement. *Measurement Science and Technology*, 24(3):032001, 2013. DOI.

[161] J. Westerweel, G. E. Elsinga, and R. J. Adrian. Particle image velocimetry for complex and turbulent flows. *Annual Review of Fluid Mechanics*, 45(1):409–436, 2013. DOI.

[162] J. O. Dabiri, S. Bose, B. J. Gemmell, S. P. Colin, and J. H. Costello. An algorithm to estimate unsteady and quasi-steady pressure fields from velocity field measurements. *Journal of Experimental Biology*, 217(3):331–336, 2014. DOI.

[163] A. C. DeVoria, Z. R. Carr, and M. J. Ringuette. On calculating forces from the flow field with application to experimental volume data. *Journal of Fluid Mechanics*, 749:297–319, June 2014. DOI.

[164] K. Gharali and D. A. Johnson. PIV-based load investigation in dynamic stall for different reduced frequencies. *Experiments in Fluids*, 55(8):1803, 2014. DOI.

[165] C. Grouthier, S. Michelin, Y. Modarres-Sadeghi, and E. de Langre. Energy harvesting using vortex-induced vibrations of a hanging cable. In *Volume 4: Fluid-Structure Interaction*, V004T04A015, Anaheim, California, USA. American Society of Mechanical Engineers, July 2014. DOI.

[166] J. Kriegseis and D. E. Rival. Vortex force decomposition in the tip region of impulsively-started flat plates. *Journal of Fluid Mechanics*, 756:758–770, October 2014. DOI.

[167] K. P. Lynch and F. Scarano. Material acceleration estimation by four-pulse tomo-PIV. *Measurement Science and Technology*, 25(8):084005, 2014. DOI.

[168] C. Morton and S. Yarusevych. On vortex shedding from low aspect ratio dual step cylinders. *Journal of Fluids and Structures*, 44:251–269, January 2014. DOI.

[169] D. Schiavazzi, F. Coletti, G. Iaccarino, and J. K. Eaton. A matching pursuit approach to solenoidal filtering of three-dimensional velocity measurements. *Journal of Computational Physics*, 263:206–221, April 2014. DOI.

[170] A. Sciacchitano. *Uncertainty quantification in particle image velocimetry and advances in time-resolved image and data analysis.* PhD Thesis, Delft University of Technology, 2014. URL.

[171] A. Villegas and F. J. Diez. Evaluation of unsteady pressure fields and forces in rotating airfoils from time-resolved PIV. *Experiments in Fluids*, 55(4):1697, 2014. DOI.

[172] M. Zhao and L. Cheng. Vortex-induced vibration of a circular cylinder of finite length. *Physics of Fluids*, 26(1):015111, 2014. DOI.

[173] F. Auteri, M. Carini, D. Zagaglia, D. Montagnani, G. Gibertini, C. B. Merz, and A. Zanotti. A novel approach for reconstructing pressure from PIV velocity measurements. *Experiments in Fluids*, 56(2):45, 2015. DOI.

[174] I. Azijli and R. P. Dwight. Solenoidal filtering of volumetric velocity measurements using Gaussian process regression. *Experiments in Fluids*, 56(11):198, 2015. DOI.

[175] J. McClure, C. Morton, and S. Yarusevych. Flow development and structural loading on dual step cylinders in laminar shedding regime. *Physics of Fluids*, 27(6):063602, 2015. DOI.

[176] N. J. Neeteson and D. E. Rival. Pressure-field extraction on unstructured flow data using a Voronoi tessellation-based networking algorithm: a proof-of-principle study. *Experiments in Fluids*, 56(2):44, 2015. DOI.

[177] A. A. Rodríguez, E. Bertolazzi, and A. Valli. Simple finite element schemes for the solution of the curl-div system. *arXiv:1512.08532 [math]*, December 2015. URL.

[178] F. Scarano, S. Ghaemi, G. C. A. Caridi, J. Bosbach, U. Dierksheide, and A. Sciacchitano. On the use of helium-filled soap bubbles for large-scale tomographic PIV in wind tunnel experiments. *Experiments in Fluids*, 56(2):42, 2015. DOI.

[179] A. Sciacchitano, D. R. Neal, B. L. Smith, S. O. Warner, P. P. Vlachos, B. Wieneke, and F. Scarano. Collaborative framework for PIV uncertainty quantification: comparative assessment of methods. *Measurement Science and Technology*, 26(7):074004, 2015. DOI.

[180] T. Tronchin, L. David, and A. Farcy. Loads and pressure evaluation of the flow around a flapping wing from instantaneous 3D velocity measurements. *Experiments in Fluids*, 56(1):7, 2015. DOI.

[181] C. Wang and J. Wang. Discretization of div-curl systems by weak Galerkin finite element methods on polyhedral partitions. *arXiv:1501.04616 [math]*, January 2015. URL.

[182] I. Azijli, A. Sciacchitano, D. Ragni, A. Palha, and R. P. Dwight. A posteriori uncertainty quantification of PIV-based pressure data. *Experiments in Fluids*, 57(5):72, 2016. DOI.

[183] P. Blinde, D. Michaelis, B. V. Oudheusden, P.-E. Weiss, R. D. Kat, A. Laskari, J. Y. Jeon, L. David, D. Schanz, F. Huhn, S. Gesemann, M. Novara, C. Mcphaden, N. Neeteson, D. Rival, J. F. G. Schneiders, and F. Schrijer. Comparative assessment of PIV-based pressure evaluation techniques applied to a transonic base flow. In *18th International Symposium on applications of laser techniques to fluid mechanics*, page 35, Lisbon, Portugal, July 2016. URL.

[184] S. Gesemann, F. Huhn, D. Schanz, and A. Schröder. From noisy particle tracks to velocity, acceleration and pressure fields using B-splines and penalties. In *18th International Symposium on the Application of Laser and Imaging Techniques to Fluid Mechanics*, page 17, Lisbon, Portugal, July 2016. URL.

[185] F. Huhn, D. Schanz, S. Gesemann, and A. Schröder. FFT integration of instantaneous 3D pressure gradient fields measured by Lagrangian particle tracking in turbulent flows. *Experiments in Fluids*, 57(9):151, 2016. DOI.

[186] A. Laskari, R. de Kat, and B. Ganapathisubramani. Full-field pressure from snapshot and time-resolved volumetric PIV. *Experiments in Fluids*, 57(3):44, 2016. DOI.

[187] X. Liu, J. R. Moreto, and S. Siddle-Mitchell. Instantaneous pressure reconstruction from measured pressure gradient using rotating parallel ray method. In *54th AIAA Aerospace Sciences Meeting*, San Diego, California, USA. American Institute of Aeronautics and Astronautics, January 2016. DOI.

[188] J. McClure and S. Yarusevych. Surface and wake pressure fluctuations of a cylinder in transitional flow regime. In *18th International Symposium on the Application of Laser and Imaging Techniques to Fluid Mechanics*, Lisbon, Portugal, July 2016. URL.

[189] J. McClure and S. Yarusevych. Vortex shedding and structural loading characteristics of finned cylinders. *Journal of Fluids and Structures*, 65:138–154, August 2016. DOI.

[190] Z. Pan, J. Whitehead, S. Thomson, and T. Truscott. Error propagation dynamics of piv-based pressure field calculations: how well does the pressure poisson solver perform inherently? *Measurement Science and Technology*, 27(8):084012, 2016. DOI.

[191] D. Schanz, S. Gesemann, and A. Schröder. Shake-The-Box: Lagrangian particle tracking at high particle image densities. *Experiments in Fluids*, 57(5):70, 2016. DOI.

[192] J. F. G. Schneiders, G. C. A. Caridi, A. Sciacchitano, and F. Scarano. Large-scale volumetric pressure from tomographic PTV with HFSB tracers. *Experiments in Fluids*, 57(11):164, 2016. DOI.

[193] J. F. G. Schneiders, S. Pröbsting, R. P. Dwight, B. W. van Oudheusden, and F. Scarano. Pressure estimation from single-snapshot tomographic PIV in a turbulent boundary layer. *Experiments in Fluids*, 57(4):53, 2016. DOI.

[194] J. F. G. Schneiders and F. Scarano. Dense velocity reconstruction from tomographic PTV with material derivatives. *Experiments in Fluids*, 57(9):139, 2016. DOI.

[195] A. Sciacchitano and B. Wieneke. PIV uncertainty propagation. *Measurement Science and Technology*, 27(8):084006, 2016. DOI.

[196] Z. Wang, Q. Gao, C. Wang, R. Wei, and J. Wang. An irrotation correction on pressure gradient and orthogonal-path integration for PIV-based pressure reconstruction. *Experiments in Fluids*, 57(6):104, 2016. DOI.

[197] W. R. Graham, C. W. Pitt Ford, and H. Babinsky. An impulse-based approach to estimating forces in unsteady flow. *Journal of Fluid Mechanics*, 815:60–76, March 2017. DOI.

[198] A. Guissart, L. P. Bernal, G. Dimitriadis, and V. E. Terrapon. PIV-based estimation of unsteady loads on a flat plate at high angle of attack using momentum equation approaches. *Experiments in Fluids*, 58(5):53, 2017. DOI.

[199] K. N. Lucas, J. O. Dabiri, and G. V. Lauder. A pressure-based force and torque prediction technique for the study of fish-like swimming. *PLOS ONE*, 12(12):e0189225, 2017. R. Gurka, editor. DOI.

[200] J. McClure and S. Yarusevych. Instantaneous PIV/PTV-based pressure gradient estimation: a framework for error analysis and correction. *Experiments in Fluids*, 58(8):92, 2017. DOI.

[201] J. McClure and S. Yarusevych. Optimization of planar PIV-based pressure estimates in laminar and turbulent wakes. *Experiments in Fluids*, 58(5):62, 2017. DOI.

[202] D. E. Rival and B. v. Oudheusden. Load-estimation techniques for unsteady incompressible flows. *Experiments in Fluids*, 58(3):20, 2017. DOI.

[203] D. E. Schiavazzi, A. Nemes, S. Schmitter, and F. Coletti. The effect of velocity filtering in pressure estimation. *Experiments in Fluids*, 58(5):50, 2017. DOI.

[204] W. Terra, A. Sciacchitano, and F. Scarano. Aerodynamic drag of a transiting sphere by large-scale tomographic-PIV. *Experiments in Fluids*, 58(7):83, 2017. DOI.

[205] P. L. van Gent, D. Michaelis, B. W. van Oudheusden, P. .-É. Weiss, R. de Kat, A. Laskari, Y. J. Jeon, L. David, D. Schanz, F. Huhn, S. Gesemann, M. Novara, C. McPhaden, N. J. Neeteson, D. E. Rival, J. F. G. Schneiders, and F. F. J. Schrijer. Comparative assessment of pressure field reconstructions from particle image velocimetry measurements and Lagrangian particle tracking. *Experiments in Fluids*, 58(4):33, 2017. DOI.

[206] C. Y. Wang, Q. Gao, R. J. Wei, T. Li, and J. J. Wang. Spectral decomposition-based fast pressure integration algorithm. *Experiments in Fluids*, 58(7):84, 2017. DOI.

[207] F. Huhn, D. Schanz, P. Manovski, S. Gesemann, and A. Schröder. Time-resolved large-scale volumetric pressure fields of an impinging jet from dense Lagrangian particle tracking. *Experiments in Fluids*, 59(5):81, 2018. DOI.

[208] Y. J. Jeon, G. Gomit, T. Earl, L. Chatellier, and L. David. Sequential least-square reconstruction of instantaneous pressure field around a body from TR-PIV. *Experiments in Fluids*, 59(2):27, 2018. DOI.

[209] E. Limacher, C. Morton, and D. Wood. Generalized derivation of the added-mass and circulatory forces for viscous flows. *Physical Review Fluids*, 3(1):014701, 2018. DOI.

[210] C. J. McPhaden and D. E. Rival. Unsteady force estimation using a Lagrangian drift-volume approach. *Experiments in Fluids*, 59(4):64, 2018. DOI.

[211] G. Riches and C. Morton. One degree-of-freedom vortex-induced vibrations at constant Reynolds number and mass-damping. *Experiments in Fluids*, 59(10):157, 2018. DOI.

[212] J. F. G. Schneiders, F. Avallone, S. Pröbsting, D. Ragni, and F. Scarano. Pressure spectra from single-snapshot tomographic PIV. *Experiments in Fluids*, 59(3):57, 2018. DOI.

[213] T. Suzuki, L. Chatellier, Y. J. Jeon, and L. David. Unsteady pressure estimation and compensation capabilities of the hybrid simulation combining PIV and DNS. *Measurement Science and Technology*, 29(12):125305, 2018. DOI.

[214] R. Van De Meerendonk, M. Percin, and B. W. Van Oudheusden. Three-dimensional flow and load characteristics of flexible revolving wings. *Experiments in Fluids*, 59(10):161, 2018. DOI.

[215] P. L. van Gent, F. F. J. Schrijer, and B. W. van Oudheusden. Assessment of the pseudo-tracking approach for the calculation of material acceleration and pressure fields from time-resolved PIV: part I. Error propagation. *Measurement Science and Technology*, 29(4):045204, 2018. DOI.

[216] H.-P. Wang, Q. Gao, S.-Z. Wang, Y.-H. Li, Z.-Y. Wang, and J.-J. Wang. Error reduction for time-resolved PIV data based on Navier–Stokes equations. *Experiments in Fluids*, 59(10):149, 2018. DOI.

[217] E. Limacher, J. McClure, S. Yarusevych, and C. Morton. Comparison of momentum and impulse methods of force estimation using PIV data. In *13th International Symposium on Particle Image Velocimetry*, Munich, Germany, July 2019. URL.

[218] J. McClure, C. Pavan, and S. Yarusevych. Secondary vortex dynamics in the cylinder wake during laminar-to-turbulent transition. *Physical Review Fluids*, 4(12):124702, 2019. DOI.

[219] J. McClure and S. Yarusevych. Planar momentum balance in three-dimensional flows: applications to load estimation. *Experiments in Fluids*, 60(3):41, 2019. DOI.

[220] A. Spoelstra, L. de Martino Norante, W. Terra, A. Sciacchitano, and F. Scarano. On-site cycling drag analysis with the ring of fire. *Experiments in Fluids*, 60(6):90, 2019. DOI.

[221] J. W. Van der Kindere, A. Laskari, B. Ganapathisubramani, and R. de Kat. Pressure from 2D snapshot PIV. *Experiments in Fluids*, 60(2):32, 2019. DOI.

[222] E. Limacher, J. McClure, S. Yarusevych, and C. Morton. Comparison of momentum and impulse formulations for PIV-based force estimation. *Measurement Science and Technology*, 31(5):054001, 2020. DOI.

[223] G. Liu, H. Li, Z. Qiu, D. Leng, Z. Li, and W. Li. A mini review of recent progress on vortex-induced vibrations of marine risers. *Ocean Engineering*, 195:106704, 2020. DOI.

[224] A. Pirnia, J. McClure, S. D. Peterson, B. T. Helenbrook, and B. D. Erath. Estimating pressure fields from planar velocity data around immersed bodies; a finite element approach. *Experiments in Fluids*, 61(2):55, 2020. DOI.

[225] N. Sakib, A. Mychkovsky, J. Wiswall, R. Samaroo, and B. Smith. Effect of the boundary conditions, temporal, and spatial resolution on the pressure from PIV for an oscillating flow. *14th International Symposium on Particle Image Velocimetry*, 1(1), 2021. DOI.

[226] M. Nie, J. P. Whitehead, G. Richards, B. L. Smith, and Z. Pan. Error propagation dynamics of PIV-based pressure field calculation (3): what is the minimum resolvable pressure in a reconstructed field? *Experiments in Fluids*, 63(11):168, 2022. DOI.

[227] N.-P. Pallas and D. Bouris. Calculation of the pressure field for turbulent flow around a surface-mounted cube using the simple algorithm and piv data, 2022

[228] Y. Lin and H. Xu. Divergence–curl correction for pressure field reconstruction from acceleration in turbulent flows. *Experiments in Fluids*, 64(8):137, 2023. DOI.

Appendices

Appendix A

Circulation Calculation

Measurements of the circulation of the primary and secondary vortices in the wakes of stationary and oscillating cylinders support extended analysis of work presented in this thesis. The definition of vortex circulation, is the area integral of the plane normal vorticity inside a closer contour, Ω, defining a particular vortex (equation A.1).

$$\Gamma = \int_{\Omega} (\boldsymbol{\omega} \cdot \hat{\boldsymbol{n}}) \mathrm{d}A \tag{A.1}$$

The primary concern in computing vortex circulation, is the selection of the contour, Ω, defining the boundaries of a vortex. In fact, there is no accepted objective definition of a vortex (Hunt *et al.* 1988, Jeong and Hussain 1995, Haller 2005) despite improvements aimed at reducing dependencies on user specified thresholds and coordinate systems (Haller 2005). For the purposes of the current study, vortex identification is informed by the context of the quantitative analysis it serves. The demand for circulation measurements of the primary and secondary vortices in the wake is to deduce the vortex force acting on the cylinder, and the vorticity transport in the forming wake. Inspection of equation A.2, defining the vortex force in an infinite domain, reveals that the vortex force is dependent on the dynamics of all vorticity present in the flow field (Saffman 1993, Wu *et al.* 2006).

$$F_v = -\rho \frac{1}{N-1} \frac{\mathrm{d}}{\mathrm{d}t} \int_V (\boldsymbol{x} \times \boldsymbol{\omega}) \mathrm{d}V \tag{A.2}$$

This means vorticity present in highly sheared regions of the flow remains dynamically significant. However, these sheared regions are typically omitted from the bounds of many popular vortex detection methods, such as λ_2 and Q criterion metrics (Hunt *et al.* 1988, Jeong and Hussain 1995). For this reason, a vorticity thresholding method is utilized for defining the bounds of a vortex, in order to capture the entire extent of each wake vortex. The goal is to associate all vorticity in the wake with a particular vortex of a certain orientation, circulation, and size.

The thresholding method defines vortex boundaries according to a contour of constant vorticity, $\alpha\|\boldsymbol{\omega_{max}}\|$, practically chosen as a particular fraction of the global maximum vorticity. The threshold value (α) must be chosen carefully since the extent of the vortex boundaries is strongly dependent on the particular value. Therefore, any computed vortex statistics such as circulation will depend on the choice. For a single vortex in an unbounded flow, the threshold value could be lowered to approach zero and encompass the entirety of the vorticity associated with the vortex; however, in real flows, where multiple vortices and vorticity generating surfaces are present, a practical limit is reached when the vortex under consideration begins to coalesce with same signed vortices or boundary layers.

In order to account for the vorticity missed by the finite threshold, a linear fit of the circulation measurements with varying vorticity threshold is used to estimate the true circulation. The circulation predicted by the linear fits intersection with the y-axis ($\alpha = 0$) forms the measurement of the circulation. This methodology has practical benefits for use with experimental PIV-data, which yields phase averaged fields with noise, and with more limited field of views where only a limited view of the vortex core is available. It also eliminates the subjectivity involved in selecting a threshold value. The presupposing of a linear relationship with vorticity threshold is equivalent to the assumption that vorticity has a Gaussian distribution in space, centred at the point of maximum vorticity in the core of the vortex. The Gaussian distribution of vorticity arises in analytical solutions of the Navier-Stokes equations, such as the Lamb-Oseen vortex (Batchelor 2000).

$$\omega_z(r,t) = \frac{\Gamma}{\pi r_c^2(t)} \exp\left(-\frac{r^2}{r_c^2(t)}\right) \tag{A.3}$$

where $r_c(t) = \sqrt{(4\nu t + r_c(0)^2)}$ is the core radius of the vortex, which grows in time through viscous diffusion.

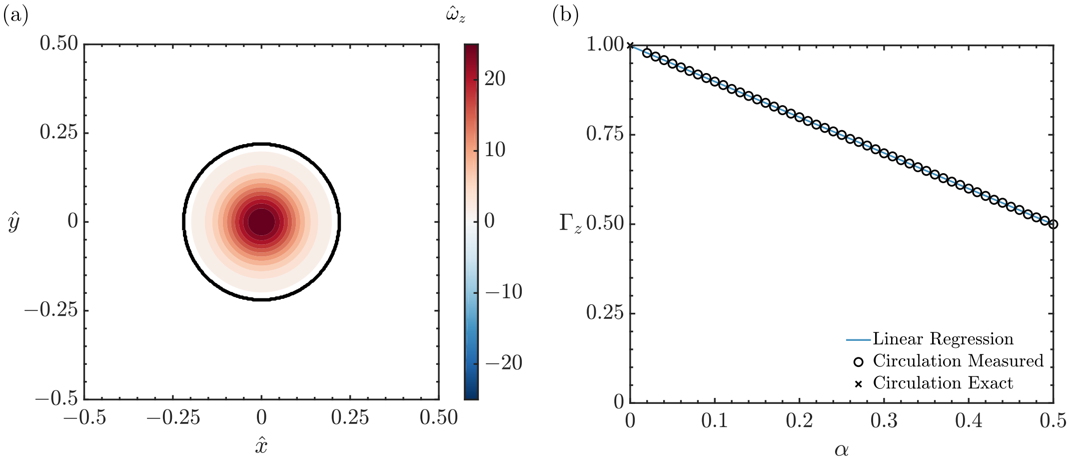

Figure A.1: Circulation measurement of a Lamb-Oseen vortex by vorticity thresholding: (a) vortex boundary for $\alpha = 0.01$ and (b) variation of circulation measurement with α compared to exact analytic solution.

Figure A.1 shows the results of measuring circulation using the vorticity thresholding method on the Lamb-Oseen vortex. A clear linear trend is observed with the threshold value, and an extrapolation of the linear trend intercepts the y-axis at the analytic value for the circulation. The uncertainty in the measurement can therefore be computed from the uncertainty associated with the extrapolation of the linear fit to the y-axis. If circulation measurements Γ_n are computed at n different threshold values α_n, then the best estimate (Rencher and Schaalje 2008) for the true circulation at $\alpha = 0$, assuming a Gaussian distribution of vorticity, is:

$$\Gamma = \overline{\Gamma}_n - \frac{\text{cov}(\alpha_n, \Gamma_n)}{\sigma_\alpha^2}\overline{\alpha}_n \tag{A.4}$$

and the uncertainty in the true circulation estimate, based on the goodness of the linear fit is:

$$\text{SE}(\Gamma) = \sqrt{\frac{1}{n-2}\left(\frac{\sigma_\Gamma^2}{\sigma_\alpha^2} - \frac{\text{cov}(\alpha_n, \Gamma_n)^2}{\sigma_\alpha^4}\right)} \tag{A.5}$$

A.1 Circulation calculation of primary vortices in the cylinder wake

In order to compute the circulation of the primary von Kármán vortices in the wakes of cylindrical bodies, a phase average of the vorticity fields is employed. For a stationary cylinder, the phase average is obtained from the the first two temporal coefficients of the POD (equation A.6), while for oscillating bodies, through a Hilbert transform of the position signal $y(t)$ (equation A.7), with a phase bin size of $\Delta\theta = 10°$.

$$\theta(t) = \arctan\left(\frac{\sqrt{\lambda_1}}{\sqrt{\lambda_2}}\frac{a_2}{a_1}\right) \tag{A.6}$$

$$\begin{aligned} \mathscr{H}(y)(t) &= \frac{1}{\pi}\int_{\infty}^{\infty}\left(\frac{y(\tau)}{t-\tau}\right)\mathrm{d}\tau \\ \theta(t) &= \arctan\left(\frac{\mathscr{H}(y)(t)}{y(t)}\right) \end{aligned} \tag{A.7}$$

A range of threshold values is then used to define the vortex boundary, typically $\alpha = 0.02-0.25$, with the vorticity threshold defined as $\alpha\|\boldsymbol{\omega_{max}}\|$, where $\|\boldsymbol{\omega_{max}}\|$ is the maximum of the spanwise vorticity in the wake region ($\hat{x} > 0.5$) over the set of phase averaged fields. The domain for searching for vortices was restricted to the wake region at $\hat{x} > 0.5$, and vortex boundaries which intersected the boundaries of the domain were deemed invalid

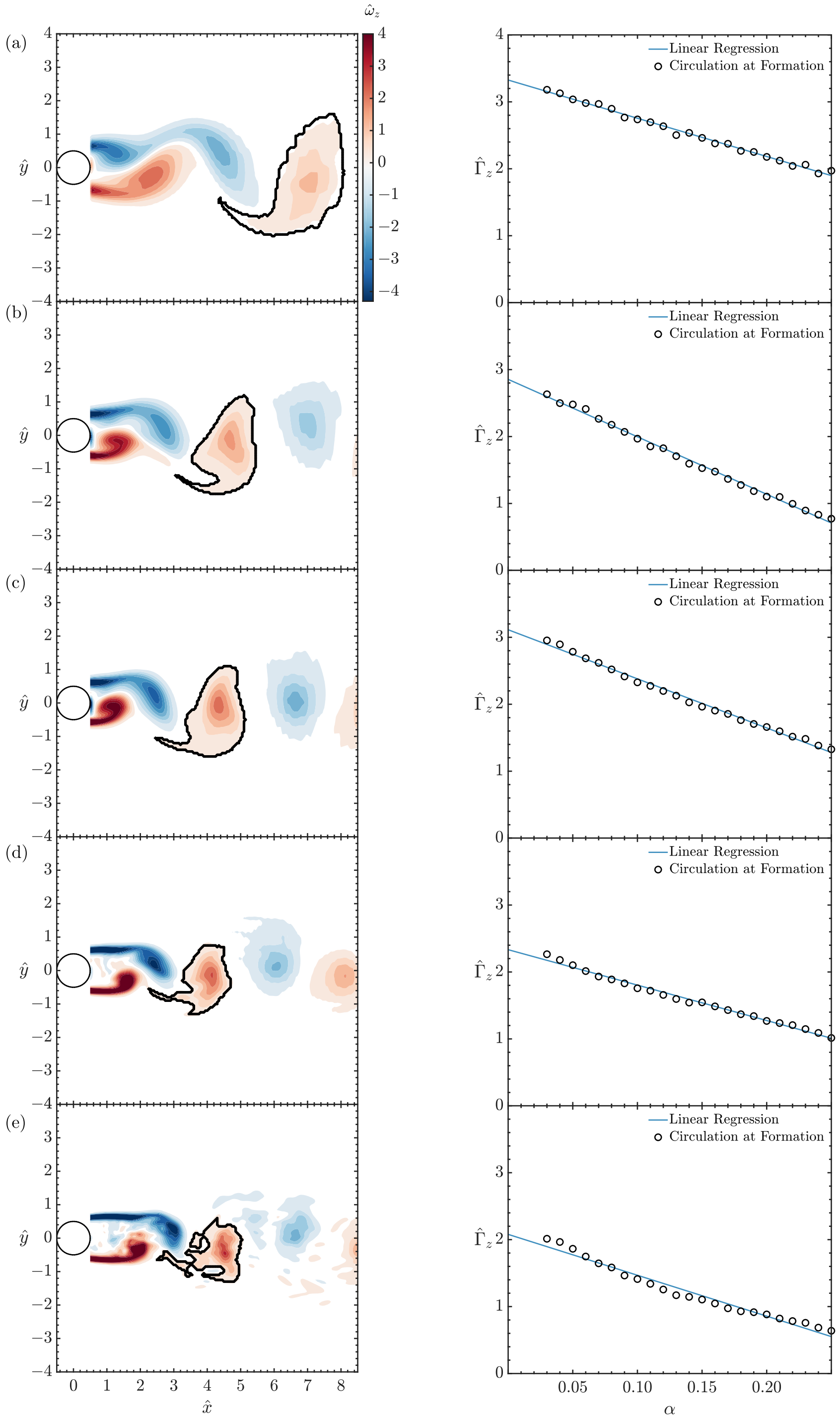

Figure A.2: Measurements of spanwise circulation for (a) $\mathrm{Re_D} = 100$, (b) $\mathrm{Re_D} = 220$, (c) $\mathrm{Re_D} = 300$, (d) $\mathrm{Re_D} = 800$, and (e) $\mathrm{Re_D} = 1575$. (left) Phase averaged vorticity fields showing the vortex boundary, and (right) variation of vortex circulation with vorticity threshold $\alpha\|\boldsymbol{\omega}\|$.

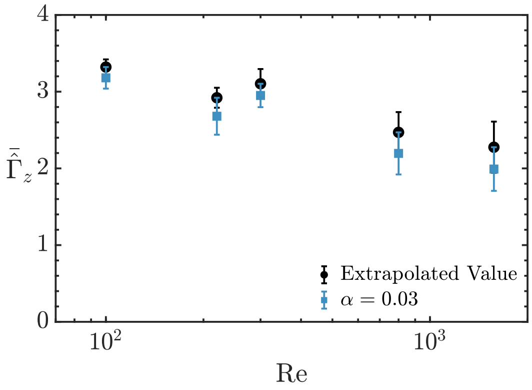

Figure A.3: Comparison of circulation measurements using extrapolated values and a threshold value of $\alpha = 0.03$. Error bars computed according to equation A.5, and the difference of the two measurements, respectively.

vortices in order to filter out vortices detected which were still attached to the separated shear layers. A circulation measurement of the largest vortex detected at each phase angle and at each threshold value is tabulated. The phase angle which yields the largest circulation measurements is then identified, which corresponds to a phase angle shortly following the shedding of the vortex and its detachment from the separated shear layer. The trend of measured circulation versus threshold value is analyzed, and data points are omitted corresponding to coalesced vortices which cause a sharp increase in the measured circulation with decreased α. For the DNS results at $\mathrm{Re_D} = 100 - 1575$, the contour defining the separated vortex at the lowest permissible α is shown in figure A.2. When the measured circulation of the vortex is plotted against the vorticity threshold value (figure A.2, right), a robust linear relationship is observed, validating the proposed extrapolation technique. The estimate of the true circulation is then the y-intercept value of the blue lines defining the linear fit of the data in figure A.2, and the uncertainty is defined by equation A.5. The differences between the extrapolated circulation estimates compared to those obtained for a vorticity threshold of $\alpha = 0.03$ are shown in figure A.3 along with the concomitant uncertainty estimates.

The same procedure is used for the measurement of phase-averaged circulation in experimental PIV data (figure A.4), where the field of view limits the extent of the vortex that can be measured, limiting the lowest value of α that can be utilized. For the 2P shedding regime case (figures A.4c,d), the close proximity of the two same-signed vortices during formation limits the permissible threshold values significantly, leading to a larger extrapolation region in the methodology, and correspondingly, an amplification of the uncertainty in the measurement. Despite the increase in complexity of the wake vortices for the oscillating cases, and the addition of experimental error, linear dependence of circulation on vorticity threshold values can be found for all the cases investigated.

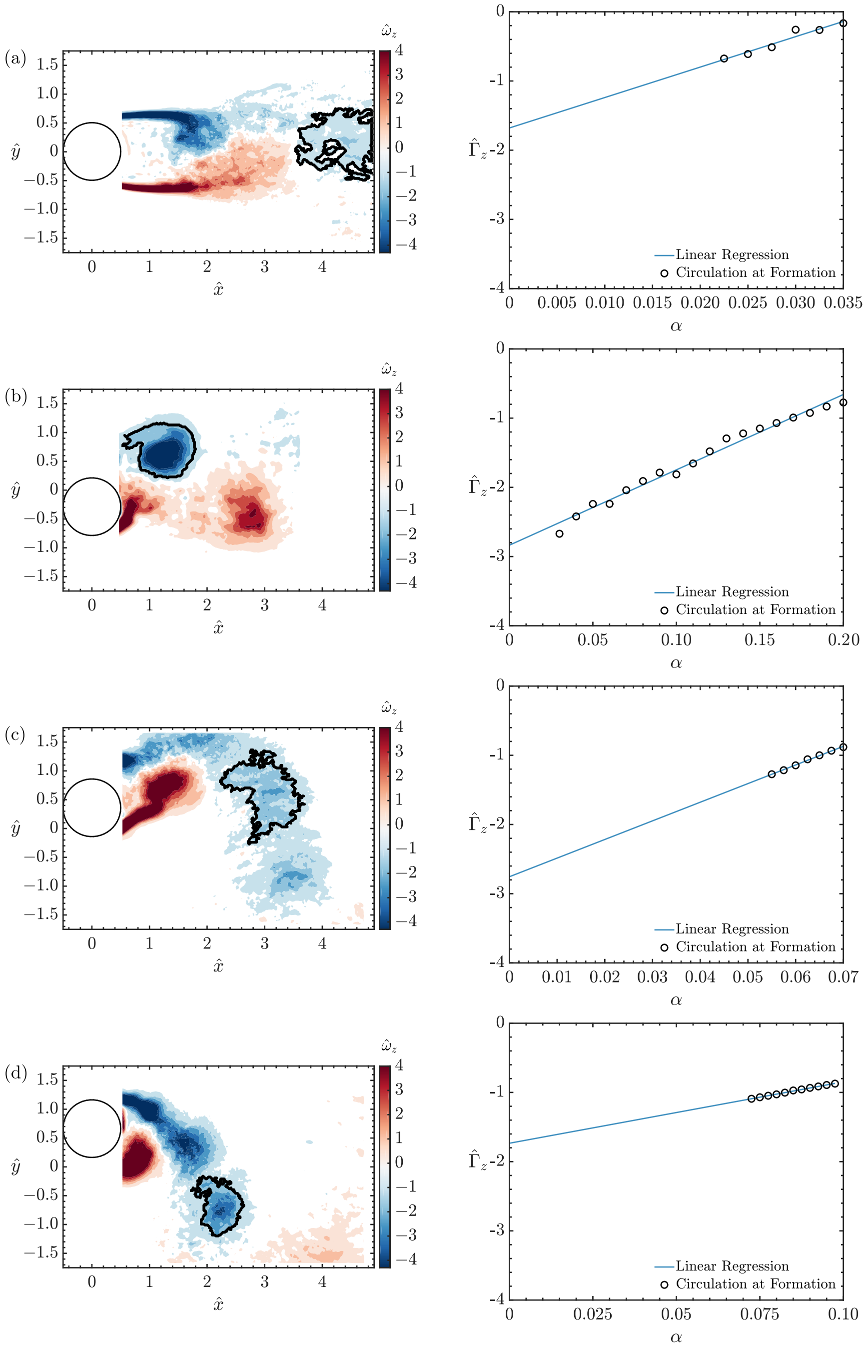

Figure A.4: Measurements of spanwise circulation for (a) stationary cylinder, (b) 2S, (c) 2P - upper vortex, and (d) 2P - lower vortex. (left) Phase averaged vorticity fields showing the vortex boundary, and (right) variation of vortex circulation with vorticity threshold $\alpha\|\boldsymbol{\omega}\|$.

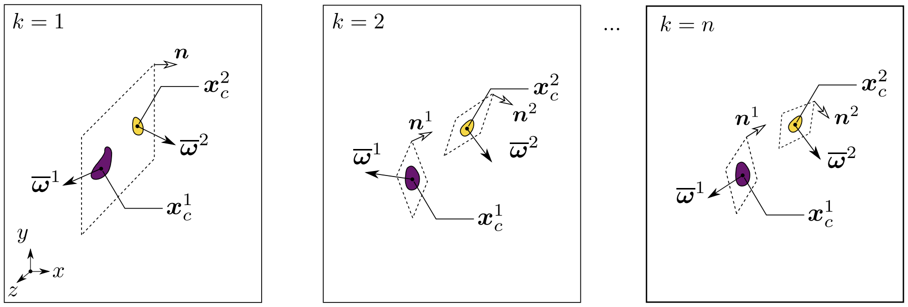

Figure A.5: Schematic of the iterative, three-dimensional vortex detection code. The code converges on the individual vortex orientation ($\overline{\varpi}_i^j$), centroid ($\overline{x}_i^j$), diameter (d^j), and circulation (Γ^j).

A.2 Circulation calculation of secondary vortices in the cylinder wake

The quantitative analysis of vortex statistics in three dimensions is explored in McClure *et al.* (2019). Vortex detection in three-dimensions is significantly more challenging due to the need to resolve vortex orientation along with the bounds of the vortices in three-dimensional space. No established tool exists for quantifying vortex orientation; hence, to facilitate the accurate measurement of statistics pertaining to the primary and secondary vortices, an iterative, three-dimensional, vortex identification code is developed. The code operates as follows: for a three-dimensional realization of a velocity field at a certain time, $\mathbf{u}(\mathbf{x}, t)$, an initial streamwise normal plane is specified at $\hat{x} = 2.5$ and vortices intersecting the plane are detected, where the j^{th} vortex is defined by its boundary, Ω^j. The code then computes the three-dimensional orientation ($\bar{\boldsymbol{\omega}}^j$), centroid ($\bar{\boldsymbol{x}}^j$), diameter ($d^j$), and circulation ($\Gamma^j$) for the j vortices intersecting the plane, as defined in equations A.8-A.11.

$$\bar{\boldsymbol{\omega}} = \frac{\int_\Omega \boldsymbol{\omega} \mathrm{d}A}{\|\int_\Omega \boldsymbol{\omega} \mathrm{d}A\|} \tag{A.8}$$

$$\bar{\mathbf{x}} = \frac{\int_\Omega \mathbf{x}(\boldsymbol{\omega} \cdot \hat{\mathbf{n}}) \mathrm{d}A}{\int_\Omega (\boldsymbol{\omega} \cdot \hat{\mathbf{n}}) \mathrm{d}A} \tag{A.9}$$

$$d = \sqrt{\frac{4}{\pi} \int_\Omega \mathrm{d}A} \tag{A.10}$$

$$\Gamma = \int_\Omega (\boldsymbol{\omega} \cdot \hat{\mathbf{n}}) \mathrm{d}A \tag{A.11}$$

Specifically, the code proceeds iteratively for each vortex by realigning the sample plane normal to the orientation according to the schematic shown in figure A.5. In the first iteration ($k = 1$), a binary image is obtained by thresholding the input slice plane for $Q > 0.01$, and continuous regions of the thresholded criterion are identified (e.g., yellow and purple regions of high streamwise vorticity in figure A.5). The regions which intersect the domain boundaries are discarded, thereby avoiding calculating statistics based on partially resolved vortices. Each identified region defines an independent vortex Ω^j and the first iteration estimate for the vortex orientation (equation A.8) and centroid (equation A.9) are calculated. In general, the vortex orientation will not be aligned with the original sample plane, rendering any statistics calculated inaccurate (Huang *et al.* 2006), hence, in the second iteration ($k = 2$), each vortex region is re-sampled from a plane normal to the average of the previous iterations vortex orientation and slice plane normal vector ($\hat{\mathbf{n}}^{(k+1)} = \hat{\mathbf{n}}^{(k)}/2 + \bar{\boldsymbol{\omega}}^{(k)}/2$), that intersects the previous iteration vortex centroid ($\bar{\mathbf{x}}^{(k)}$). From the re-sampled planes, continuous regions of the thresholded criterion field are once again detected and the one whose centroid is closest to that of the previous iteration is considered. The vortex orientation and centroid position are then updated based on equations A.8 and A.9. Since the updated centroid may now lay off the original input plane, the average between the previous iteration centroid and the centroid calculated on the new sample plane is projected onto the original slice plane to carry forward instead. The vortex detection code is considered converged when the centroid location residual ($\bar{\mathbf{x}}^{(k+1)} - \bar{\mathbf{x}}^{(k)}$) becomes less than the grid resolution. Once converged, the definition of the vortex boundaries is recomputed using a range of vorticity thresholds, $\alpha = \{0.01, 0.025, 0.05, 0.1, 0.25\}$, specified according to a contour of constant vorticity $\alpha||\boldsymbol{\omega}_{max}||$, facilitating the more accurate computation of vortex circulation according to equation A.4 with uncertainty specified by equation A.5.

Figure A.6 shows the results of the three-dimensional secondary vortex detection code for the DNS results for the range of $\mathrm{Re_D}$ investigated. However, before computing the final measurements of the secondary vortices, it is required to omit certain data obtained from the algorithm to avoid erroneous computation of statistics. First, duplicate vortex detections are omitted by filtering the data such that only vortices with unique centroid positions and time stamps are included. Second, vortex detections corresponding to the larger strength, spanwise oriented primary vortices must be omitted. To do so, the distributions of the vortex circulations with the solid angle their orientation makes with the spanwise z-axis is considered. Using k-mean clustering (Lloyd 1982) with the $L1$ distance metric for the solid angle data normalized such that $90° = 1$ and circulation data normalized by the maximum, the distributions are split into two, with the one with the higher mean, corresponding to the higher strength spanwise vortices, discarded for computation of any secondary vortex statistics. Figure A.7 shows the distributions of vortex circulation against the solid angle of the orientation of the detected vortex makes with the spanwise axis, for each Re.

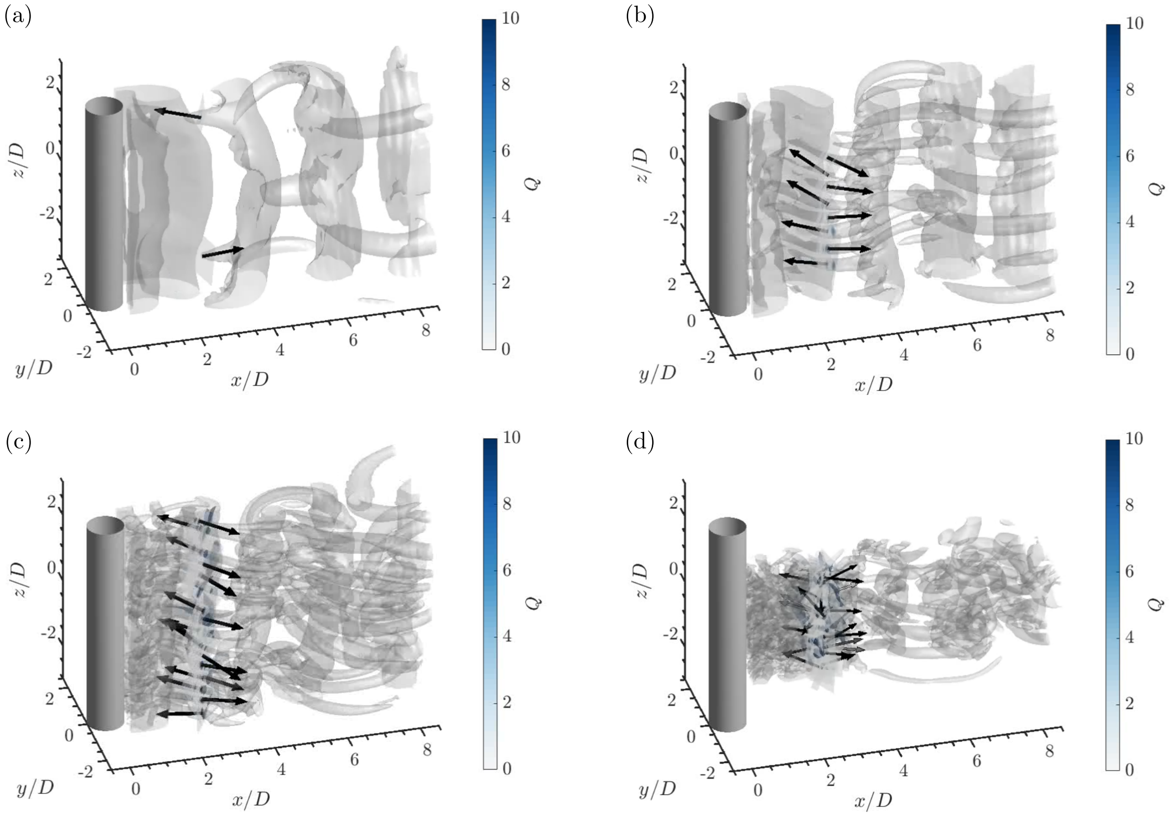

Figure A.6: Three-dimensional vortex tracking code detecting vortices crossing through $\hat{x} = 2.5$ at (a) $\mathrm{Re_D} = 220$, (b) $\mathrm{Re_D} = 300$, (c) $\mathrm{Re_D} = 800$, and (d) $\mathrm{Re_D} = 1575$.

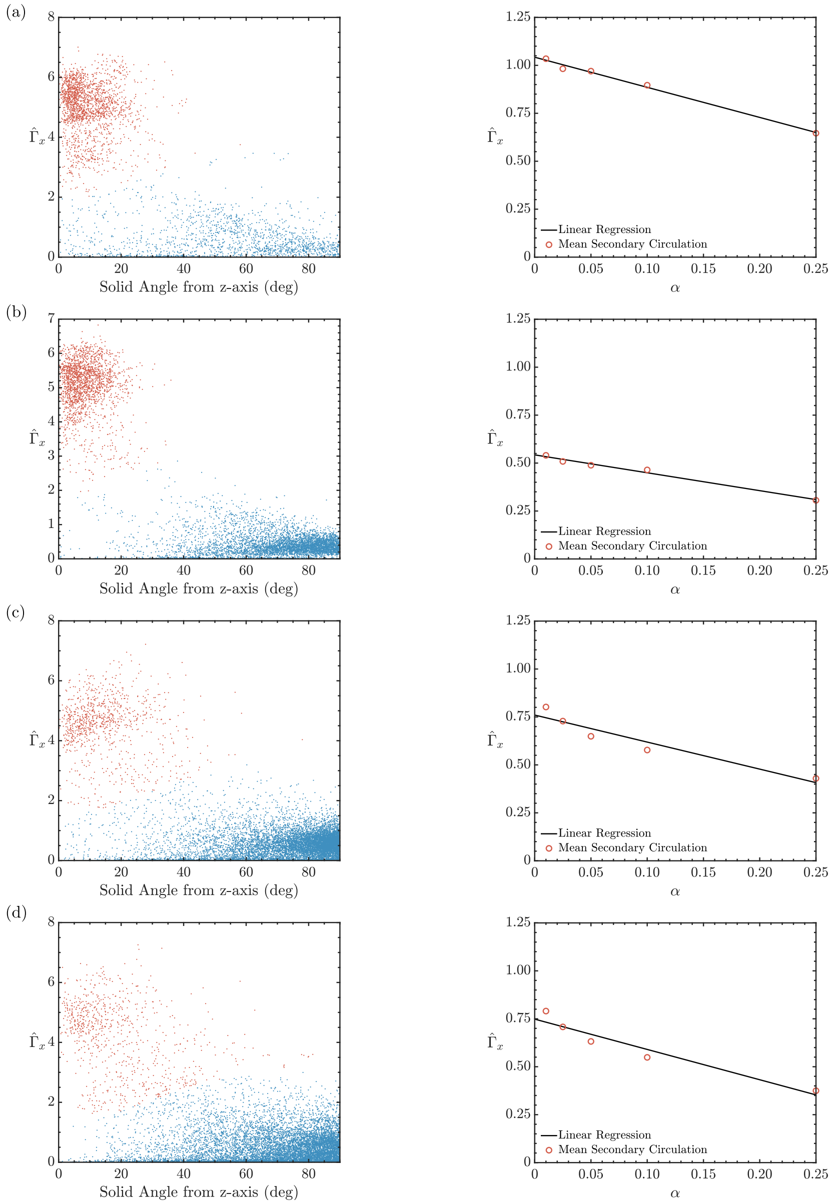

Figure A.7: (left) Distribution of the circulation of secondary vortices and the solid angle of their orientation with the spanwise axis, and (right) measurement and extrapolation of average secondary vortex circulation based on varying α for (a) $\mathrm{Re_D} = 220$, (b) $\mathrm{Re_D} = 300$, (c) $\mathrm{Re_D} = 800$, and (d) $\mathrm{Re_D} = 1575$.

Appendix B

Small Amplitude Force Model

B.1 Small amplitude coupled model

To investigate the coupling between the fluid-induced forcing and the cylinder response in VIV, the case of an infinitely small amplitude response at a single harmonic is considered. For infinitely small vibrations, the stability of several secondary mechanisms that affect the wake vortex dynamics and the forcing function will not be changed. Specifically, oblique vortex shedding modes will persist and not be forced to lock-in at a constant phase relation with the response frequency, as can be the case at higher amplitude VIV above the critical $A^\star > 0.05$ (Koopmann 1967, Bearman 1984). It is assumed that the primary shedding instability governing the symmetry and formation position of the primary vortices will be unaffected by the perturbations introduced into the flow field by small response oscillations.

B.1.1 Vortex force model

In the stationary cylinder wake, the fluctuating lift force is due entirely to the vortex force. In order to relate the magnitude of the forcing function to a function of wake vortex dynamics, an inviscid model is employed. Inviscid models of the stationary cylinder wake have been developed since the work of Kármán (1911), primarily using an infinite array of opposing signed vortices in order to evaluate the stability of the wake vortex structure and estimate mean drag (Saffman and Schatzman 1982). Recently, Stremler *et al.* (2011) also modeled 2P and 2C vortex wakes typically found in high amplitude VIV to investigate the spatio-temporally developing wake dynamics and their stability.

In order to predict the magnitude of fluctuating lift forces, an inviscid model of the wake is developed in the formation region where the wake vortices, due to their proximity to the cylinder surface and the vortex formation process, have not approached the wake equilibrium predicted by classical inviscid vortex street models (Kármán 1911, Chen 1972). Previous models (Chen 1972) consider the fluctuating lift induced by an infinite vortex

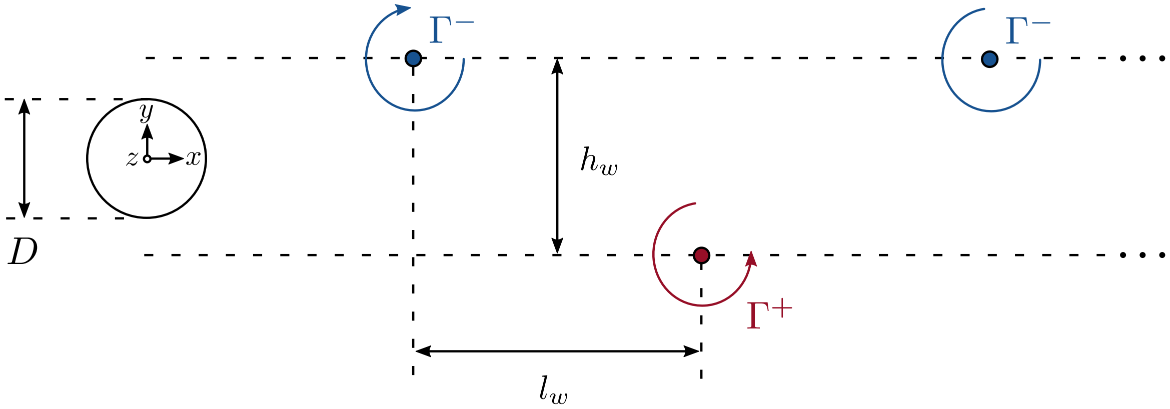

Figure B.1: Equilibrium inviscid model of the von Kármán wake.

street with equilibrium streamwise spacing (l_w) and transverse spacing (h_w) (figure B.1). However, since the induced forcing is due primarily to the vortex forming closest to the cylinder surface (Chen 1972), deviations from the equilibrium at formation before the vortices diffuse and increase their spacing in the wake (Kármán 1911) are necessary for model accuracy.

Since wake equilibrium arguments cannot be employed to compute the position of the forming vortices, the proposed model will instead focus on the magnitude of the surface pressure fluctuations predicted by the inviscid model. This is justified by the experimental observation that the sectional fluctuating lift force can be approximated accurately by the characteristics of the fluctuating surface pressures at the shoulders of the cylinder ($\theta = 90°$) (Ribeiro 1992, Norberg 2003), and the flow outside the boundary layers is primarily inviscid preceding separation at approximately $\theta \gtrsim 80°$, depending on $\mathrm{Re_D}$. The exact formulation of the RMS fluctuating sectional lift coefficient ($C_{L'}$), is based on the integration of the magnitude of all the measured RMS surface pressure coefficients ($C_{p'}$) weighted by their respective correlations with one another ($R_{pp}(\phi_1, \phi_2)$) (Norberg 2003):

$$C_{L'} = \frac{1}{2}\left(\int_0^{2\pi}\int_0^{2\pi} R_{pp}(\phi_1,\phi_2)C_{p'}(\phi_1)C_{p'}(\phi_2)\sin\phi_1\sin\phi_2 \mathrm{d}\phi_1\mathrm{d}\phi_2\right)^{1/2} \tag{B.1}$$

The sectional lift coefficient ($C_{L'}$) is then related to the total lift coefficient by integration of the spanwise coherence of the sectional lift ($R_{LL}(s)$) over the length of the cylinder (Kacker *et al.* 1974):

$$\gamma_L = \frac{C'_{L,T}}{LC'_L} = \frac{1}{L}\left(2\int_0^L (L-s)R_{LL}(s)\mathrm{d}s\right)^{1/2} \tag{B.2}$$

Notably, the spanwise coherence of the sectional lift is directly related to the spanwise coherence of the surface pressures at a given angular position ($R_{pp}(s)$) and the spanwise coherence of the wake vortex shedding ($R_{uu}(s)$) (Sarpkaya 1979).

If the approximation is made that the surface pressures measured on the respective top and bottom surfaces are completely out-of-phase (Norberg 2003), then the correlation between surface pressures on the top and bottom surface can be lumped into a single correlation (R_{BS}). This allows the sectional lift coefficient to be approximated according to equation B.3 (Ribeiro 1992, Norberg 2003). Assuming the fluctuating surface pressures have constant RMS as that measured at $\theta = \pm 90°$ ($C_{p'}(90°)$), and R_{BS} measured simply by the correlation of surface pressures on the top and bottom shoulders of the cylinder $R_{BS} = R_{pp}(90°, -90°)$, leads to further simplification of equation B.3.

$$\begin{aligned} C_{L'} &\approx \frac{1}{2}(1 - R_{BS}) \int_0^{\pi} C_{p'}(\phi) \sin\phi \mathrm{d}\phi \\ &\approx (1 - R_{pp}(90°, -90°)) C_{p'}(90°) \end{aligned} \tag{B.3}$$

Practically, the assumption that the RMS fluctuating surface pressures are constant on the surface of the cylinder is poor. However, due to the geometry of the cylinder, the lift force contribution will be dominated by the fluctuating pressure acting at $\theta = \pm 90°$, and measurements of RMS fluctuating surface pressure are nearly constant for $\theta > 90°$ (Norberg 2003). A weighted scheme for the integration of equation B.3 can be proposed instead, shown in equation B.4 where $C_{p'}(\theta)$ grows linearly from $0° < \theta \leq 90°$ and remains constant for $\theta > 90°$.

$$\begin{aligned} C_{L'} &\approx \frac{1}{2}(1 - R_{BS}) \left(\int_0^{\pi/2} \frac{2\phi}{\pi} C_{p'}(\phi) \sin\phi \mathrm{d}\phi + \int_{\pi/2}^{\pi} C_{p'}(\phi) \sin\phi \mathrm{d}\phi \right) \\ &\approx 0.818(1 - R_{pp}(90°, -90°)) C_{p'}(90°) \end{aligned} \tag{B.4}$$

This results in a reduction of the predicted fluctuating lift force of about 18%. Figure B.2a plots measurements of the RMS pressure coefficient at $\theta = 90°$, and figure B.2b plots measurements of the correlation coefficient between pressures at $\theta = \pm 90°$ for a range of $500 < \mathrm{Re_D} < 3.28 \times 10^5$ by (Norberg 2003). The magnitude of the surface pressure fluctuations and their correlation between sides of the cylinder are shown to vary considerably with $\mathrm{Re_D}$. Specifically, the pressure fluctuations on opposing sides of the cylinder are highly correlated in the range $1.0 \times 10^4 < \mathrm{Re_D} < 3.0 \times 10^5$, but are nearly uncorrelated in a region surrounding $\mathrm{Re_D} \approx 1.5 \times 10^3$ and following the drag crisis at $\mathrm{Re_D} > 3.0 \times 10^5$. Similarly, the RMS pressure coefficient is at a minimum of $C_{p'} \approx 0.05$ in a region surrounding $\mathrm{Re_D} \approx 1.5 \times 10^3$, but increases up to 700% in the higher $\mathrm{Re_D}$ range $1.0 \times 10^4 < \mathrm{Re_D} < 3.0 \times 10^5$.

In order to validate the model for the sectional RMS lift coefficient in equation B.4, the sectional RMS lift coefficient measurements of (Norberg 2003) are plotted in figure B.3 against the model proposed in Norberg (2003) of $C_{L'} \approx 1.5 C_{p'}(90°)$ and the model derived presently in equation B.4, which incorporates the changes in correlation of the fluctuating pressures that were shown to be significant in figure B.2b. A comparative

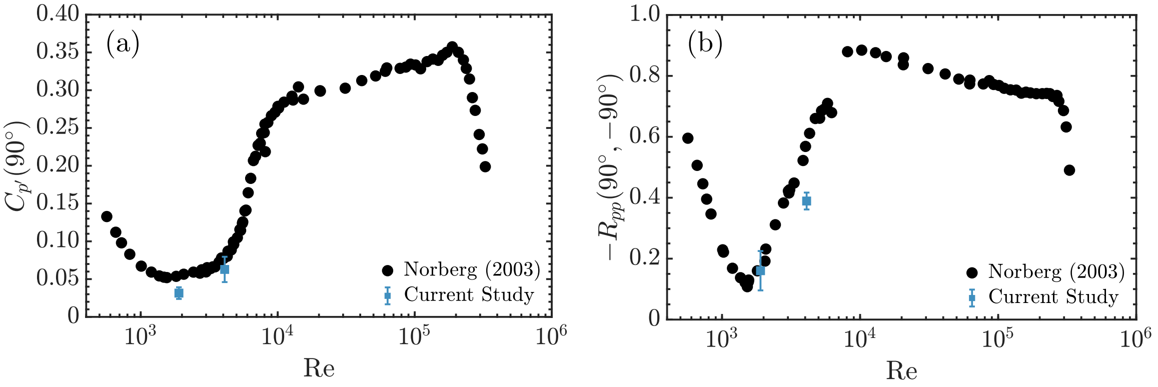

Figure B.2: Experimental measurements of (Norberg 2003) of (a) the RMS pressure coefficient at $\theta = 90°$ and (b) correlation coefficient of fluctuating pressures at $\theta = \pm 90°$.

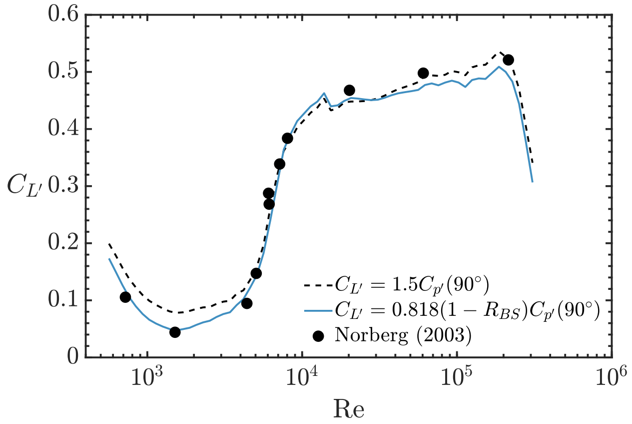

Figure B.3: Sectional RMS lift coefficient predicted by $1.5C_{p'}(90°)$, compared to equation B.4 and experimental data of (Norberg 2003).

analysis of the results in figure B.3 indicates that the model in equation B.4 predicts the fluctuating lift coefficient data with high fidelity over a wide range of $\mathrm{Re_D}$ compared to the simplified model, as it properly accounts for changes in surface pressure correlations with $\mathrm{Re_D}$, particularly in the range $0.75 \times 10^3 < \mathrm{Re_D} < 1.5 \times 10^3$ where the fluctuating lift is attenuated strongly due to both the weaker anti-correlation of the surface pressures and the reduction of the total magnitude of the pressure fluctuations at the shoulders of the cylinder. The model yields a small under prediction of the sectional RMS lift coefficient for higher $\mathrm{Re_D}$. Presumably, this is due to the use of only one RMS pressure coefficient at $\theta = 90°$ in the model. As $\mathrm{Re_D}$ increases, the peak RMS pressure coefficient occurs closer to $\theta = 80°$ and its magnitude becomes more pronounced (McClure and Yarusevych 2016a), causing the model to systematically under predict the sectional RMS lift coefficient by a small margin. Nevertheless, the model predicts sectional RMS lift within 10% over the large range of $\mathrm{Re_D}$, giving high confidence for its general application.

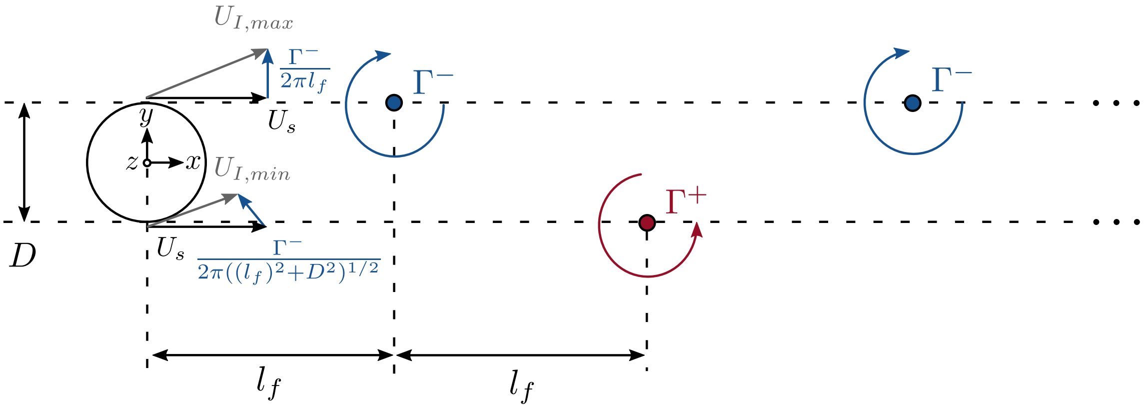

Figure B.4: Inviscid model of induced effects of vortex formation at $\theta = \pm 90^{\circ}$.

With the dependency of the fluctuating lift on the magnitude and correlation of surface pressures laid out, an inviscid model of the vortex formation is now used to gain an estimate for the magnitude of the surface pressure fluctuations in terms of quantifiable vortex properties near formation (figure B.4). Instead of modelling an infinite equilibrium wake, the primary focus of the model will be on a single vortex reaching its maximum circulation at the shedding time. The shedding vortex is positioned at a distance downstream of the cylinder axis determined by the vortex formation length (l_f) and a transverse position inline with the side of the cylinder ($\hat{y} = 0.5$). Secondary effects of previously formed vortices are considered by an infinite vortex street positioned a further distance ($l_w/2$) downstream of the shedding vortex, representing the equilibrium streamwise vortex spacing, and at constant transverse locations. In reality, the previously formed vortices will be continuously evolving towards a downstream wake equilibrium, which involves the gradual expansion of the transverse spacing of the vortices. However, we will soon neglect induced effects of previously formed vortices, and they are currently only included for illustrative purposes to estimate the magnitude of the second order effect of including them in the model.

The amplitude of the pressure fluctuation at $\theta = 90°$ is computed through the difference of the mean pressure at separation and the pressure at separation when a vortex reaches its maximum circulation at formation. The mean pressure at separation is determined by the edge velocity of the boundary layer at separation (U_s) and the steady Bernoulli equation ($p_s = p_0 + 1/2\rho(U_0^2 - U_s^2)$). The induced velocity of the formed vortex then leads to a perturbation away from the mean pressure through Bernoulli's equation $C_{p'}(90^{\circ}) = \frac{1}{2\sqrt{2}}(U_{I,max}^2 - U_{I,min}^2)/U_0^2$ (figure B.4). Justification of omission of the unsteady term in Bernoulli's equation can be obtained form the following argument. Suppose that the unsteady velocity fluctuations upstream of flow separation extending along a streamline to $x = -\infty$ are induced precisely in phase with the fluctuations at separation, reaching their maximum amplitude at the time of vortex formation considered in the model in figure B.4. This assumption is valid due to the global nature of the primary shedding instability and the incompressible flow assumption. Hence, along a streamline from a point s_1 at $x = -\infty$ to point s_2 at separation, the velocity fluctuations can be described by $u' = \beta(s)\sin(\omega_v t)$, where $\beta(s)$ is a weighted scalar function that is U_I at s_2 and decays to zero as s approaches s_1. Then the pressure induced at the separation point can be described by equation B.5.

$$p_I = p_0 - \int_{s_1}^{s_2} \rho \frac{\partial}{\partial t}(\boldsymbol{u} \cdot \hat{\boldsymbol{s}})\mathrm{d}s + \frac{1}{2}\rho(U_0^2 - (U_s^2 + U_I^2 \sin^2(\omega_v t))) \tag{B.5}$$

$$p_I = p_0 - \int_{s_1}^{s_2} \frac{\partial}{\partial t}(\beta(s)\sin(\omega_v t))\mathrm{d}s + \frac{1}{2}\rho(U_0^2 - (U_s^2 + U_I^2 \sin^2(\omega_v t))) \tag{B.6}$$

$$p_I = p_0 + \int_{s_1}^{s_2} \beta(s)\omega_v \cos(\omega_v t)\mathrm{d}s + \frac{1}{2}\rho(U_0^2 - (U_s^2 + U_I^2 \sin^2(\omega_v t))) \tag{B.7}$$

and it can be deduced from equation B.7 that at the times when the induced velocity at separation reaches its maximum (e.g., $t = n\pi/2\omega_v$: $n \in \mathbb{Z}$), the contribution of the unsteady integral term is exactly zero.

Assuming the contribution to the induced velocity near the cylinder surface is dominated by the currently forming vortex, the induced velocity at the top surface (figure B.4) is:

$$\begin{aligned} U_{I,max}^2 = &\left(U_s - \frac{\Gamma D}{2\pi((2l_f)^2 + D^2)} - \frac{\Gamma D}{2\pi((4l_f)^2 + D^2)} - \ldots\right)^2 \\ &+ \left(\frac{\Gamma}{2\pi l_f} - \frac{\Gamma(2l_f)}{2\pi((2l_f)^2 + D^2)} + \frac{\Gamma}{2\pi(3l_f)} - \ldots\right)^2 \end{aligned} \tag{B.8}$$

and the induced velocity at the bottom surface is:

$$\begin{aligned} U_{I,min}^2 = &\left(U_s - \frac{\Gamma D}{2\pi(l_f^2 + D^2)} - \frac{\Gamma D}{2\pi((3l_f)^2 + D^2)} - \frac{\Gamma D}{2\pi((5l_f)^2 + D^2)} + \ldots\right)^2 \\ &+ \left(\frac{\Gamma l_f}{2\pi(l_f^2 + D^2)} - \frac{\Gamma}{2\pi(2l_f)} + \frac{\Gamma(3l_f)}{2\pi((3l_f)^2 + D^2)} + \ldots\right)^2 \end{aligned} \tag{B.9}$$

It can be shown that the for $U_{I,max}$, truncation to the leading term results in omission of terms whose partial sums equate to a maximum of approximately 10% of the magnitude of the leading term, for characteristics values of vortex formation length and vortex wake spacing. For example, in the first term in equation B.8, the secondary terms have magnitudes $[-0.1, -0.02, -0.0082, -0.0044, -0.0028, \ldots]$, and in the second term in equation B.8, the sum of the alternating pairs beyond the leading term have magnitudes $[-0.0318, -0.0092, -0.0042, -0.0024, -0.0015, \ldots]$ when expressed as fractions of the leading term and $\hat{l}_f = 1$ and $\hat{l}_w = 4$. For $U_{I,min}$, leading terms in both squared term in equation B.9 may be significant, as they are both induced by the formed vortex, and secondary terms are neglected, leading to the following truncated model for the induced velocities.

$$U_{I,max}^2 = \left(U_s - \frac{\Gamma D}{2\pi(l_f^2 + D^2)}\right)^2 + \frac{\Gamma^2}{4\pi^2 l_f^2} \tag{B.10}$$

$$U_{I,min}^2 = \left(U_s - \frac{\Gamma D}{2\pi(l_f^2 + D^2)}\right)^2 + \left(\frac{\Gamma l_f}{2\pi(l_f^2 + D^2)} - \frac{\Gamma}{2\pi(2l_f)}\right)^2 \tag{B.11}$$

expanding terms and substituting in the typical non-dimensional relations for vortex circulation ($\hat{\Gamma} = \Gamma/U_0 D$) and formation length ($\hat{l}_f = l_f/D$) gives the following model for fluctuating pressure RMS at $\theta = 90^{\circ}$ based on the peak-to-peak pressures obtained from plugging in the minimum and maximum induced velocities into the unsteady Bernoulli equation:

$$\begin{aligned} C_{p'}(90^{\circ}) &= \frac{1}{2\sqrt{2}}(U_{I,max}^2 - U_{I,min}^2)/U_0^2 \\ &= \frac{3\hat{\Gamma}^2}{16\pi^2 \hat{l}_f^2} + \frac{\hat{\Gamma}}{\pi(\hat{l}_f^2 + 1)} - \frac{\hat{\Gamma}}{\pi(4\hat{l}_f^2 + 1)} \end{aligned} \tag{B.12}$$

and the RMS sectional lift coefficient is:

$$C_L' = 0.818(1 - R_{pp}(90°, -90°)) \left(\frac{3\hat{\Gamma}^2}{16\pi^2 \hat{l}_f^2} + \frac{\hat{\Gamma}}{\pi(\hat{l}_f^2 + 1)} - \frac{\hat{\Gamma}}{\pi(4\hat{l}_f^2 + 1)}\right) \tag{B.13}$$

This reproduces some characteristics of models for fluctuating lift acting on a bluff body with a Kármán vortex street, derived using an infinite ideal inviscid vortex street (equation B.14, Chen 1972), such as a dependency on $\hat{\Gamma}^2$ and an approximate dependency on the square inverse of a streamwise length scale.

$$C_L' = \left(\frac{\hat{\Gamma}}{\hat{l}_w}\right)^2 \hat{l}_w \tanh\left(\pi \frac{\hat{h}}{\hat{l}_w}\right) \tag{B.14}$$

However, the consideration of the near wake formation characteristics in the current model, as opposed to the far wake, leads to additional dependencies on the correlation of the surface pressure fluctuations, and an additional linear dependency on vortex circulation. The explicit modelling of the near wake effects presumably is vital to the accuracy of the model as the vortex positions and strengths are far from their far wake equilibrium values (Kármán 1911).